UNIVERSITY OF OKLAHOMA
GRADUATE COLLEGE

CONSTRAINT OF VEGETATION PHOTOSYNTHESIS AND RESPIRATION MODEL (VPRM) PARAMETER UNCERTAINTY USING A MARKOV CHAIN MONTE CARLO (MCMC) TECHNIQUE

A THESIS
SUBMITTED TO THE GRADUATE FACULTY
in partial fulfillment of the requirements for the
Degree of
MASTER OF SCIENCE

By

STEVEN JESTER
Norman, Oklahoma
2023

CONSTRAINT OF VEGETATION PHOTOSYNTHESIS AND RESPIRATION MODEL (VPRM) PARAMETER UNCERTAINTY USING A MARKOV CHAIN MONTE CARLO (MCMC) TECHNIQUE

A THESIS APPROVED FOR THE
SCHOOL OF METEOROLOGY

BY THE COMMITTEE CONSISTING OF

Dr. Xuguang Wang, Chair

Dr. Sean Crowell

Dr. Jason Furtado

Acknowledgments

First, I'd like to thank my advisors, Sean Crowel, Xuguang Wang, and Jason Furtado for all the help and advice they have given me throughout my time at the University of Oklahoma. With their help, I have learned to be a better student and researcher and I hope to carry their lessons on into the next step in my career. I'd also like to thank the faculty and staff of the OU School of Meteorology for giving me the opportunity to continue my education. Thanks must also be given to Xiao-Ming Hu for his help with the inner workings of the VPRM. I want to thank the members of the GeoCarb Mission Collaboration and in particular Qingyu Wang, Will Keely, and Hélène Peiro for their support.

Data for this study comes from the Mead, Nebraska (Ne2, Ne3), Battle Creek, Michigan (KM1), and Rosemount, Minnesota (Ro1) eddy flux towers as part of the AmeriFlux flux tower network and is used under the AmeriFlux CC-BY-4.0 License. Funding for the AmeriFlux data portal was provided by the U.S. Department of Energy Office of Science.

The computing for this project was performed at the OU Supercomputing Center for Education & Research (OSCER) at the University of Oklahoma (OU).

I would not be where I am today without my late parents, Edward and Rebecca Jester, and the guidance that they provided me in my formative years. Though they are no longer here, I know that they would be proud of how far I have come. I'd also like to thank my brother, Rick. His stoicism and dry wit combined with his knowledge of software engineering have proven invaluable. I send my sincerest gratitude to my wife's parents, Chuck and Eileen Rankin, for accepting me into their family with open arms.

Most importantly, to my wonderful and amazing wife, Marie: your constant presence and reassurance has been the greatest support I have received over the last few

years. You are simultaneously my rock and my constant companion on the journey of life. Thank you for always being at my side. I love you.

Contents

List Of Tables

List Of Figures

Abstract

Modeling the changes to the carbon cycle and their effects on the atmosphere is a key area of research for understanding climate change. The Vegetation Photosynthesis and Respiration Model (VPRM) is a light-use efficiency model that models the biogenic flux of carbon dioxide (CO_2) known as Net Ecosystem Exchange (NEE). Previous studies used methods such as non-linear least squares in order to calibrate the parameters. One other method of calibrating parameters is the Metropolis-Hastings Markov Chain Monte Carlo (MCMC) technique. The MCMC technique has not been used previously due to how computationally expensive it is. The benefit of the MCMC technique is that it is a Bayesian technique that generates a probability distribution of the posterior parameters. This probability distribution can be used to quantify uncertainty in the posterior parameters.

This study compares the MCMC technique to a non-linear least squares technique to determine its viability for use in the calibration of the VPRM. Observation data from four cropland sites from the AmeriFlux eddy covariance tower network were used with both techniques to fit the model to observations. Using the parameter correlations generated from the posterior probability distributions, a series of experiments were conducted to determine the sensitivity of the optimization of VPRM to the state vector.

The analysis of this study found that the MCMC technique reduced the RMSE of the VPRM predicted flux by more than a factor of two. The technique is viable on a site-by-site scale. However, scaling up the algorithm to more sites and land use types (LUTs) would be very computationally expensive and would necessitate the use of small batches of sites and averaging the results to prove viable. Using a single LUT to cover all cropland may also be too general and splitting the cropland LUT into different types of crops may further improve the VPRM overall.

Chapter 1

Introduction

The impact of greenhouse gasses on climate change and the atmosphere is indisputable. Carbon dioxide (CO_2) is the most important greenhouse gas with concentrations of CO_2 rising to over 410 ppm in 2020 (Friedlingstein et al., 2022). The full effects of this greenhouse gas on the climate and its feedback on land-atmosphere fluxes are beginning to be understood. This better understanding comes from monitoring stations at the in-situ level such as the AmeriFlux eddy covariance tower network and atmospheric inversions using data from satellites such as the Orbiting Carbon Observatory-2 (OCO-2) and the Orbiting Carbon Observatory-3 (OCO-3) instrument on the International Space Station (ISS) (Crisp et al., 2017).

An important tool for understanding the carbon cycle and its feedback on climate change is the use of numerical modeling. The interaction between land and atmospheric carbon is modeled via tracking concentrations of CO_2 in the atmosphere as CO_2 moves in and out of the atmosphere in the form of biogenic flux. The Vegetation Photosynthesis and Respiration Model (VPRM) developed by Mahadevan et al. (2008) is a simple light-efficiency model that models the net ecosystem exchange (NEE) flux of CO_2 by splitting this flux into equations covering ecosystem respiration (ER) and gross ecosystem exchange (GEE) which represents the CO_2 taken up by photosynthesis and summing them to produce an estimate of NEE (Gourdji et al., 2022). VPRM adds onto a previous model called the Vegetation Photosynthesis Model (VPM) by adding the equation for ER and adding a non-linear term to the equation for GEE that takes into account the response of GEE to light (Xiao et al., 2004a,b; Mahadevan et al., 2008).

The VPRM employs several parameters that must be calibrated to each land use type (LUT) in order to estimate NEE. This calibration is usually done by minimizing mismatches between model predictions and eddy covariance data, such as from AmeriFlux (Hilton et al., 2013, 2014; Gourdji et al., 2022). Previous studies used this method because methods such as Markov Chain Monte Carlo (MCMC) are computationally expensive (Hastings, 1970; Hilton et al., 2013; Metropolis et al., 1953). This study uses the MCMC method to provide a distribution of estimated parameter values to quantify the uncertainty of the parameters involved with their full joint posterior distribution.

1.1 Past Work on the VPRM

Many studies have examined estimating the flux of CO_2 using numerical modeling and satellite data (Xiao et al., 2004a,b; Mahadevan et al., 2008; Hilton et al., 2013, 2014; Hu et al., 2020, 2021; Gourdji et al., 2022). Xiao et al. (2004a) developed the predecessor to the VPRM, the VPM, to estimate GEE in the needleleaf evergreen forest of Howland Forrest, Maine during the growing periods from April to early November for the years 1998 until 2001. The authors used EVI and LSWI derived from the VEGETATION (VGT) sensor on the SPOT-4 satellite, as well as observations of GEE from the AmeriFlux eddy covariance tower at Howland Forrest. They also analyzed the seasonal and interannual dynamics of the Enhanced Vegetation Index (EVI) and the Land Surface Water Index (LSWI) compared to other satellite-derived indices such as the Normalized Difference Vegetation Index (NDVI) and the Moisture Stress Index (MSI) respectively. Xiao et al. (2004a) found that while the seasonal dynamics of EVI were different in magnitude and phase from NDVI, EVI had a stronger linear relationship to GEE than NDVI. They also found that there was a close relationship between MSI and LSWI at the Howland Forrest site. The authors found that using the VPM with EVI and LSWI produced a reasonable agreement

between modeled and observed GEE in terms of seasonal dynamics and in a simple linear regression model. Xiao et al. (2004a) acknowledge that there were discrepancies between modeled and observed GEE in certain periods of their study time frame and attribute the errors to three factors: the sensitivity of the VPM to PAR and air temperature, the error in calculating the observed GEE from the measured NEE at the site, and errors from how EVI and LSWI are derived and the effects of angular geometry on reflectance data.

Xiao et al. (2004b) expanded the work of the previous paper by using the VPM to estimate GEE in the deciduous broadleaf forest of Harvard Forest, Massachusetts. The authors compared using EVI and LSWI derived from the VGT sensor on the SPOT-4 satellite during the period of April 1998 to December 2001 against EVI and LSWI derived from the MODIS sensor on the NASA Terra satellite from the year 2001. As the orbiting periods are different for each satellite, 10 and 8 days respectively, the authors used different length composites of flux and meteorological data for use in their modeling simulations. Xiao et al. (2004b) also compared EVI derived from the VGT sensor to NDVI. Similarly to their previous study, the authors found that the seasonal dynamics of EVI better match the phase and amplitude of GEE than NVDI. They also found a stronger linear relationship between EVI and GEE than between NVDI and GEE. When modeling GEE, both VGT and MODIS performed reasonably well in their respective VPM simulations.

The study by Mahadevan et al. (2008) added to the previous studies by introducing a respiration component and developing the original VPRM. The authors used flux tower data from 11 sites for calibration of the VPRM parameters across LUTs and another 11 sites were used for testing. Mahadevan et al. (2008) used nonlinear least squares to optimize the model parameters. Overall, correlation coefficients for results from the calibration sites ranged from 0.6 to 0.9, indicating a relatively good fit to the observed NEE. Correlation coefficients from the testing sites also indicated a good

fit for the parameters, except for one outlying site. The authors noted that certain elements of water stress may not be accurately captured using the VPRM due to satellite-derived indices not capturing the aftereffects of severe drought. Uncertainties in the VPRM arise partly from the limited resolution of vegetation classification and differences in the vegetation makeup between calibration and validation sites.

Hilton et al. (2013) expanded on the previous study by using 65 observation sites in their optimization. The authors examined the time period between 2000 and 2006 due to the availability of the MODIS and flux observation data respectively. They chose to find parameter values that minimized the sum of squared errors (SSE) through an algorithm known as differential evolution (DE) (Price et al., 2005). The authors chose this algorithm instead of MCMC due to the computational expense that would be required, even though DE only provides point estimates of the parameters and not a probability density function for each parameter. The authors partitioned the observations based on different temporal and spatial groupings to form nine unique parameter sets. Hilton et al. (2013) focused much of their analysis on spatial structure, devising a covariance function to test for spatial correlation. The authors found that their parameter values across all parameter sets were similar to those found in Mahadevan et al. (2008). They note that while the VPRM parameters seem to be similar for many LUTs, the limits of the spatial density of eddy covariance towers at the time made it difficult to rule out any covariances that could contribute to both observation and model error.

Hilton et al. (2014) used the parameter optimizations from their previous paper and performed a cross-validation analysis using a further 27 flux tower locations. The authors evaluated model performance using a penalized sum of squared errors (PSSE). They also evaluated the spatial performance of the VPRM on a continental scale by using surface temperature and downward surface radiation from reanalysis products and satellite-based indices derived from upscaled MODIS data. Results

from this analysis indicate that grouping a number of sites by LUT and using all available data provides a set of parameters that best fits the observations without overfitting the data. Using these parameters going forward in their analysis, Hilton et al. (2014) found that the optimal parameter set was able to upscale both temporally and spatially. They do acknowledge that how the sites were chosen and the simplicity of the VPRM itself could explain many of the mismatches found as the model was upscaled.

Hu et al. (2020) used the WRF model coupled with the VPRM (WRF-VPRM) and the median values found from the optimization performed by Hilton et al. (2013) to perform a downscaling analysis over the contiguous United States (CONUS). The authors also investigated three case studies using WRF-VPRM simulations and CO_2 concentration observations from the ACT-America 2016 summer field campaign. Evaluating the meteorology output of the WRF-VPRM against observations found that the model exhibited high correlation coefficients for surface temperature and surface dew point temperature. Correlation coefficients for the amount of precipitation were lower. Comparisons of WRF-VPRM CO_2 concentrations to posterior fluxes from the CarbonTracker 2017 (CT2017) products show a general agreement with regional and temporal differences through the domain. The case studies, in particular the case of August 5, 2016, near Lincoln, Nebraska, showed that the WRF-VPRM concentration distributions in height were similar to the observations from the ACT-America aircraft.

Gourdji et al. (2022) conducted a study into expanding the VPRM and used the results to develop the new respiration equation shown in Equation (2.3). The parameters for the new equation were optimized using a least squares approach, first by optimizing the respiration equation using nighttime data and then optimizing the GEE equation using daytime data. The authors then compared the simulations of VPRM to other similar biosphere models, the Carnegie-Ames Stanford Approach

(CASA) model and the Simple Biosphere model version 4 (SiB4), to analyze the sensitivity between models. The authors found that comparing the newer respiration to the older one on a site-to-site basis showed a remarkable improvement in modeling respiration with the newer equation. The VPRM using the new respiration equation was shown to be mostly unbiased compared to the observations throughout the year whereas other variations of the VPRM as well as CASA and SiB4 showed greater magnitude in biases. This improvement is also shown in the spatial simulations. However, the new model does not perform better in these spatial simulations than CASA. This suggests that there are some processes that are still not captured by the improved respiration equation.

Hu et al. (2021) revisited their previous paper and used the improved respiration equation from Gourdji et al. (2022) to investigate the August 5, 2016, Lincoln, Nebraska case study. The authors also compared the skill of the improved respiration equation to simulate nighttime CO_2 peaks against the original equation from Mahadevan et al. (2008). The authors found that simulations using Equation (2.3) matched the observations of nighttime peaks better than simulations using Equation (2.2). The improved respiration equation also simulates the CO_2 concentration band ahead of a cold front from the case study of August 5, 2016, from the previous study better than the original equation from Mahadevan et al. (2008).

1.2 Connecting the Past to This Study

The methods used in prior studies have been shown to produce results that have investigated how changes in weather over time have affected NEE and the concentrations of CO_2 in our atmosphere. Because the VPRM is a land-surface model, it can be used to investigate short-to-medium-term effects on future climate change. The MCMC process allows for a new examination of these ideas. Given the joint posterior parameter distribution, correlation analyses can be conducted to investigate the

effects of photosynthesis and respiration and how correlated each physical process represented in the VPRM equations, such as temperature and water stress, are to each other.

1.3 Thesis Structure

In Chapter 2, the methodology of this study is discussed including the technical details regarding the VPRM and MCMC algorithm. Chapters 3 and 4 present and discuss results that are the most interesting with regard to the science questions presented above. Additional results are included in Appendices A - D. Finally, conclusions for this study are discussed in Chapter 5.

Chapter 2

Methodology

2.1 Observations from AmeriFlux Towers

Table 2.1: AmeriFlux sites used in this study

Site ID	Location	Crop Type	Water Source	Data Available	Data Frequency	Reference
Ne2	Mead, NE	Soybean and corn rotation	Irrigated	2001-2020	Hourly	Suyker (2022a)
Ne3	Mead, NE	Soybean and corn rotation	Rainfed	2001-2020	Hourly	Suyker (2022b)
KM1	Battle Creek, MI	Corn	Rainfed	2009-2021	Half-hourly	Robertson and Chen (2022)
Ro1	Rosemount MN	Soybean and corn rotation	Rainfed	2004-2016	Half-hourly	Baker et al. (2022)

The observation data used in this study comes from the AmeriFlux eddy covariance towers as depicted in Table 2.1. The data used in this study, plotted in Figure 2.1, comes from a five-year period beginning January 1, 2010, 00:00 UTC and ending January 1, 2015, 00:00 UTC. All NEE data are smoothed using a three-hour running

mean and then filtered for any missing flux or meteorological data. The data is filtered again by dropping any data with a nighttime friction velocity, u^*, less than 0.1 ms^{-1} and also dropping any data where NEE or u^* falls outside 2σ from the mean (Mahadevan et al., 2008).

Looking at the patterns that are shown in Figure 2.1, the respiration and GEE balance each day leading to a neutral net flux during the non-growing season between late autumn and early spring, while there is a large diurnal variability in NEE during the summer growing season. The time series for the Mead, NE AmeriFlux sites (Ne2 and Ne3) show little to no gaps in the data while the results for the Battle Creek, MI (KM1) and Rosemount, MN (Ro1) sites show some gaps where the data were not gap-filled. The second time series for each site shows the annual and seasonal patterns of the observed 2 m temperature and incoming solar radiation.

2.2 Data from the NASA MODIS Sensors

EVI and LSWI for use with VPRM were calculated using Equations (2.6) and (2.7) with data from the NASA MODIS MCD43A4.V061 nadir reflectance product and bands as mentioned in Section 2.3 (Schaaf and Wang, 2021). The MODIS data were downloaded using the Application for Extracting and Exploring Analysis Ready Samples (AppEEARS) developed by the NASA EOSDIS Land Processes Distributed Active Archive Center (LP DAAC, AppEEARS Team, 2022). Shown in the top panels of Figure 2.1, EVI and LSWI have clear annual and seasonal patterns where LSWI and EVI reach minima during the non-growing season and maxima in the growing season. While data from MODIS was filtered for quality-checked data, there are times outside the growing season where the calculated EVI and LSWI show anomalous readings.

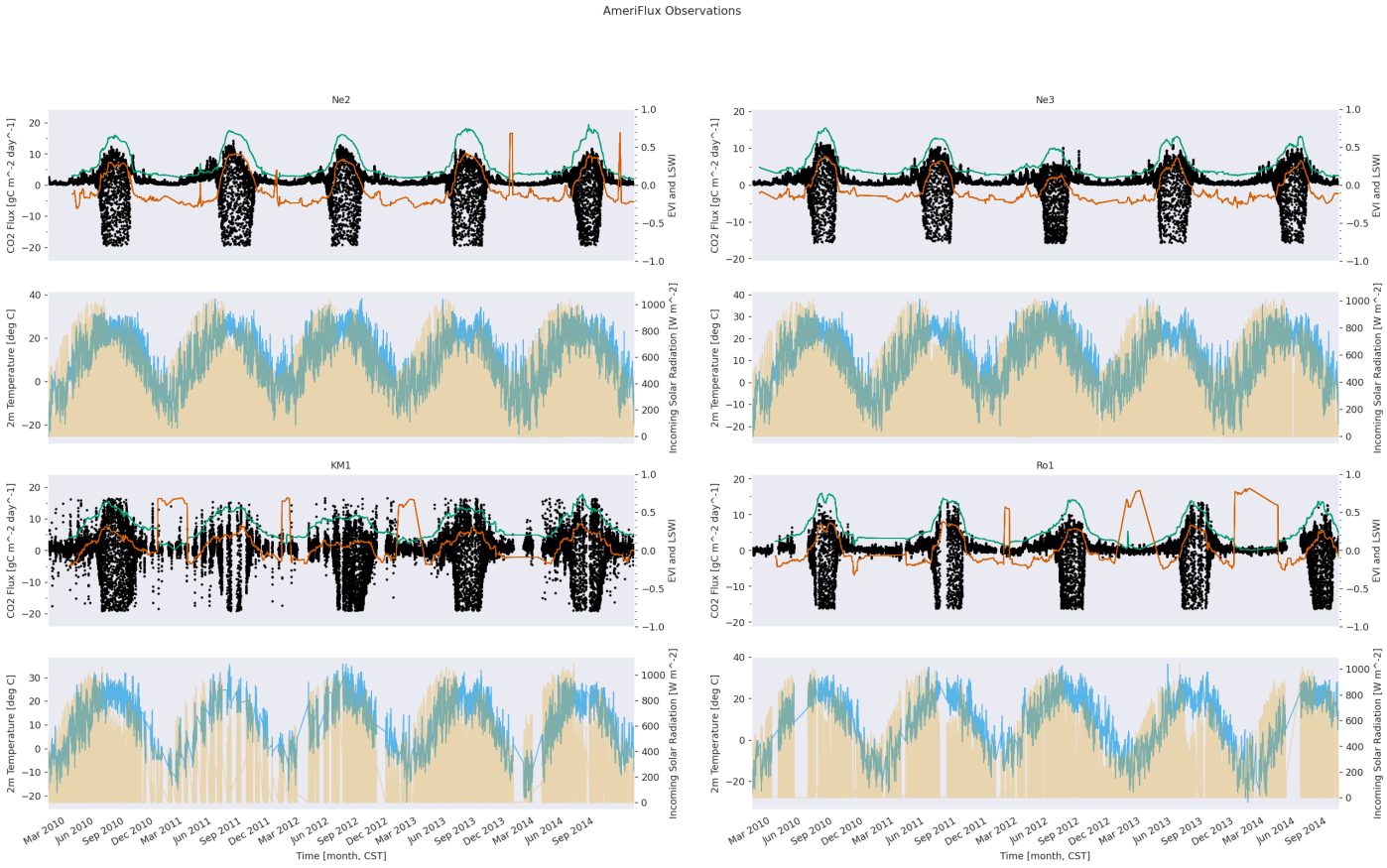

Figure 2.1: A set of time series plots showing the observation variables from the (top left:) Ne2, (top right:) Ne3, (bottom left:) KM1, and (bottom left:) Ro1 AmeriFlux eddy tower sites. Plotted here are (top panels:) the observed NEE (black), EVI (green), LSWI (orange), (bottom panels:) observed 2m temperature (sky blue) and observed incoming shortwave radiation (yellow).

2.3 The Vegetation Photosynthesis and Respiration Model (VPRM)

The VPRM is a simple light-efficiency diagnostic model providing a system of equations that predict NEE (Mahadevan et al., 2008). At its core, the VPRM models the two aspects of NEE into a source term in ER and a sink term in GEE (Eq. (2.1)).

$$NEE = ER + GEE \tag{2.1}$$

Originally, Mahadevan et al. (2008) developed the ER equation as a linear function of air temperature alone using an offset and a linear parameter (Eq. (2.2)). This was chosen by Mahadevan et al. (2008) as a deliberately simple model in order to facilitate online calculations (Gourdji et al., 2022). As a function of temperature, Mahadevan et al.'s original formulation for respiration did not take into account variables such as moisture or biomass. Recent studies have expanded upon the ER equation to take these factors into account as well as to add a non-linear response to temperature that better captures respiration response to changes in temperature (Gourdji et al., 2022; Hu et al., 2021). Equation (2.3) shows this by using EVI as a representation of biomass, adding scaling terms that quantify water stress, and using a quadratic dependence on temperature (Gourdji et al., 2022; Nagler et al., 2005).

$$ER = \alpha \cdot T + \beta \tag{2.2}$$

$$ER = \beta + \alpha_1 \cdot T + \alpha_2 \cdot T^2 + \gamma \cdot EVI + k_1 \cdot W_{scale2} + k_2 \cdot W_{scale2} \cdot T + k_3 \cdot W_{scale2} \cdot T^2 \tag{2.3}$$

The temperature used in Equation (2.3) is the surface air temperature for most situations. When the air temperature is below a certain threshold during the winter, the temperature is modified using Equation (2.4). This allows for situations where the

soil temperature would be warmer than the air which would allow for some respiration to continue (Gourdji et al., 2022). Vegetation water stress is quantified using a scaling term that incorporates LSWI as shown in Equation (2.5) (Chandrasekar et al., 2010).

$$T_a < T_{crit}: \quad T = (T_a - T_{crit}) \cdot T_{scale2} + T_{crit} \tag{2.4}$$

$$W_{scale2} = \frac{LSWI - LSWI_{min}}{LSWI_{max} - LSWI_{min}} \tag{2.5}$$

EVI and LSWI are indices derived from reflectance data from satellite-borne sensors such as the Moderate Resolution Imaging Spectrometer (MODIS) sensors on the NASA Aqua and Terra satellites (Chandrasekar et al., 2010; Nagler et al., 2005; Huete et al., 2002). EVI, calculated using Equation (2.6), parameterizes photosynthesis in terms of reflectance in the near-infrared band (841-876 nm, Band 2) and the visible red (620-670 nm, Band 1) and blue (459-479 nm, Band 3) bands. The values of G, C_1, C_2, and L used in Equation (2.6) in this study are 2.5, 6.0, 7.5, and 1 respectively (Xiao et al., 2004a). Xiao et al. (2004a) noted that EVI was correlated with leaf area index (LAI) and therefore could be used as a representation of vegetation greenness. LSWI, shown in Equation (2.7), uses reflectances in both near-infrared and shortwave infrared (1628-1652 nm, Band 6) bands to represent how much water is found in the vegetation canopy and surrounding soil (Chandrasekar et al., 2010; Xiao et al., 2004a).

$$EVI = G \times \frac{\rho_{nir} - \rho_{red}}{\rho_{nir} + (C_1 \times \rho_{red} - C_2 \times \rho_{blue}) + L} \tag{2.6}$$

$$LSWI = \frac{\rho_{nir} - \rho_{swir}}{\rho_{nir} + \rho_{swir}} \tag{2.7}$$

VPRM uses Equation (2.8) to model the sink term of GEE (Mahadevan et al., 2008). This equation is similar to the equation of the VPM developed to simulate GEE (Xiao et al., 2004a,b). Mahadevan et al. (2008) added the final, non-linear term

to account for the response of GEE to the saturation of light. This response to light takes the form of photosynthetically active radiation (PAR) and its half-saturation constant (PAR_0). Equation (2.8) uses multiple scaling terms that modify the uptake of CO_2 based on temperature, water stress, and leaf age (Mahadevan et al., 2008).

$$GEE = \lambda \cdot T_{scale1} \cdot W_{scale1} \cdot P_{scale} \cdot EVI \cdot PAR \cdot \frac{1}{1 + \frac{PAR}{PAR_0}} \tag{2.8}$$

The temperature scaling factor in Equation (2.9) limits light-use efficiency as a function of air temperature and the minimum, maximum, and optimal temperatures for photosynthesis (Xiao et al., 2004a). These minimum, maximum, and optimal temperatures vary by LUT and are generally taken from values in literature (Mahadevan et al., 2008). If the air temperature falls below the minimum for photosynthesis, the temperature scaling factor is set to zero (Mahadevan et al., 2008; Xiao et al., 2004a,b).

$$T_{scale1} = \frac{(T - T_{min})(T - T_{max})}{\left[(T - T_{min})(T - T_{max}) - (T - T_{opt})^2\right]} \tag{2.9}$$

The water stress factor for GEE is different than the one shown in Equation (2.5). Hu et al. (2021) and Gourdji et al. (2022) used (2.5) in the ER equation because it had a better fit for some LUTs when compared to Equation (2.10) and equivalent fits for the remaining LUTs. GEE still uses Equation (2.10) which is found in both VPM and VPRM (Mahadevan et al., 2008; Xiao et al., 2004a,b)

$$W_{scale1} = \frac{1 + LSWI}{1 + LSWI_{max}} \tag{2.10}$$

Leaf age, also known as phenology, measures the effects of the stresses of age on the production of photosynthesis and is measured in Equation (2.11) (Xiao et al., 2004a,b). For the evergreen LUT, the leaf age factor is assumed to be equal to 1 year-round (Mahadevan et al., 2008).

$$P_{scale} = \begin{cases} \frac{1+LSWI}{2} & \text{green up period} \\ 1 & \text{full leaf period} \\ \frac{1+LSWI}{2} & \text{senescence period} \end{cases} \tag{2.11}$$

The parameters for Equations (2.3) and (2.8) (β, α_1, α_2, γ, k_1, k_2, k_3, λ, and PAR_0) form the state vector that is optimized for VPRM. Prior parameter values come from the cropland LUT parameters found in Hu et al. (2021), with parameter uncertainty derived from the standard deviation (σ) of the parameter values across the different land surface types (Table 2.2).

Table 2.2: VPRM parameters, their units, and the prior values from Hu et al. (2021)

Parameter	Units	Prior Values	Prior σ
β	$\mu mol\ CO_2\ m^{-2}s^{-1}$	-0.156	4.925
α_1	$\mu mol\ CO_2$ $m^{-2}s^{-1}{}^{\circ}C^{-1}$	0.072	0.599
α_2	$\mu mol\ CO_2$ $m^{-2}s^{-1}{}^{\circ}C^{-2}$	-0.001	0.017
γ	$\mu mol\ CO_2\ m^{-2}s^{-1}$	5.501	2.281
k_1	$\mu mol\ CO_2\ m^{-2}s^{-1}$	0.145	3.160
k_2	$\mu mol\ CO_2$ $m^{-2}s^{-1}{}^{\circ}C^{-1}$	-0.152	0.437
k_3	$\mu mol\ CO_2$ $m^{-2}s^{-1}{}^{\circ}C^{-2}$	0.016	0.013
λ	$\mu mol\ CO_2/\mu mol$ PAR	-0.078	0.019
PAR_0	$\mu mol\ PAR$ $m^{-2}s^{-1}$	2,782	79.1

2.4 Non-linear Least Squares Curve Fitting

As mentioned above, previous studies have used least squares techniques to optimize the VPRM (Hilton et al., 2013; Hu et al., 2021; Gourdji et al., 2022). Replicating these techniques as a first-principles analysis will give insight into what can be expected during the MCMC analysis. The drawback is that the subspace trust region interior reflective approach (STIR) technique used in this study itself is not Bayesian and therefore will not give a true sense of quantifying posterior uncertainty. In order to quantify posterior uncertainty, samples from a prior distribution must be used with the STIR technique to produce a posterior distribution.

This study uses the STIR non-linear least squares algorithm developed by Branch et al. (1999) in the SciPy Python module to fit the equations of the VPRM to the observed data. Two sensitivity analysis experiments of the STIR approach are conducted in this study. Each experiment is given 1,000 prior parameter values drawn randomly from a Gaussian distribution of the priors mentioned in Table 2.2. The first experiment fits the parameters to the entire five-year set of observations at once (Sec. 3.1). The other experiment fits the respiration parameters to Equation (2.3) using nighttime data and fits the photosynthesis parameters to Equation (2.8) using daytime data assuming the optimized respiration parameters in the first step. By sampling the prior parameter space, an estimate of the posterior uncertainty distribution can be derived from the STIR fitting technique.

2.5 Metropolis-Hastings Markov Chain Monte Carlo (MCMC)

The Markov Chain Monte Carlo (MCMC) algorithm was first developed by Metropolis et al. (1953) in an effort to find a general method to calculate properties of state

equations. Hastings (1970) expanded on this method by generalizing the method further in cases of asymmetric proposal distributions. The combined algorithm, called the Metropolis-Hastings MCMC algorithm, is computationally expensive. However, this algorithm is useful for finding and quantifying posterior parameter distributions in many applications (Xu et al., 2006).

The Metropolis-Hastings MCMC algorithm starts with an *a priori* first guess for the state vector of the model for each separate chain ($\boldsymbol{\theta_0}$, Eq. (2.12)). A new guess for the state vector is generated as a random draw from a proposal distribution ($q(\boldsymbol{\theta'}|\boldsymbol{\theta_t})$, Eq. (2.13)). A symmetric distribution, such as a Gaussian or uniform distribution centered at $\boldsymbol{\theta_t}$, is generally used so that ${}^{q(\boldsymbol{\theta'}|\boldsymbol{\theta_t})}/_{q(\boldsymbol{\theta_t}|\boldsymbol{\theta'})} = 1$. In this study, $q(\boldsymbol{\theta'}|\boldsymbol{\theta_t})$ is chosen to be a Gaussian distribution centered at $\boldsymbol{\theta_t}$.

$$\boldsymbol{\theta} = \begin{bmatrix} \beta & \alpha_1 & \alpha_2 & \gamma & k_1 & k_2 & k_3 & \lambda & PAR_0 \end{bmatrix}^T \tag{2.12}$$

$$\boldsymbol{\theta'} \sim q(\boldsymbol{\theta'}|\boldsymbol{\theta_t}), \quad t = 0, 1, ..., N \tag{2.13}$$

The next step is to calculate log-likelihood for both $\boldsymbol{\theta_t}$ and $\boldsymbol{\theta'}$ (Eq. (2.14)). Using these log-likelihood values and the proposal distributions, an acceptance ratio (A) is calculated using Equation (2.15). Since the proposal distribution in this study is a symmetric, Gaussian distribution, the acceptance ratio becomes the ratio of log-likelihood values.

$$L = \ln(\sigma^2_{NEEmodeled}\sqrt{2\pi}) - \frac{\sum_{i=0}^{M}((NEE_{modeled,i} - NEE_{obs,i})^2)}{2\sigma^2_{NEEmodeled}} \tag{2.14}$$

$$A = \min\left\{1, \frac{L_{\boldsymbol{\theta'}}}{L_{\boldsymbol{\theta_t}}} \frac{q(\boldsymbol{\theta'}|\boldsymbol{\theta_t})}{q(\boldsymbol{\theta_t}|\boldsymbol{\theta'})}\right\} \tag{2.15}$$

The acceptance ratio is then compared against a random number (U) generated from a uniform distribution ranging $[0, 1]$ to determine whether to accept the proposed $\boldsymbol{\theta'}$ (Eq. (2.16)). If the acceptance ratio is greater than or equal to this random

number, then the proposed $\boldsymbol{\theta'}$ is carried over to the next iteration. Otherwise, the current $\boldsymbol{\theta_t}$ is carried over to the next iteration. The algorithm continues in this fashion for a set number of iterations to tune the covariance of the underlying proposal distribution. Then, the algorithm uses the tuned covariance and runs for a larger number of iterations in order to sample enough of the parameter space to generate the underlying posterior probability distribution (Metropolis et al., 1953; Hastings, 1970; Xu et al., 2006).

$$\boldsymbol{\theta_{t+1}} = \begin{cases} \boldsymbol{\theta'} & A \geq U \\ \boldsymbol{\theta_t} & A < U \end{cases}, \quad t = 0, 1, ..., N-1 \tag{2.16}$$

This study uses the PyMC Python module to run the MCMC algorithm in four parallel chains for 1,000 tuning iterations and 10,000 main sampling iterations per chain for a total of 40,000 posterior sampling iterations per study site (Wiecki et al., 2022). The PyMC module also generates 10,000 prior parameter sets for comparison of the tuned prior and posterior distributions. The 95% confidence intervals of each distribution along with their medians are compared against the observations from each site. This study runs several fitting experiments by fitting nighttime data using Equation (2.3) via the MCMC technique and daytime data using (2.8) via the STIR approach. This two-step approach is used to limit the computational expense of running a second MCMC step. Other experiments look into the parameter correlations for both prior and posterior distributions and how dropping variables that have high correlations in the posterior affects the model's fit to the observation data. Two of these experiments focus on setting the α_2 and k_3 parameters to zero while the other two experiments set λ and PAR_0 to the values that Hu et al. (2021) set them. Holding the light-use parameters to these values is necessary for these experiments because setting them to zero would either result in Equation (2.8) equaling zero or a division by zero in the non-linear term.

Chapter 3

Results

3.1 Comparing Simultaneous and Night/Day Separate Fitting

3.1.1 Root Mean Squared Error Analysis

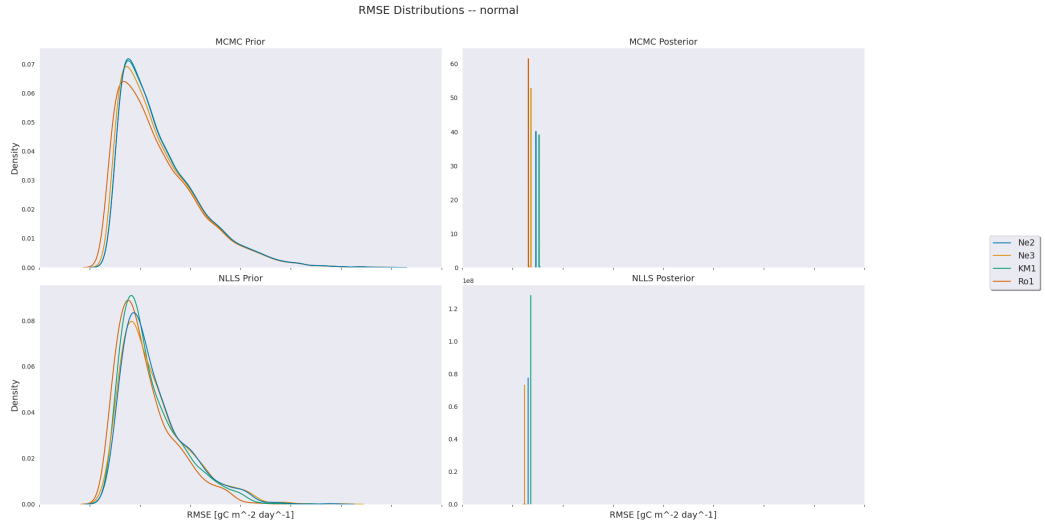

Figure 3.1: A kernel density estimate (KDE) plot of VPRM root mean square error (RMSE) for using MCMC (top row) and NLLS (bottom row) fitting techniques for the Ne2 (blue), Ne3 (gold), KM1 (green) and Ro1 (red) AmeriFlux sites when fitting all data points simultaneously. The left (right) column represents the RMSE of the prior (posterior) distributions of parameters.

In order to compare the goodness of fit between the prior and posterior distributions, this study uses root mean square error (RMSE) of model predicted net flux within each parameter set. Figure 3.1 and the top sections of Tables 3.1 and 3.2 show the RMSE distributions when fitting the whole dataset simultaneously. In general, NLLS posterior RMSE medians for all four AmeriFlux sites show a general agreement

in fit within 1.6 $gC\ m^{-2}\ day^{-1}$ of each other. This is in contrast with MCMC where the MCMC RMSE medians for each site are within 2.2 $gC\ m^{-2}\ day^{-1}$ of each other. Prior distributions for both fitting techniques agree among the sites with around 10 and 16 $gC\ m^{-2}\ day^{-1}$ for the NLLS and MCMC prior median RMSE distributions respectively. The improvement in the posterior fits is statistically significant with median RMSEs around 3 and 4 $gC\ m^{-2}\ day^{-1}$ for NLLS and MCMC respectively. The spread of these distributions, represented in this study by the median absolute deviation from the median (MAD), shows an expected decrease. Using the NLLS, the prior MAD dropped from around 3.5 $gC\ m^{-2}\ day^{-1}$ to below the threshold of significant digits (<0.001 $gC\ m^{-2}\ day^{-1}$) for every site. The MCMC technique narrowed the MAD spread from around 7 $gC\ m^{-2}\ day^{-1}$ to around 2 $gC\ m^{-2}\ day^{-1}$, representing a significant decrease in the spread of the distribution.

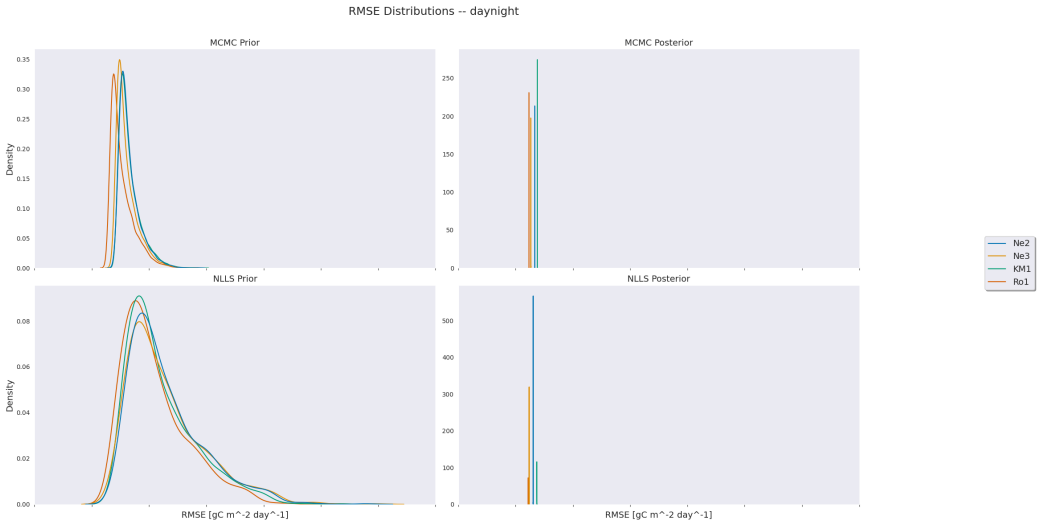

Figure 3.2: Same as Figure 3.1 but fitting ER and GEE separately.

In contrast, fitting ER to nighttime data and GEE to daytime data separately produces a different improvement of fit for the MCMC fitting technique (Fig. 3.2, Table 3.2). While the MCMC improvement from around 6 $gC\ m^{-2}\ day^{-1}$ prior median RMSE to around 3 $gC\ m^{-2}\ day^{-1}$ posterior median RMSE is still significant, it only improves the fit to the data to half of the prior median RMSE. The MCMC prior

MAD when fitting the two processes separately from around 3.15 $gC\ m^{-2}\ day^{-1}$ to around 0.3 $gC\ m^{-2}\ day^{-1}$ for the posterior MAD, representing a change in magnitude in terms of the spread. Fitting the STIR NLLS algorithm separately produces similar results as fitting the whole data set simultaneously (Table 3.1). Prior median RMSE improves from around 10 $gC\ m^{-2}\ day^{-1}$ to a posterior median RMSE around 3 $gC\ m^{-2}\ day^{-1}$. The narrowing of the MAD spread is not as drastic when fitting the NLLS using the two-step method ranging from a prior MAD of around 3.5 $gC\ m^{-2}\ day^{-1}$ to a posterior of around 0.002 $gC\ m^{-2}\ day^{-1}$. Only one AmeriFlux site, the irrigated Ne2 from Mead, Nebraska, showed a posterior MAD below the threshold of significant digits using this two-step fitting method.

3.1.2 Parameter Distributions

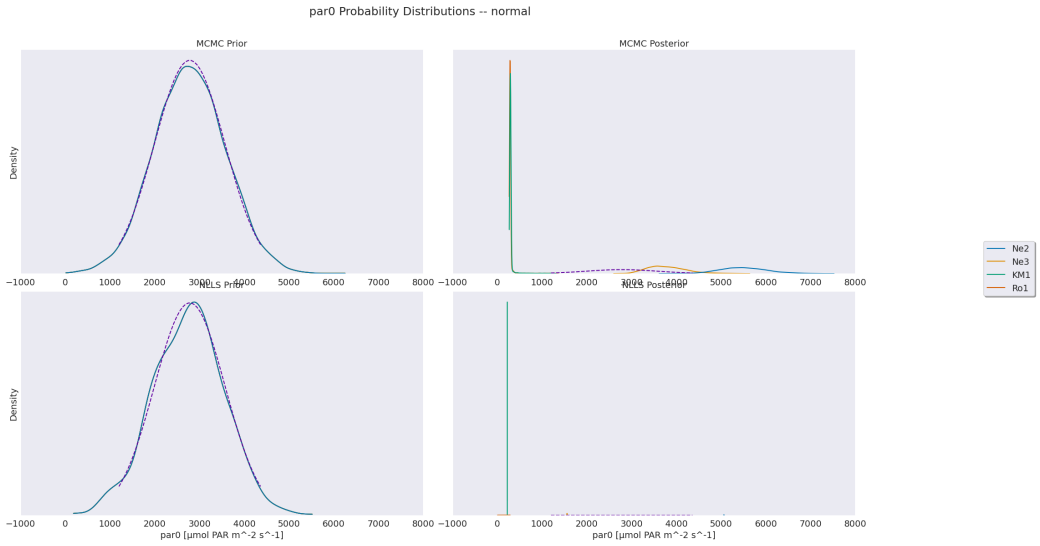

Figure 3.3: A KDE plot similar to Figure 3.1 except for the PAR_0 parameter distributions while fitting all data points simultaneously. A normal distribution based on the prior values and standard deviation from Hu et al. (2021) is included in a purple-dashed line.

Fitting the whole dataset simultaneously significantly reduced the MAD of all parameters (Tables A.1 and A.2, Figs. 3.3 - 3.5). Most parameters, such as the γ and λ parameters, demonstrate a unimodal posterior distribution that appears Gaussian

Table 3.1: NEE RMSE and Median Absolute Deviation (MAD) for each NLLS experiment using the medians of the prior and posterior parameter distributions. Units $gC\ m^{-2}\ day^{-1}$

		Ne2	Ne3	KM1	Ro1
Normal	Prior Median RMSE	10.955	11.150	10.205	9.507
	Prior MAD	3.477	3.817	3.358	3.239
	Posterior Median RMSE	3.046	2.350	3.650	2.129
	Posterior MAD	<0.001	<0.001	<0.001	<0.001
ER/GEE Separately	Prior Median RMSE	10.955	11.150	10.205	9.507
	Prior MAD	3.477	3.817	3.358	3.239
	Posterior Median RMSE	3.068	2.360	3.693	2.182
	Posterior MAD	<0.001	0.001	0.002	0.004
α_2 drop	Prior Median RMSE	10.257	10.053	9.610	8.842
	Prior MAD	3.181	3.340	2.951	3.158
	Posterior Median RMSE	3.065	2.365	3.694	2.179
	Posterior MAD	<0.001	0.001	0.002	0.005
k_3 drop	Prior Median RMSE	11.269	10.997	10.542	9.494
	Prior MAD	3.814	4.060	3.743	3.434
	Posterior Median RMSE	3.155	2.474	3.695	2.199
	Posterior MAD	0.002	0.001	0.002	0.002
λ drop	Prior Median RMSE	10.830	10.899	10.185	9.355
	Prior MAD	3.467	3.709	3.375	3.201
	Posterior Median RMSE	3.104	2.376	3.721	2.205
	Posterior MAD	<0.001	<0.001	0.001	0.001
PAR_0 drop	Prior Median RMSE	11.117	11.143	10.246	9.633
	Prior MAD	3.532	3.823	3.334	3.322
	Posterior Median RMSE	3.067	2.358	3.878	2.326
	Posterior MAD	<0.000	0.001	0.015	0.015

Table 3.2: NEE RMSE and Median Absolute Deviation (MAD) for each MCMC experiment using the medians of the prior and posterior parameter distributions. Units $gC\ m^{-2}\ day^{-1}$

		Ne2	Ne3	KM1	Ro1
Normal	Prior Median RMSE	16.443	16.270	16.462	16.003
	Prior MAD	6.963	6.954	6.980	6.945
	Posterior Median RMSE	4.645	3.654	5.269	3.151
	Posterior MAD	2.215	1.743	2.514	1.504
ER/GEE Separately	Prior Median RMSE	6.829	6.401	6.881	5.692
	Prior MAD	3.148	3.143	3.175	3.142
	Posterior Median RMSE	3.340	2.649	3.790	2.327
	Posterior MAD	0.038	0.031	0.030	0.021
α_2 drop	Prior Median RMSE	6.804	6.410	6.806	5.681
	Prior MAD	3.136	3.131	3.164	3.124
	Posterior Median RMSE	3.389	2.693	3.825	2.390
	Posterior MAD	0.038	0.030	0.030	0.020
k_3 drop	Prior Median RMSE	7.827	7.252	7.672	6.223
	Prior MAD	3.098	3.098	3.101	3.099
	Posterior Median RMSE	3.203	2.501	3.718	2.211
	Posterior MAD	0.037	0.029	0.029	0.020
λ drop	Prior Median RMSE	6.793	6.372	6.843	5.666
	Prior MAD	3.136	3.134	3.158	3.135
	Posterior Median RMSE	3.406	2.693	3.821	2.356
	Posterior MAD	0.038	0.031	0.031	0.021
PAR_0 drop	Prior Median RMSE	6.848	6.413	6.896	5.698
	Prior MAD	3.129	3.126	3.146	3.130
	Posterior Median RMSE	3.343	2.645	3.977	2.479
	Posterior MAD	0.038	0.031	0.031	0.021

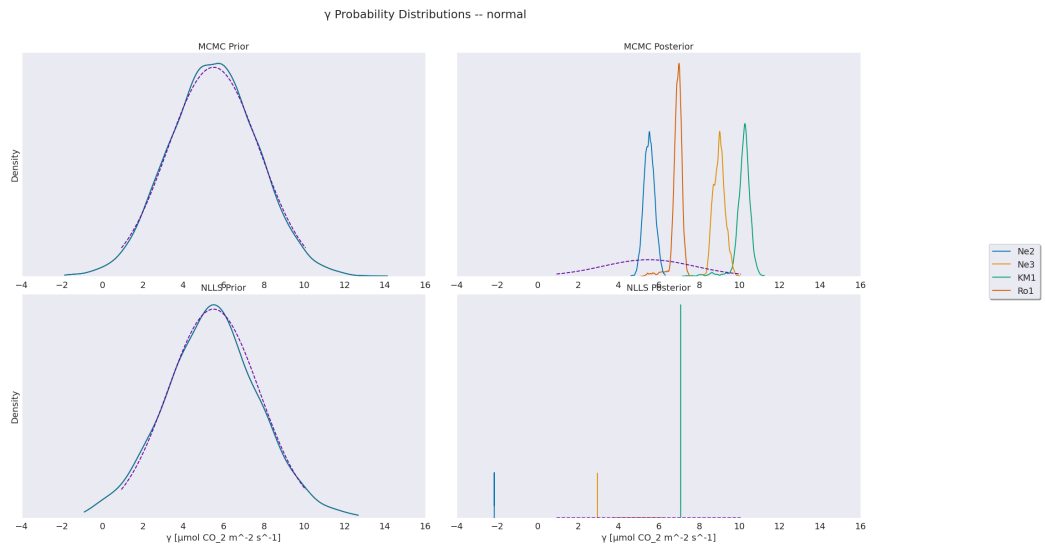

Figure 3.4: Same as Figure 3.3 but for the γ parameter distributions.

in nature (Figs. 3.4 and 3.5). The posterior parameter fit for these two parameters in particular shows some significant disagreement among the different AmeriFlux tower sites. Figure 3.4 shows that both the MCMC and NLLS median prior distributions for the γ parameter representing vegetative greenness agree at approximately 5.45 $\mu mol\ CO_2\ m^{-2}s^{-1}$. The posterior median MCMC fits for each of the sites range from 5.53 $\mu mol\ CO_2\ m^{-2}s^{-1}$ for the Ne2 site to 10.24 $\mu mol\ CO_2\ m^{-2}s^{-1}$ for the KM1 site, a difference of 4.71 $\mu mol\ CO_2\ m^{-2}s^{-1}$. The NLLS displays a larger range in posterior medians at 9.24 $\mu mol\ CO_2\ m^{-2}s^{-1}$. These ranges are significantly larger than the posterior MAD for both fitting techniques. The MCMC posterior MAD was about 0.170 $\mu mol\ CO_2\ m^{-2}s^{-1}$ for each site while the NLLS posterior MAD fell below the significant digit threshold (<0.0001 $\mu mol\ CO_2\ m^{-2}s^{-1}$). Similarly, the λ parameter shows the same general agreement among the AmeriFlux sites for the MCMC and NLLS median prior parameter fit at -0.078 $\mu mol\ CO_2/\mu mol\ PAR$ (Fig. 3.5). Median posterior fits show a range of 0.164 and 0.135 $\mu mol\ CO_2/\mu mol\ PAR$ for NLLS and MCMC respectively which is significantly larger than the posterior MAD which was around 0.001 $\mu mol\ CO_2/\mu mol\ PAR$ for the MCMC posterior MAD and below the significant figure threshold for the NLLS posterior MAD. Some parameters

such as PAR_0 and the λ posterior for the Ro1 AmeriFlux have some skewness to their posterior distributions (Fig. 3.3). In particular, the KM1 and Ro1 AmeriFlux sites have their posterior PAR_0 distributions heavily skewed to the left with posterior medians below 300 $\mu mol\ PAR\ m^{-2}s^{-1}$ for both MCMC and NLLS fits. This is in contrast to the fits for the Mead, Nebraska sites which were >3,000 $\mu mol\ PAR\ m^{-2}s^{-1}$ for the MCMC posterior medians and the Ne2 NLLS posterior median while the Ne3 NLLS posterior median was around 1,600 $\mu mol\ PAR\ m^{-2}s^{-1}$. These median values for Ne2 and Ne3 seem more realistic than the median values for KM1 and Ro1 given the prior value from Hu et al. (2021) of 2,782 $\mu mol\ PAR\ m^{-2}s^{-1}$.

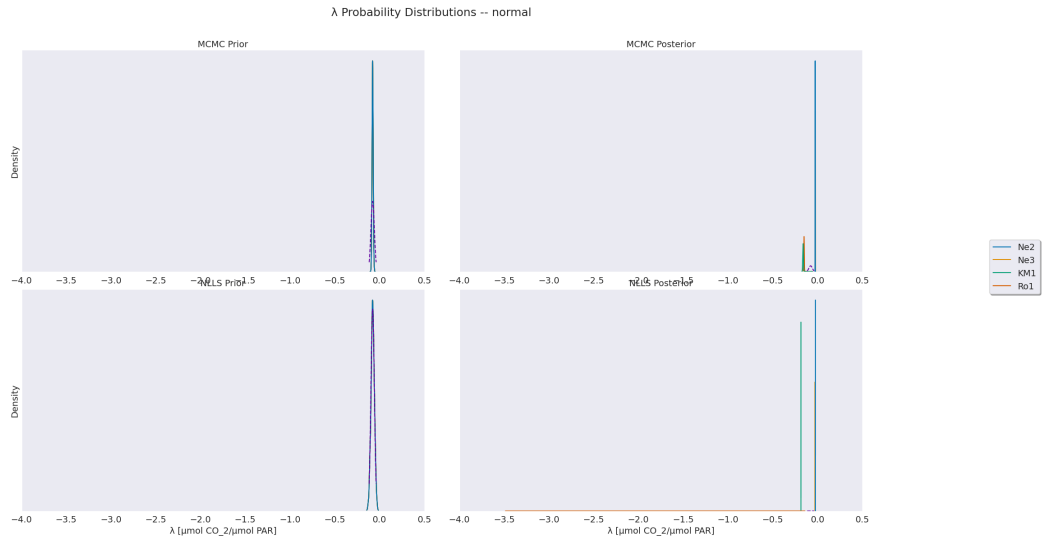

Figure 3.5: Same as Figure 3.3 but for the λ parameter distributions.

Fitting the parameters in the two-step process of fitting ER to nighttime data and GEE to daytime data shows similar results to fitting the whole dataset simultaneously. An outlier in the results is the PAR_0 posterior distribution medians (Fig. 3.6). The value that the NLLS algorithm found of 6,000 $\mu mol\ PAR\ m^{-2}s^{-1}$ is at the upper bound set prior to the experiment. Because the NLLS algorithm searches for a least-squares solution to fitting the data, boundaries must be set for certain parameters to keep the values realistic. The upper bound of 6,000 $\mu mol\ PAR\ m^{-2}s^{-1}$ was chosen to represent a value slightly above the global mean of shortwave radiation reaching

the top of the atmosphere converted into PAR via Equation (3.1) (Mahadevan et al., 2008; Hu et al., 2020). The posterior MAD for the PAR_0 parameter is essentially 0 $\mu mol\ PAR\ m^{-2}\ s^{-1}$. This is due to the entire posterior distribution reaching the upper bound set for the NLLS approach that was used for fitting the light-use parameters.

$$PAR \approx SW \times 0.505 \tag{3.1}$$

The MAD of the posterior probability distributions of γ and λ in this two-step experiment such as those shown are larger than their counterparts when fitting the full dataset (Figs. 3.7 and 3.8). For γ, the posterior MAD of the MCMC posterior is around 0.2 $\mu mol\ CO_2\ m^{-2}s^{-1}$ while the NLLS posterior MAD is around 0.08 $\mu mol\ CO_2\ m^{-2}s^{-1}$. The λ parameter had a posterior MAD of around 0.0003 $\mu mol\ CO_2/\mu mol\ PAR$ for the MCMC posterior distributions and the NLLS posterior distributions for the Ne2 and Ne3 sites while the KM1 and Ro1 NLLS posterior MAD for the λ parameter are around 0.0036 $\mu mol\ CO_2/\mu mol\ PAR$. This indicates that this method of fitting the ER and GEE equations separately creates more uncertainty in the posterior distributions. This is possibly due to fitting less amount of data than fitting the whole data set simultaneously. However, the MAD of each parameter's posterior distribution significantly decreased when compared to the prior parameter distributions with γ MCMC and NLLS prior MAD of around 1.5 $\mu mol\ CO_2\ m^{-2}s^{-1}$. The prior MAD for the λ parameter differs as the MCMC prior MAD is 0.0044 $\mu mol\ CO_2/\mu mol\ PAR$ while the NLLS prior MAD is 0.0123 $\mu mol\ CO_2/\mu mol\ PAR$.

3.1.3 Time Series Comparison

Analyzing the time series of modeled NEE compared to the observed shows that while the NLLS and MCMC techniques may find posterior parameters that show a better RMSE when compared to the prior, the overall fit to the observed NEE contains

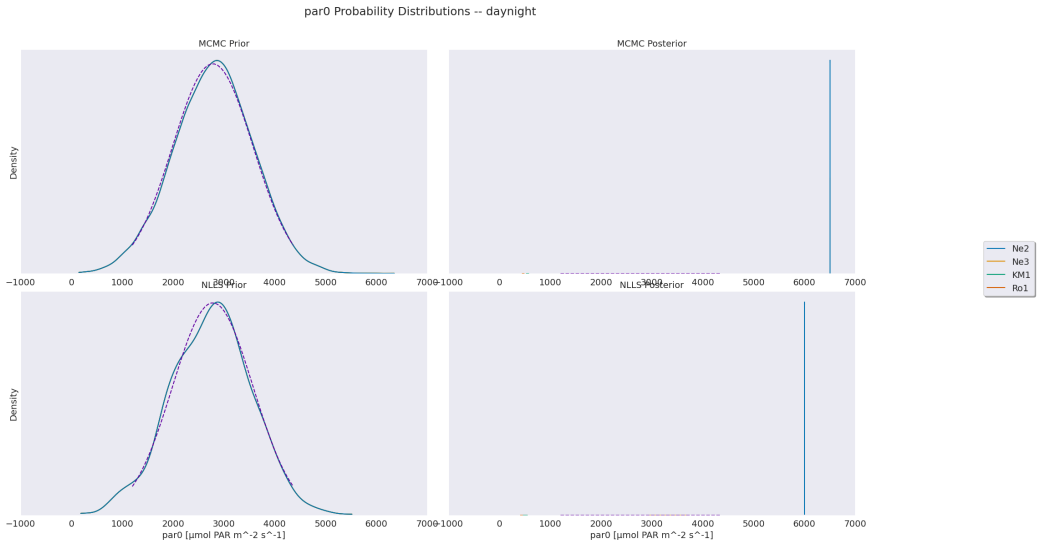

Figure 3.6: Same as Figure 3.3 but with fitting ER and GEE separately

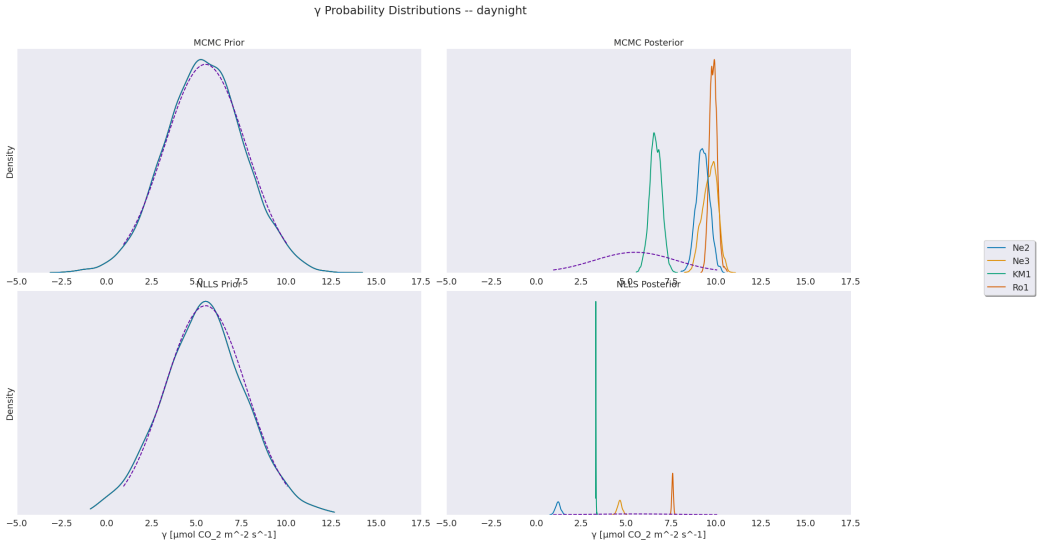

Figure 3.7: Same Figure 3.4 but with fitting ER and GEE separately

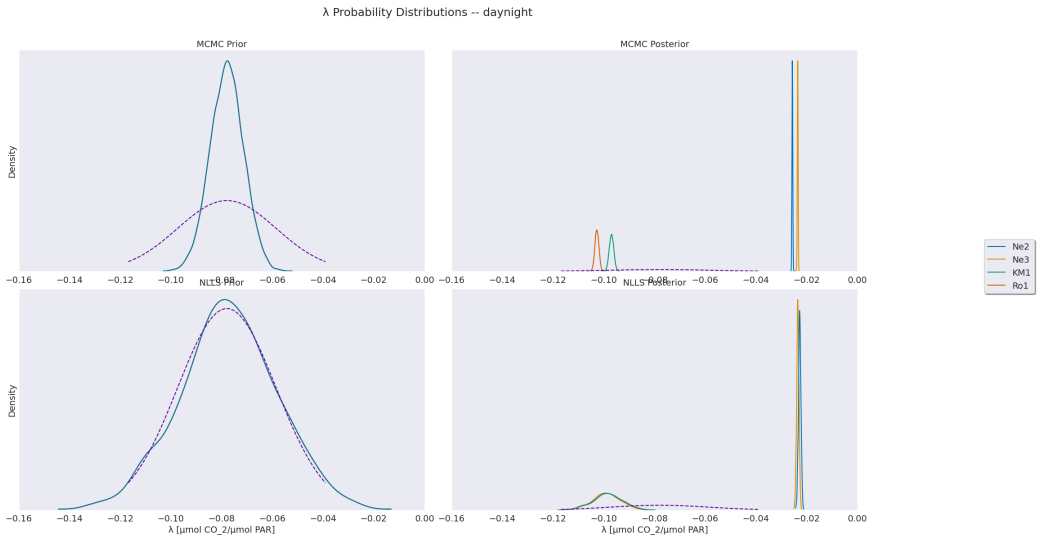

Figure 3.8: Same as Figure 3.5 but fitting ER and GEE separately.

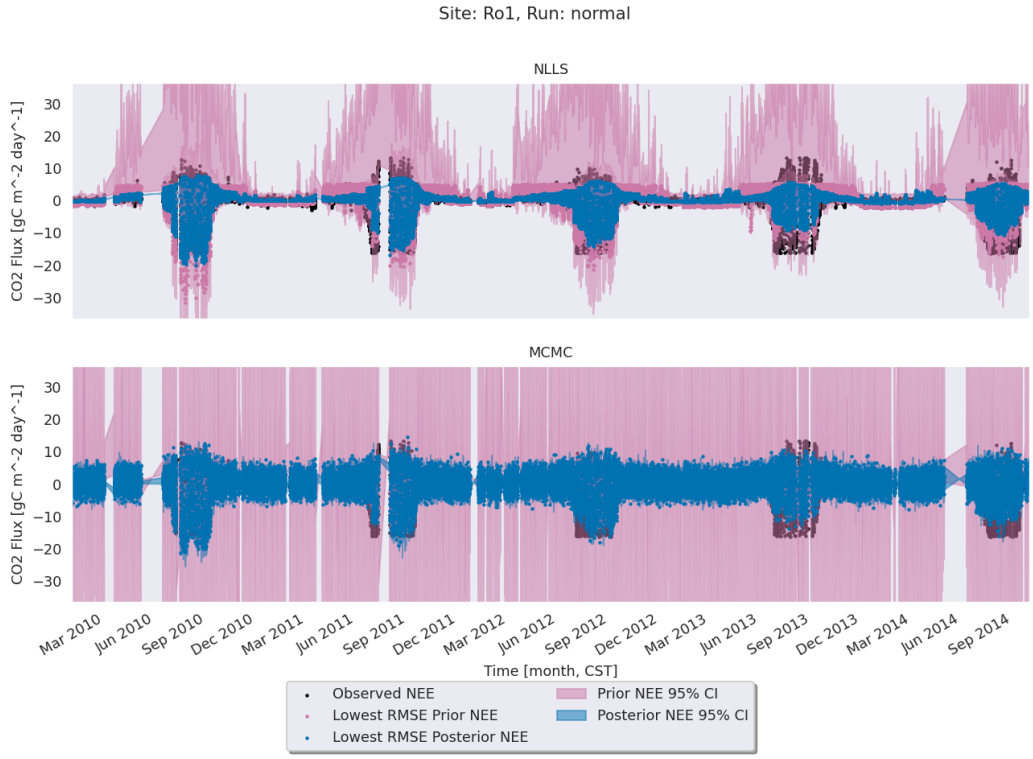

Figure 3.9: A time series plot of NEE observations (black), VPRM NEE with parameters from the parameter sets corresponding to the lowest RMSE and 95% confidence interval of the prior RMSE distribution (red), and VPRM NEE using parameter sets corresponding to the lowest RMSE and 95% confidence interval of the posterior RMSE distribution (blue), for the STIR non-linear least squares (top panel) and the MCMC (bottom panel) parameter fitting techniques fitting the whole dataset simultaneously for the Ro1 AmeriFlux site.

Figure 3.10: A time series plot of VPRM NEE residuals ($NEE_{modeled} - NEE_{observed}$) with a parameter set representing the lowest RMSE of the prior distribution (red) and a parameter set representing the lowest RMSE of the posterior distribution (blue) from the STIR non-linear least squares algorithm (top panel) and MCMC algorithm (bottom panel) while fitting the whole data set simultaneously for the Ro1 site.

error, especially during the summer growing season (Figs. 3.9,). Figures 3.10 and 3.11 demonstrate that the posterior modeled NEE can underestimate the observed NEE by as much as -15 $gC\ m^{-2}\ day^{-1}$ during the summer growing seasons. While lower in magnitude overall than the prior parameter error, with both parameter sets reaching near-zero error during the non-growing seasons, there is still large uncertainty involved in the modeled estimates.

Figure 3.11: Same as Figure 3.10 but after fitting ER and GEE separately.

The MCMC technique shows an over 10 $gC\ m^{-2}\ day^{-1}$ reduction in RMSE for all four AmeriFlux sites when fitting the entire dataset simultaneously (Table 3.2). The modeled NEE generated by the 95% confidence interval of the prior and posterior parameter distributions fit the observations with the posterior 95% confidence interval shrinking closer around the data as expected (Fig. 4.7). Taken as a whole, the posterior modeled NEE fits the observed data well for every year except 2013. As

discussed in Section 2.1, this is possibly due to the drop in two-meter temperature and incoming solar radiation found in the summer of 2013.

Figure 3.12: Same as Figure 3.9 but fitting ER and GEE separately.

3.2 Parameter Drop Experiments

3.2.1 Parameter Correlations Motivating Experiments

Correlation analysis on the posterior parameter distributions shows that fitting the full dataset simultaneously produces a strong positive correlation of 0.91 for the Ne2 AmeriFlux site between the λ and PAR_0 parameters of Equation (2.8) (Fig. 3.13). Other strong correlations common among the parameter distributions of the AmeriFlux sites are the -0.66 anti-correlation between the α_1 and α_2 and the moderate -0.41 anti-correlation between the k_2 and k_3 parameters concerning the effects of

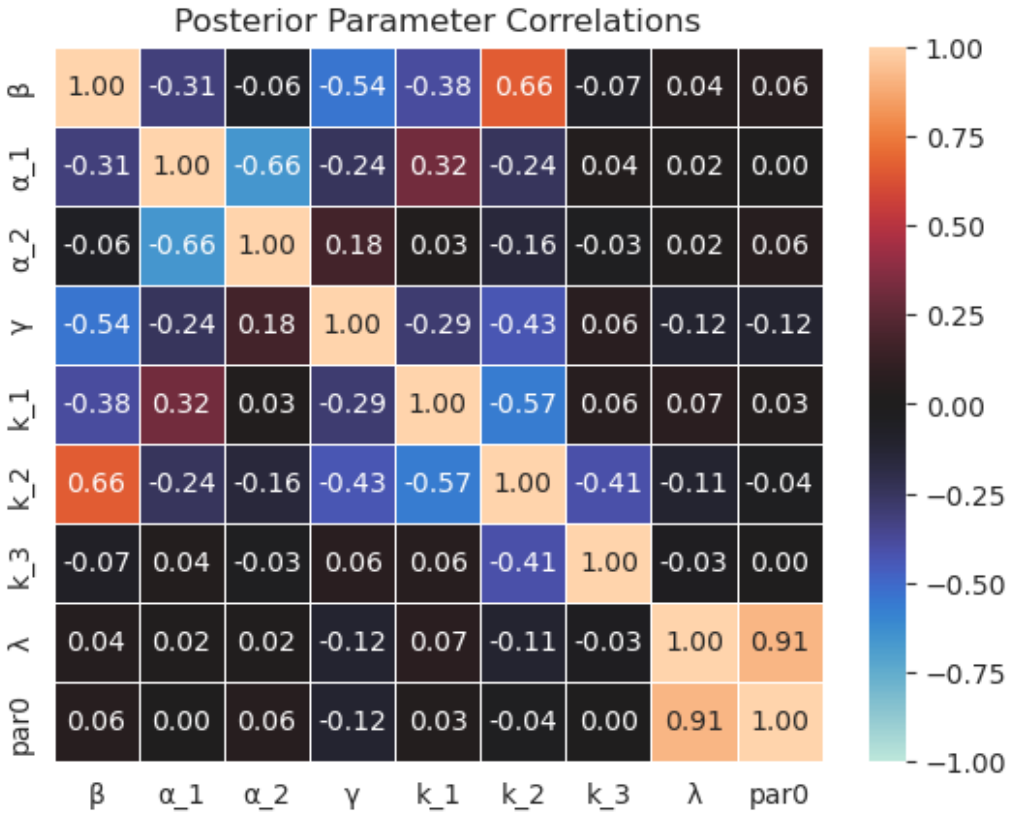

Figure 3.13: A plot of parameter correlations of the posterior parameter distributions for the Ne2 normal MCMC experiment.

temperature and square of temperature on Equation (2.3) respectively. These correlations are also present in the results from Hu et al. (2021) with strong -0.99 and -0.97 anti-correlations for the α_1/α_2 and k_2/k_3 correlations respectively while the λ/PAR_0 prior correlation was a modest 0.41 (Fig. 3.14). The k_2 and k_3 parameters combine the impact of water stress with the effects of temperature while exhibiting a negative correlation similar to the α_1/α_2 correlation. The resulting correlation is lessened in magnitude than the correlation of the parameters representing the effects of temperature alone. Correlations for the two-step ER/GEE fit were generally similar to fitting the whole data set simultaneously. A notable exception is the λ/PAR_0 correlation for the Ne2 and Ne3 sites where, as shown for Ne2 in Figure 3.15, the correlation is essentially absent (0.08). Correlations in the prior distributions for each experiment were calculated; however, due to the random draw nature for both the MCMC and NLLS algorithms, the correlations were near-zero. With strong correlations regarding parameters that represent similar physical characteristics in respiration and photosynthesis, this indicates that these parameters are not independent of each other. Because of this, it is difficult to separate any interpretations regarding the correlated parameters. Fixing the parameters relating to the effects of the square of temperature (α_2 and k_3) and the parameters related to light use efficiency (λ and PAR_0) are the focus of the experiments discussed in Section 3.2.

3.2.2 Parameter Distributions and RMSE Analyses

Tables 3.1 and 3.2 summarize that the posterior distribution RMSE for all experiments at all sites dropped by about half when compared to the prior distribution RMSE. The MAD for all parameters that aren't held constant follows the same trend as the MAD reductions for fitting the two-step ER/GEE process. (Tables A.1 and A.2).

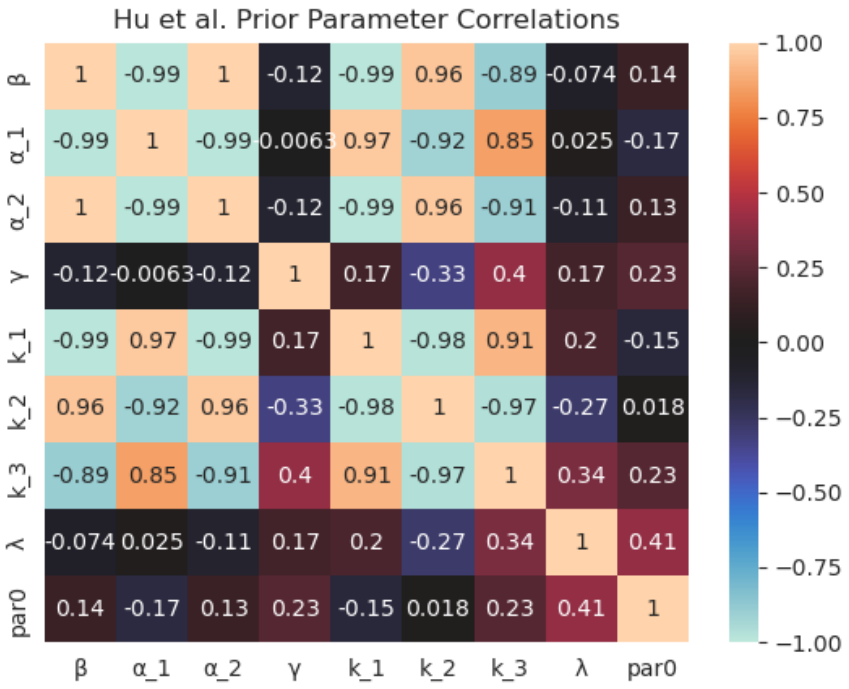

Figure 3.14: Simillar to Figure 3.13 but for the prior parameter referenced in Hu et al. (2021)

The k_3 parameter drop experiments, discussed in greater detail in Sections 4.1 and 4.2, offer some interesting results in their posterior parameter distributions and RMSE. Median prior RMSEs for the k_3 parameter drop experiment increased when compared to the median prior RMSEs from the full state vector using the two-step process (Fig. 3.16). For the NLLS, the median prior RMSEs were about 11 $gC\ m^{-2}\ day^{-1}$ which isn't much of an increase while the MCMC median prior RMSEs were about 7.5 $gC\ m^{-2}\ day^{-1}$. Both of these values are about 1 $gC\ m^{-2}\ day^{-1}$ greater than the median prior RMSEs for the full state vector. This is within the prior MADs for both experiments and so the while the change is larger than other experiments, it does not represent a statistically significant change overall. Median posterior RMSEs for the k_3 drop experiment are significantly lower using the MCMC with the difference between the full state vector median posterior RMSEs and the k_3 drop experiment around 0.12 $gC\ m^{-2}\ day^{-1}$. This difference is significant as it is much larger than the

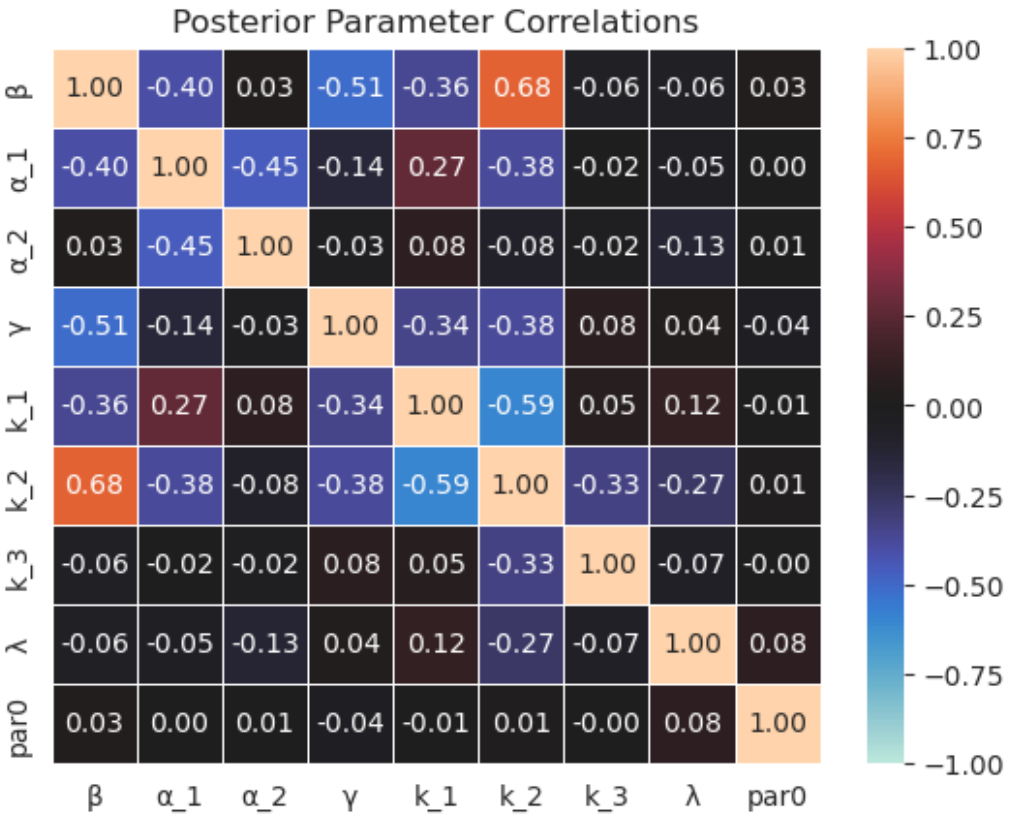

Figure 3.15: Same as Figure 3.13 but after fitting ER and GEE separately.

0.03 $gC\ m^{-2}\ day^{-1}$ posterior MAD for both experiments. Using the NLLS method, the difference of around -0.06 $gC\ m^{-2}\ day^{-1}$ is also significant when compared to the posterior MAD of around 0.003 $gC\ m^{-2}\ day^{-1}$. The difference for the NLLS method is negative as there was a general increase in median posterior RMSE when dropping k_3 using this method while there was a decrease in median posterior RMSE when using MCMC.

Figure 3.17 shows that the posterior distributions for PAR_0 were maximized against the upper boundary condition of 6,000 $\mu mol\ PAR\ m^{-2}\ s^{-1}$. This indicates that the way PAR_0 is optimized in this study tends toward a potentially unrealistic result. Figure 3.18 shows that the maximum light-use efficiency tends to cluster based on latitude. The Mead, Nebraska sites tend towards a weaker maximum efficiency with a median posterior value of around -0.024 $\mu mol\ CO_2/\mu mol\ PAR$ while the Battle Creek and Rosemount sites which are further north tend to try to make as much use of the more angled sunlight as possible during the growing season with a median posterior of around -0.10 $\mu mol\ CO_2/\mu mol\ PAR$. These values are relatively unchanged from their values for the two-step ER/GEE full-state vector median posteriors.

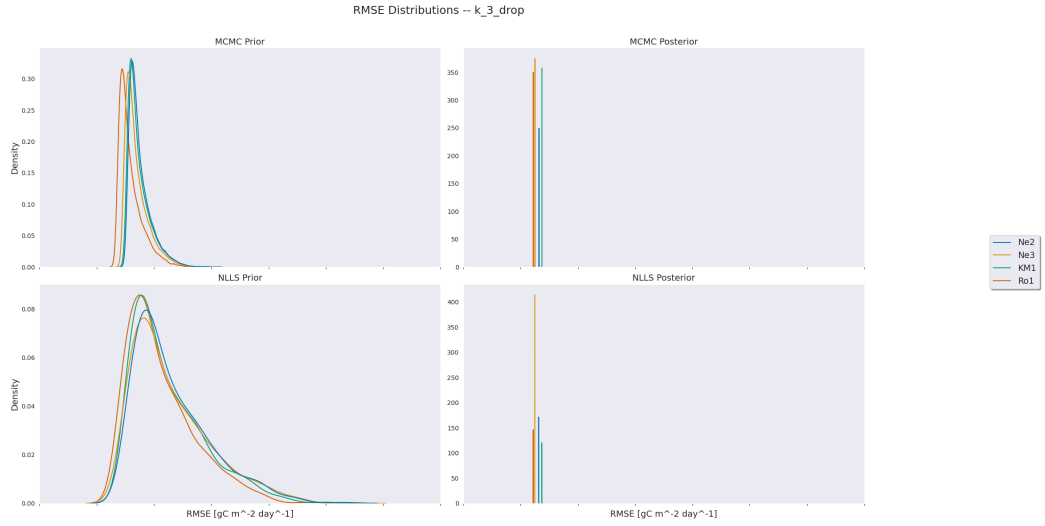

Figure 3.16: Same as Figure 3.1 but for the k_3 parameter drop experiment.

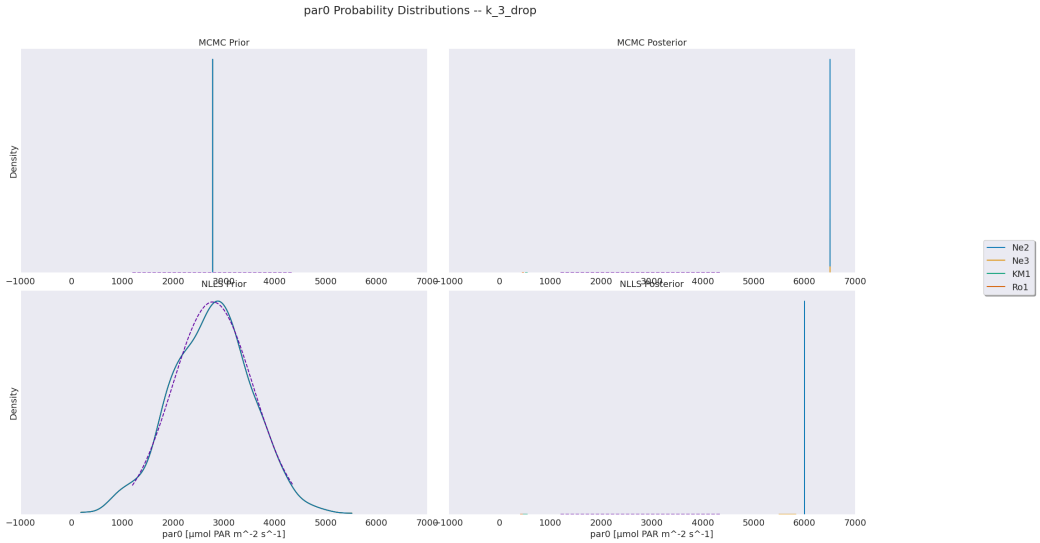

Figure 3.17: Same as Figure 3.3 but for the k_3 parameter drop experiment.

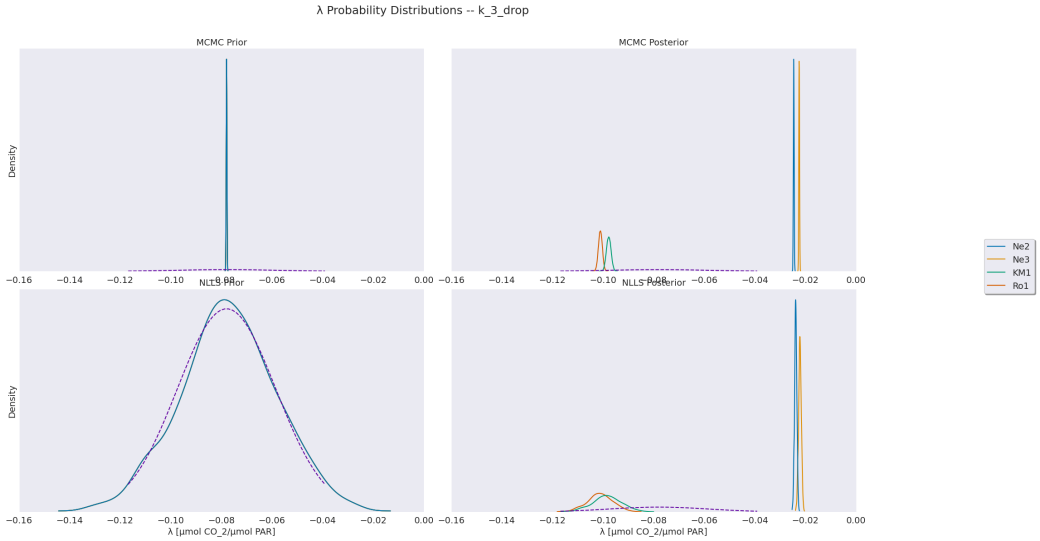

Figure 3.18: Same as Figure 3.5 but for the k_3 parameter drop experiment.

3.2.3 Time Series Analysis

Differences in how the modeled NEE fits the observed values are illustrated in Figures 3.19 and 3.20. Holding PAR_0 constant transforms the parameter fitting problem from a non-linear one to a linear problem. The posterior modeled NEE for the PAR_0 experiment shown in Figure 3.19 fits the observed negative drawdowns in NEE better than holding λ constant (Fig. 3.20). Despite the strong correlation between the two parameters, it seems from the time series alone that tuning the λ parameter may bring about a better fit. However, when looking at the median posterior RMSEs the two experiments demonstrate similar median posterior RMSEs of around 2.9 and 3.1 $gC\ m^{-2}\ day^{-1}$ for NLLS and MCMC respectively.

Figure 3.19: Same as Figure 3.9 but for the PAR_0 parameter drop experiment.

Figure 3.20: Same as Figure 3.9 but for the λ parameter drop experiment.

Chapter 4

Discussion

4.1 Monthly and Seasonal Cycle Analysis

The monthly average of the observed NEE as well as modeled NEE from the parameter sets representing the median RMSE of both the prior and posterior distribution from the MCMC experiments were calculated to analyze the effectiveness of the VPRM to capture the seasonal and sub-seasonal patterns of the carbon cycle. Five-year means for each month were also calculated to determine how each month deviates from the five-year average. The top panel of Figure 4.1 shows that the VPRM follows the general monthly pattern observed at Ne2. The posterior-modeled NEE performs closer to the observation then the prior for most of the temporal domain. However, as time progresses the posterior NEE does not match the magnitude of the summertime negative flux. This is best indicated with June 2013 and 2014 where the monthly-mean posterior modeled NEE are roughly 0 and -1 $gC\ m^{-2}\ day^{-1}$ respectively. For June 2014, both the observed monthly mean and the prior-modeled monthly mean NEE reach around -4 $gC\ m^{-2}\ day^{-1}$. The bottom panel of Figure 4.1 shows that the deviation of the posterior NEE from the five-year monthly means was within $|1\ gC\ m^{-2}\ day^{-1}|$ for every month between 2010 and 2015. The deviation of the observed NEE and the prior NEE from the five-year monthly means extend to $\geq |3\ gC\ m^{-2}\ day^{-1}|$.

For most cases, the parameter drop experiments produced similar results. One notable exception is the k_3 parameter drop experiment for the Ne2 site shown in Figure 4.2. The main difference between the normal experiment and the k_3 drop

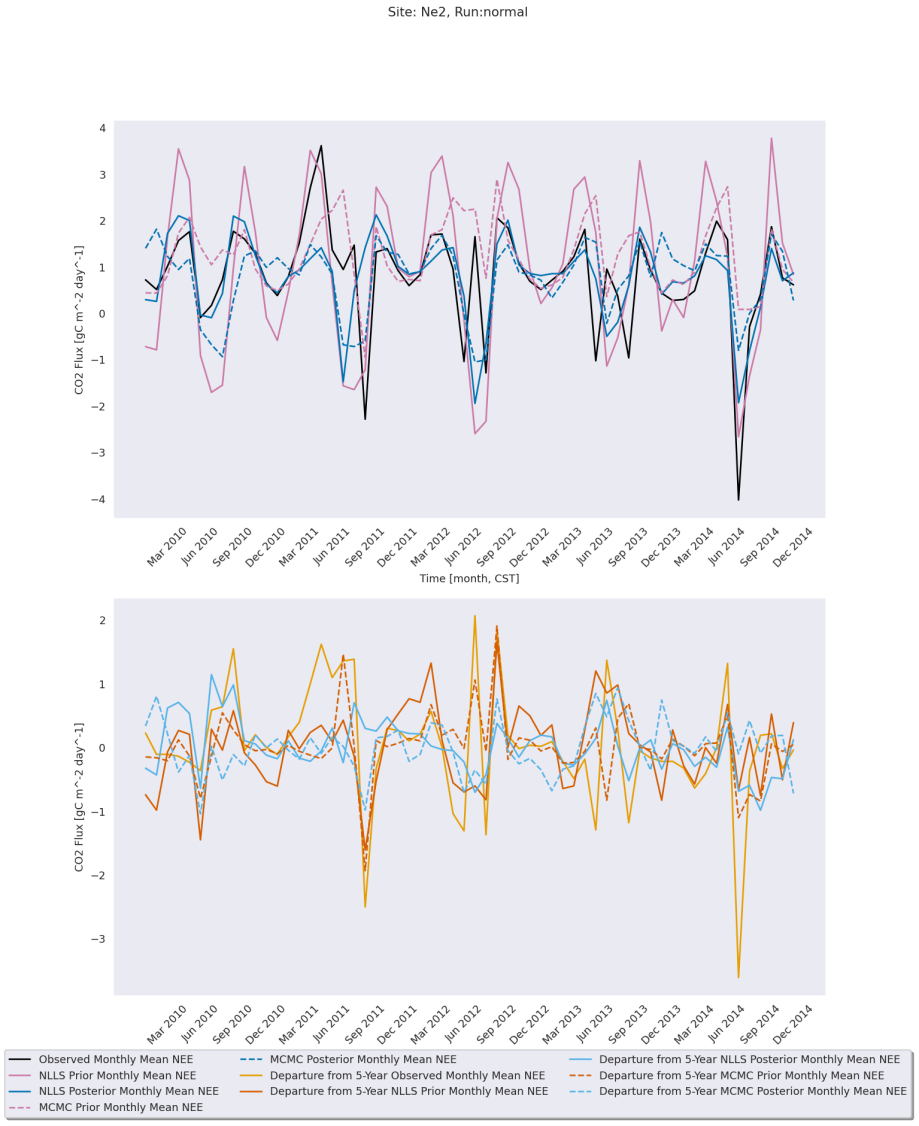

Figure 4.1: A time series plot of (top panel:) the monthly observed (black), VPRM NEE using the parameter set representing the lowest RMSE from the prior NLLS (solid) and MCMC (dashed) distributions (red), VPRM NEE using the parameter set representing the lowest RMSE from the posterior NLLS (solid) and MCMC (dashed) distributions (blue), (bottom panel:) the departure from the 5-year monthly mean of the observed (light orange), the departure from the 5-year monthly mean of the VPRM NEE using the parameter set representing the lowest RMSE from the prior NLLS (solid) and MCMC (dashed) distributions (dark orange) and the departure from the 5-year monthly mean of the VPRM NEE using the parameter set representing the lowest RMSE from the posterior NLLS (solid) and MCMC (dashed) distribution (sky blue) for the Ne2 AmeriFlux site fitting the whole dataset simultaneously.

experiment is that the summertime negative prior monthly average NEE for the k_3 is more negative than $-7\ gC\ m^{-2}\ day^{-1}$. This is likely due to how the remaining priors, which were optimized in Hu et al. (2021) with k_3 in mind, are unable to compensate for the lack of the combined effects of water stress and temperature.

There are some similar patterns when comparing the posterior parameter correlations of the two-step ER/GEE separate experiment shown in Figure 3.15 to those of the k_3 drop experiment shown in Figure 4.3. There is a greater magnitude of correlation between the light-use parameters of λ and PAR_0 in the k_3 drop experiment with the correlation going from 0.08 to -0.22. This indicates that the MCMC k_3 drop experiment increases its dependence on the light-use parameters in order to compensate for the lack of the k_3 parameter The anti-correlation between the temperature parameters of α_1 and α_2 is also lessened slightly in magnitude from -0.45 to -0.39. Other correlations are similar between the two experiments. The bottom panels of Figures 4.1 and 4.2 have similar patterns, however, Figure 4.2 shows a spike of a 4 $gC\ m^{-2}\ day^{-1}$ departure from the five-year monthly mean in the prior NEE during the summer of 2012 and around a 3 $gC\ m^{-2}\ day^{-1}$ departure during the summer of 2014. The magnitude of the 2012 spike in the departure from the prior NEE five-year monthly average is lessened to about 3 $gC\ m^{-2}\ day^{-1}$ and the 2014 spike is inverted to a trough of $-2\ gC\ m^{-2}\ day^{-1}$ in the normal experiment (Fig. 4.1). The patterns of the observed and posterior NEE departure from the five-year monthly mean are similar between the two experiments.

Figures 4.4 and 4.5 show the one-to-one relation of the observed to the modeled NEE for the summer months in the temporal domain. The modeled NEE from the median of the prior parameter distribution of the k_3 parameter drop experiment is generally more negative than the observed with the majority of the data points and the 95% confidence interval below the one-to-one line (Fig. 4.5). This is in contrast to the prior-modeled NEE from the normal MCMC experiment where the 95% confidence

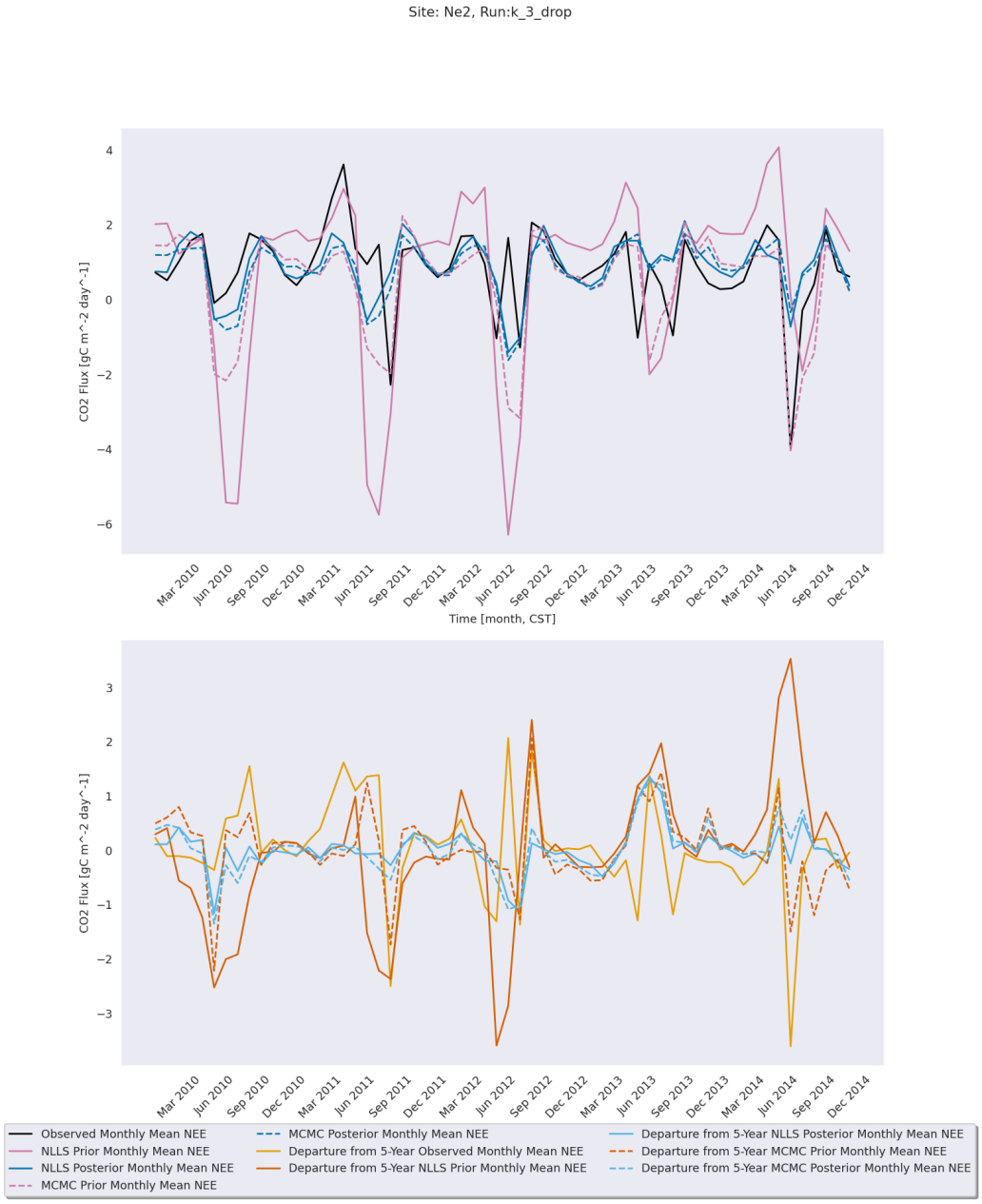

Figure 4.2: Same as Figure 4.1 but for the k_3 drop experiment.

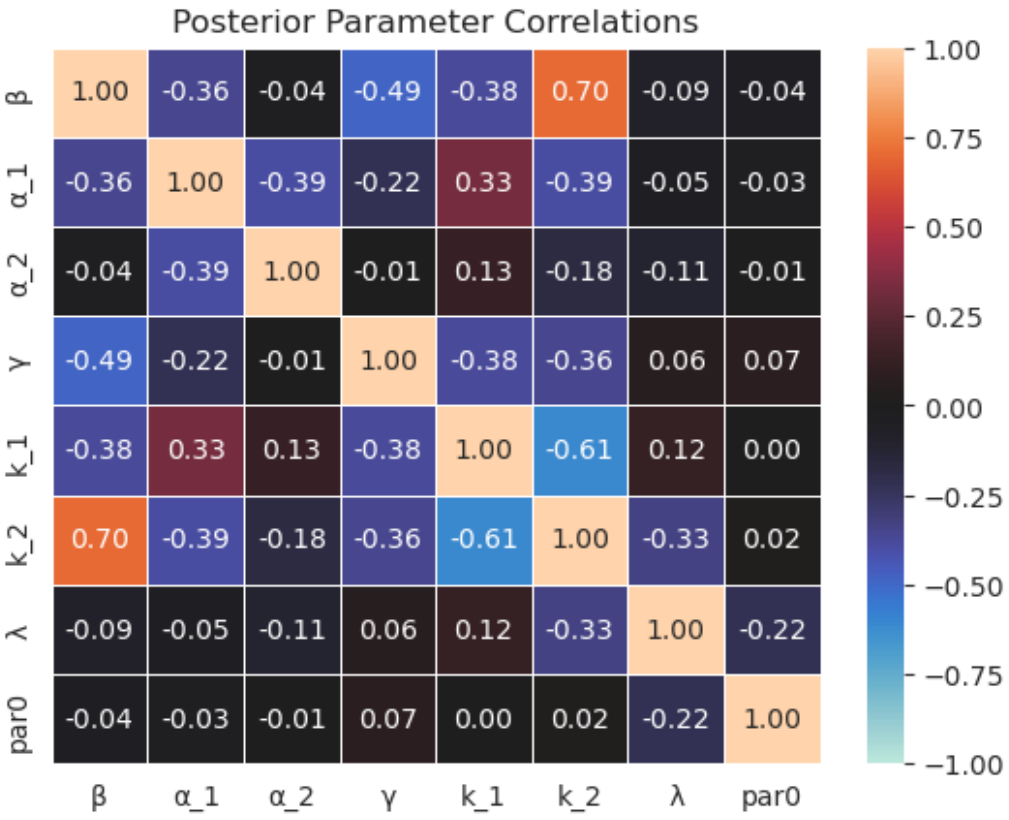

Figure 4.3: Same as Figure 3.13 but for the k_3 parameter drop experiment.

interval is generally the same magnitude of distance away from the one-to-one line (Fig. 4.4). The posterior-modeled NEE from both experiments generally falls within the same general distance from the one-to-one line with more positive bias in the modeled NEE for more negative observed NEE.

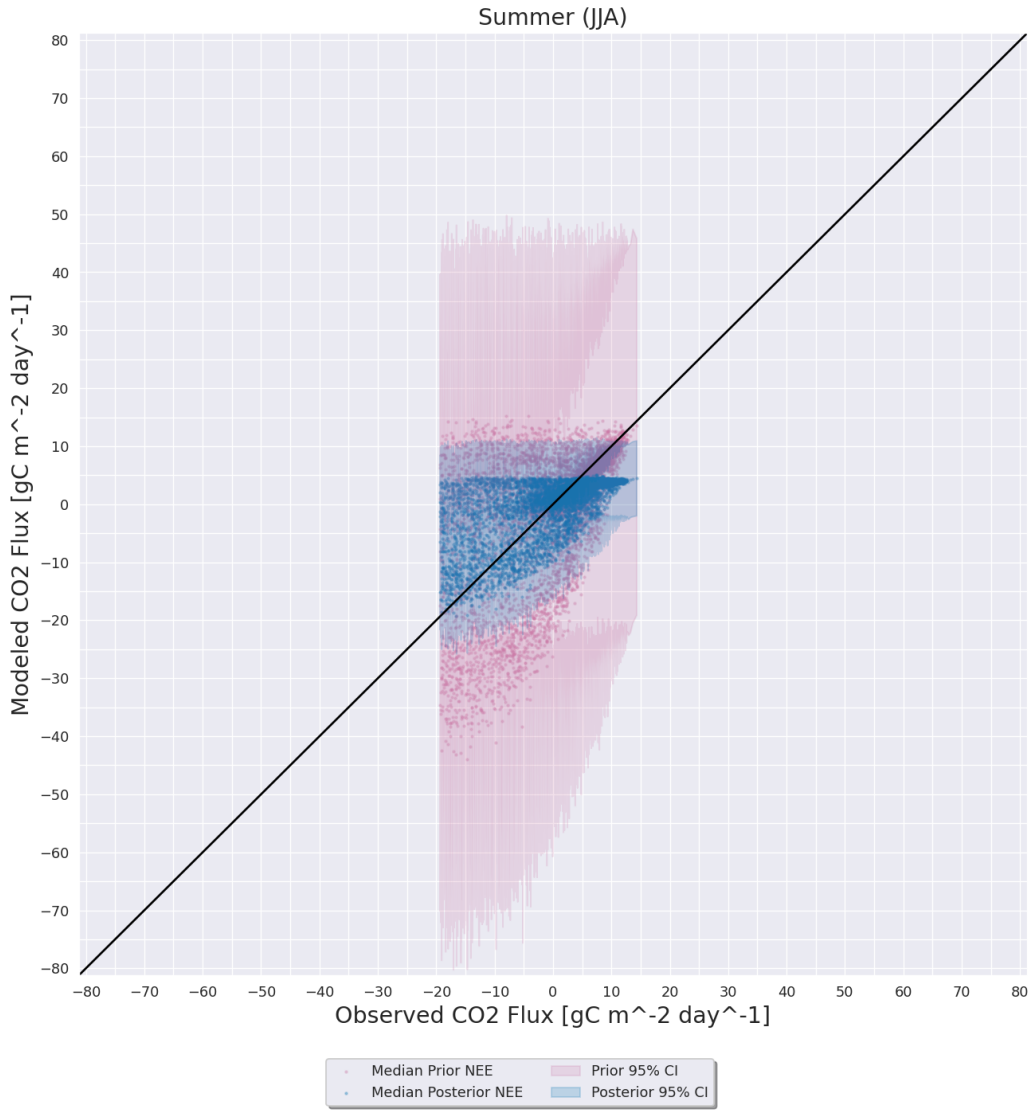

Figure 4.4: A one-to-one plot showing observed NEE on the x-axis and modeled NEE from the medians of the prior (red) and posterior (blue) parameter distributions as well as their respective 95% confidence intervals for the Ne2 normal MCMC experiment during the summer (JJA) months.

The observed diurnal cycle of NEE shows a stronger degree of variability during the peak growing season of June through September than in the other months of

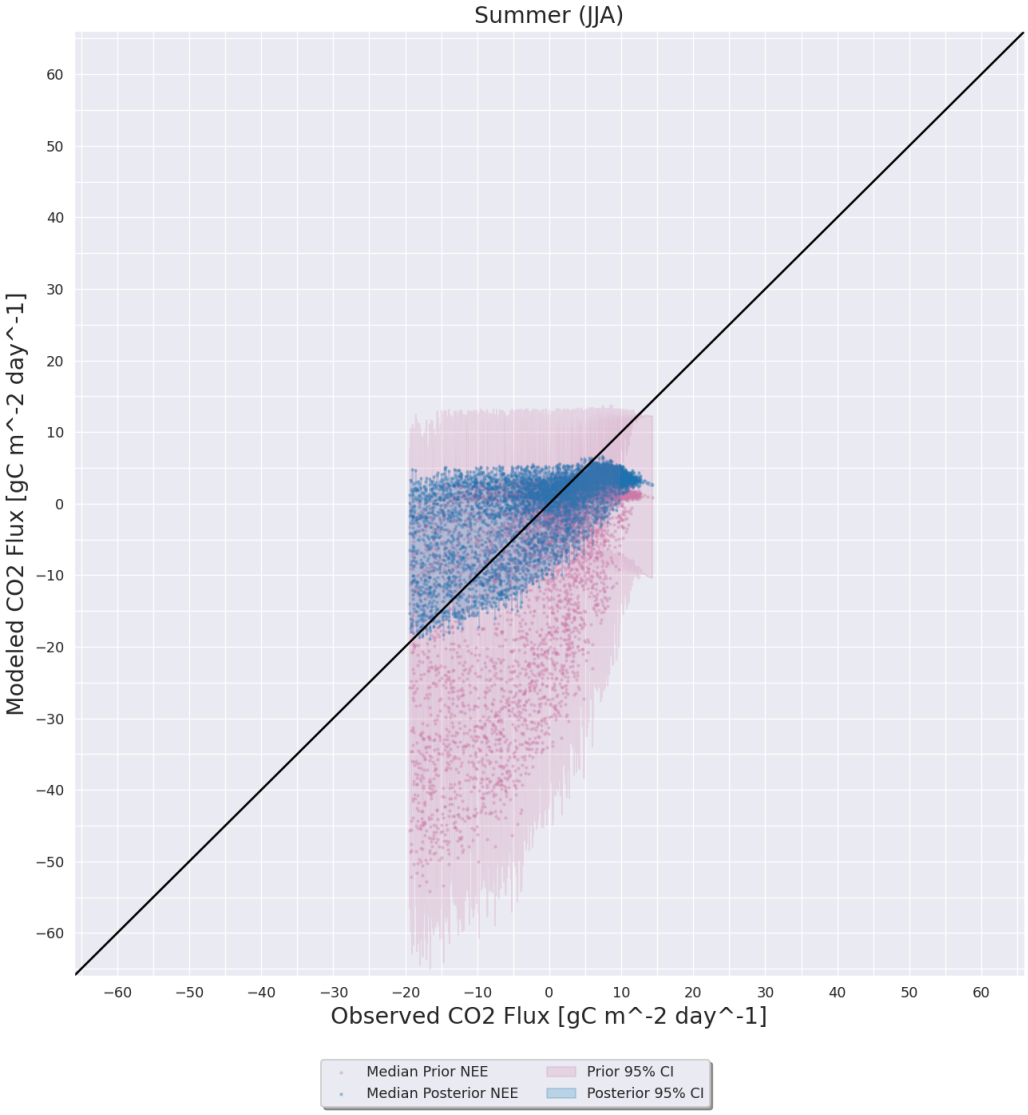

Figure 4.5: Same as Figure 4.4 but for the k_3 drop MCMC experiment.

the year (Fig. 4.6). The diurnal minima of around $-12\ gC\ m^{-2}\ day^{-1}$ during the afternoon and evening periods of July and August correspond to the monthly minima found in the top panel of Figure 4.1. The VPRM NEE calculated from the median of the posterior parameter distribution follows a similar monthly pattern as the observed NEE with a negative bias earlier in the temporal domain and a positive bias beginning in the summer of 2013. It is not the goal to match the peaks and troughs exactly for the monthly trends, but rather that matching the general pattern shows that the VPRM can be used.

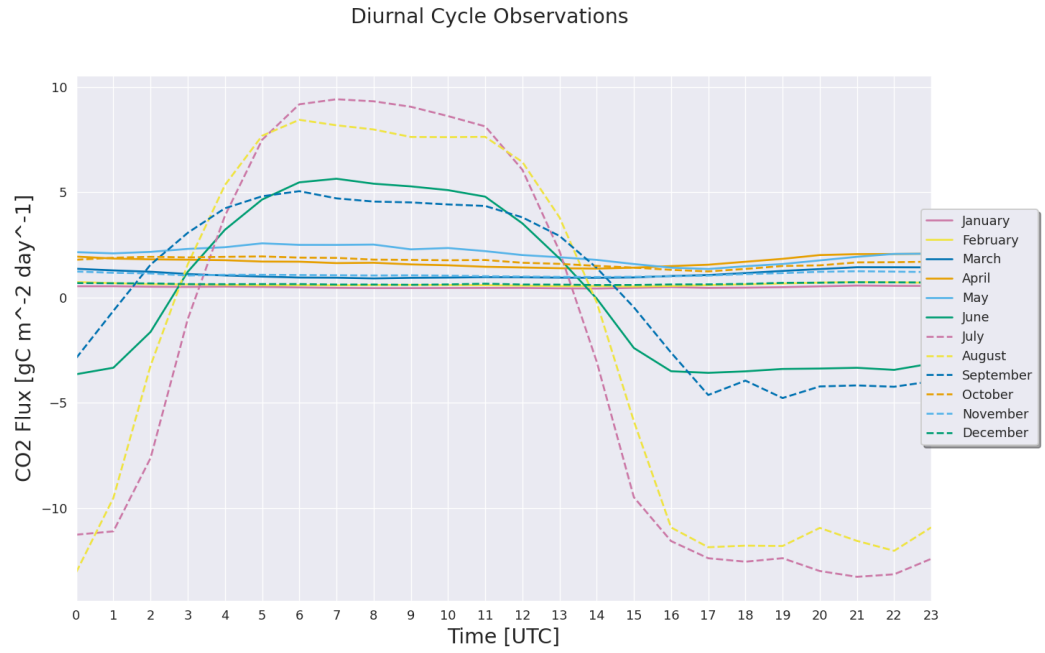

Figure 4.6: Observed monthly diurnal cycle average NEE for the Ne2 AmeriFlux site. Months are as in the key.

4.2 Comparing Irrigated and Rainfed Sites

The VPRM NEE using the median of the parameter posterior distribution has a lower RMSE indicating a better overall fit to the observations when modeling the rainfed Ne3 AmeriFlux site when compared to the irrigated Ne2 site (Table 3.2, Figs.

Figure 4.7: Same as Figure 3.10 but for the Ne2 AmeriFlux site.

Figure 4.8: Same as Figure 3.10 but for the Ne3 AmeriFlux site.

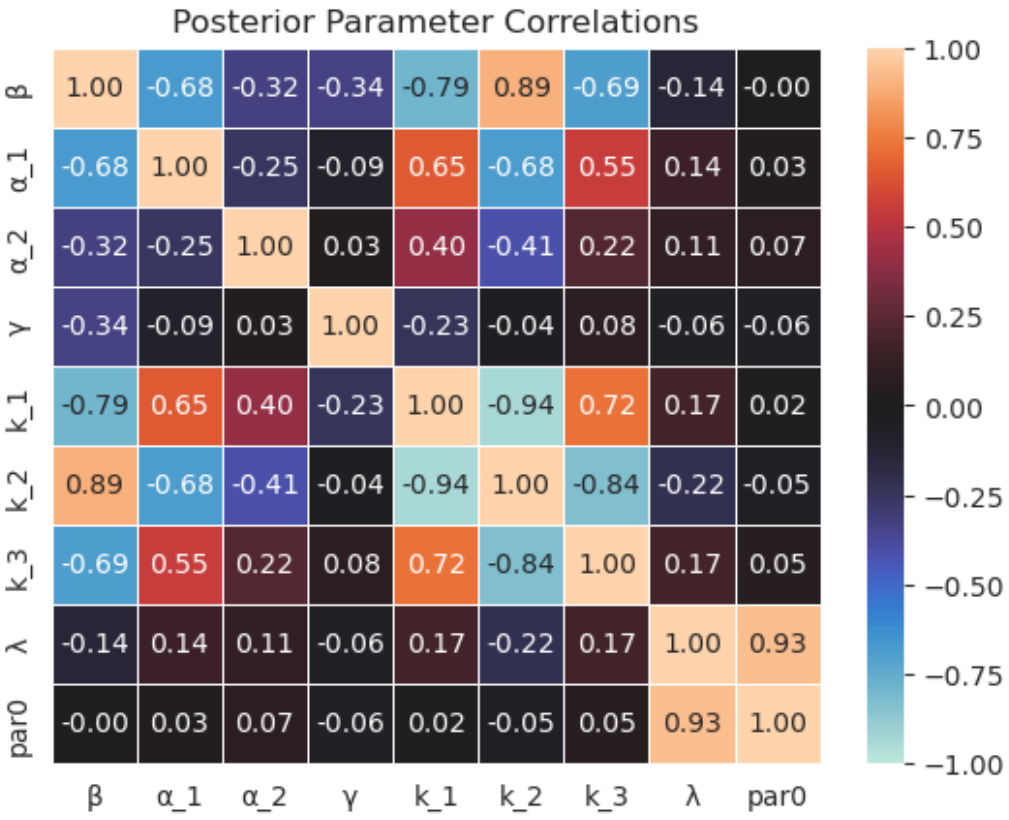

Figure 4.9: Same as Figure 3.13 but for the Ne3 AmeriFlux site.

4.7 & 4.8). The Ne3 posterior more closely matches the observed summer negative NEE in 2013 than the Ne2 posterior.

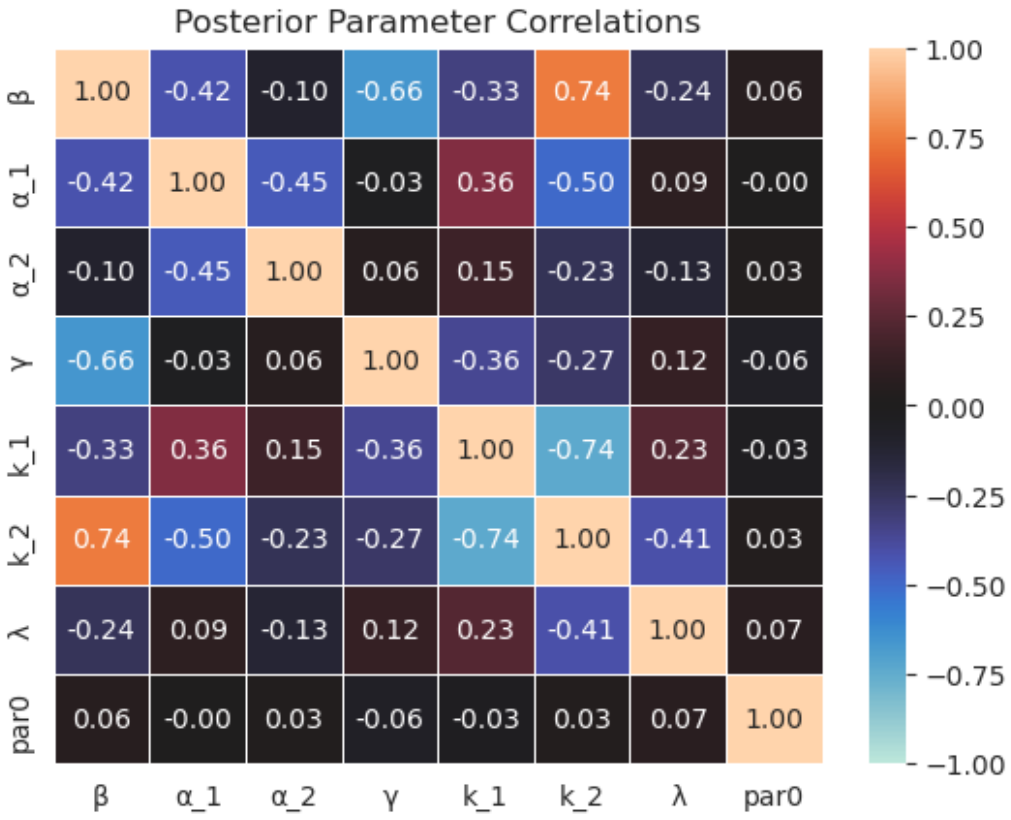

Figure 4.10: Same as Figure 4.3 but for the Ne3 AmeriFlux site.

Posterior parameter correlations for the Ne3 normal MCMC parameter experiment demonstrate a higher correlation among the parameters related to water stress (k_1-k_3). LSWI calculated for Ne3 is lower on average during the summer months compared to LSWI for Ne2 which could account for the increased correlations in the water stress parameters. Comparing the k_3 drop parameter experiment posterior parameter distribution correlations show a similar pattern in the posterior correlations to that of the Ne2 k_3 parameter drop experiment.

The one-to-one relation analysis for Ne3 shows that the k_3 parameter drop MCMC experiment has a similar pattern to that of the k_3 parameter drop experiment for Ne2

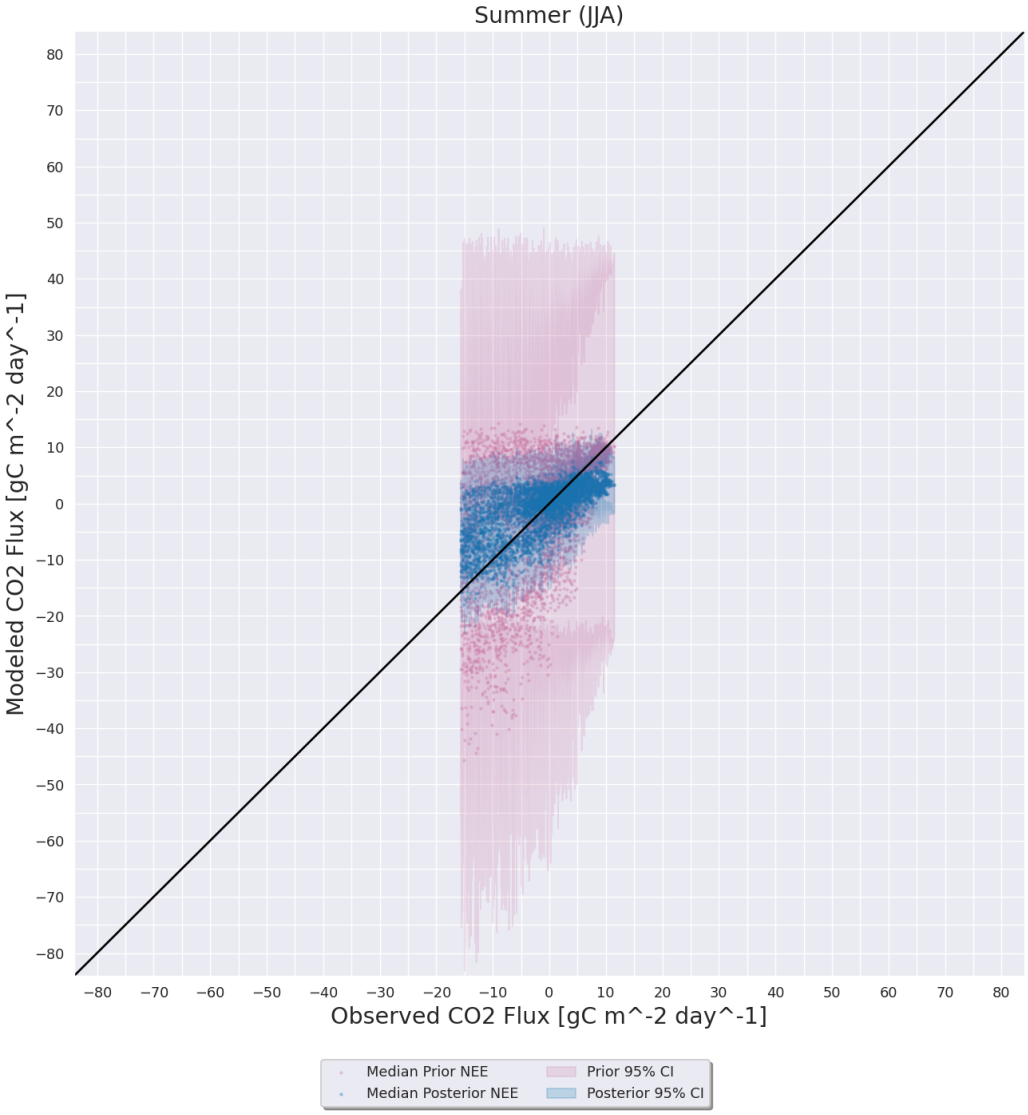

Figure 4.11: Same as Figure 4.4 but for the Ne3 normal MCMC experiment.

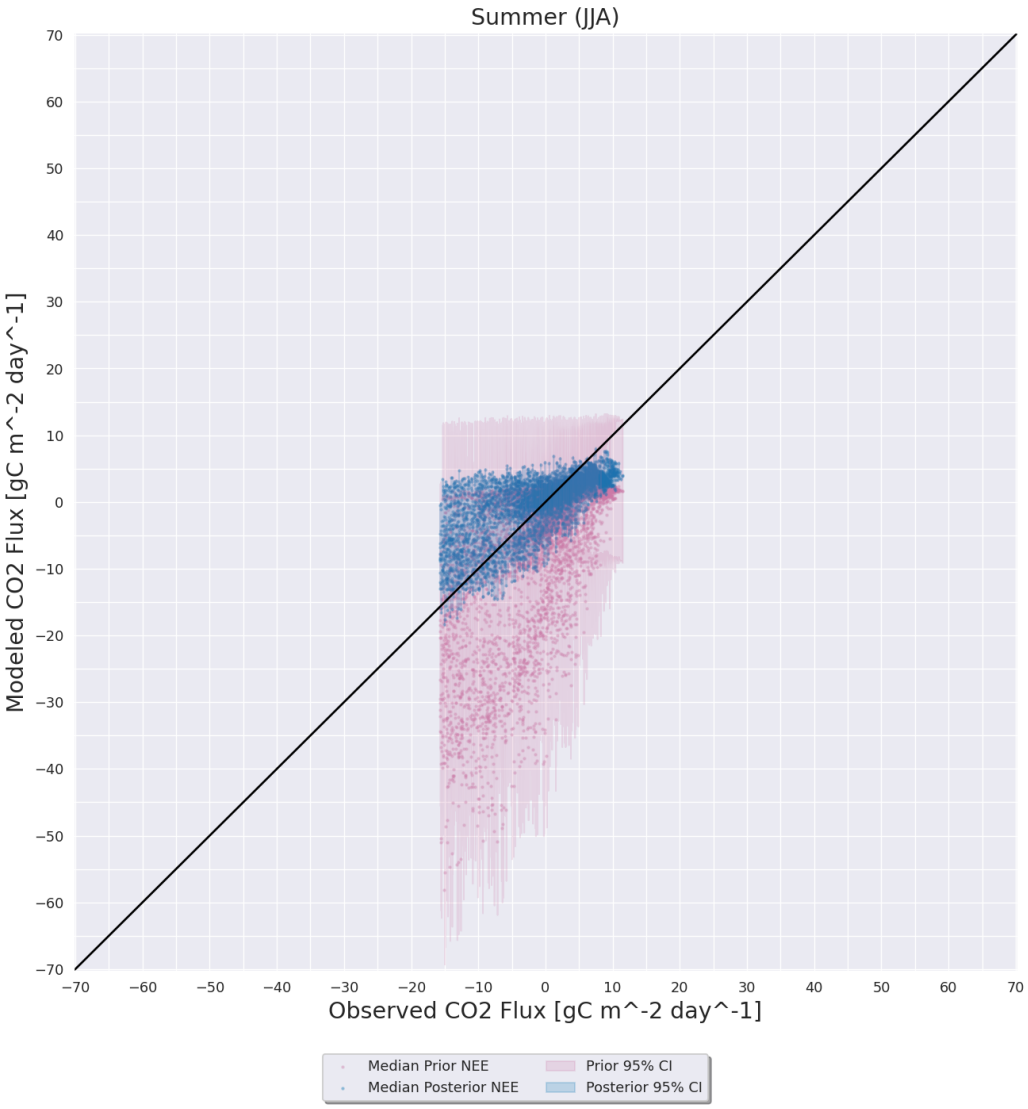

Figure 4.12: Same as Figure 4.5 but for the Ne3 k_3 parameter drop MCMC experiment.

(Fig. 4.12). However, the normal MCMC experiment for Ne3 shows a closer one-to-one relationship between posterior-modeled NEE and observed NEE than the same experiment for Ne2 (Fig. 4.11). This corresponds to the bottom panels of Figures 4.13 and 4.14 where the departure from the five-year monthly mean posterior-modeled NEE says closer to 0 $gC\ m^{-2}\ day^{-1}$ than the equivalent experiments from the Ne2 site.

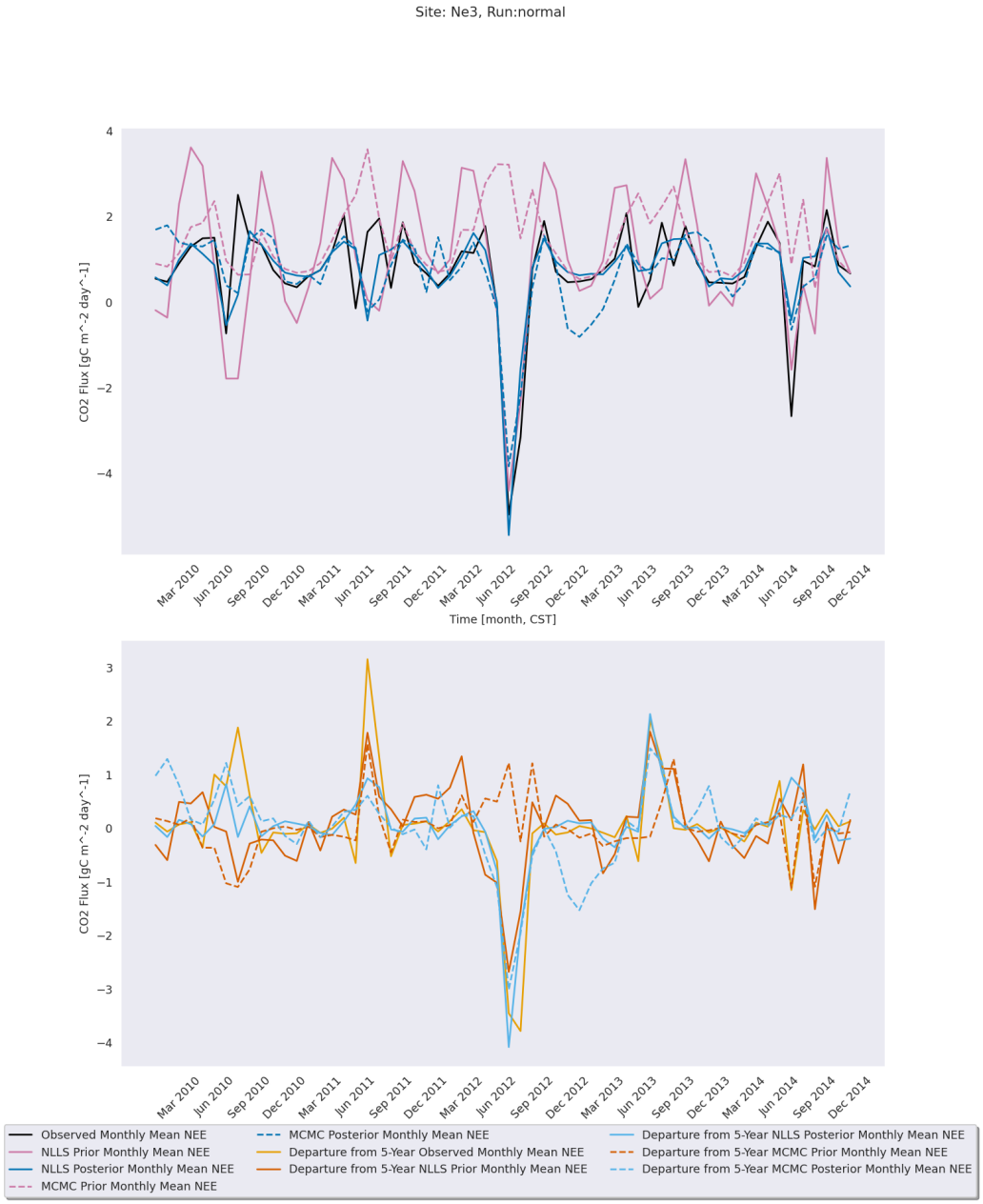

Figure 4.13: Same as Figure 4.1 but for the Ne3 AmeriFlux site.

Figure 4.14: Same as Figure 4.2 but for the Ne3 AmeriFlux site.

Chapter 5

Conclusions and Future Work

5.1 Sources of Error Compared to Previous Work

Xiao et al. (2004a) identified three sources of potential error in their paper: the sensitivity of the VPM to PAR and air temperature, the error in calculating the observed GEE from the measured NEE at the site, and errors from how EVI and LSWI are derived and the effects of angular geometry on reflectance data (Section 1.1). This study faced similar sources of error that may explain the remaining uncertainty in the results.

The correlations of the temperature parameters (α_1 and α_2) with the rest of the respiration equation indicate that parameter estimation is not able to separate the effects of temperature from the other terms. While the correlations aren't as strong in the irrigated Ne2 site, they are of a higher magnitude in the rest of the sites (Figs. 3.13, 4.9). This sensitivity is also shown in the α_2 and k_3 parameter drop experiments. Figure 5.1 shows that the positive summertime NEE response is flatter when not accounting for the effects of the square of temperature than the normal MCMC experiment. The effect of setting the k_3 parameter to 0 $\mu mol\ CO_2\ m^{-2}\ s^{-1}\ {}^{\circ}C^{-2}$ reduces the negative valued prior-modeled NEE during the summer to a value well below what was observed as expected since the other parameters were optimized by Hu et al. (2021) with the k_3 parameter included in the state vector (Fig. 4.12). The k_3 drop posterior parameter correlations and the summertime posterior-modeled NEE show that the MCMC can adjust the remaining parameters to compensate for dropping the k_3 parameter, increasing the correlations for parameters such as the γ

and k_2 parameters with the β parameter and the correlation between k_1 and k_2 (Figs. 4.3 and 4.5).

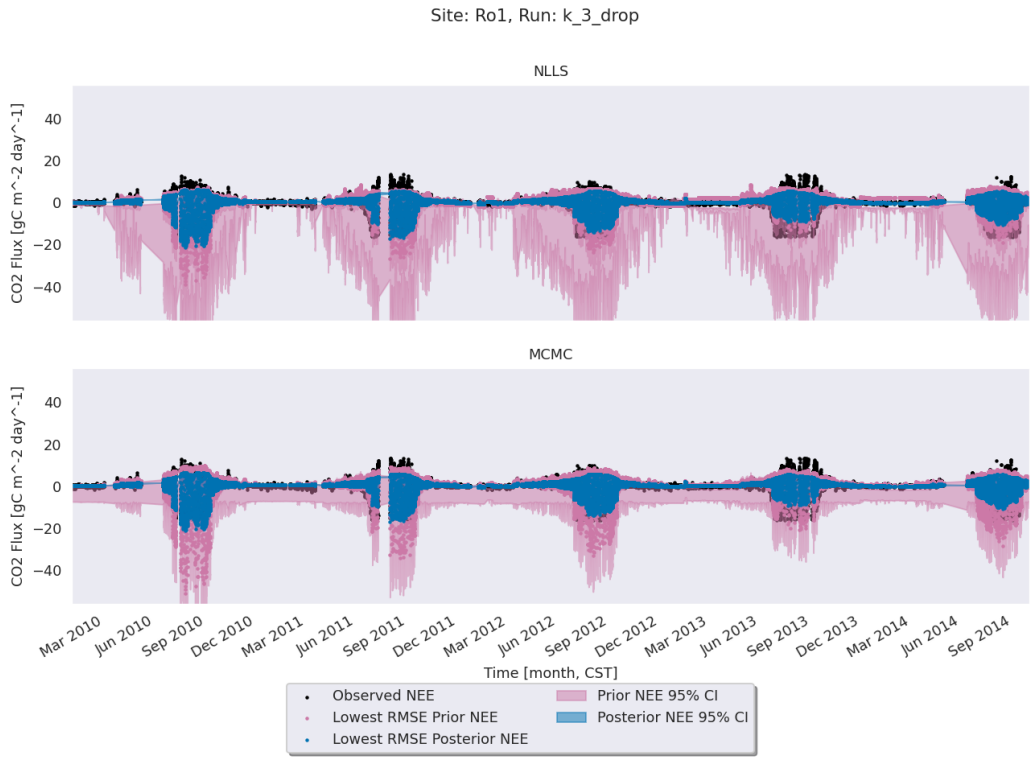

Figure 5.1: Same as Figure 3.9 but for the k_3 parameter drop experiment.

The data from the AmeriFlux eddy covariance tower sites used in this site provided measured NEE and so calculations were not needed to derive observed NEE. However, instrument uncertainty can still factor into the uncertainty of results using these data. The heights above ground level of the sensors at Ne2 and Ne3 are not consistent which can account for some degree of uncertainty. These data were not gap-filled or quality checked and therefore contain uncertainty that may not have been filtered out in the running means and removal of outliers discussed in Section 2.1. Eddy covariance data are also impacted by different turbulence regimes. Using a filtering technique on u^* is an attempt to account for these impacts, but it is not a perfect method. When strong advection or weak vertical mixing is present, errors in eddy covariance data are common (Mahadevan et al., 2008).

The derivation of EVI and LSWI from the MODIS data using Equations (2.6) and (2.7) respectively also is a potential source of error. Calculations from the raw data produced data points where the EVI ended up being ≤ 0. These data points were dropped from the data used in subsequent calculations which produces gaps in the EVI and LSWI. MODIS reflectance used for these calculations came from the nadir reflectance product and so the effects of angular geometry on the data should be negligible. However, the effects of partial cloud cover and aerosol activity can still lead to uncertainty in the reflectance measurements.

Other sources of uncertainty that are unique to this study are the use of the STIR algorithm to curve fit the daytime GEE parameters after the MCMC was used to fit nighttime respiration and the randomness of the MCMC algorithm. The inherent randomness of the MCMC algorithm requires the use of a random seed in the Python code to generate randomness that can be reproducible with each experiment. The use of a different random seed, or not using a seed at all and letting the random state of the computer hardware memory determine the randomness could affect the results found from this technique. The use of STIR for fitting the daytime GEE parameters presents uncertainty in calculating the posterior distribution for λ and PAR_0. The STIR technique itself is inherently non-Bayesian and thus does not lend itself to generating a posterior distribution without drawing from a random distribution of priors. This technique was used for certain experiments in this study because conducting a second round of MCMC for the daytime GEE parameters would be more computationally expensive. Redoing these experiments in the future with the MCMC technique used for fitting both of the main VPRM equations would be beneficial to explore the implications of using MCMC on all variables. As VPRM is a simple model, processes and factors that are present in other similar models such as CASA may lead to errors as well (Gourdji et al., 2022).

5.2 AmeriFlux Tower Site Selection

Sites selected for this study were selected in order to examine the differences among observation sites with the same general VPRM LUT. The irrigated Ne2 site performed the most predictably in terms of parameter correlations. This suggests that irrigated sites provide better control of NEE output than rainfed sites. The northernmost site at Ro1 produced the lowest RMSEs of all experiments while the corn-only KM1 site produced the highest RMSEs when compared to the other sites. The higher RMSEs at KM1 suggest that separating the cropland LUT into LUTs for different types of crops may be beneficial to the fit of VPRM as a whole.

The small number of sites used in this study may not be representative of the full capabilities of the MCMC technique to quantify the uncertainty of the VPRM parameters. Future work on these experiments could use more flux tower sites by either fitting them separately as in this study or by fitting all sites simultaneously.

5.3 Viability of MCMC as a Parameter Calibration Technique

This study shows that the MCMC technique reduces the MAD of both the modeled NEE and the posterior parameter distributions (Tables 3.2 and A.2). The use of MAD instead of σ as the measure of uncertainty and median instead of mean for the measure of the center of the distribution was due to the robustness of MAD and median to outliers in the distribution. As shown in Figures 3.3 and 3.5, many parameters show disagreement regarding the posterior distributions. Combining the data sets into one larger data set and fitting them together may provide a parameter distribution that better agrees with the aggregate observations while not fitting individual sites as accurately. Fitting the whole dataset simultaneously has a greater magnitude of reduction in MAD, but fitting the ER and GEE equations separately produces the

most overall reduction in modeled-NEE MAD and the second lowest RMSE of all experiments. The lowest RMSE comes from the posterior-modeled NEE of the k_3 parameter drop experiment. This suggests that not including the combined effects of water stress and the square of temperature in the model may provide a better fit overall than using Equation (2.3) derived by Gourdji et al. (2022).

Constraining and quantifying sources of uncertainty using methods such as this study shows that the MCMC technique may be a viable way of tuning the parameters of the VPRM equations on a site-by-site scale. Scaling the technique to a more general use with more sites and different LUTs may be very computationally expensive. The benefit is that once fitting is complete on a larger data set the generated posterior distribution may provide more accurate estimates that scale to continental and global scales. Using small batches of sites and averaging the results may provide a less computationally expensive method.

5.4 Future Work

Future work on the VPRM using MCMC includes scaling up the MCMC fitting algorithm to include more sites and LUTs to generalize the VPRM to larger spatial scales. This in turn would allow the posterior parameter sets to be incorporated into WRF-VPRM for analysis in regional and continental scales of the carbon cycle. Incorporating a data assimilation technique such as Three-dimensional Variational Assimilation (3DVAR) or Ensemble Kalman Filter (EnKF) and assimilating the observed NEE on a set assimilation cycle may also assist in minimizing uncertainty in the VPRM. Another technique that could be explored in future work is creating more LUTs based on crop type for work with the VPRM and classifying all AmeriFlux observation sites using the new set of LUTs. More LUTs would allow for more accurate parameter sets depending on crop type which in turn would allow for a more accurate VPRM as a whole.

Bibliography

AppEEARS Team, 2022: Application for Extracting and Exploring Analysis Ready Samples (AppEEARS). Ver 3.16. NASA EOSDIS Land Processes Distributed Active Archive Center (LP DAAC), USGS/Earth Resources Observation and Science (EROS) Center, Sioux Falls, South Dakota, USA., URL https://appeears.earthdatacloud.nasa.gov, accessed: 2022-11-7.

Baker, J., T. Griffis, and T. Griffis, 2022: AmeriFlux BASE US-Ro1 Rosemount-G21, Ver. 5-5, (Dataset). AmeriFlux; University of Minnesota; USDA-ARS.

Branch, M. A., T. F. Coleman, and Y. Li, 1999: Subspace, interior, and conjugate gradient method for large-scale bound-constrained minimization problems. *SIAM Journal of Scientific Computing*, **21 (1)**, 1–23, https://doi.org/10.1137/S1064827595289108, URL https://epubs-siam-org.ezproxy.lib.ou.edu/doi/10.1137/S1064827595289108.

Chandrasekar, K., M. V. Sesha Sai, P. S. Roy, and R. S. Dwevedi, 2010: Land Surface Water Index (LSWI) response to rainfall and NDVI using the MODIS vegetation index product. *International Journal of Remote Sensing*, **31 (15)**, 3987–4005, https://doi.org/10.1080/01431160802575653, URL https://www.tandfonline.com/doi/abs/10.1080/01431160802575653.

Crisp, D., and Coauthors, 2017: The on-orbit performance of the Orbiting Carbon Observatory-2 (OCO-2) instrument and its radiometrically calibrated products. *Atmospheric Measurement Techniques*, **10 (1)**, 59–81, https://doi.org/10.5194/AMT-10-59-2017.

Friedlingstein, P., and Coauthors, 2022: Global Carbon Budget 2021. *Earth System Science Data*, **14 (4)**, 1917–2005, https://doi.org/10.5194/ESSD-2021-386, URL https://research-portal.uea.ac.uk/en/publications/global-carbon-budget-2021.

Gourdji, S. M., and Coauthors, 2022: A Modified Vegetation Photosynthesis and Respiration Model (VPRM) for the Eastern USA and Canada, Evaluated With Comparison to Atmospheric Observations and Other Biospheric Models. *Journal of Geophysical Research: Biogeosciences*, **127 (1)**, https://doi.org/10.1029/2021JG006290.

Hastings, W. K., 1970: Monte carlo sampling methods using Markov chains and their applications. *Biometrika*, **57 (1)**, 97–109, https://doi.org/10.1093/biomet/57.1.97, URL https://academic.oup.com/biomet/article/57/1/97/284580.

Hilton, T. W., K. J. Davis, and K. Keller, 2014: Evaluating terrestrial CO2 flux diagnoses and uncertainties from a simple land surface model and its residuals. *Biogeosciences*, **11 (2)**, 217–235, https://doi.org/10.5194/BG-11-217-2014.

Hilton, T. W., K. J. Davis, K. Keller, and N. M. Urban, 2013: Improving North American terrestrial CO2 flux diagnosis using spatial structure in land surface model residuals. *Biogeosciences*, **10 (7)**, 4607–4625, https://doi.org/10.5194/BG-10-4607-2013.

Hu, X. M., and Coauthors, 2020: Dynamical Downscaling of CO2 in 2016 Over the Contiguous United States Using WRF-VPRM, a Weather-Biosphere-Online-Coupled Model. *Journal of Advances in Modeling Earth Systems*, **12 (4)**, https://doi.org/10.1029/2019MS001875.

Hu, X. M., and Coauthors, 2021: Implementation of Improved Parameterization of Terrestrial Flux in WRF-VPRM Improves the Simulation of Nighttime CO2 Peaks and a Daytime CO2 Band Ahead of a Cold Front. *Journal of Geophysical Research: Atmospheres*, **126 (10)**, e2020JD034 362, https://doi.org/10.1029/2020JD034362, URL https://onlinelibrary.wiley.com/doi/full/10.1029/2020JD034362,https://onlinelibrary.wiley.com/doi/abs/10.1029/2020JD034362,https://agupubs.onlinelibrary.wiley.com/doi/10.1029/2020JD034362.

Huete, A., K. Didan, T. Miura, E. P. Rodriguez, X. Gao, and L. G. Ferreira, 2002: Overview of the radiometric and biophysical performance of the MODIS vegetation indices. *Remote Sensing of Environment*, **83 (1-2)**, 195–213, https://doi.org/10.1016/S0034-4257(02)00096-2, URL www.elsevier.com/locate/rse.

Mahadevan, P., and Coauthors, 2008: A satellite-based biosphere parameterization for net ecosystem CO2 exchange: Vegetation Photosynthesis and Respiration Model (VPRM). *Global Biogeochemical Cycles*, **22 (2)**, https://doi.org/10.1029/2006GB002735.

Metropolis, N., A. W. Rosenbluth, M. N. Rosenbluth, A. H. Teller, and E. Teller, 1953: Equation of state calculations by fast computing machines. *The Journal of Chemical Physics*, **21 (6)**, 1087–1092, https://doi.org/10.1063/1.1699114, URL https://aip.scitation.org/doi/abs/10.1063/1.1699114.

Nagler, P. L., R. L. Scott, C. Westenburg, J. R. Cleverly, E. P. Glenn, and A. R. Huete, 2005: Evapotranspiration on western U.S. rivers estimated using the Enhanced Vegetation Index from MODIS and data from eddy covariance and Bowen ratio flux towers. *Remote Sensing of Environment*, **97 (3)**, 337–351, https://doi.org/10.1016/j.rse.2005.05.011, URL www.elsevier.com/locate/rse.

Price, K. V., R. M. Storn, and J. A. Lampinen, 2005: *Differential evolution : a practical approach to global optimization*. Springer, 538 pp.

Robertson, G., and J. Chen, 2022: AmeriFlux BASE US-KM1 KBS marshall farms corn, Ver. 3-5, (Dataset). AmeriFlux; Michigan State University.

Schaaf, C., and Z. Wang, 2021: MODIS/Terra+Aqua BRDF/Albedo Nadir BRDF Adjusted Ref Daily L3 Global - 500m V061. NASA EOSDIS Land Processes DAAC, accessed: 2022-11-7, https://doi.org/10.5067/MODIS/MCD43A4.061.

Suyker, A., 2022a: AmeriFlux BASE US-Ne2 mead - irrigated maize-soybean rotation site, Ver. 11-5, (Dataset). AmeriFlux; University of Nebraska - Lincoln.

Suyker, A., 2022b: AmeriFlux BASE US-Ne3 Mead - rainfed maize-soybean rotation site, Ver. 11-5, (Dataset). AmeriFlux AMP; University of Nebraska - Lincoln, https://doi.org/10.17190/AMF/1246086.

Wiecki, T., and Coauthors, 2022: PyMC-devs/PyMC: v4.4.0. Zenodo, URL https://zenodo.org/record/7338345, https://doi.org/10.5281/ZENODO.7338345.

Xiao, X., D. Hollinger, J. Aber, M. Goltz, E. A. Davidson, Q. Zhang, and B. Moore, 2004a: Satellite-based modeling of gross primary production in an evergreen needleleaf forest. *Remote Sensing of Environment*, **89 (4)**, 519–534, https://doi.org/10.1016/j.rse.2003.11.008, URL http://public.ornl.gov/ameriflux/Data/index.cfm.

Xiao, X., Q. Zhang, B. Braswell, S. Urbanski, S. Boles, S. Wofsy, B. Moore, and D. Ojima, 2004b: Modeling gross primary production of temperate deciduous broadleaf forest using satellite images and climate data. *Remote Sensing of Environment*, **91 (2)**, 256–270, https://doi.org/10.1016/j.rse.2004.03.010, URL www.elsevier.com/locate/rse.

Xu, T., L. White, D. Hui, and Y. Luo, 2006: Probabilistic inversion of a terrestrial ecosystem model: Analysis of uncertainty in parameter estimation and model prediction. *Global Biogeochemical Cycles*, **20 (2)**, https://doi.org/10.1029/2005GB002468.

Appendix A

Parameter Distributions

A.1 Distribution Tables

Table A.1: A table of distribution medians and median absolute deviation (MAD) for the NLLS parameter fitting experiments. Values marked with 'N/A' were held constant for the experiment indicated. Units are described in Table 2.2

Site	Experiment	Statistic	β	α_1	α_2	γ	k_1	k_2	k_3	λ	PAR_0
Ne2	Normal	Prior Median	-0.48	0.1165	-0.0011	5.4268	0.1662	-0.1616	0.0163	-0.0774	2769.8776
Ne2	Normal	Prior MAD	3.3369	0.3982	0.0117	1.5261	2.1784	0.2916	0.0089	0.0123	532.2794
Ne2	Normal	Posterior Median	0.9969	0.011	0.001	-2.1476	-0.3261	1.0509	-0.0381	-0.0237	5061.4007
Ne2	Normal	Posterior MAD	<0.0001	<0.0001	<0.0001	<0.0001	<0.0001	<0.0001	<0.0001	<0.0001	0.9416
Ne2	ER/GEE Separately	Prior Median	-0.48	0.1165	-0.0011	5.4268	0.1662	-0.1616	0.0163	-0.0774	2769.8776
Ne2	ER/GEE Separately	Prior MAD	3.3369	0.3982	0.0117	1.5261	2.1784	0.2916	0.0089	0.0123	532.2794
Ne2	ER/GEE Separately	Posterior Median	0.6496	-0.0238	0.0032	1.2055	-0.767	1.0838	-0.0433	-0.0228	6000.0
Ne2	ER/GEE Separately	Posterior MAD	0.0135	0.0001	0.0001	0.0842	0.0214	0.0214	0.0009	0.0003	<0.0001
Ne2	α_2 drop	Prior Median	-0.48	0.1165	N/A	5.4268	0.1662	-0.1616	0.0163	-0.0774	2769.8776
Ne2	α_2 drop	Prior MAD	3.3369	0.3982	N/A	1.5261	2.1784	0.2916	0.0089	0.0123	532.2794
Ne2	α_2 drop	Posterior Median	0.5251	0.042	N/A	1.5972	-0.5573	0.9448	-0.0375	-0.0227	6000.0
Ne2	α_2 drop	Posterior MAD	0.0167	0.0018	N/A	0.0944	0.0266	0.0252	0.0011	0.0003	<0.0001
Ne2	k_3 drop	Prior Median	-0.48	0.1165	-0.0011	5.4268	0.1662	-0.1616	N/A	-0.0774	2769.8776
Ne2	k_3 drop	Prior MAD	3.3369	0.3982	0.0117	1.5261	2.1784	0.2916	N/A	0.0123	532.2794
Ne2	k_3 drop	Posterior Median	-0.4689	0.2607	-0.0097	6.0284	2.2288	-0.1297	N/A	-0.0239	6000.0
Ne2	k_3 drop	Posterior MAD	0.0098	0.0059	0.0004	0.0168	0.0409	0.0039	N/A	0.0003	<0.0001

Table A.1 continues on next page

Table A.1 continued from previous page

Site	Experiment	Statistic	β	α_1	α_2	γ	k_1	k_2	k_3	λ	PAR_0
Ne2	λ drop	Prior Median	-0.48	0.1165	-0.0011	5.4268	0.1662	-0.1616	0.0163	N/A	2769.8776
Ne2	λ drop	Prior MAD	3.3369	0.3982	0.0117	1.5261	2.1784	0.2916	0.0089	N/A	532.2794
Ne2	λ drop	Posterior Median	0.6481	-0.0238	0.0032	1.2136	-0.7649	1.0818	-0.0432	N/A	353.1329
Ne2	λ drop	Posterior MAD	0.0008	0.0001	<0.0001	0.0042	0.0024	0.002	0.0001	N/A	0.5852
Ne2	PAR_0 drop	Prior Median	-0.48	0.1165	-0.0011	5.4268	0.1662	-0.1616	0.0163	-0.0774	N/A
Ne2	PAR_0 drop	Prior MAD	3.3369	0.3982	0.0117	1.5261	2.1784	0.2916	0.0089	0.0123	N/A
Ne2	PAR_0 drop	Posterior Median	0.6488	-0.0238	0.0032	1.2093	-0.766	1.0829	-0.0432	-0.0271	N/A
Ne2	PAR_0 drop	Posterior MAD	0.0139	0.0001	0.0001	0.0872	0.0217	0.0219	0.0009	0.0004	N/A
Ne3	Normal	Prior Median	-0.48	0.1165	-0.0011	5.4268	0.1662	-0.1616	0.0163	-0.0774	2769.8776
Ne3	Normal	Prior MAD	3.3369	0.3982	0.0117	1.5261	2.1784	0.2916	0.0089	0.0123	532.2794
Ne3	Normal	Posterior Median	0.4565	-0.0368	0.003	2.9516	-2.8892	1.0701	-0.0403	-0.0307	1557.7215
Ne3	Normal	Posterior MAD	<0.0001	<0.0001	<0.0001	<0.0001	<0.0001	<0.0001	<0.0001	<0.0001	0.1521
Ne3	ER/GEE Separately	Prior Median	-0.48	0.1165	-0.0011	5.4268	0.1662	-0.1616	0.0163	-0.0774	2769.8776
Ne3	ER/GEE Separately	Prior MAD	3.3369	0.3982	0.0117	1.5261	2.1784	0.2916	0.0089	0.0123	532.2794
Ne3	ER/GEE Separately	Posterior Median	0.2274	-0.0708	0.0045	4.6425	-3.0653	1.0953	-0.0425	-0.0235	3339.6652
Ne3	ER/GEE Separately	Posterior MAD	0.038	0.0039	<0.0001	0.0755	0.1968	0.0439	0.0015	0.0003	77.0683
Ne3	α_2 drop	Prior Median	-0.48	0.1165	N/A	5.4268	0.1662	-0.1616	0.0163	-0.0774	2769.8776
Ne3	α_2 drop	Prior MAD	3.3369	0.3982	N/A	1.5261	2.1784	0.2916	0.0089	0.0123	532.2794
Ne3	α_2 drop	Posterior Median	-0.0057	0.0244	N/A	5.2461	-2.4218	0.8705	-0.0336	-0.0239	3144.7395
Ne3	α_2 drop	Posterior MAD	0.036	0.0031	N/A	0.0706	0.1909	0.0417	0.0015	0.0003	73.7012
Ne3	k_3 drop	Prior Median	-0.48	0.1165	-0.0011	5.4268	0.1662	-0.1616	N/A	-0.0774	2769.8776
Ne3	k_3 drop	Prior MAD	3.3369	0.3982	0.0117	1.5261	2.1784	0.2916	N/A	0.0123	532.2794
Ne3	k_3 drop	Posterior Median	-1.4105	0.2097	-0.0066	8.1268	4.6816	-0.2698	N/A	-0.0222	5769.4036

Table A.1 continues on next page

Table A.1 continued from previous page

Site	Experiment	Statistic	β	α_1	α_2	γ	k_1	k_2	k_3	λ	PAR_0
Ne3	k_3 drop	Posterior MAD	0.0212	0.0063	0.0004	0.0497	0.0799	0.0053	N/A	0.0003	17.6257
Ne3	λ drop	Prior Median	-0.48	0.1165	-0.0011	5.4268	0.1662	-0.1616	0.0163	N/A	2769.8776
Ne3	λ drop	Prior MAD	3.3369	0.3982	0.0117	1.5261	2.1784	0.2916	0.0089	N/A	532.2794
Ne3	λ drop	Posterior Median	0.2237	-0.0705	0.0045	4.6501	-3.0445	1.091	-0.0424	N/A	305.6309
Ne3	λ drop	Posterior MAD	0.004	0.0004	<0.0001	0.0055	0.0242	0.0049	0.0002	N/A	0.7359
Ne3	PAR_0 drop	Prior Median	-0.48	0.1165	-0.0011	5.4268	0.1662	-0.1616	0.0163	-0.0774	N/A
Ne3	PAR_0 drop	Prior MAD	3.3369	0.3982	0.0117	1.5261	2.1784	0.2916	0.0089	0.0123	N/A
Ne3	PAR_0 drop	Posterior Median	0.2256	-0.0707	0.0045	4.6463	-3.0541	1.0931	-0.0424	-0.0248	N/A
Ne3	PAR_0 drop	Posterior MAD	0.0384	0.0039	<0.0001	0.0781	0.201	0.0445	0.0016	0.0005	N/A
KM1	Normal	Prior Median	-0.48	0.1165	-0.0011	5.4268	0.1662	-0.1616	0.0163	-0.0774	2769.8776
KM1	Normal	Prior MAD	3.3369	0.3982	0.0117	1.5261	2.1784	0.2916	0.0089	0.0123	532.2794
KM1	Normal	Posterior Median	-1.023	0.1307	-0.0038	7.0886	0.8848	0.3404	-0.0096	-0.188	225.8973
KM1	Normal	Posterior MAD	<0.0001	<0.0001	<0.0001	<0.0001	<0.0001	<0.0001	<0.0001	<0.0001	0.0023
KM1	ER/GEE Separately	Prior Median	-0.48	0.1165	-0.0011	5.4268	0.1662	-0.1616	0.0163	-0.0774	2769.8776
KM1	ER/GEE Separately	Prior MAD	3.3369	0.3982	0.0117	1.5261	2.1784	0.2916	0.0089	0.0123	532.2794
KM1	ER/GEE Separately	Posterior Median	-0.0108	0.0851	-0.0007	3.3123	0.5697	0.4547	-0.0149	-0.0984	502.1505
KM1	ER/GEE Separately	Posterior MAD	0.0097	0.0003	0.0001	0.0057	0.0377	0.0395	0.0028	0.0036	7.4397
KM1	α_2 drop	Prior Median	-0.48	0.1165	N/A	5.4268	0.1662	-0.1616	0.0163	-0.0774	2769.8776
KM1	α_2 drop	Prior MAD	3.3369	0.3982	N/A	1.5261	2.1784	0.2916	0.0089	0.0123	532.2794
KM1	α_2 drop	Posterior Median	-0.0057	0.0717	N/A	3.3252	0.5725	0.4816	-0.0164	-0.0984	503.3742
KM1	α_2 drop	Posterior MAD	0.0092	0.0009	N/A	0.0053	0.038	0.0419	0.003	0.0036	7.58
KM1	k_3 drop	Prior Median	-0.48	0.1165	-0.0011	5.4268	0.1662	-0.1616	N/A	-0.0774	2769.8776
KM1	k_3 drop	Prior MAD	3.3369	0.3982	0.0117	1.5261	2.1784	0.2916	N/A	0.0123	532.2794

Table A.1 continues on next page

Table A.1 continued from previous page

Site	Experiment	Statistic	β	α_1	α_2	γ	k_1	k_2	k_3	λ	PAR_0
KM1	k_3 drop	Posterior Median	-0.1207	0.178	-0.006	3.7351	0.5464	0.1694	N/A	-0.0985	501.0784
KM1	k_3 drop	Posterior MAD	0.031	0.0181	0.0011	0.081	0.0333	0.0149	N/A	0.0036	7.1898
KM1	λ drop	Prior Median	-0.48	0.1165	-0.0011	5.4268	0.1662	-0.1616	0.0163	N/A	2769.8776
KM1	λ drop	Prior MAD	3.3369	0.3982	0.0117	1.5261	2.1784	0.2916	0.0089	N/A	532.2794
KM1	λ drop	Posterior Median	-0.0088	0.085	-0.0007	3.3125	0.5647	0.4497	-0.0145	N/A	720.355
KM1	λ drop	Posterior MAD	0.0026	0.0001	<0.0001	0.0053	0.0058	0.0056	0.0004	N/A	3.987
KM1	PAR_0 drop	Prior Median	-0.48	0.1165	-0.0011	5.4268	0.1662	-0.1616	0.0163	-0.0774	N/A
KM1	PAR_0 drop	Prior MAD	3.3369	0.3982	0.0117	1.5261	2.1784	0.2916	0.0089	0.0123	N/A
KM1	PAR_0 drop	Posterior Median	-0.0092	0.085	-0.0007	3.3123	0.5665	0.4516	-0.0147	-0.0424	N/A
KM1	PAR_0 drop	Posterior MAD	0.0093	0.0003	0.0001	0.0017	0.0379	0.04	0.0029	0.0012	N/A
Ro1	Normal	Prior Median	-0.48	0.1165	-0.0011	5.4268	0.1662	-0.1616	0.0163	-0.0774	2769.8776
Ro1	Normal	Prior MAD	3.3369	0.3982	0.0117	1.5261	2.1784	0.2916	0.0089	0.0123	532.2794
Ro1	Normal	Posterior Median	-0.6793	0.094	-0.0022	5.0857	1.0703	0.3723	-0.014	-0.1422	284.654
Ro1	Normal	Posterior MAD	<0.0001	<0.0001	<0.0001	<0.0001	<0.0001	<0.0001	<0.0001	<0.0001	0.0007
Ro1	ER/GEE Separately	Prior Median	-0.48	0.1165	-0.0011	5.4268	0.1662	-0.1616	0.0163	-0.0774	2769.8776
Ro1	ER/GEE Separately	Prior MAD	3.3369	0.3982	0.0117	1.5261	2.1784	0.2916	0.0089	0.0123	532.2794
Ro1	ER/GEE Separately	Posterior Median	-1.0166	0.0447	0.0011	7.5832	1.1232	0.1475	-0.0102	-0.0991	469.0696
Ro1	ER/GEE Separately	Posterior MAD	0.0009	0.0017	0.0001	0.0271	0.0327	0.028	0.0019	0.0036	12.4458
Ro1	α_2 drop	Prior Median	-0.48	0.1165	N/A	5.4268	0.1662	-0.1616	0.0163	-0.0774	2769.8776
Ro1	α_2 drop	Prior MAD	3.3369	0.3982	N/A	1.5261	2.1784	0.2916	0.0089	0.0123	532.2794
Ro1	α_2 drop	Posterior Median	-1.0597	0.0671	N/A	7.6872	1.147	0.1017	-0.008	-0.0997	463.7912
Ro1	α_2 drop	Posterior MAD	0.0034	0.0001	N/A	0.0197	0.0347	0.025	0.0018	0.0035	11.8531
Ro1	k_3 drop	Prior Median	-0.48	0.1165	-0.0011	5.4268	0.1662	-0.1616	N/A	-0.0774	2769.8776

Table A.1 continues on next page

Table A.1 continued from previous page

Site	Experiment	Statistic	β	α_1	α_2	γ	k_1	k_2	k_3	λ	PAR_0
Ro1	k_3 drop	Prior Median	3.3369	0.3982	0.0117	1.5261	2.1784	0.2916	N/A	0.0123	532.2794
Ro1	k_3 drop	Posterior Median	-1.1815	0.1107	-0.0023	8.3391	1.1415	-0.0786	N/A	-0.1012	457.0564
Ro1	k_3 drop	Posterior MAD	0.0313	0.0109	0.0006	0.1176	0.0365	0.015	N/A	0.0032	9.5116
Ro1	λ drop	Prior Median	-0.48	0.1165	-0.0011	5.4268	0.1662	-0.1616	0.0163	N/A	2769.8776
Ro1	λ drop	Prior MAD	3.3369	0.3982	0.0117	1.5261	2.1784	0.2916	0.0089	N/A	532.2794
Ro1	λ drop	Posterior Median	-1.0166	0.0449	0.0011	7.5832	1.1197	0.1449	-0.01	N/A	690.9106
Ro1	λ drop	Posterior MAD	0.0009	0.0001	<0.0001	0.0031	0.0038	0.0025	0.0002	N/A	1.8943
Ro1	PAR_0 drop	Prior Median	-0.48	0.1165	-0.0011	5.4268	0.1662	-0.1616	0.0163	-0.0774	N/A
Ro1	PAR_0 drop	Prior MAD	3.3369	0.3982	0.0117	1.5261	2.1784	0.2916	0.0089	0.0123	N/A
Ro1	PAR_0 drop	Posterior Median	-1.0166	0.0448	0.0011	7.5818	1.1213	0.1463	-0.0101	-0.0437	N/A
Ro1	PAR_0 drop	Posterior MAD	<0.0001	0.0017	0.0001	0.0266	0.0334	0.0287	0.002	0.0008	N/A

End of Table A.1

Table A.2: A table of distribution medians and median absolute deviation (MAD) for the MCMC parameter fitting experiments. Values marked with 'N/A' were held constant for the experiment indicated. Units are described in Table 2.2

Site	Experiment	Statistic	β	α_1	α_2	γ	k_1	k_2	k_3	λ	PAR_0
Ne2	Normal	Prior Median	-0.1855	0.0737	-0.001	5.4866	0.1602	-0.1512	0.016	-0.0782	2783.6421
Ne2	Normal	Prior MAD	2.7654	0.0549	0.0001	1.4712	1.3049	0.0387	0.0001	0.0044	540.5935
Ne2	Normal	Posterior Median	-0.4095	0.1463	-0.0038	5.53	4.0558	-0.5344	0.0136	-0.0268	5480.3211
Ne2	Normal	Posterior MAD	0.0315	0.0026	0.0001	0.181	0.1094	0.0074	0.0001	0.0004	347.7465
Ne2	ER/GEE Separately	Prior Median	-0.146	0.0727	-0.001	5.4407	0.1324	-0.153	0.016	-0.078	2809.1055
Ne2	ER/GEE Separately	Prior MAD	2.8078	0.0553	0.0001	1.4831	1.2972	0.0379	0.0001	0.0044	526.1539
Ne2	ER/GEE Separately	Posterior Median	-0.9082	0.1273	-0.0022	9.2707	4.3143	-0.6937	0.0149	-0.0257	6500.0
Ne2	ER/GEE Separately	Posterior MAD	0.0465	0.0037	0.0001	0.2476	0.1718	0.0092	0.0001	0.0001	0.0
Ne2	α_2 drop	Prior Median	-0.1386	0.0719	N/A	5.5282	0.1301	-0.1516	0.016	-0.078	2809.1055

Table A.2 continues on next page

Table A.2 continued from previous page

Site	Experiment	Statistic	β	α_1	α_2	γ	k_1	k_2	k_3	λ	PAR_0
Ne2	α_2 drop	Prior MAD	2.7888	0.0564	N/A	1.4967	1.2819	0.0375	0.0001	0.0044	526.1539
Ne2	α_2 drop	Posterior Median	-0.9382	0.0866	N/A	9.6204	4.552	-0.7231	0.0148	-0.026	6500.0
Ne2	α_2 drop	Posterior MAD	0.0496	0.0035	N/A	0.2646	0.1755	0.0111	0.0001	0.0001	0.0
Ne2	k_3 drop	Prior Median	-0.1386	0.0719	-0.001	5.4842	0.16	-0.1535	N/A	-0.078	2782.0002
Ne2	k_3 drop	Prior MAD	2.7888	0.0564	0.0001	1.4488	1.2822	0.0381	N/A	0.0001	0.0044
Ne2	k_3 drop	Posterior Median	-0.5684	0.1119	-0.0018	7.2897	3.1204	-0.2434	N/A	-0.0247	6500.0
Ne2	k_3 drop	Posterior MAD	0.0443	0.0035	0.0001	0.2517	0.1776	0.0094	N/A	0.0001	0.0
Ne2	λ drop	Prior Median	-0.146	0.0727	-0.001	5.4407	0.1324	-0.153	0.016	N/A	2786.7462
Ne2	λ drop	Prior MAD	2.8078	0.0553	0.0001	1.4831	1.2972	0.0379	0.0001	N/A	529.1851
Ne2	λ drop	Posterior Median	-0.9082	0.1273	-0.0022	9.2707	4.3143	-0.6937	0.0149	N/A	428.788
Ne2	λ drop	Posterior MAD	0.0465	0.0037	0.0001	0.2476	0.1718	0.0092	0.0001	N/A	2.7945
Ne2	PAR_0 drop	Prior Median	-0.146	0.0727	-0.001	5.4407	0.1324	-0.153	0.016	-0.078	N/A
Ne2	PAR_0 drop	Prior MAD	2.8078	0.0553	0.0001	1.4831	1.2972	0.0379	0.0001	0.0044	N/A
Ne2	PAR_0 drop	Posterior Median	-0.9082	0.1273	-0.0022	9.2707	4.3143	-0.6937	0.0149	-0.0309	N/A
Ne2	PAR_0 drop	Posterior MAD	0.0465	0.0037	0.0001	0.2476	0.1718	0.0092	0.0001	0.0001	N/A
Ne3	Normal	Prior Median	-0.1855	0.0737	-0.001	5.4866	0.1602	-0.1512	0.016	-0.0782	2783.6421
Ne3	Normal	Prior MAD	2.7654	0.0549	0.0001	1.4712	1.3049	0.0387	0.0001	0.0044	540.5935
Ne3	Normal	Posterior Median	-2.196	0.208	-0.0039	9.0046	10.6502	-0.9139	0.0129	-0.0249	3738.6098
Ne3	Normal	Posterior MAD	0.0361	0.0027	0.0001	0.1917	0.1568	0.0073	0.0001	0.0005	284.4526
Ne3	ER/GEE Separately	Prior Median	-0.146	0.0727	-0.001	5.4407	0.1324	-0.153	0.016	-0.078	2809.1055
Ne3	ER/GEE Separately	Prior MAD	2.8078	0.0553	0.0001	1.4831	1.2972	0.0379	0.0001	0.0044	526.1539
Ne3	ER/GEE Separately	Posterior Median	-2.1932	0.1607	-0.0022	9.6946	9.9273	-0.9055	0.0147	-0.0236	6500.0
Ne3	ER/GEE Separately	Posterior MAD	0.0469	0.0034	0.0001	0.292	0.2357	0.0099	0.0001	0.0001	0.0
Ne3	α_2 drop	Prior Median	-0.1386	0.0719	N/A	5.5282	0.1301	-0.1516	0.016	-0.078	2809.1055

Table A.2 continues on next page

Table A.2 continued from previous page

Site	Experiment	Statistic	β	α_1	α_2	γ	k_1	k_2	k_3	λ	PAR_0
Ne3	α_2 drop	Prior MAD	2.7888	0.0564	N/A	1.4967	1.2819	0.0375	0.0001	0.0044	526.1539
Ne3	α_2 drop	Posterior Median	-2.2988	0.1242	N/A	9.8411	10.8338	-0.9633	0.0146	-0.0239	6500.0
Ne3	α_2 drop	Posterior MAD	0.0491	0.0029	N/A	0.2553	0.2162	0.0104	0.0001	0.0001	0.0
Ne3	k_3 drop	Prior Median	-0.1386	0.0719	-0.001	5.4842	0.16	-0.1535	N/A	-0.078	2782.0002
Ne3	k_3 drop	Prior MAD	2.7888	0.0564	0.0001	1.4488	1.2822	0.0381	N/A	0.0001	0.0044
Ne3	k_3 drop	Posterior Median	-1.5832	0.1269	-0.0017	8.3427	6.4402	-0.3808	N/A	-0.0225	6500.0
Ne3	k_3 drop	Posterior MAD	0.0497	0.003	0.0001	0.2716	0.1889	0.0092	N/A	0.0001	0.0
Ne3	λ drop	Prior Median	-0.146	0.0727	-0.001	5.4407	0.1324	-0.153	0.016	N/A	2786.7462
Ne3	λ drop	Prior MAD	2.8078	0.0553	0.0001	1.4831	1.2972	0.0379	0.0001	N/A	529.1851
Ne3	λ drop	Posterior Median	-2.1932	0.1607	-0.0022	9.6946	9.9273	-0.9055	0.0147	N/A	368.6935
Ne3	λ drop	Posterior MAD	0.0469	0.0034	0.0001	0.292	0.2357	0.0099	0.0001	N/A	2.5426
Ne3	PAR_0 drop	Prior Median	-0.146	0.0727	-0.001	5.4407	0.1324	-0.153	0.016	-0.078	N/A
Ne3	PAR_0 drop	Prior MAD	2.8078	0.0553	0.0001	1.4831	1.2972	0.0379	0.0001	0.0044	N/A
Ne3	PAR_0 drop	Posterior Median	-2.1932	0.1607	-0.0022	9.6946	9.9273	-0.9055	0.0147	-0.0283	N/A
Ne3	PAR_0 drop	Posterior MAD	0.0469	0.0034	0.0001	0.292	0.2357	0.0099	0.0001	0.0001	N/A
KM1	Normal	Prior Median	-0.1855	0.0737	-0.001	5.4866	0.1602	-0.1512	0.016	-0.0782	2783.6421
KM1	Normal	Prior MAD	2.7654	0.0549	0.0001	1.4712	1.3049	0.0387	0.0001	0.0044	540.5935
KM1	Normal	Posterior Median	-1.4217	0.0976	-0.0034	10.2445	0.9144	-0.2216	0.0145	-0.1615	291.1479
KM1	Normal	Posterior MAD	0.0456	0.0032	0.0001	0.1712	0.0522	0.0073	0.0001	0.0024	5.5715
KM1	ER/GEE Separately	Prior Median	-0.146	0.0727	-0.001	5.4407	0.1324	-0.153	0.016	-0.078	2809.1055
KM1	ER/GEE Separately	Prior MAD	2.8078	0.0553	0.0001	1.4831	1.2972	0.0379	0.0001	0.0044	526.1539
KM1	ER/GEE Separately	Posterior Median	-0.4761	0.0849	-0.0022	6.6393	0.5109	-0.2146	0.0152	-0.097	551.2912
KM1	ER/GEE Separately	Posterior MAD	0.0565	0.0039	0.0001	0.2264	0.0657	0.0095	0.0001	0.0006	3.3245
KM1	α_2 drop	Prior Median	-0.1386	0.0719	N/A	5.5282	0.1301	-0.1516	0.016	-0.078	2809.1055

Table A.2 continues on next page

Table A.2 continued from previous page

Site	Experiment	Statistic	β	α_1	α_2	γ	k_1	k_2	k_3	λ	PAR_0
KM1	α_2 drop	Prior MAD	2.7888	0.0564	N/A	1.4967	1.2819	0.0375	0.0001	0.0044	526.1539
KM1	α_2 drop	Posterior Median	-0.5509	0.0404	N/A	7.2738	0.5254	-0.2364	0.0151	-0.0966	563.3392
KM1	α_2 drop	Posterior MAD	0.0578	0.0038	N/A	0.2185	0.0664	0.0089	0.0001	0.0006	3.3842
KM1	k_3 drop	Prior Median	-0.1386	0.0719	-0.001	5.4842	0.16	-0.1535	N/A	-0.078	2782.0002
KM1	k_3 drop	Prior MAD	2.7888	0.0564	0.0001	1.4488	1.2822	0.0381	N/A	0.0001	0.0044
KM1	k_3 drop	Posterior Median	-0.3137	0.0913	-0.0015	5.17	0.5992	0.1089	N/A	-0.0978	525.3042
KM1	k_3 drop	Posterior MAD	0.0575	0.0037	0.0001	0.2198	0.066	0.0093	N/A	0.0006	3.1064
KM1	λ drop	Prior Median	-0.146	0.0727	-0.001	5.4407	0.1324	-0.153	0.016	N/A	2786.7462
KM1	λ drop	Prior MAD	2.8078	0.0553	0.0001	1.4831	1.2972	0.0379	0.0001	N/A	529.1851
KM1	λ drop	Posterior Median	-0.4761	0.0849	-0.0022	6.6393	0.5109	-0.2146	0.0152	N/A	776.2055
KM1	λ drop	Posterior MAD	0.0565	0.0039	0.0001	0.2264	0.0657	0.0095	0.0001	N/A	3.9936
KM1	PAR_0 drop	Prior Median	-0.146	0.0727	-0.001	5.4407	0.1324	-0.153	0.016	-0.078	N/A
KM1	PAR_0 drop	Prior MAD	2.8078	0.0553	0.0001	1.4831	1.2972	0.0379	0.0001	0.0044	N/A
KM1	PAR_0 drop	Posterior Median	-0.4761	0.0849	-0.0022	6.6393	0.5109	-0.2146	0.0152	-0.0445	N/A
KM1	PAR_0 drop	Posterior MAD	0.0565	0.0039	0.0001	0.2264	0.0657	0.0095	0.0001	0.0001	N/A
Ro1	Normal	Prior Median	-0.1855	0.0737	-0.001	5.4866	0.1602	-0.1512	0.016	-0.0782	2783.6421
Ro1	Normal	Prior MAD	2.7654	0.0549	0.0001	1.4712	1.3049	0.0387	0.0001	0.0044	540.5935
Ro1	Normal	Posterior Median	-0.8653	0.1458	-0.0051	6.9604	0.8827	-0.2071	0.0125	-0.1514	285.5758
Ro1	Normal	Posterior MAD	0.0267	0.0023	0.0001	0.1206	0.0332	0.0056	0.0001	0.0019	4.715
Ro1	ER/GEE Separately	Prior Median	-0.146	0.0727	-0.001	5.4407	0.1324	-0.153	0.016	-0.078	2809.1055
Ro1	ER/GEE Separately	Prior MAD	2.8078	0.0553	0.0001	1.4831	1.2972	0.0379	0.0001	0.0044	526.1539
Ro1	ER/GEE Separately	Posterior Median	-1.294	0.11	-0.0026	9.8441	0.9171	-0.4134	0.0145	-0.1028	467.4688
Ro1	ER/GEE Separately	Posterior MAD	0.0329	0.0025	0.0001	0.1467	0.0399	0.0062	0.0001	0.0005	2.6716
Ro1	α_2 drop	Prior Median	-0.1386	0.0719	N/A	5.5282	0.1301	-0.1516	0.016	-0.078	2809.1055

Table A.2 continues on next page

Table A.2 continued from previous page

Site	Experiment	Statistic	β	α_1	α_2	γ	k_1	k_2	k_3	λ	PAR_0
Ro1	α_2 drop	Prior MAD	2.7888	0.0564	N/A	1.4967	1.2819	0.0375	0.0001	0.0044	526.1539
Ro1	α_2 drop	Posterior Median	-1.2434	0.0555	N/A	10.1861	0.794	-0.4196	0.0141	-0.1016	483.9903
Ro1	α_2 drop	Posterior MAD	0.031	0.0019	N/A	0.1277	0.0388	0.0061	0.0001	0.0005	2.7149
Ro1	k_3 drop	Prior Median	-0.1386	0.0719	-0.001	5.4842	0.16	-0.1535	N/A	-0.078	2782.0002
Ro1	k_3 drop	Prior MAD	2.7888	0.0564	0.0001	1.4488	1.2822	0.0381	N/A	0.0001	0.0044
Ro1	k_3 drop	Posterior Median	-1.1584	0.0916	-0.0013	8.4229	1.0939	-0.0816	N/A	-0.1011	462.1234
Ro1	k_3 drop	Posterior MAD	0.0294	0.0024	0.0001	0.1208	0.0378	0.0054	N/A	0.0005	2.5916
Ro1	λ drop	Prior Median	-0.146	0.0727	-0.001	5.4407	0.1324	-0.153	0.016	N/A	2786.7462
Ro1	λ drop	Prior MAD	2.8078	0.0553	0.0001	1.4831	1.2972	0.0379	0.0001	N/A	529.1851
Ro1	λ drop	Posterior Median	-1.294	0.11	-0.0026	9.8441	0.9171	-0.4134	0.0145	N/A	730.8831
Ro1	λ drop	Posterior MAD	0.0329	0.0025	0.0001	0.1467	0.0399	0.0062	0.0001	N/A	2.5797
Ro1	PAR_0 drop	Prior Median	-0.146	0.0727	-0.001	5.4407	0.1324	-0.153	0.016	-0.078	N/A
Ro1	PAR_0 drop	Prior MAD	2.8078	0.0553	0.0001	1.4831	1.2972	0.0379	0.0001	0.0044	N/A
Ro1	PAR_0 drop	Posterior Median	-1.294	0.11	-0.0026	9.8441	0.9171	-0.4134	0.0145	-0.0451	N/A
Ro1	PAR_0 drop	Posterior MAD	0.0329	0.0025	0.0001	0.1467	0.0399	0.0062	0.0001	0.0001	N/A

End of Table A.2

A.2 Distribution Graphs

A.2.1 Whole Data Set Simultaneously

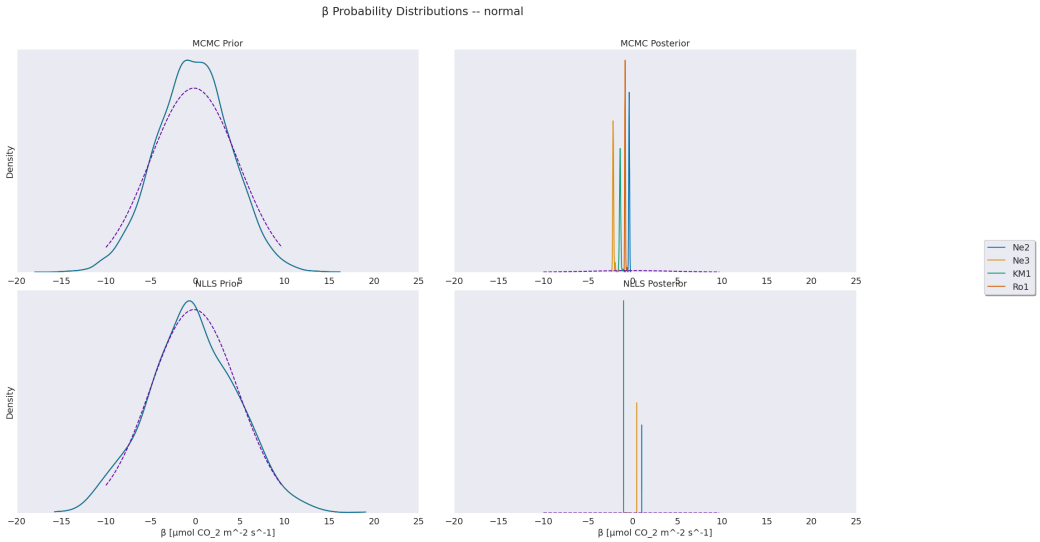

Figure A.1: Same as Figure 3.3 but for the β parameter distributions.

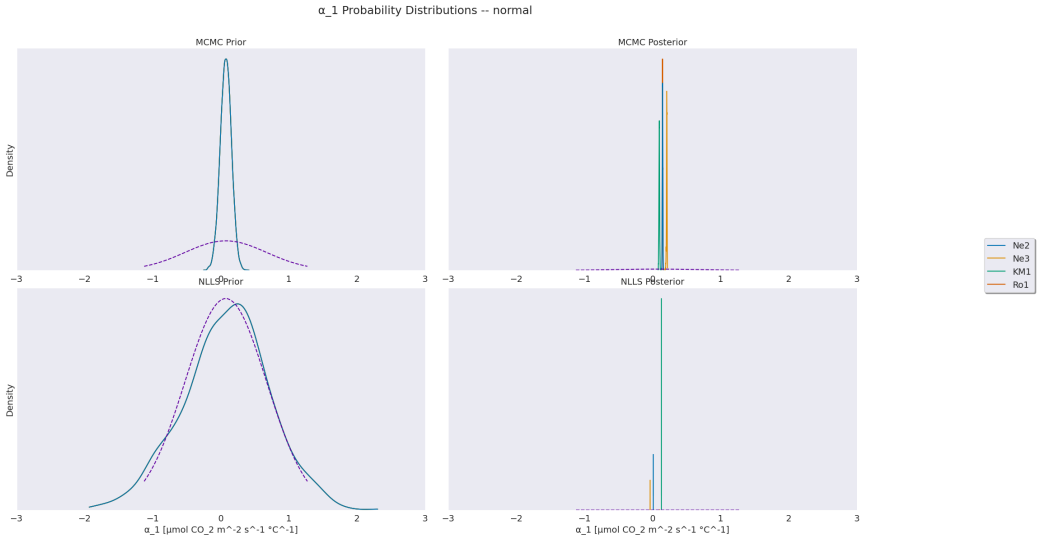

Figure A.2: Same as Figure 3.3 but for the α_1 parameter distributions.

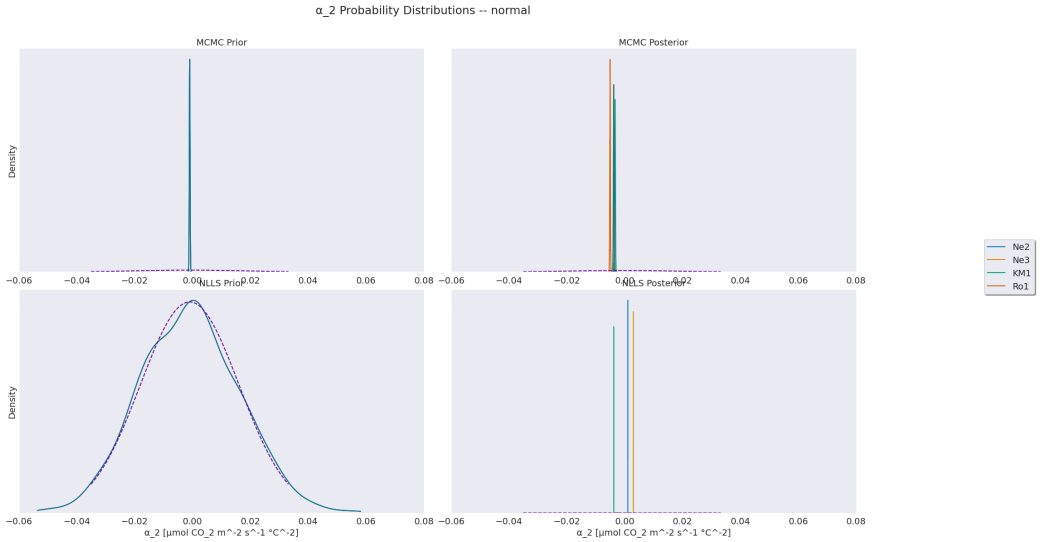

Figure A.3: Same as Figure 3.3 but for the α_2 parameter distributions.

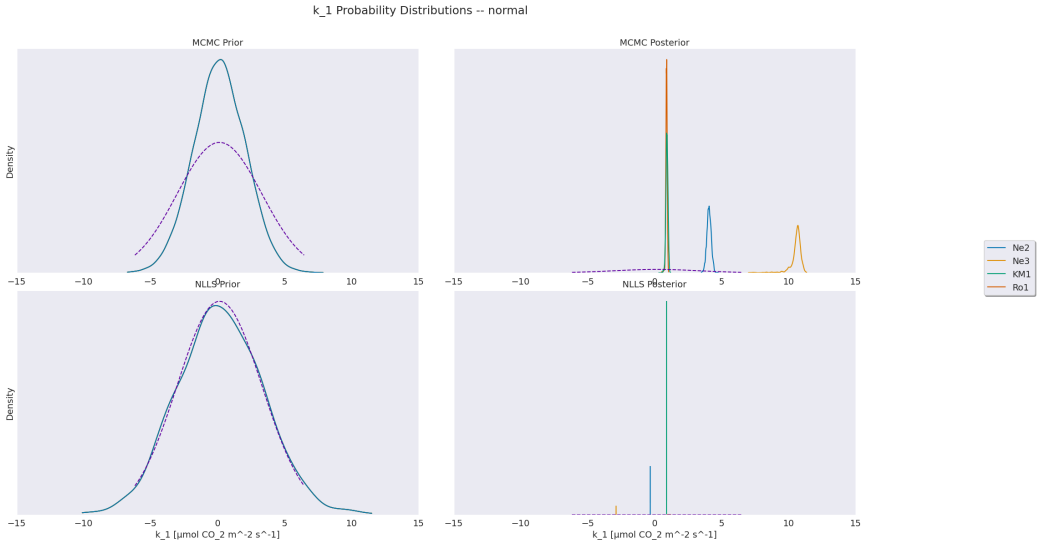

Figure A.4: Same as Figure 3.3 but for the k_1 parameter distributions.

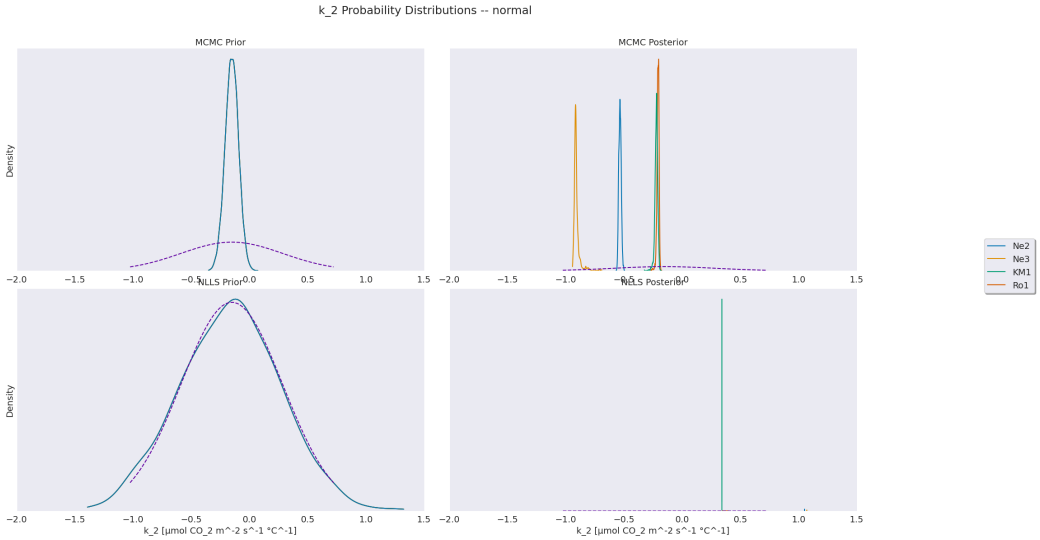

Figure A.5: Same as Figure 3.3 but for the k_2 parameter distributions.

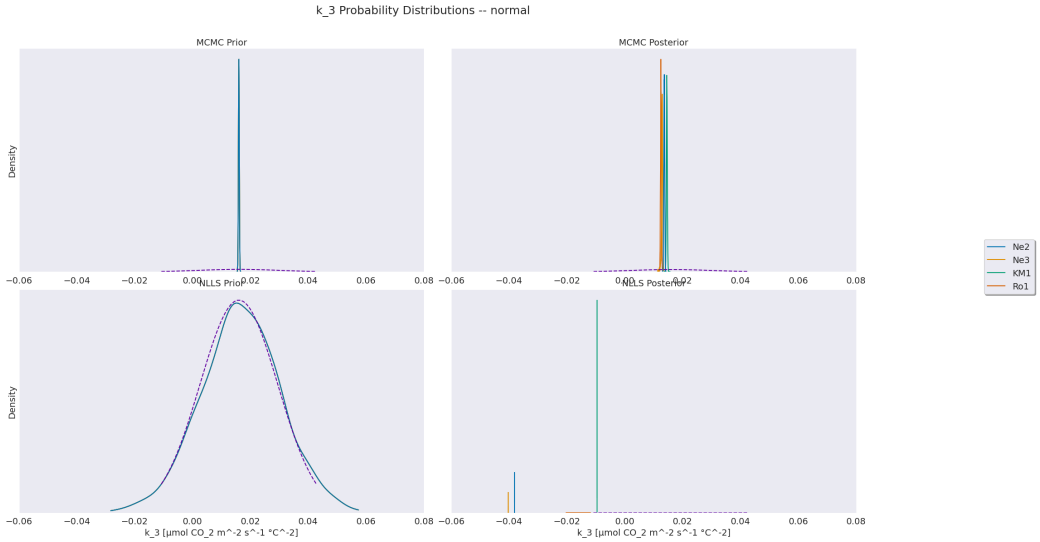

Figure A.6: Same as Figure 3.3 but for the k_3 parameter distributions.

A.2.2 ER/GEE Separately

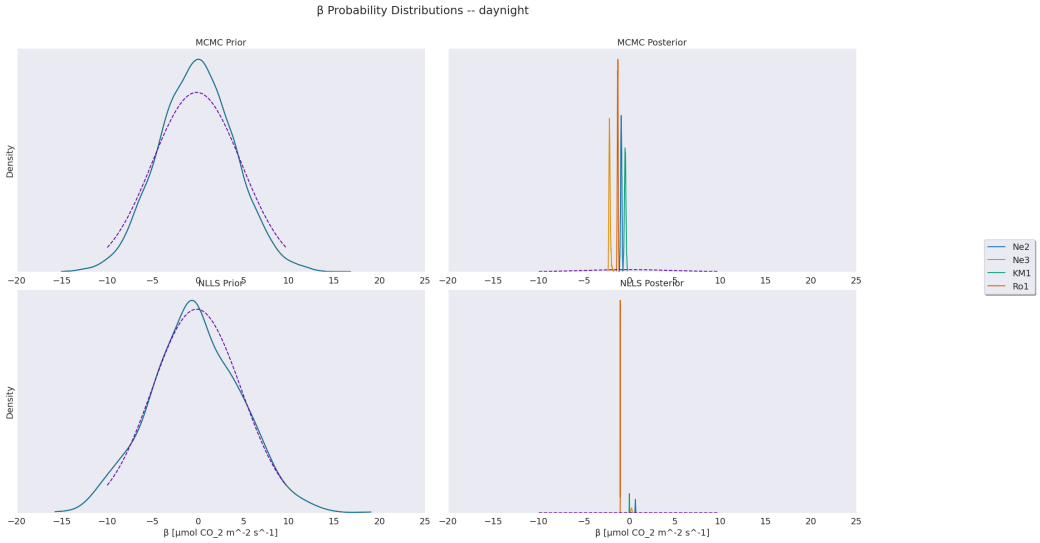

Figure A.7: Same as Figure A.1 but fitting ER and GEE separately.

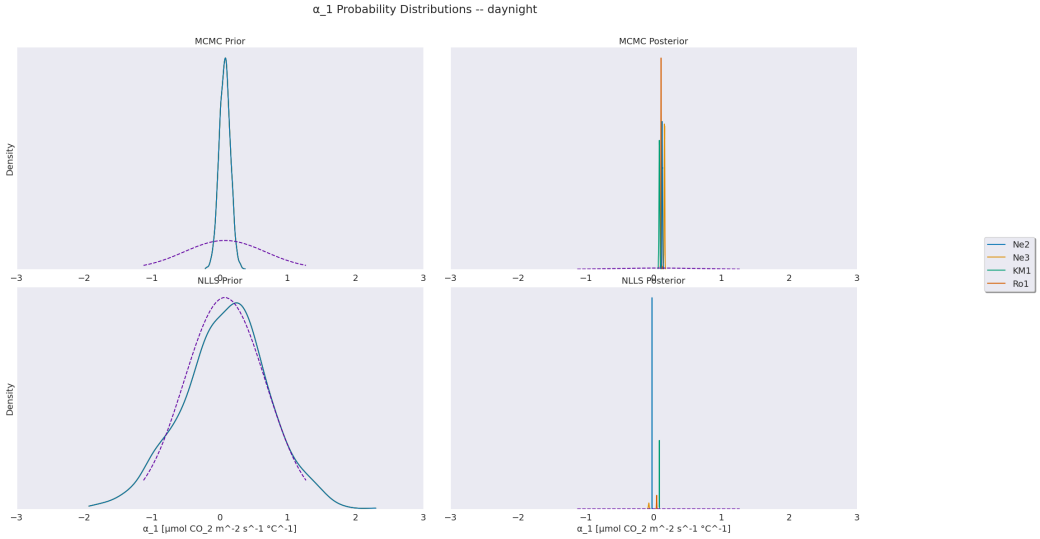

Figure A.8: Same as Figure A.2 but fitting ER and GEE separately.

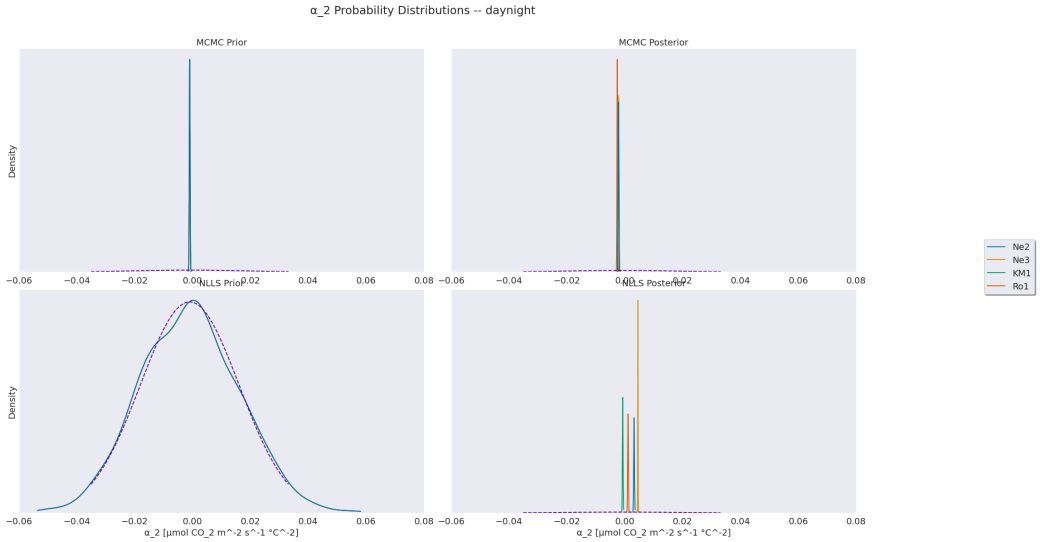

Figure A.9: Same as Figure A.3 but fitting ER and GEE separately.

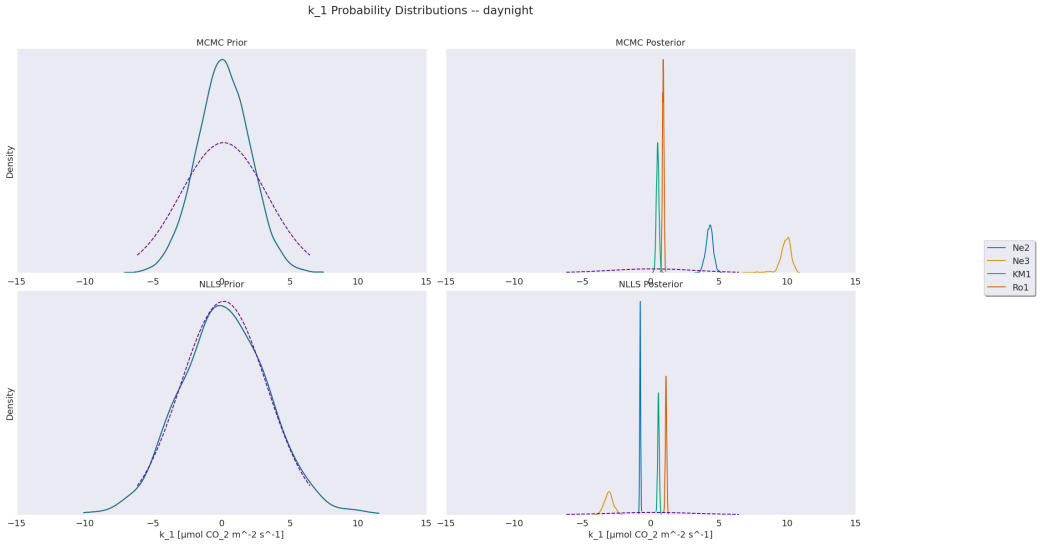

Figure A.10: Same as Figure A.4 but fitting ER and GEE separately.

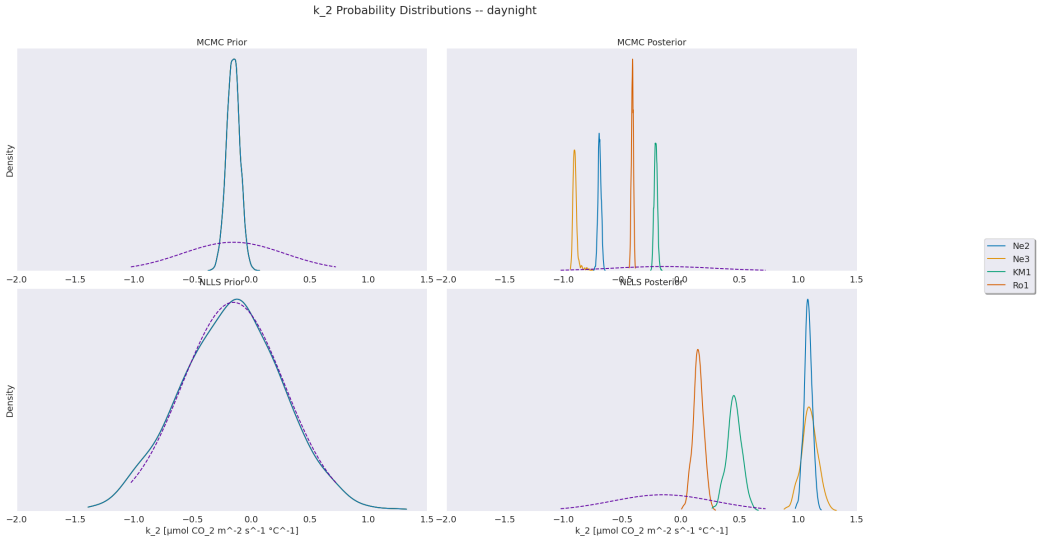

Figure A.11: Same as Figure A.5 but fitting ER and GEE separately.

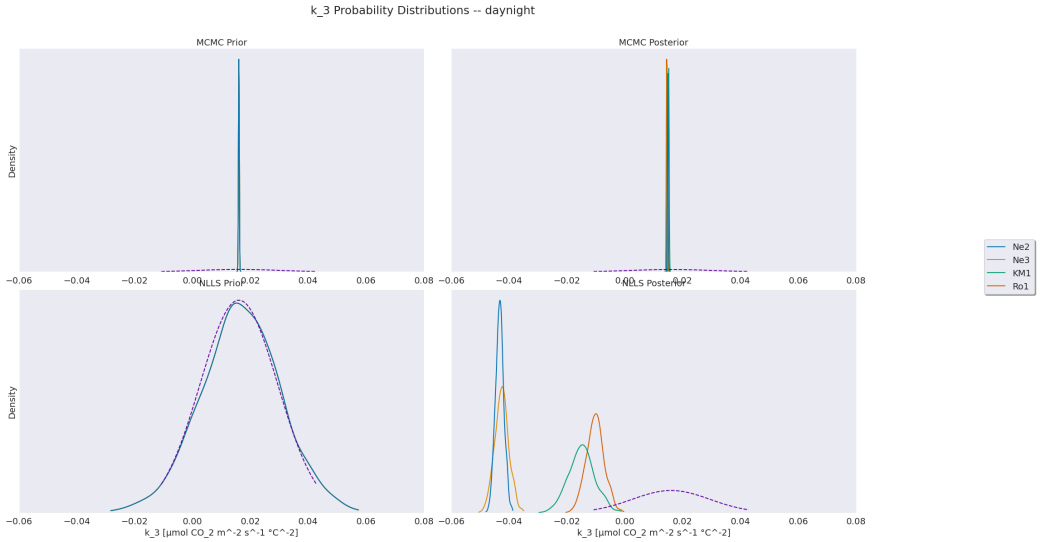

Figure A.12: Same as Figure A.6 but fitting ER and GEE separately.

A.2.3 α_2 Drop Experiment

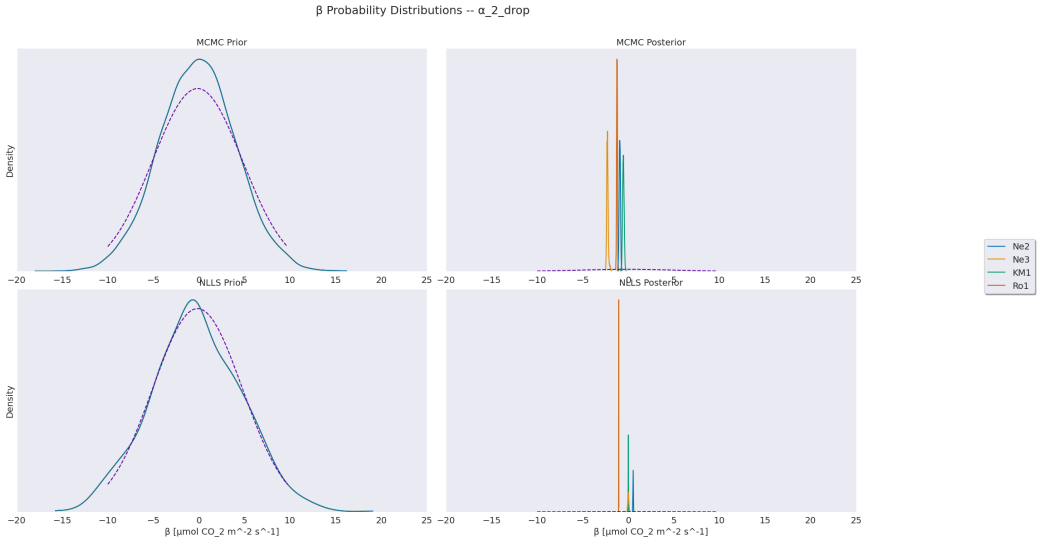

Figure A.13: Same as Figure A.1 but for the α_2 parameter drop experiment.

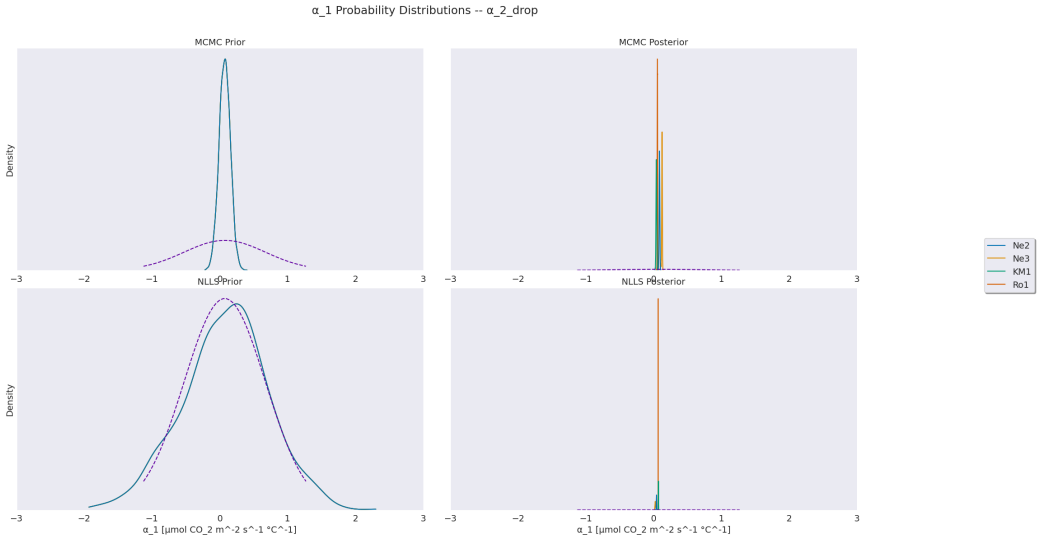

Figure A.14: Same as Figure A.2 but for the α_2 parameter drop experiment.

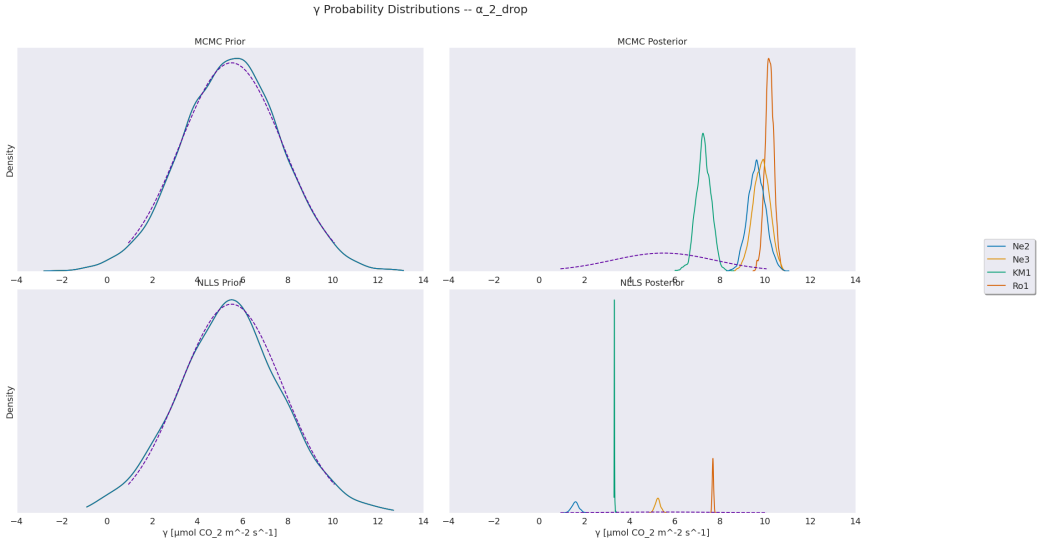

Figure A.15: Same as Figure 3.4 but for the α_2 parameter drop experiment.

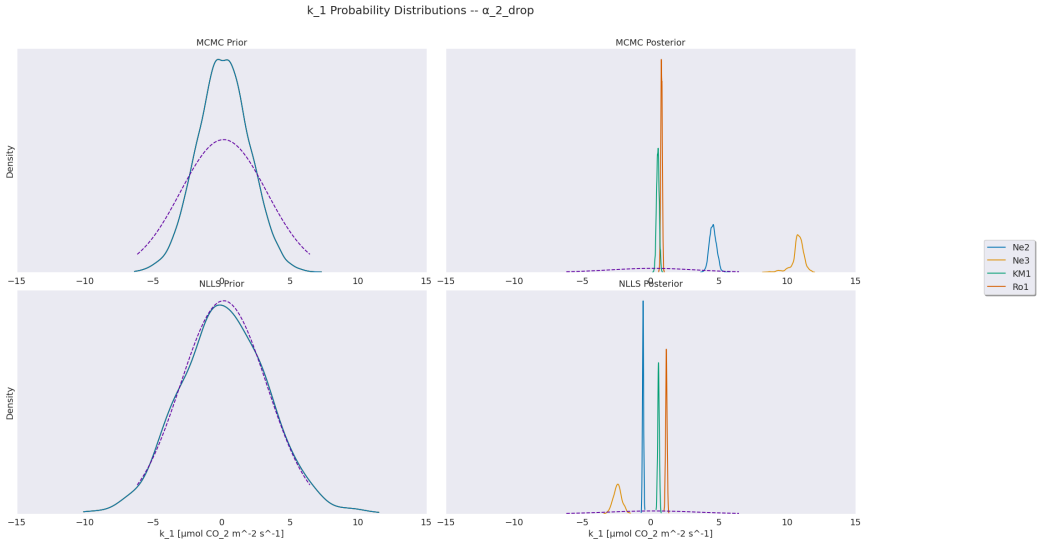

Figure A.16: Same as Figure A.4 but for the α_2 parameter drop experiment.

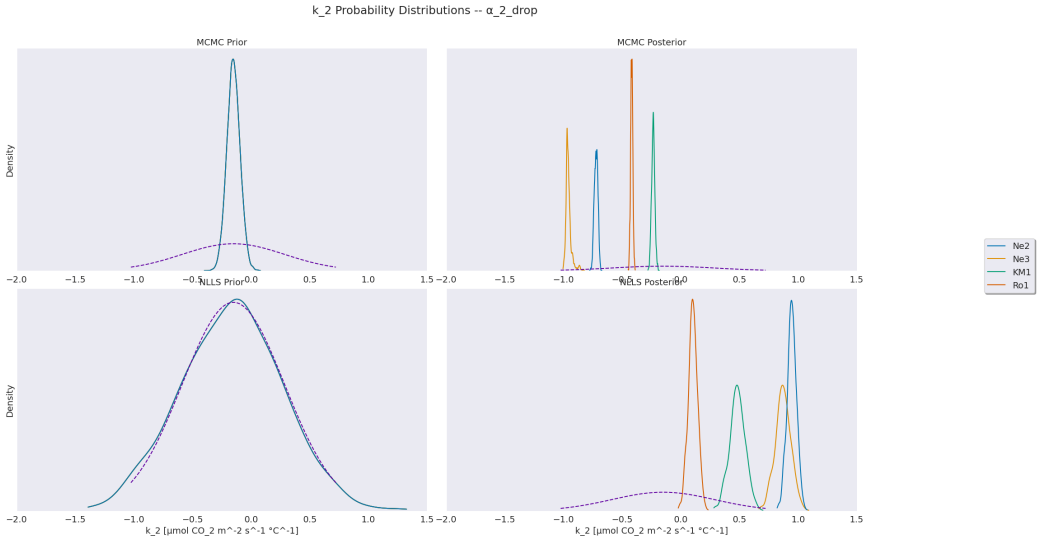

Figure A.17: Same as Figure A.5 but for the α_2 parameter drop experiment.

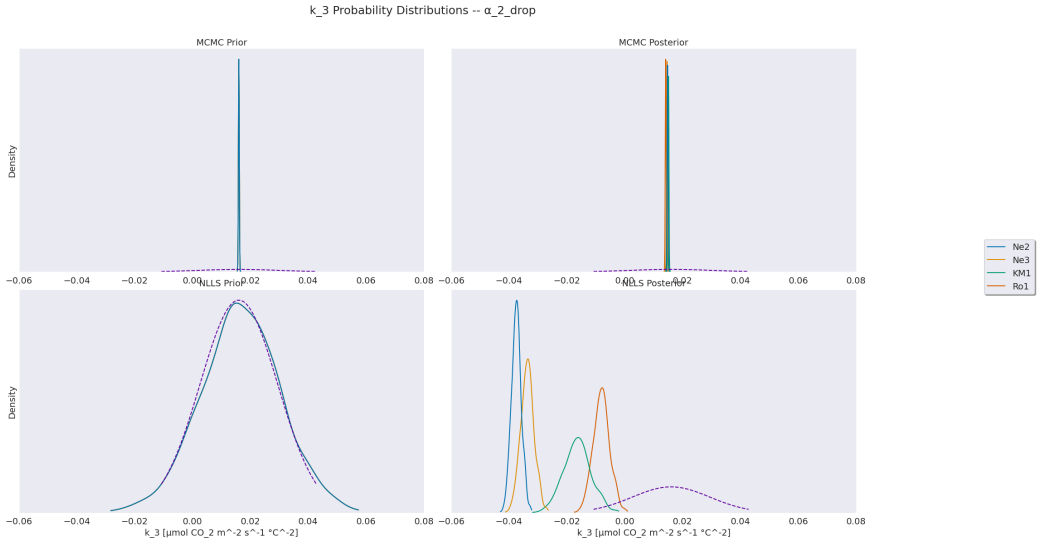

Figure A.18: Same as Figure A.6 but for the α_2 parameter drop experiment.

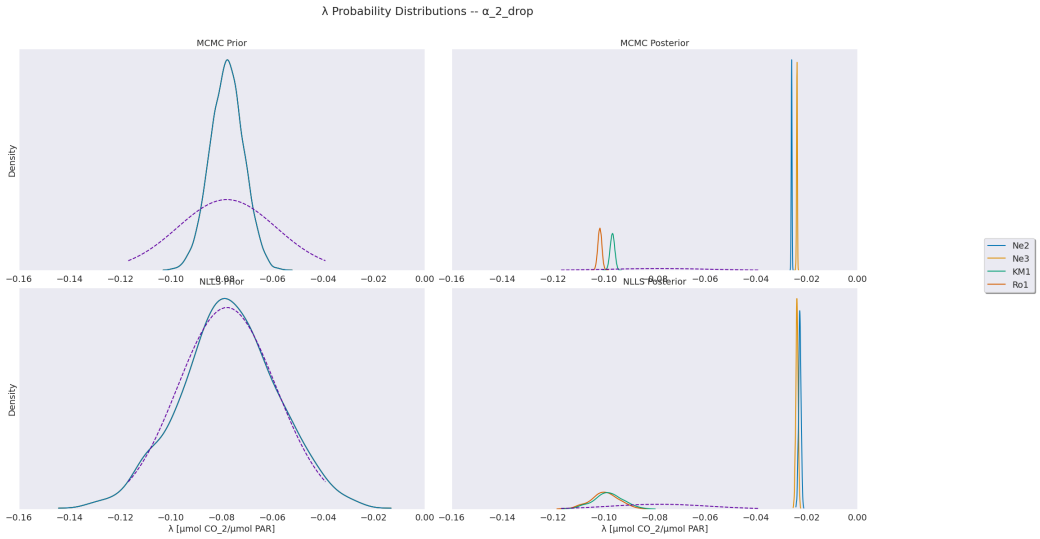

Figure A.19: Same as Figure 3.5 but for the α_2 parameter drop experiment.

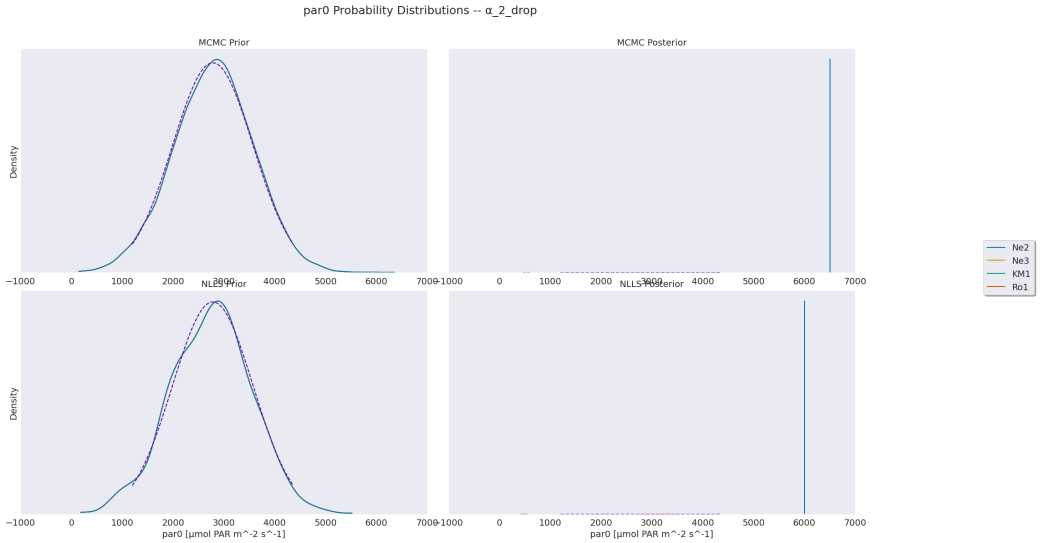

Figure A.20: Same as Figure 3.3 but for the α_2 parameter drop experiment.

A.2.4 k_3 Drop Experiment

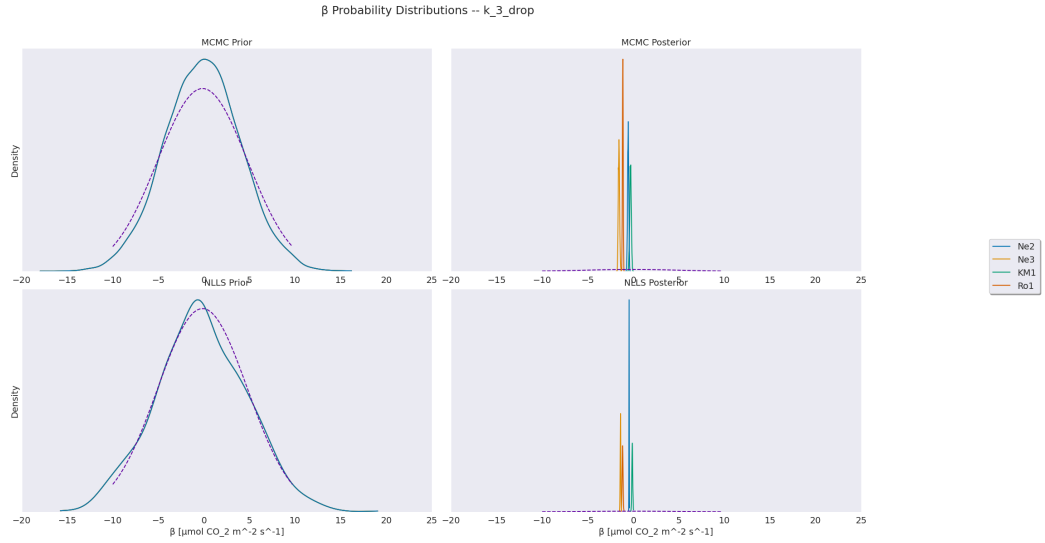

Figure A.21: Same as Figure A.1 but for the k_3 parameter drop experiment.

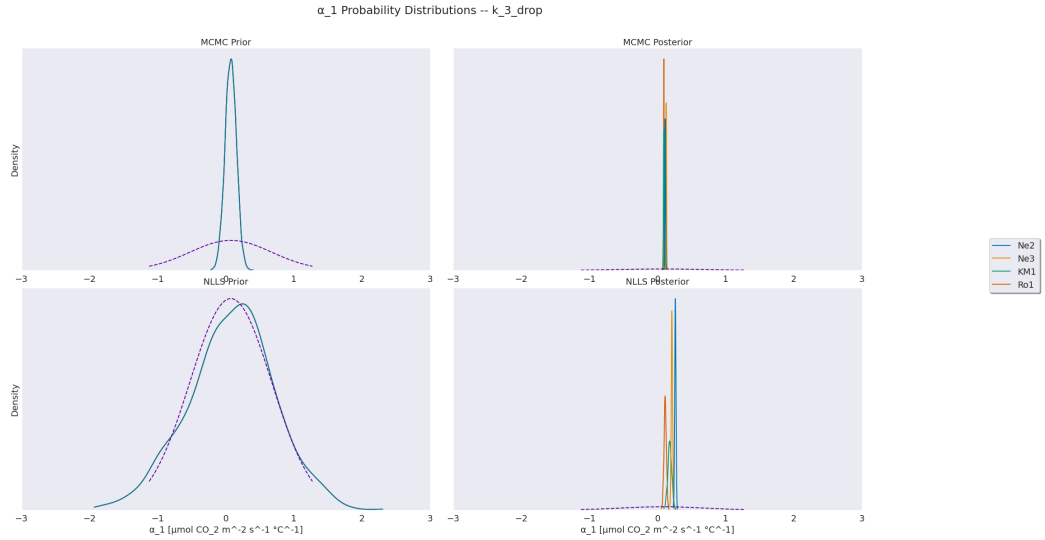

Figure A.22: Same as Figure A.2 but for the k_3 parameter drop experiment.

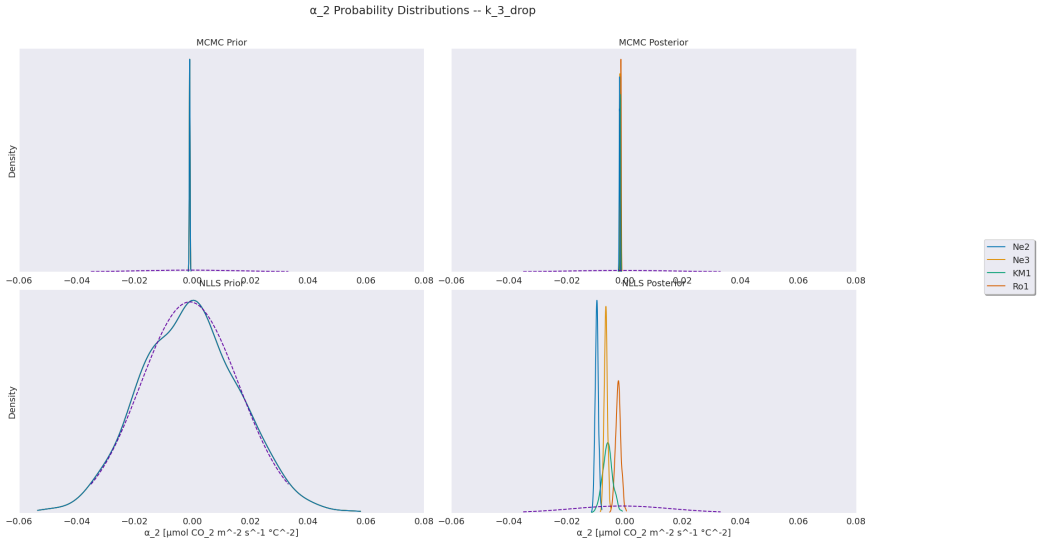

Figure A.23: Same as Figure A.3 but for the k_3 parameter drop experiment.

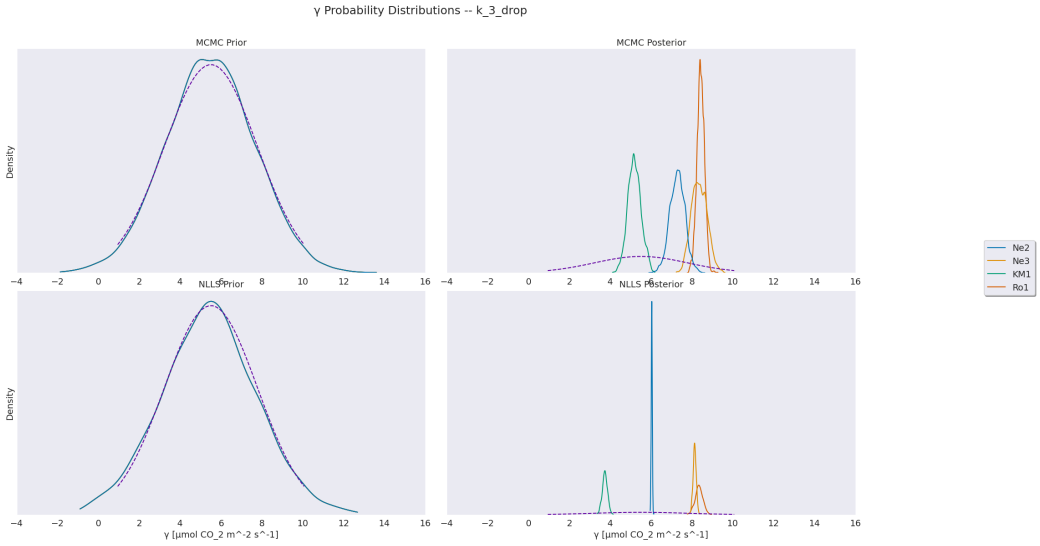

Figure A.24: Same as Figure 3.4 but for the k_3 parameter drop experiment.

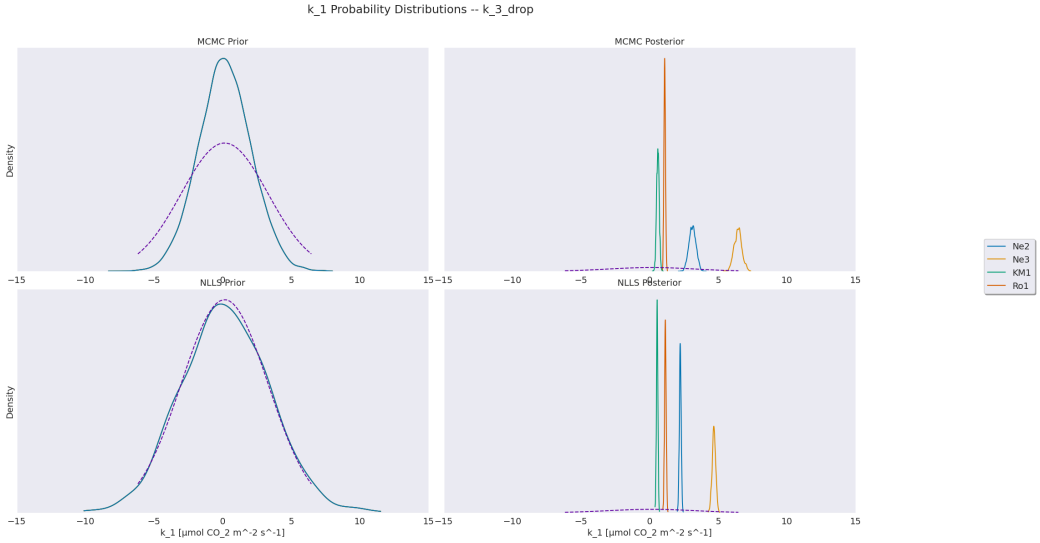

Figure A.25: Same as Figure A.4 but for the k_3 parameter drop experiment.

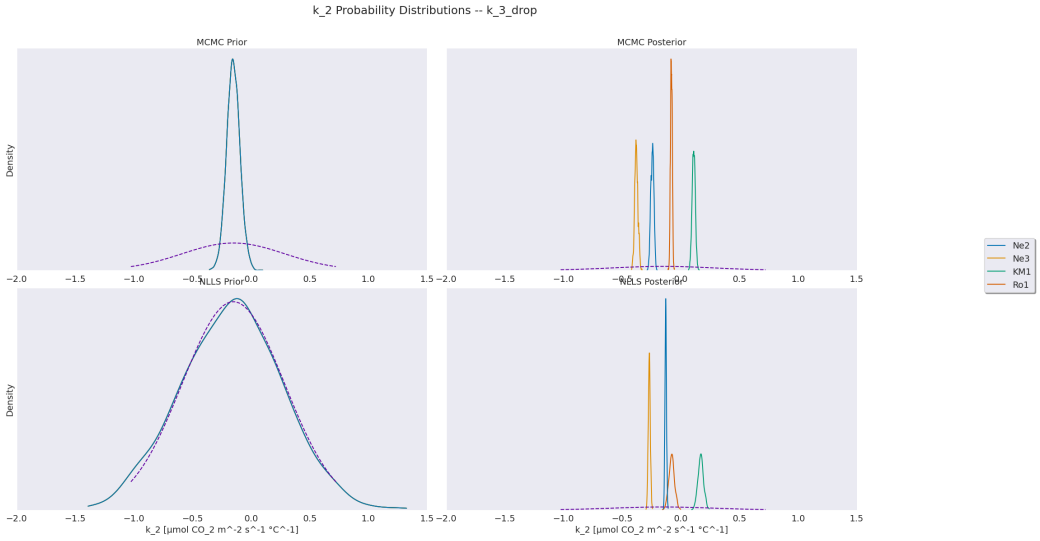

Figure A.26: Same as Figure A.5 but for the k_3 parameter drop experiment.

A.2.5 λ Drop Experiment

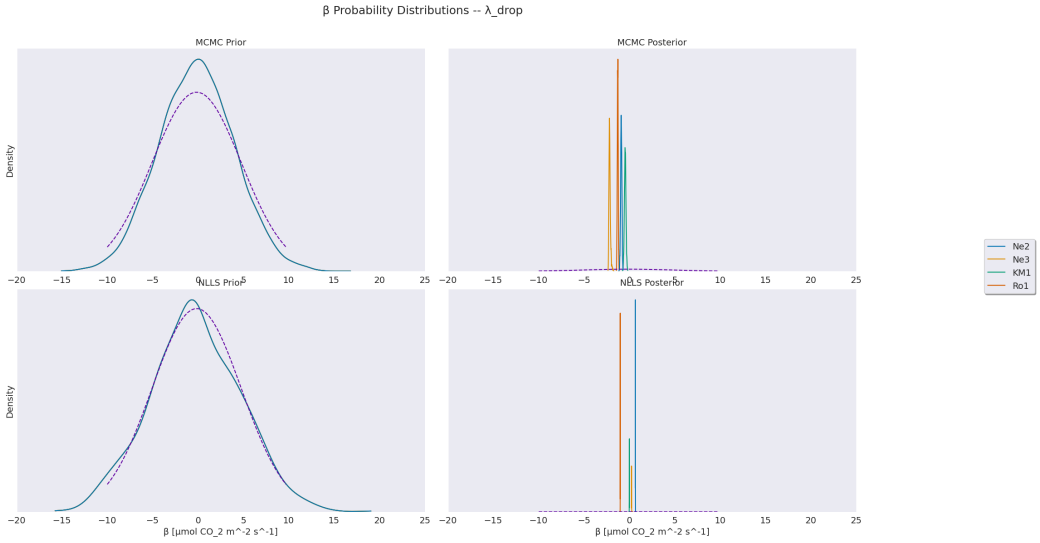

Figure A.27: Same as Figure A.1 but for the λ parameter drop experiment.

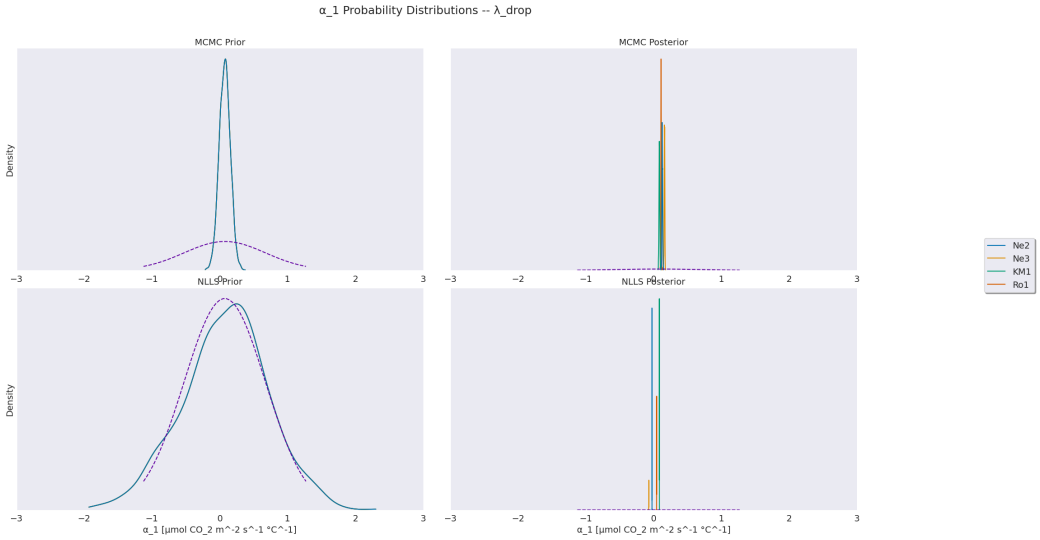

Figure A.28: Same as Figure A.2 but for the λ parameter drop experiment.

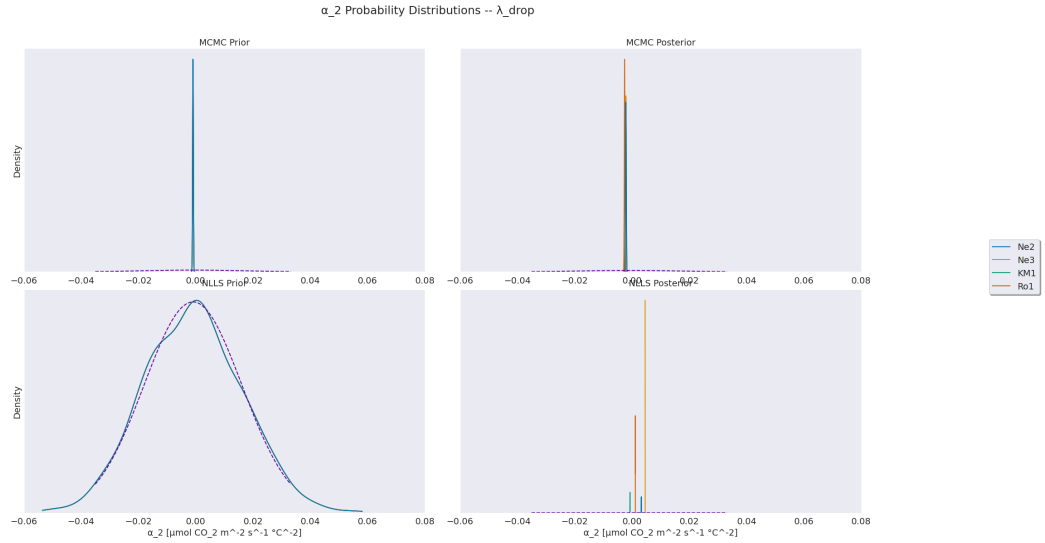

Figure A.29: Same as Figure A.3 but for the λ parameter drop experiment.

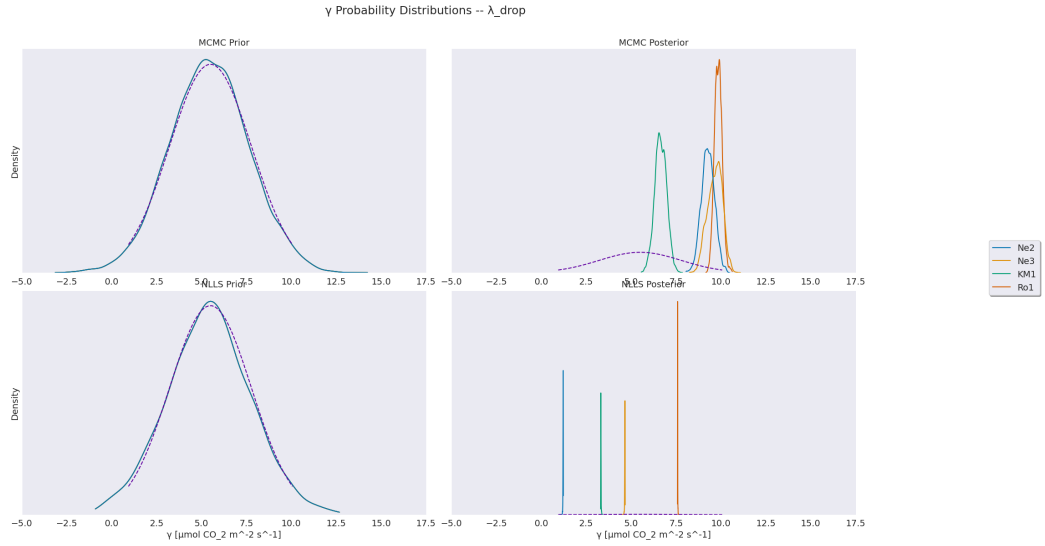

Figure A.30: Same as Figure 3.4 but for the λ parameter drop experiment.

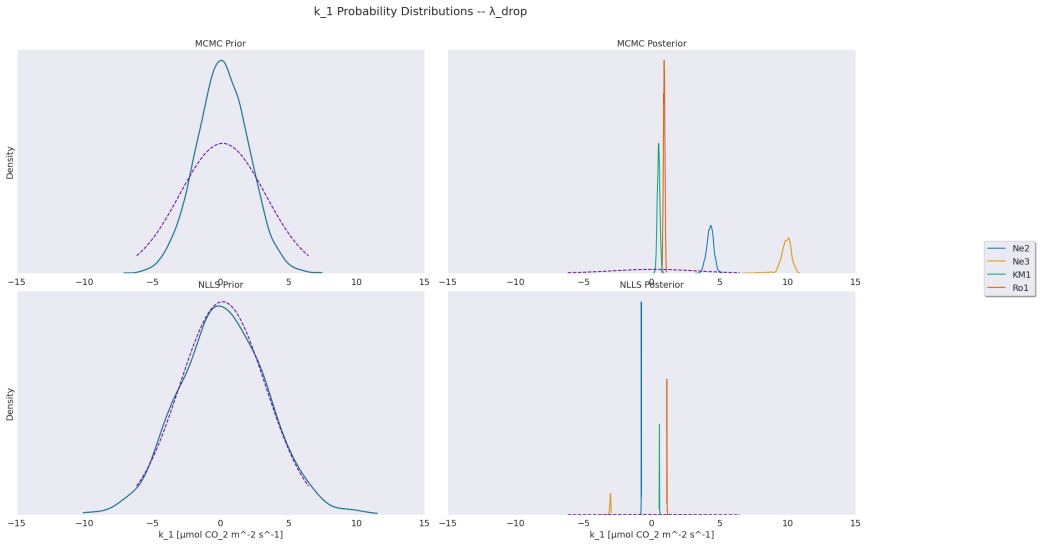

Figure A.31: Same as Figure A.4 but for the λ parameter drop experiment.

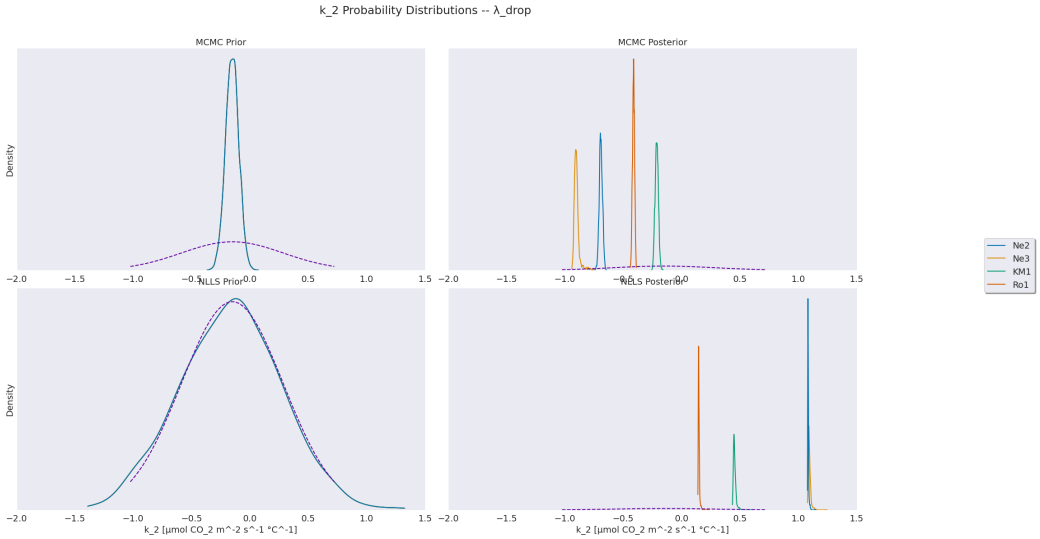

Figure A.32: Same as Figure A.5 but for the λ parameter drop experiment.

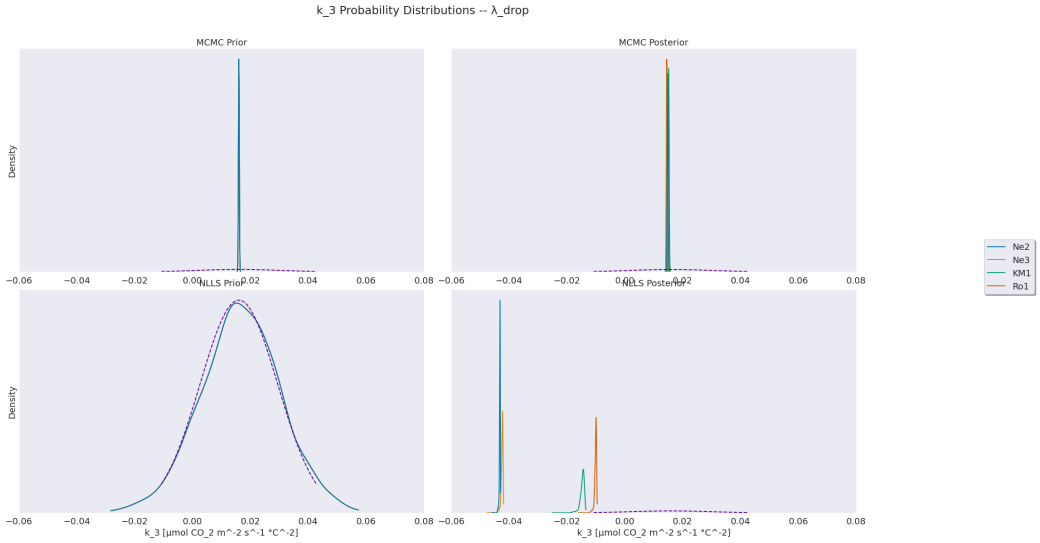

Figure A.33: Same as Figure A.6 but for the λ parameter drop experiment.

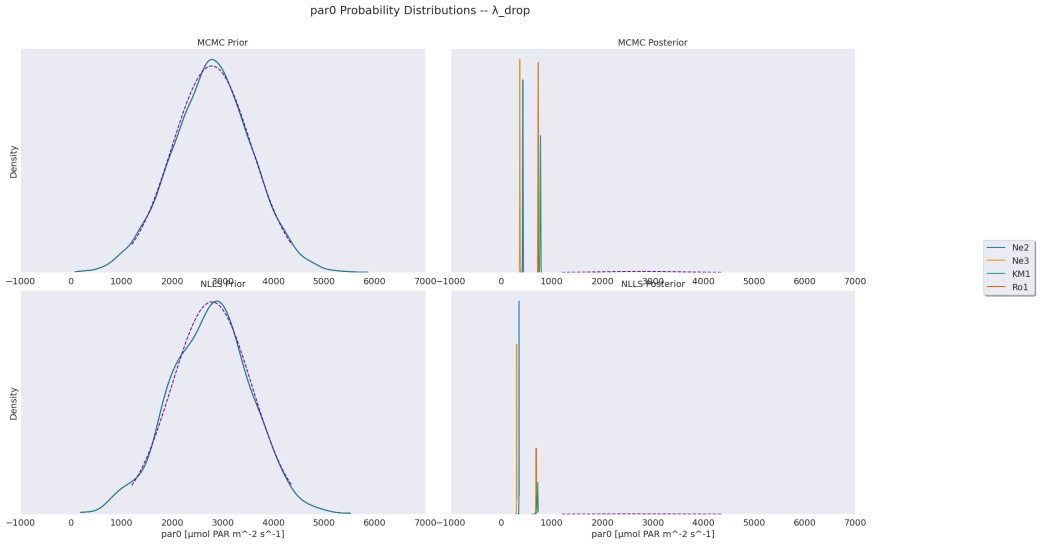

Figure A.34: Same as Figure 3.3 but for the λ parameter drop experiment.

A.2.6 PAR_0 Drop Experiment

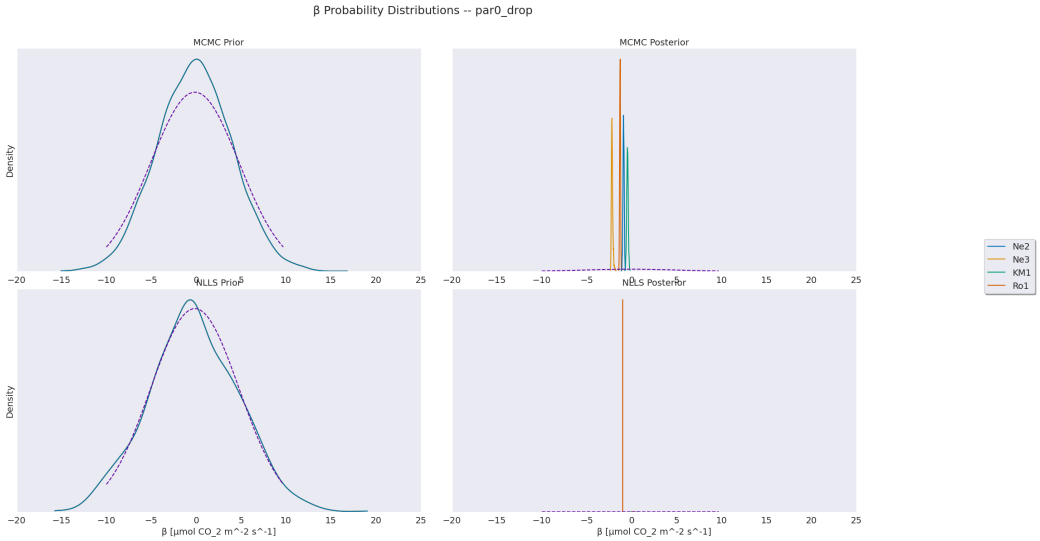

Figure A.35: Same as Figure A.1 but for the PAR_0 parameter drop experiment.

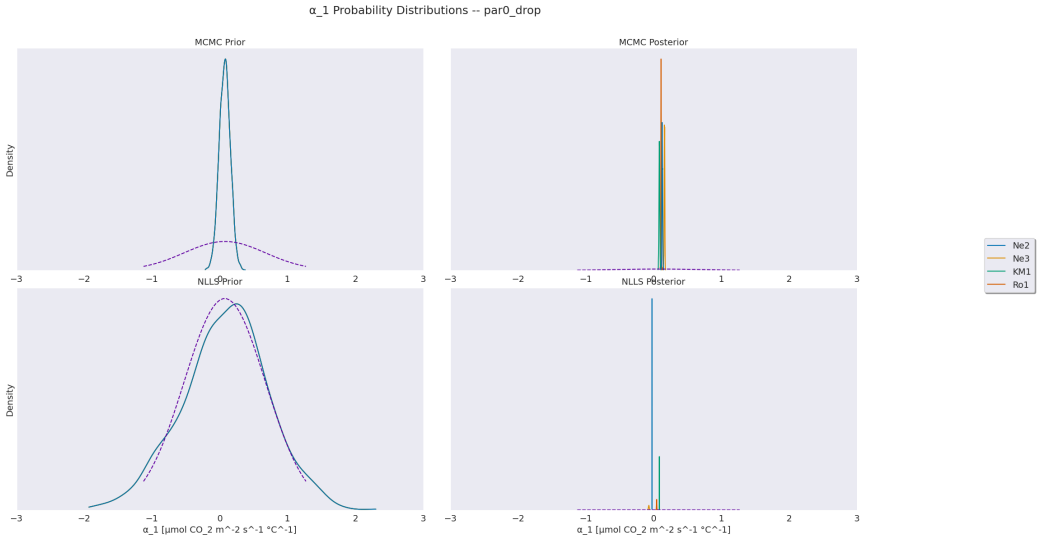

Figure A.36: Same as Figure A.2 but for the PAR_0 parameter drop experiment.

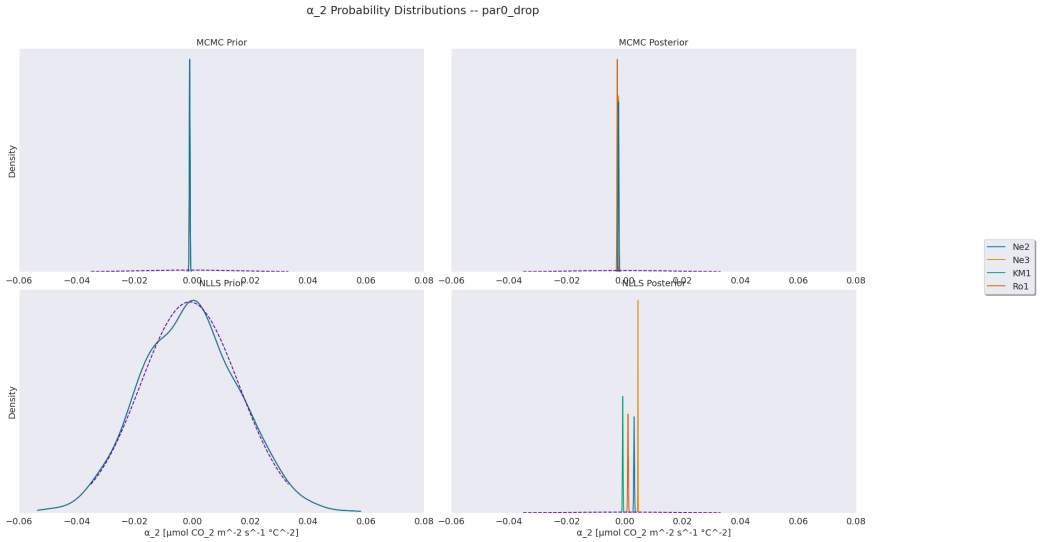

Figure A.37: Same as Figure A.3 but for the PAR_0 parameter drop experiment.

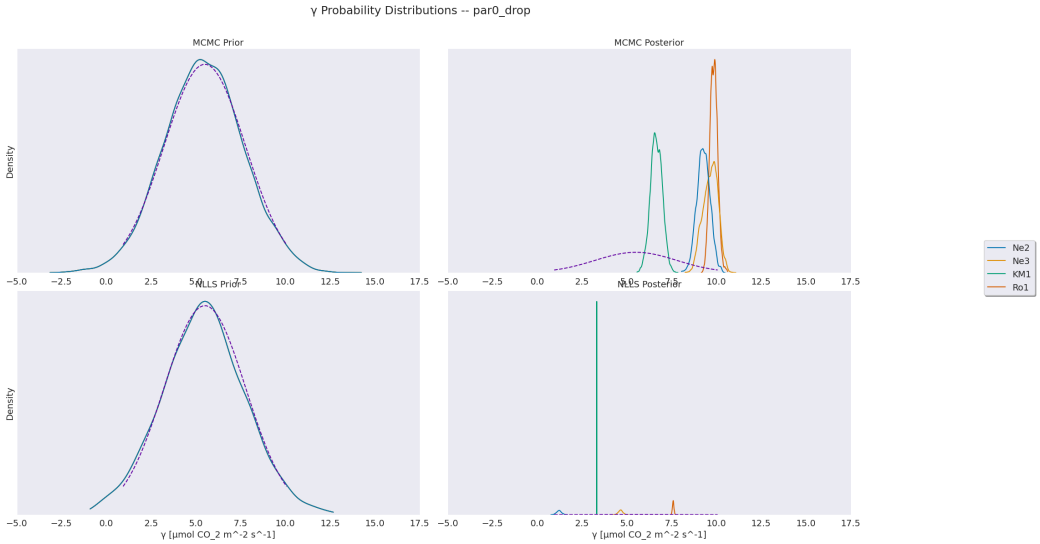

Figure A.38: Same as Figure 3.4 but for the PAR_0 parameter drop experiment.

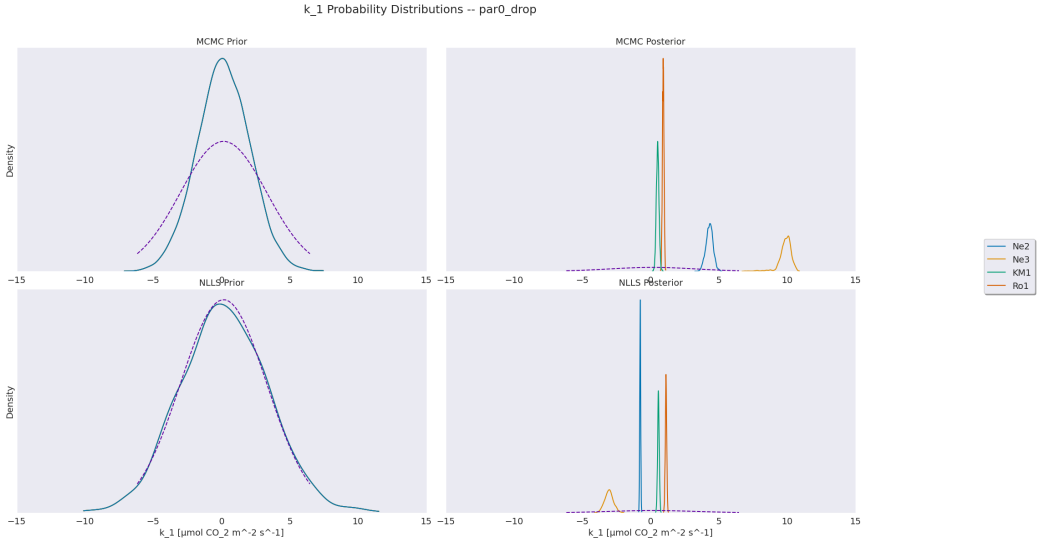

Figure A.39: Same as Figure A.4 but for the PAR_0 parameter drop experiment.

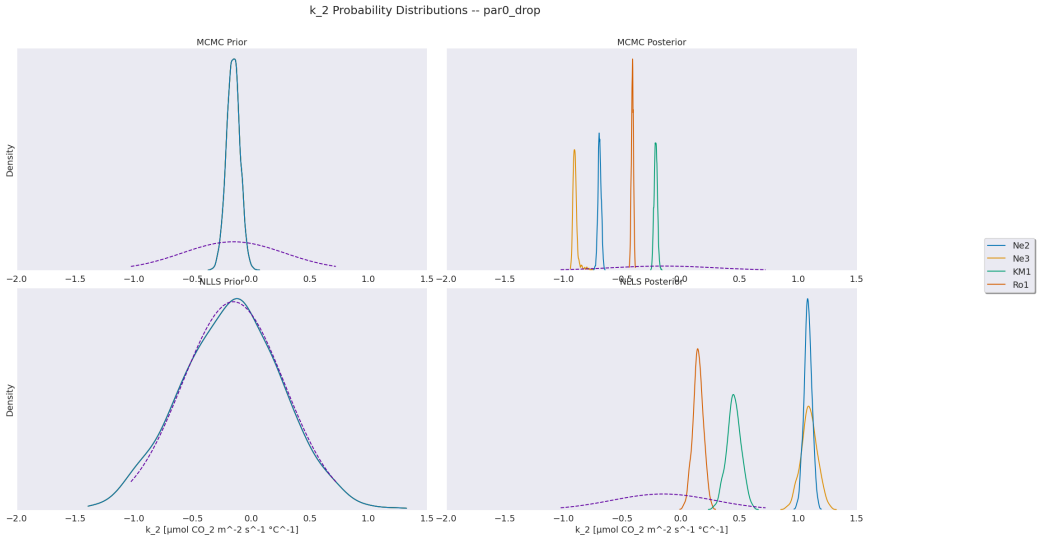

Figure A.40: Same as Figure A.5 but for the PAR_0 parameter drop experiment.

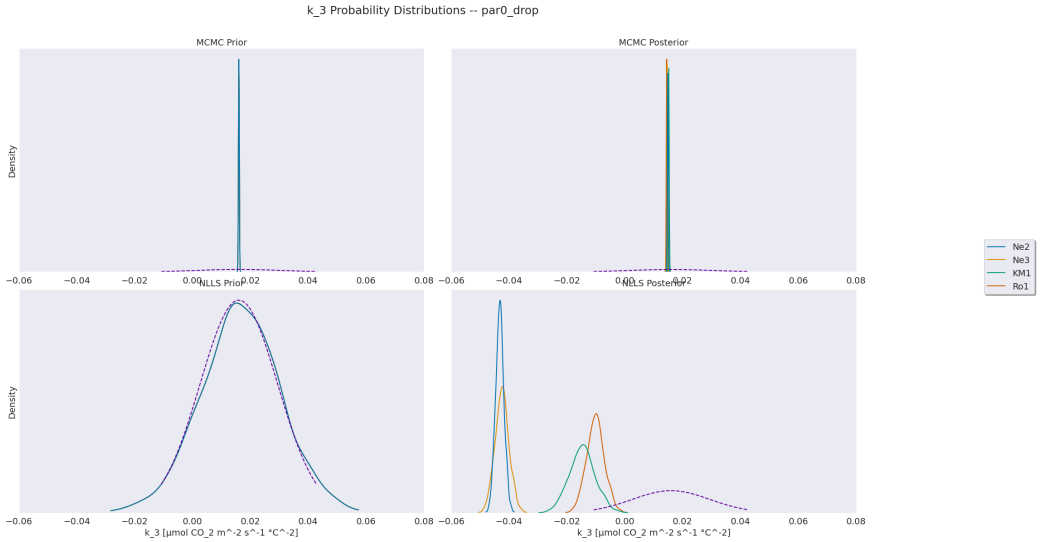

Figure A.41: Same as Figure A.6 but for the PAR_0 parameter drop experiment.

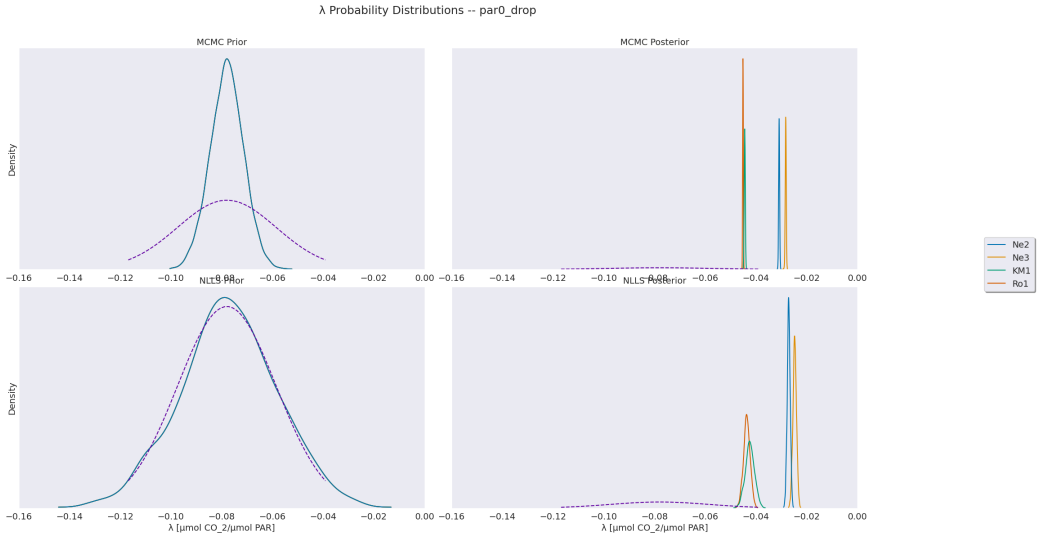

Figure A.42: Same as Figure 3.5 but for the PAR_0 parameter drop experiment.

A.3 RMSE Distributions

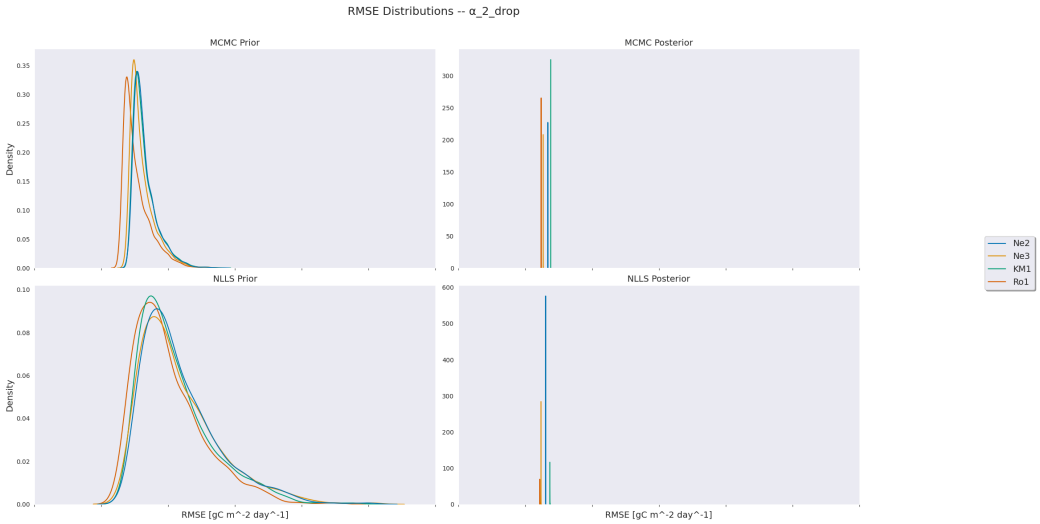

Figure A.43: Same as Figure 3.1 but for the α_2 parameter drop experiment.

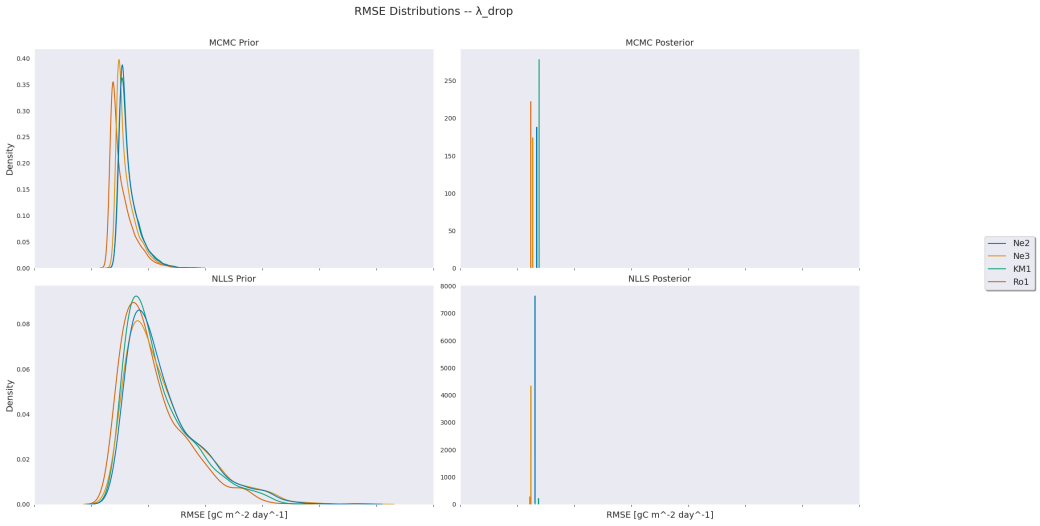

Figure A.44: Same as Figure 3.1 but for the λ parameter drop experiment.

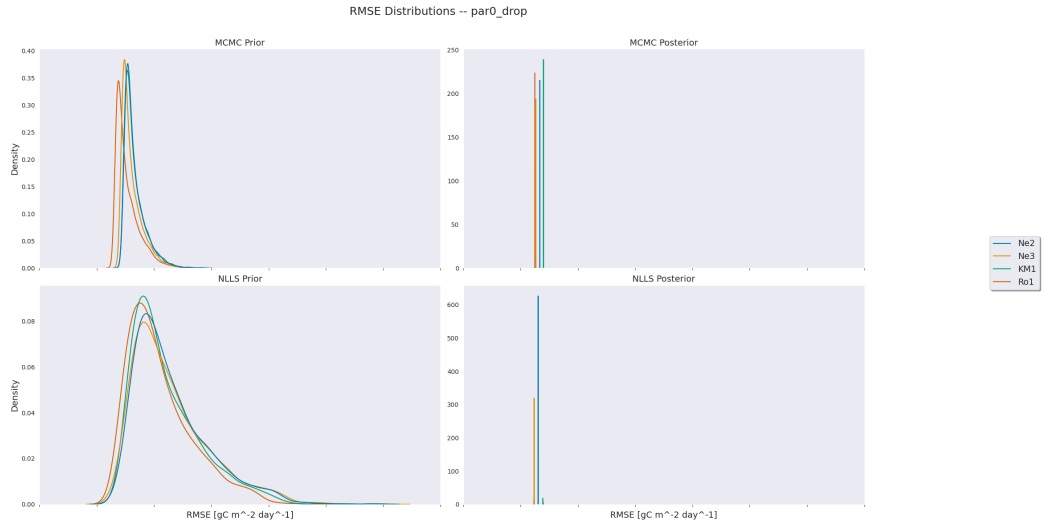

Figure A.45: Same as Figure 3.1 but for the PAR_0 parameter drop experiment.

Appendix B

Parameter Correlations

B.1 MCMC

B.1.1 Whole Data Set Simultaneously

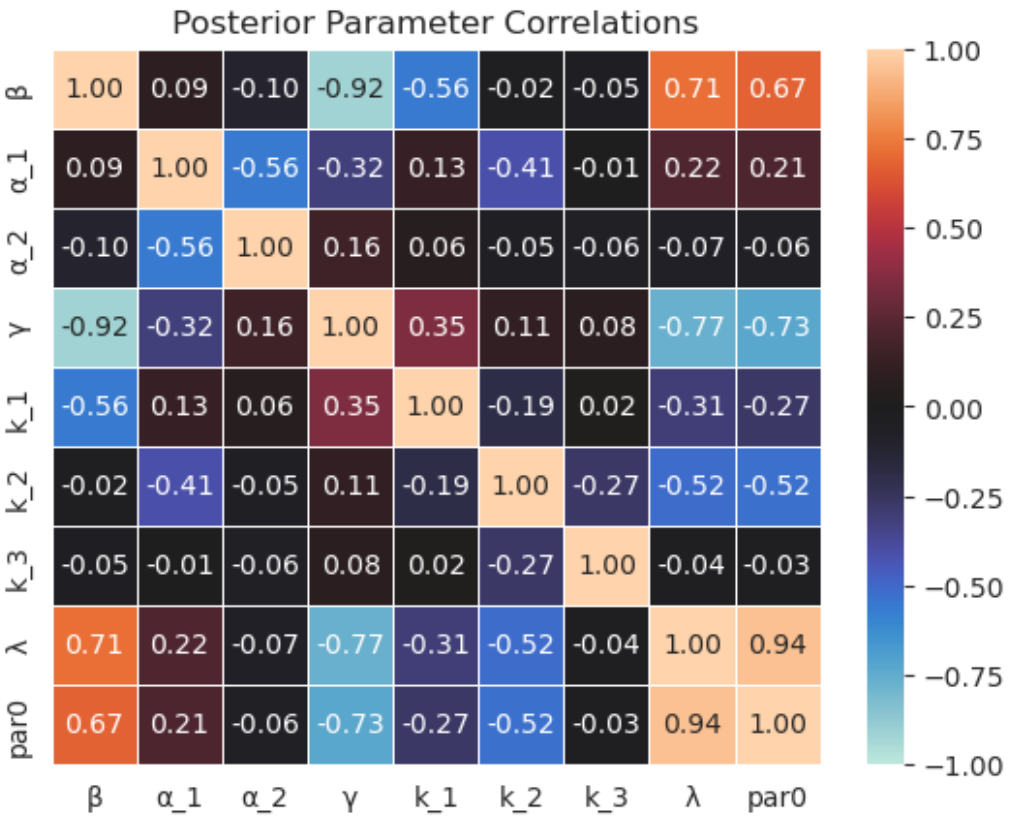

Figure B.1: Same as Figure 3.13 but for the KM1 normal MCMC experiment.

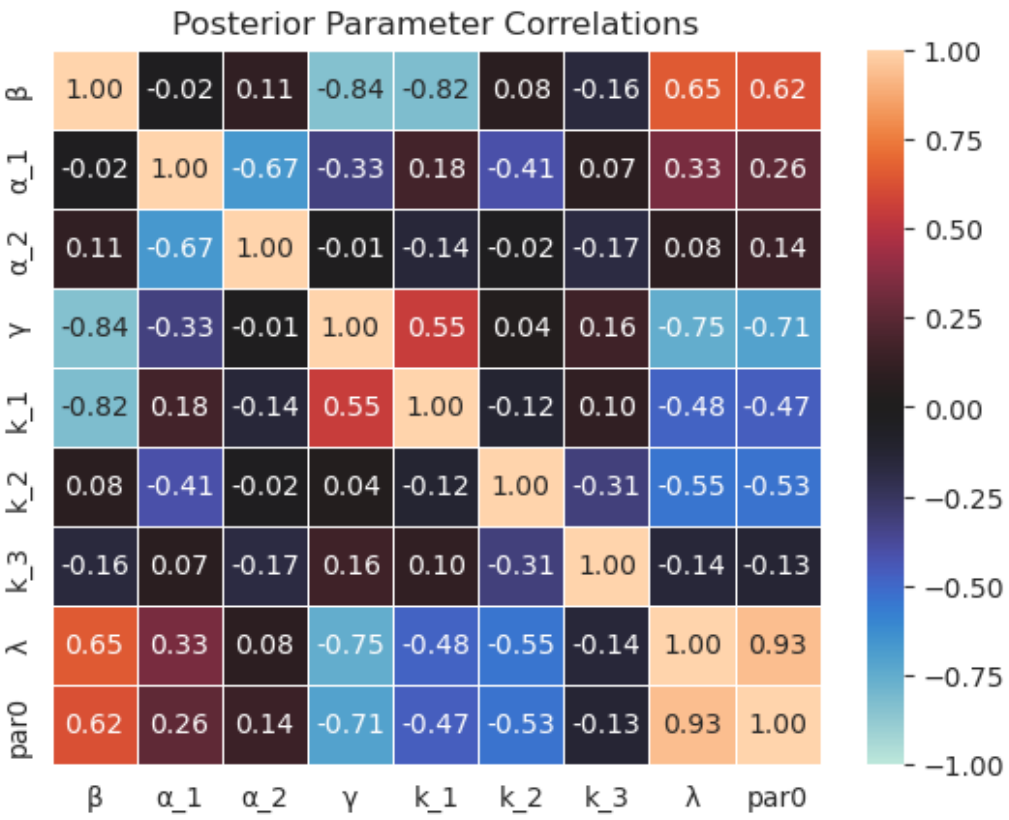

Figure B.2: Same as Figure 3.13 but for the Ro1 normal MCMC experiment.

B.1.2 ER/GEE Separately

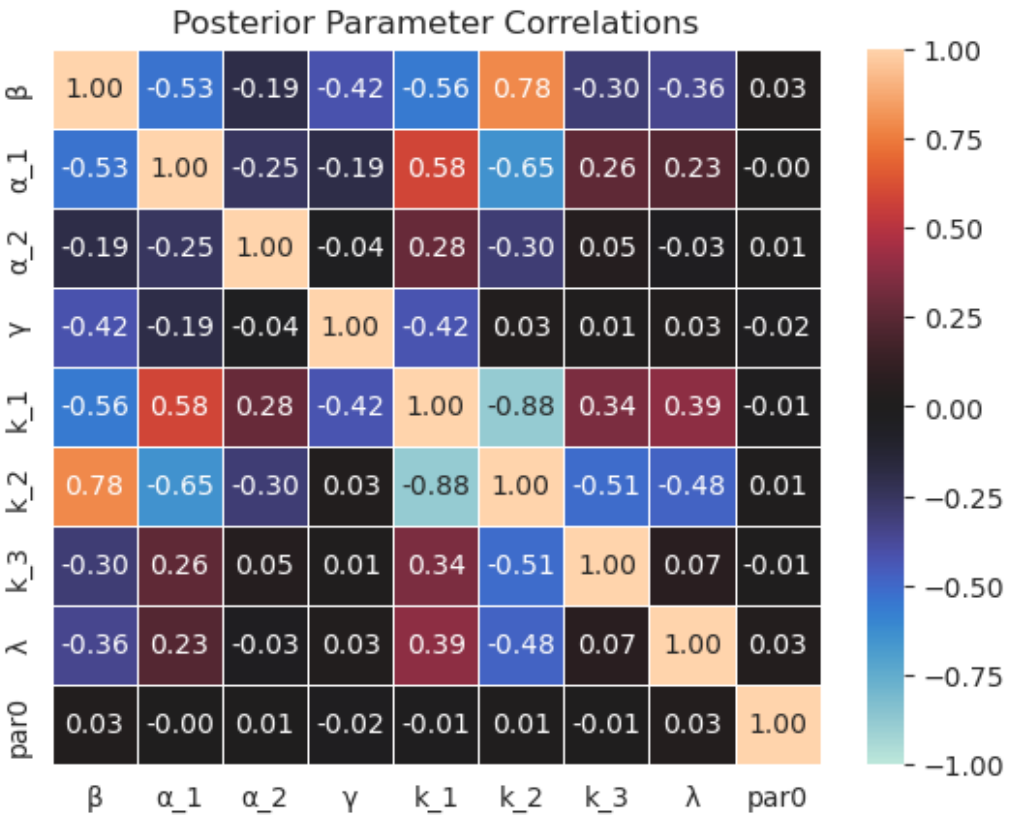

Figure B.3: Same as Figure 3.15 but for the Ne3 AmeriFlux site.

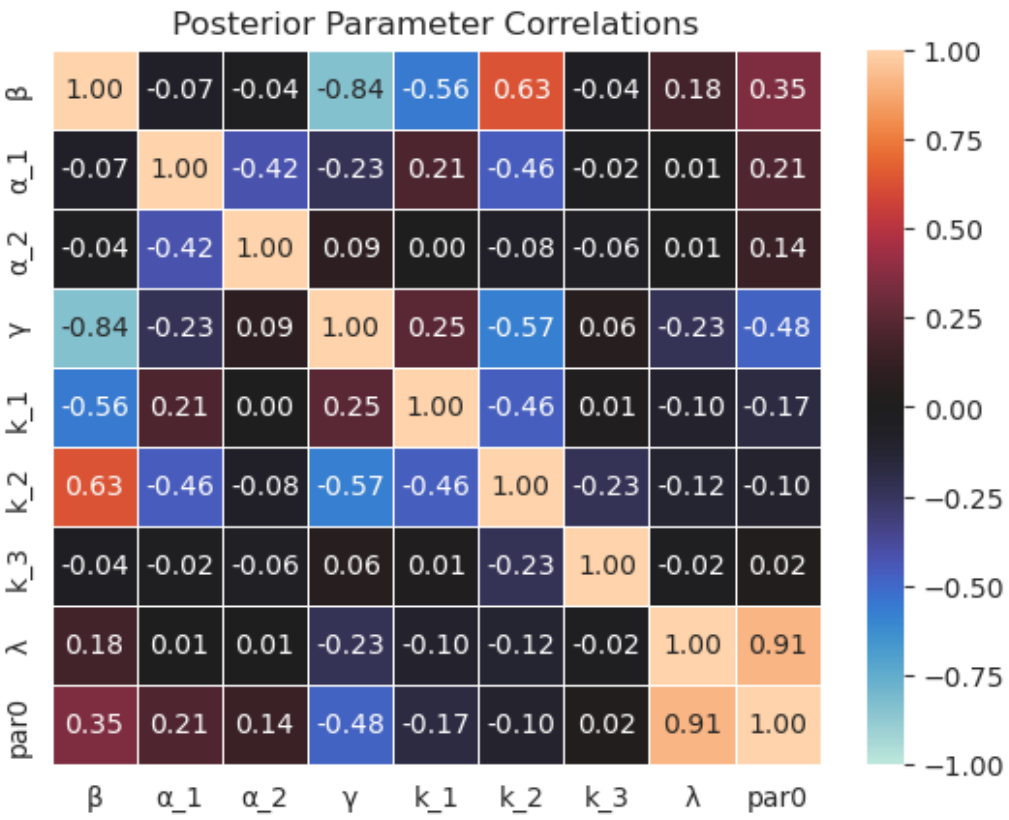

Figure B.4: Same as Figure 3.15 but for the KM1 AmeriFlux site.

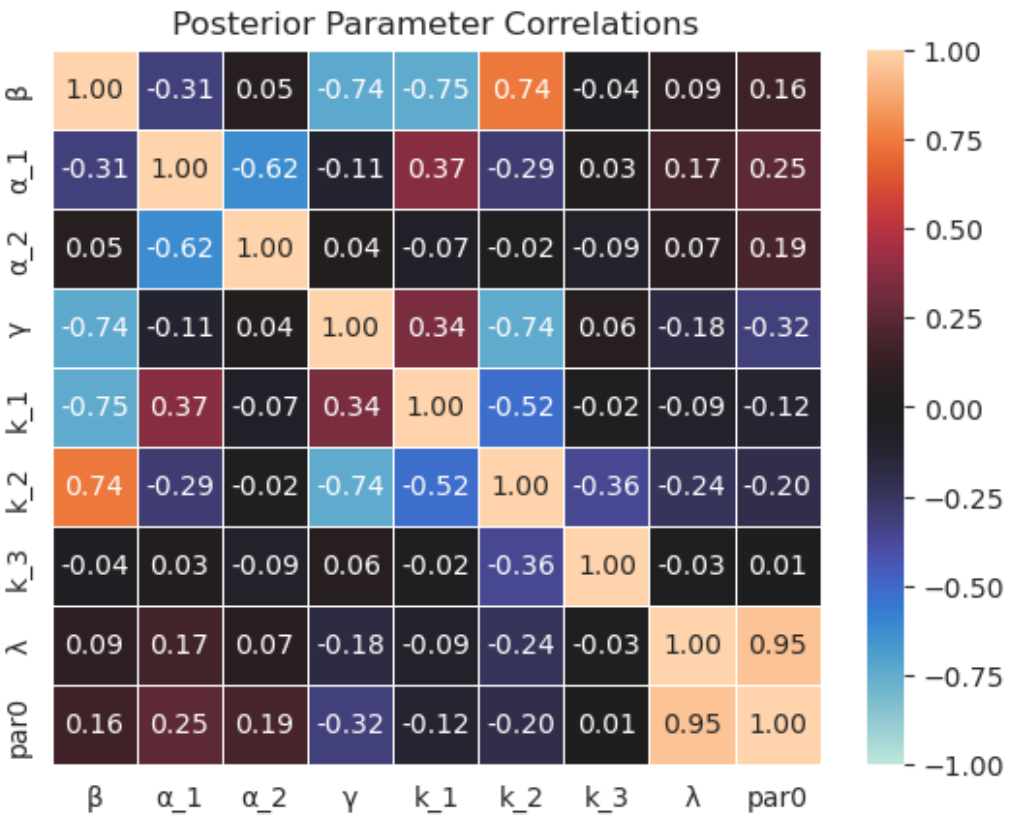

Figure B.5: Same as Figure 3.15 but for the Ro1 AmeriFlux site.

B.1.3 α_2 Drop Experiment

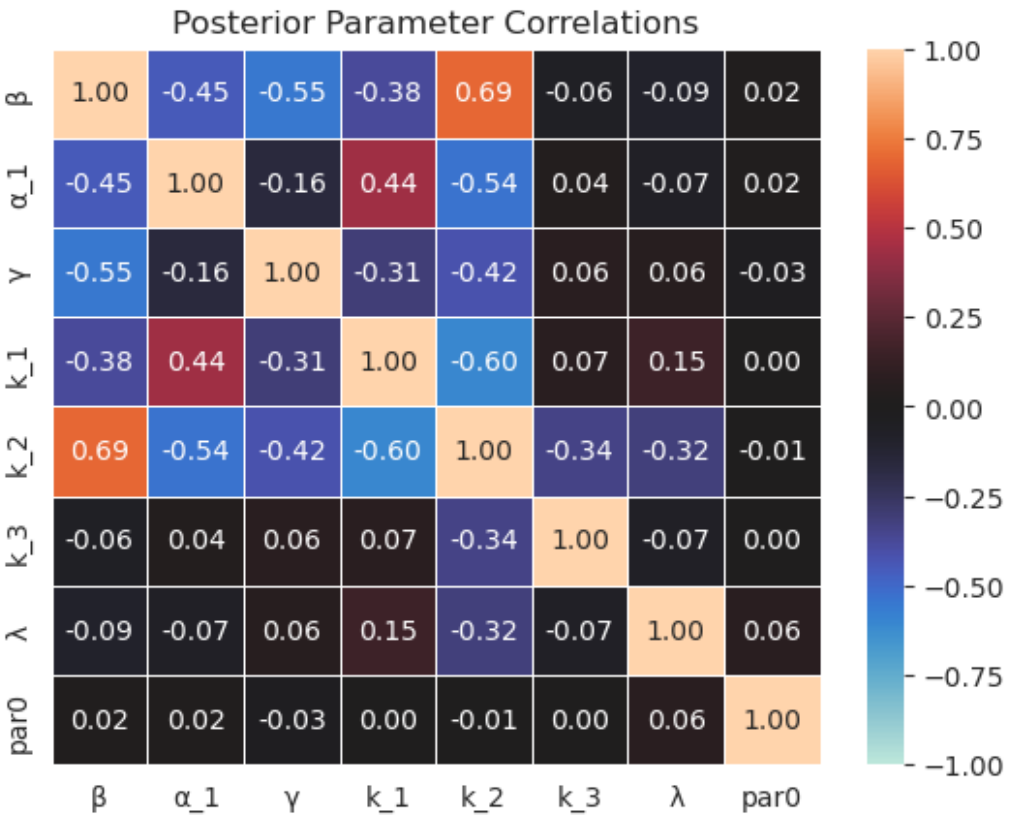

Figure B.6: Same as Figure 3.13 but for the α_2 parameter drop experiment.

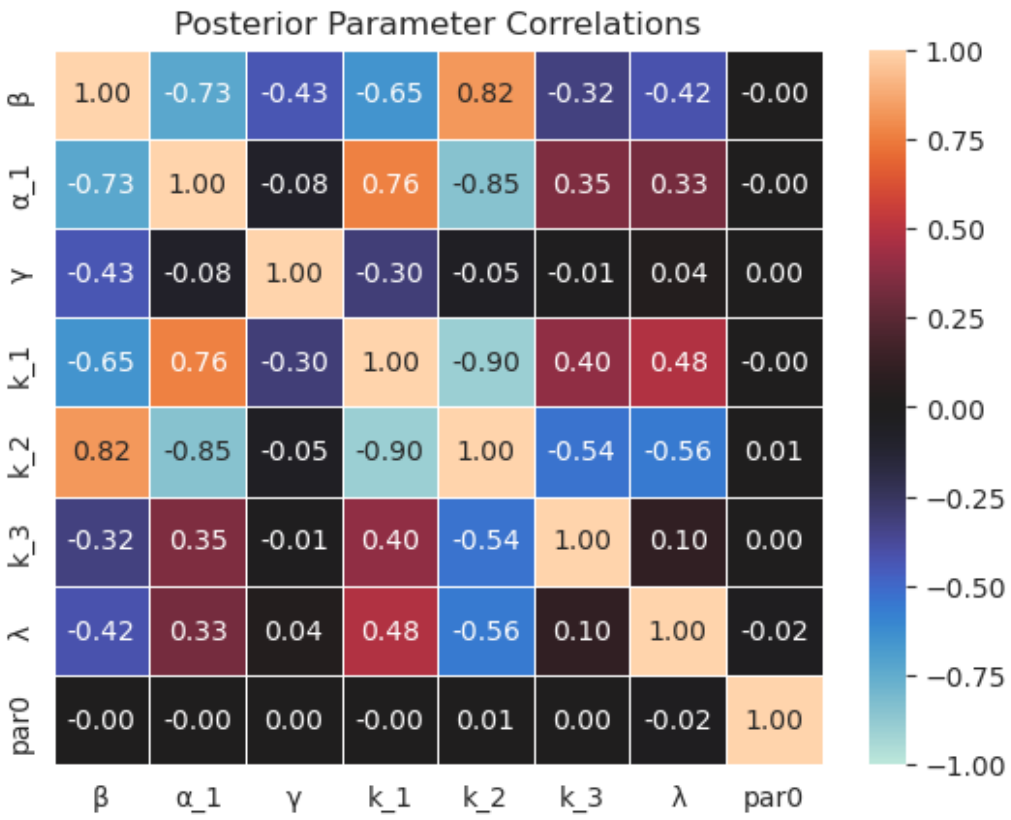

Figure B.7: Same as Figure B.6 but for the Ne3 AmeriFlux site.

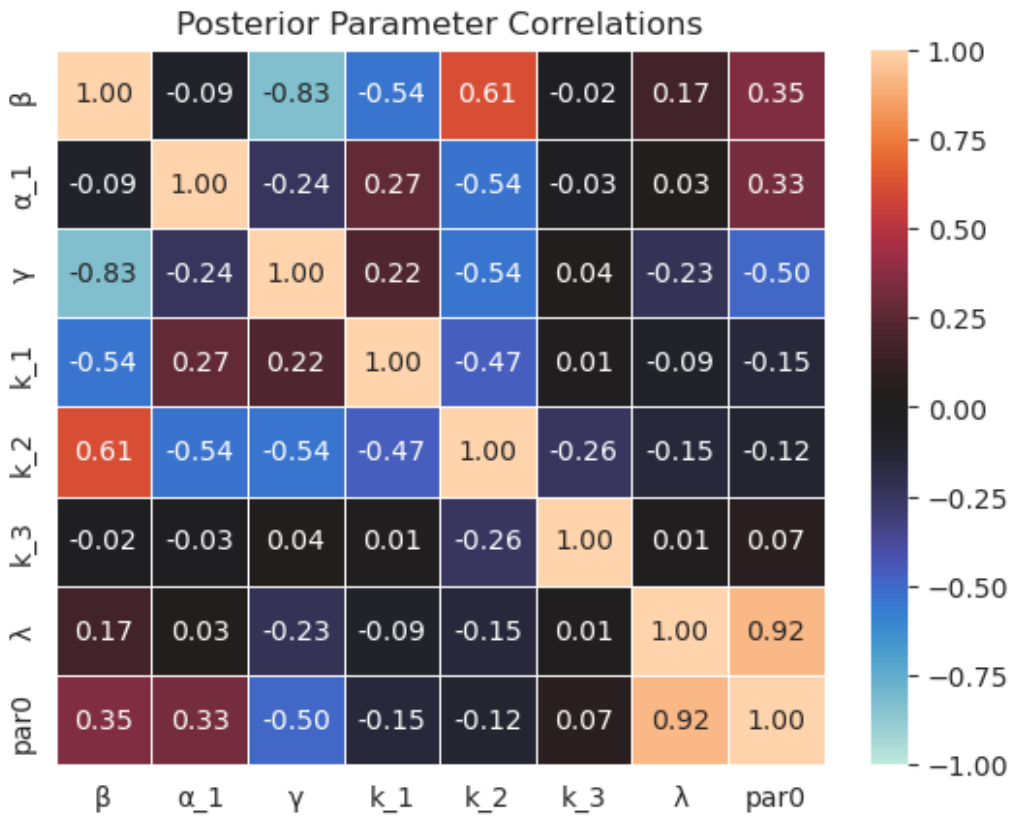

Figure B.8: Same as Figure B.6 but for the KM1 AmeriFlux site.

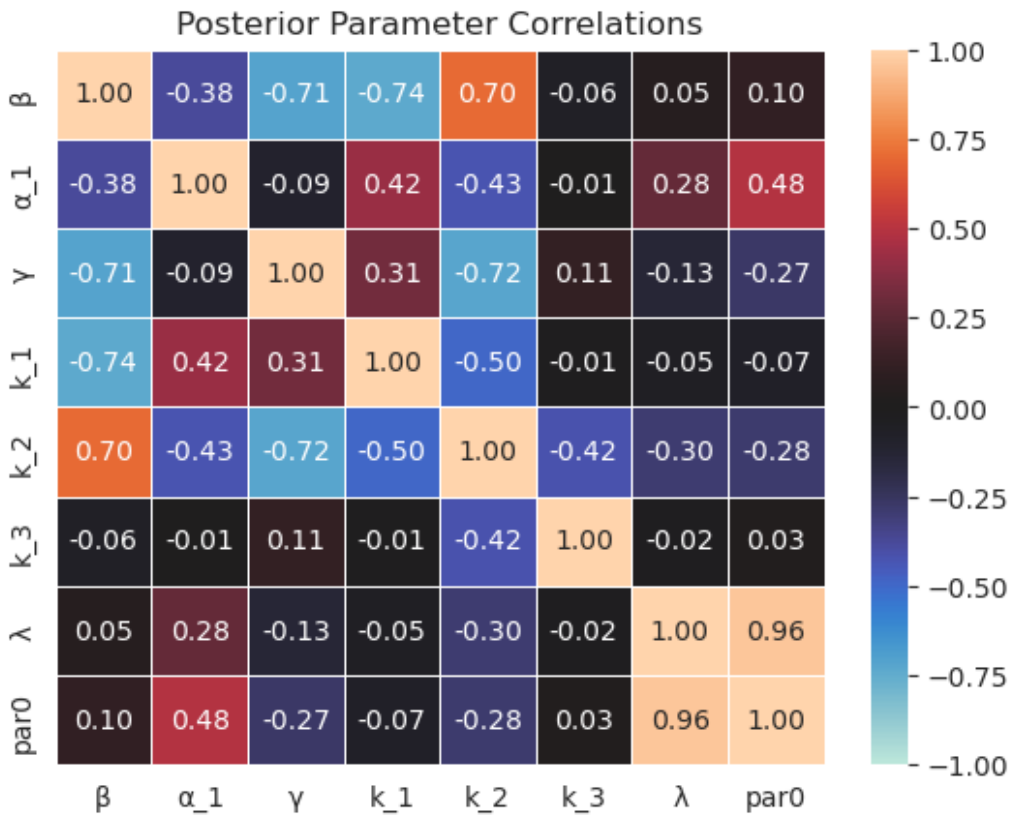

Figure B.9: Same as Figure B.6 but for the Ro1 AmeriFlux site.

B.1.4 k_3 Drop Experiment

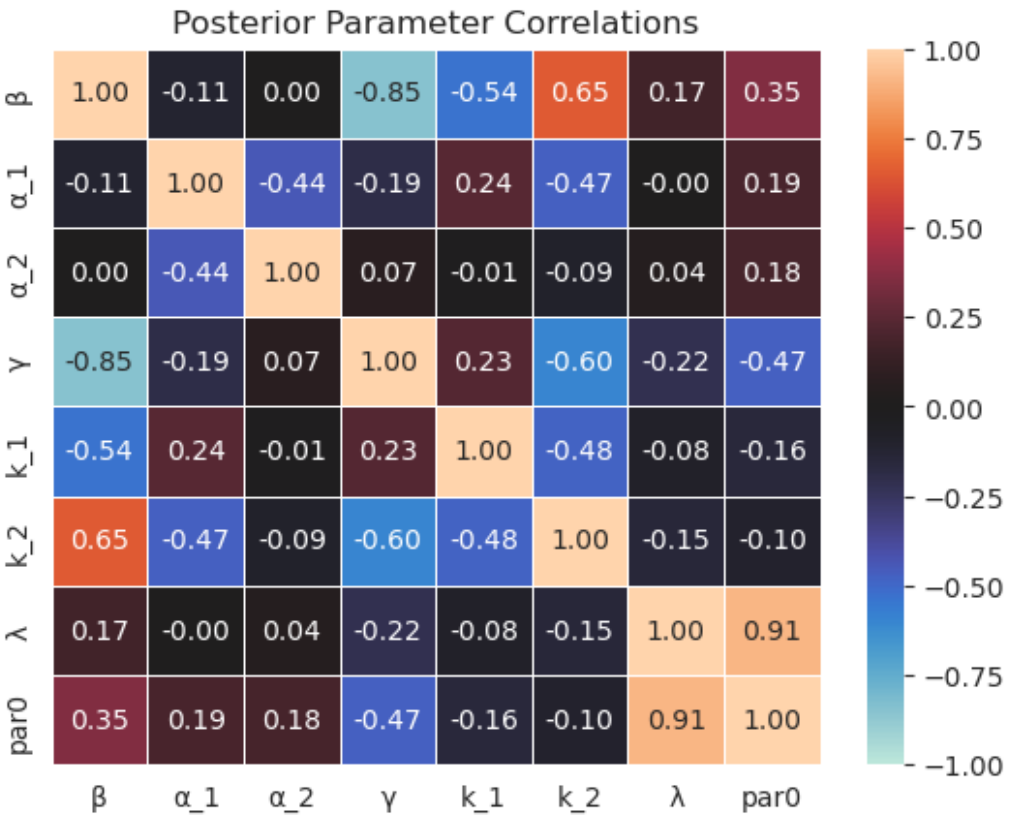

Figure B.10: Same as Figure 4.3 but for the KM1 AmeriFlux site.

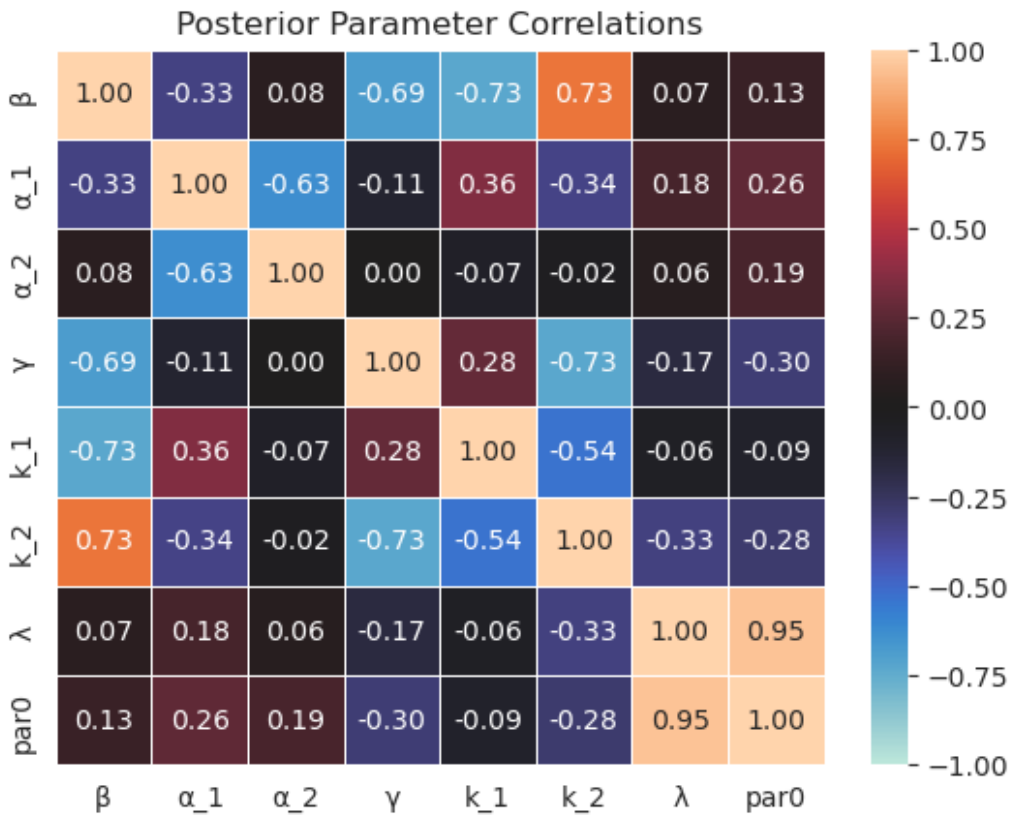

Figure B.11: Same as Figure 4.3 but for the Ro1 AmeriFlux site.

B.1.5 λ Drop Experiment

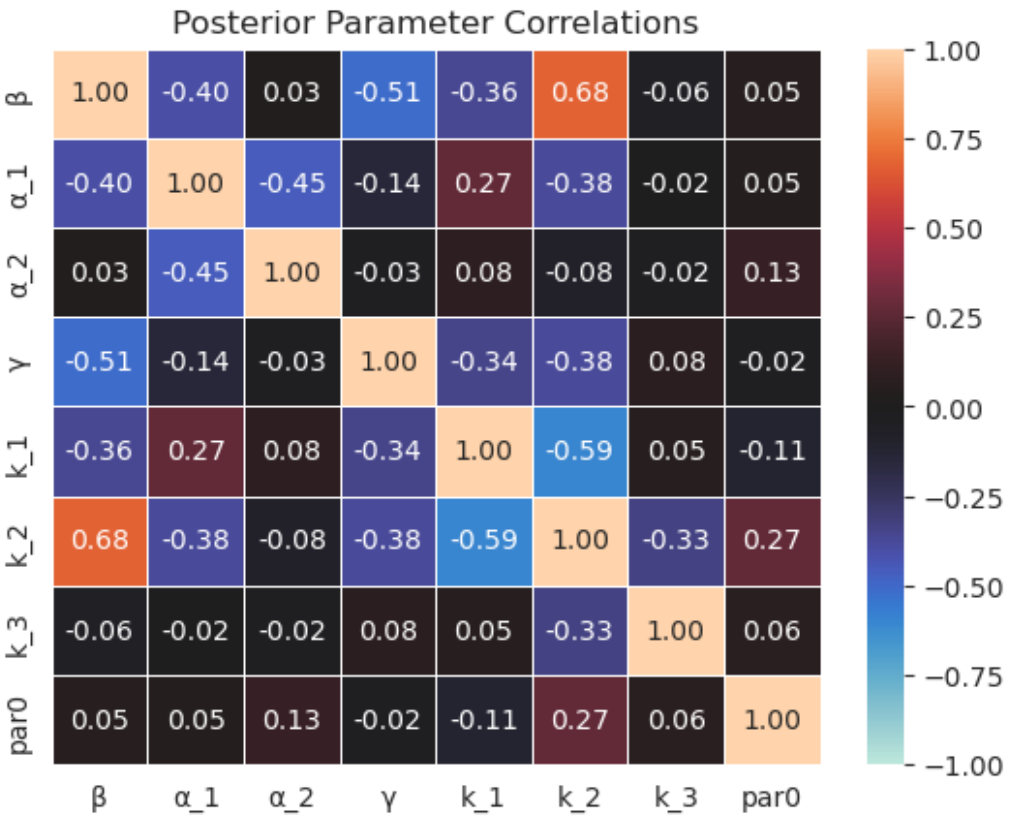

Figure B.12: Same as Figure 3.13 but for the λ parameter drop experiment.

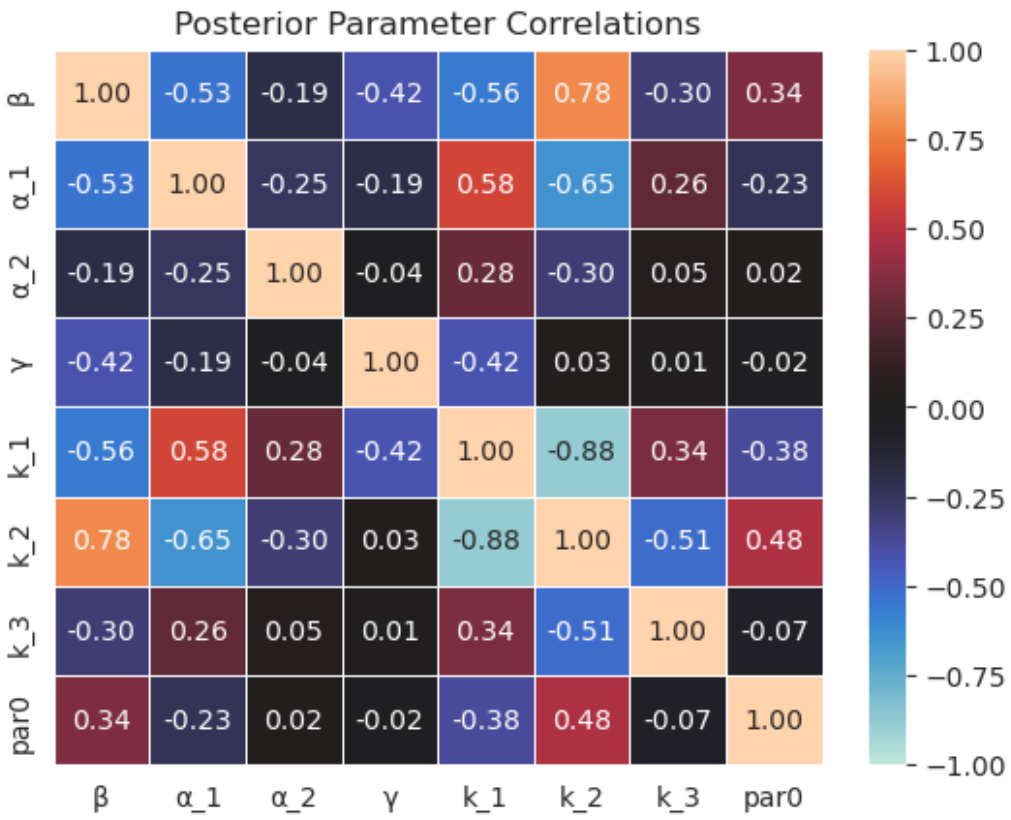

Figure B.13: Same as Figure B.12 but for the Ne3 AmeriFlux site.

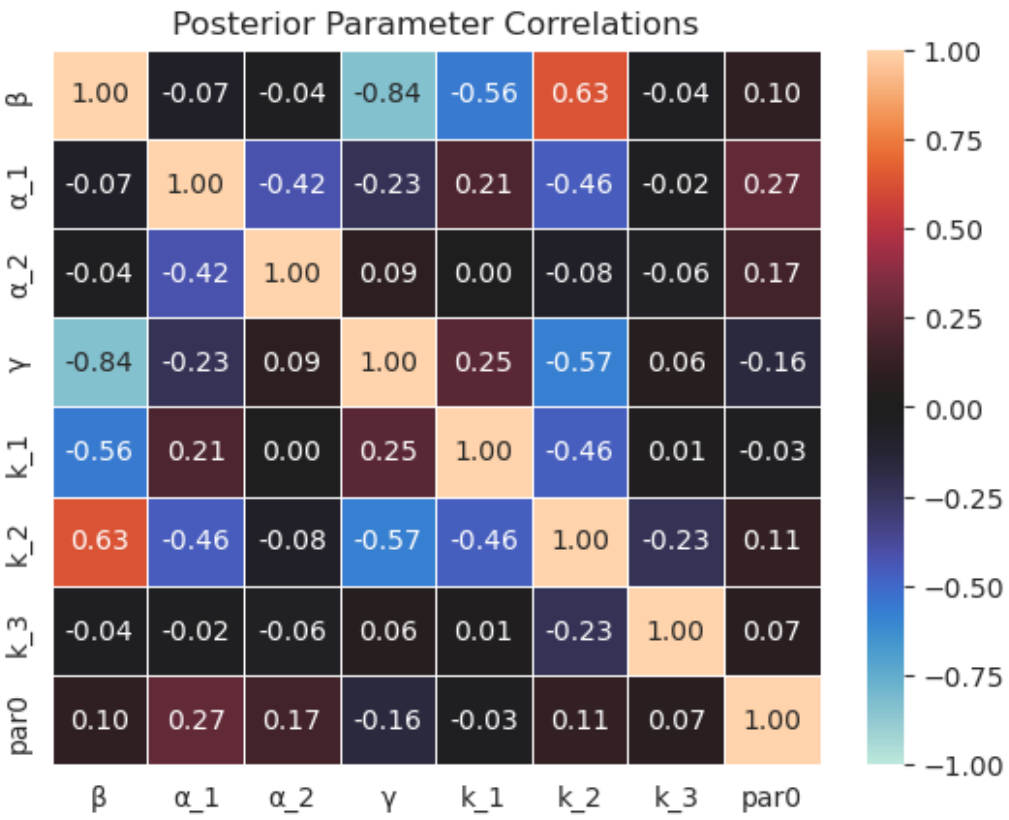

Figure B.14: Same as Figure B.12 but for the KM1 AmeriFlux site.

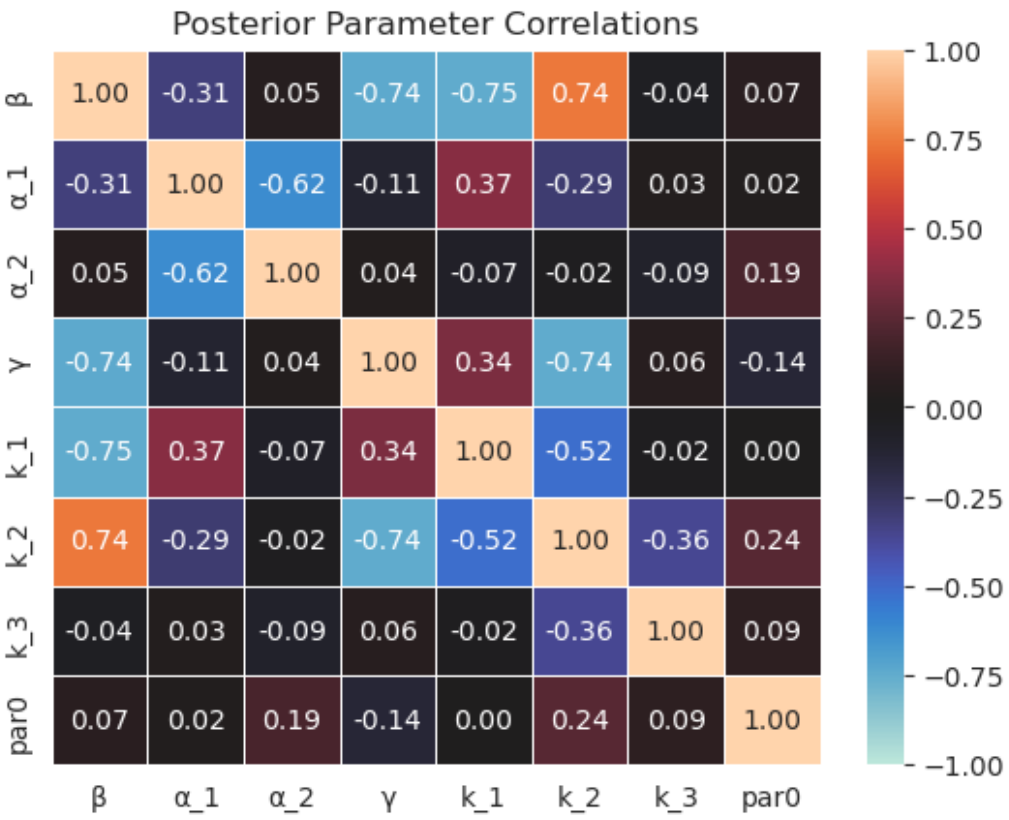

Figure B.15: Same as Figure B.12 but for the Ro1 AmeriFlux site.

B.1.6 PAR_0 Drop Experiment

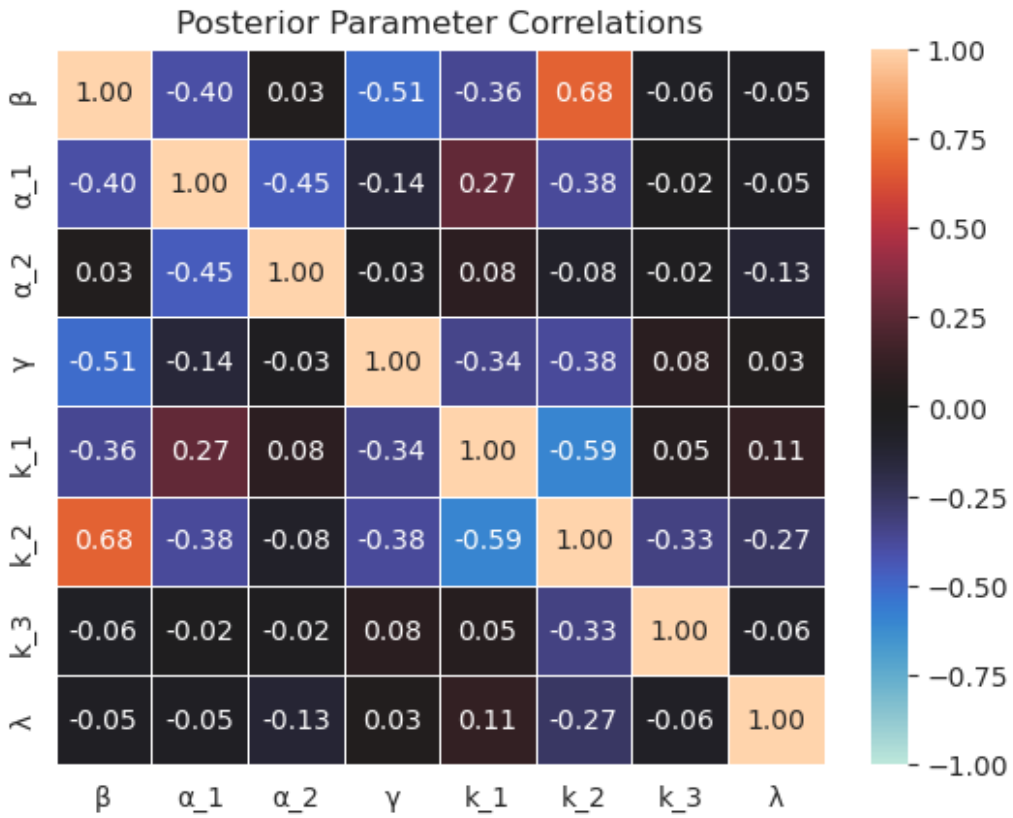

Figure B.16: Same as Figure 3.13 but for the PAR_0 parameter drop experiment.

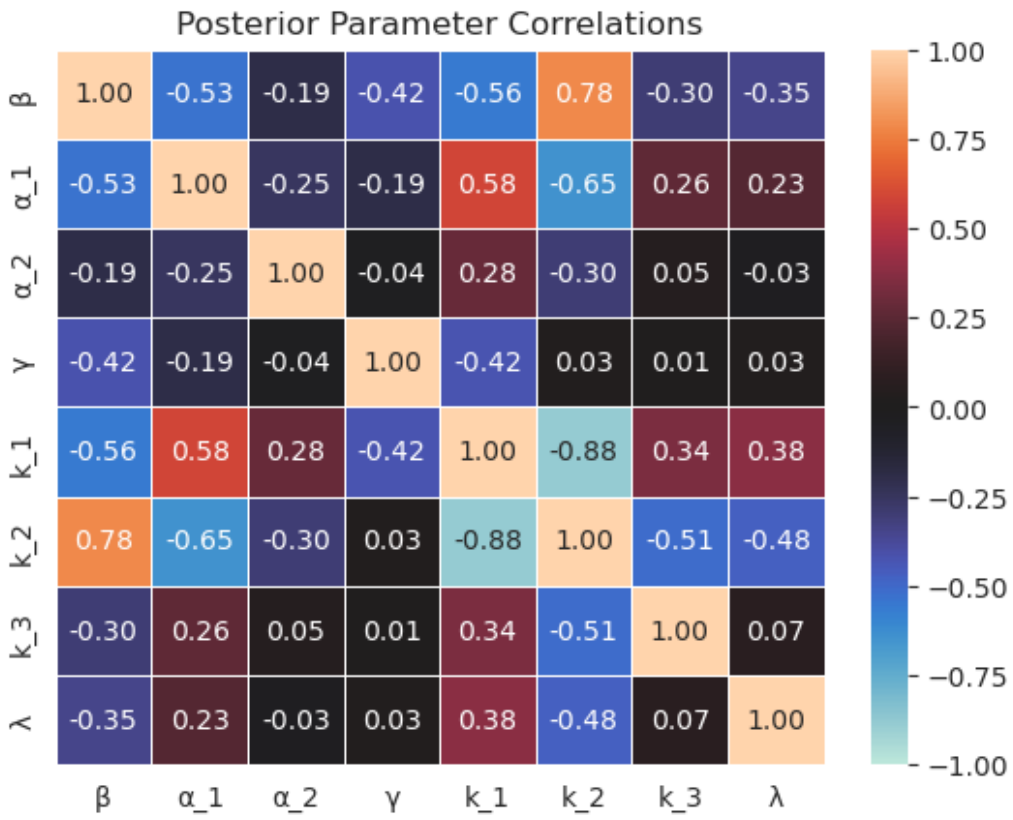

Figure B.17: Same as Figure B.16 but for the Ne3 AmeriFlux site.

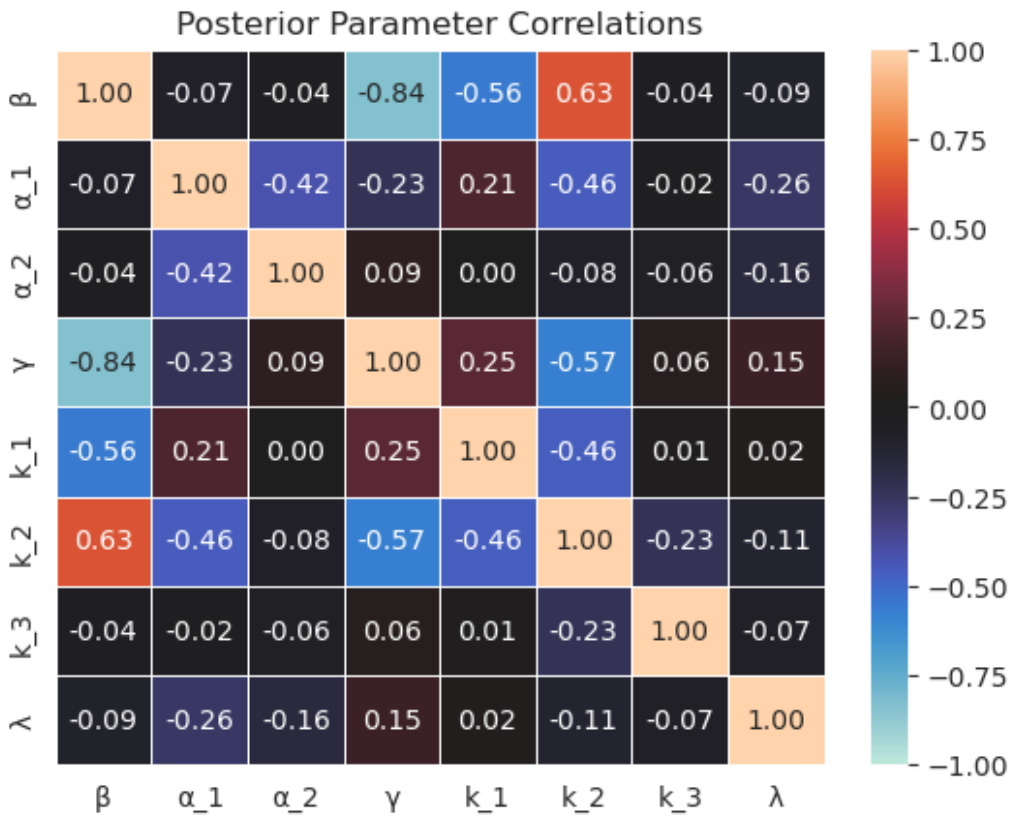

Figure B.18: Same as Figure B.16 but for the KM1 AmeriFlux site.

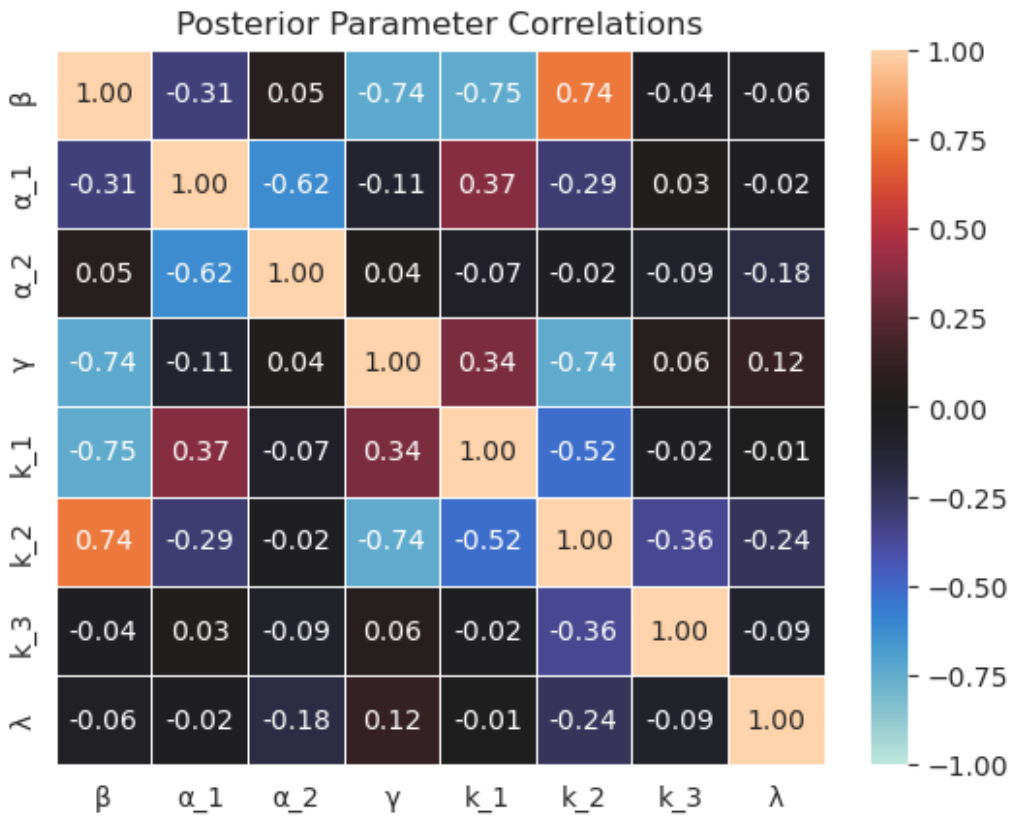

Figure B.19: Same as Figure B.16 but for the Ro1 AmeriFlux site.

B.2 NLLS

B.2.1 Whole Data Set Simultaneously

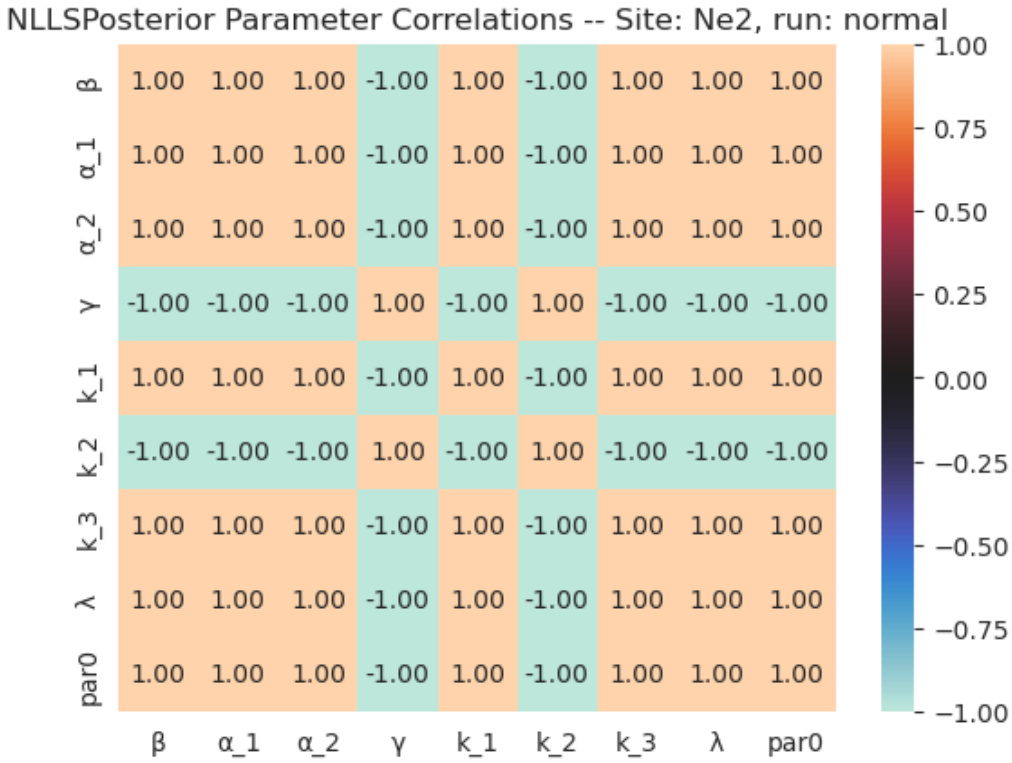

Figure B.20: Same as Figure 3.13 but for the NLLS while fitting the whole data set simultaneously.

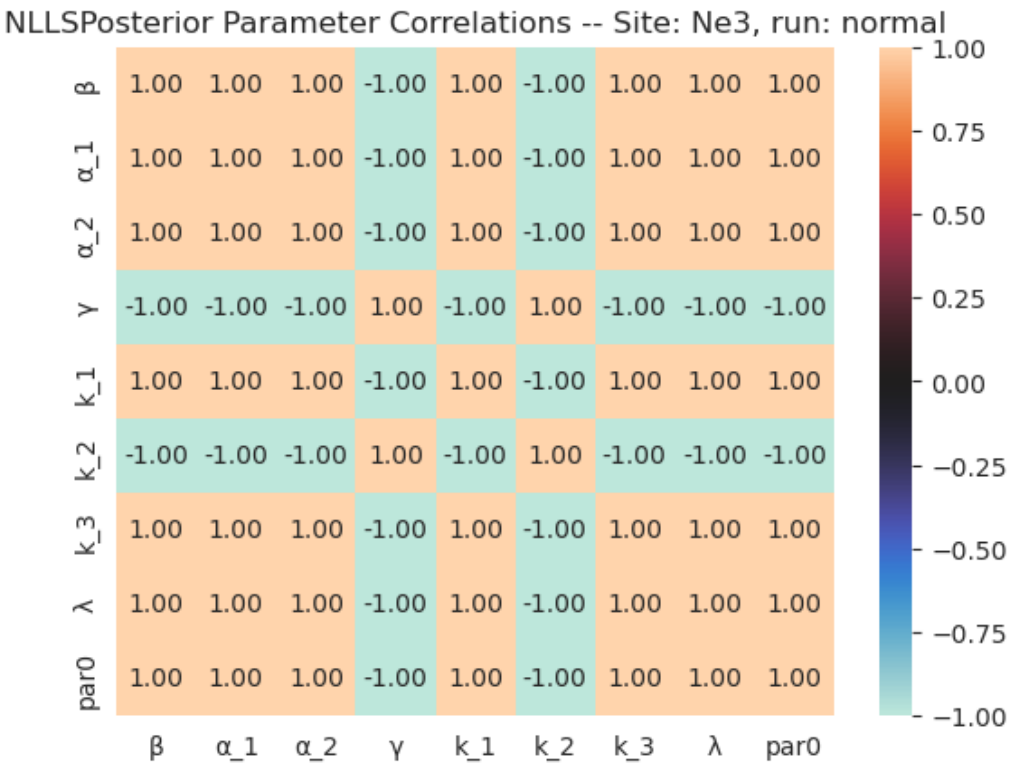

Figure B.21: Same as Figure B.20 but for the Ne3 AmeriFlux site.

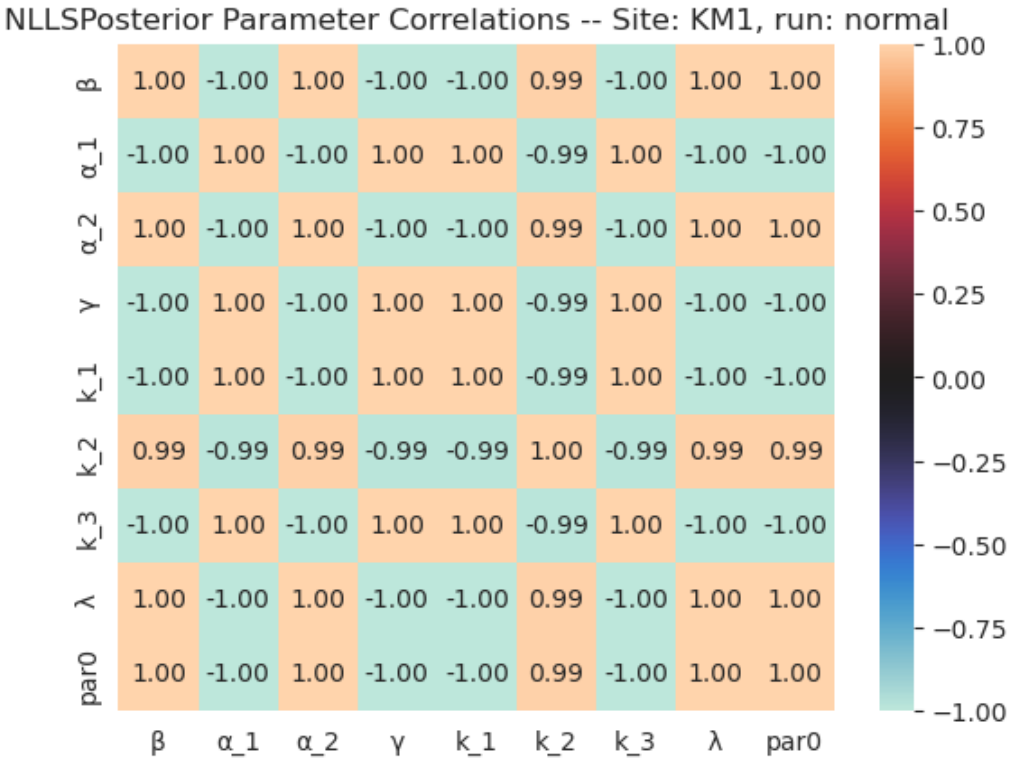

Figure B.22: Same as Figure B.20 but for the KM1 AmeriFlux site.

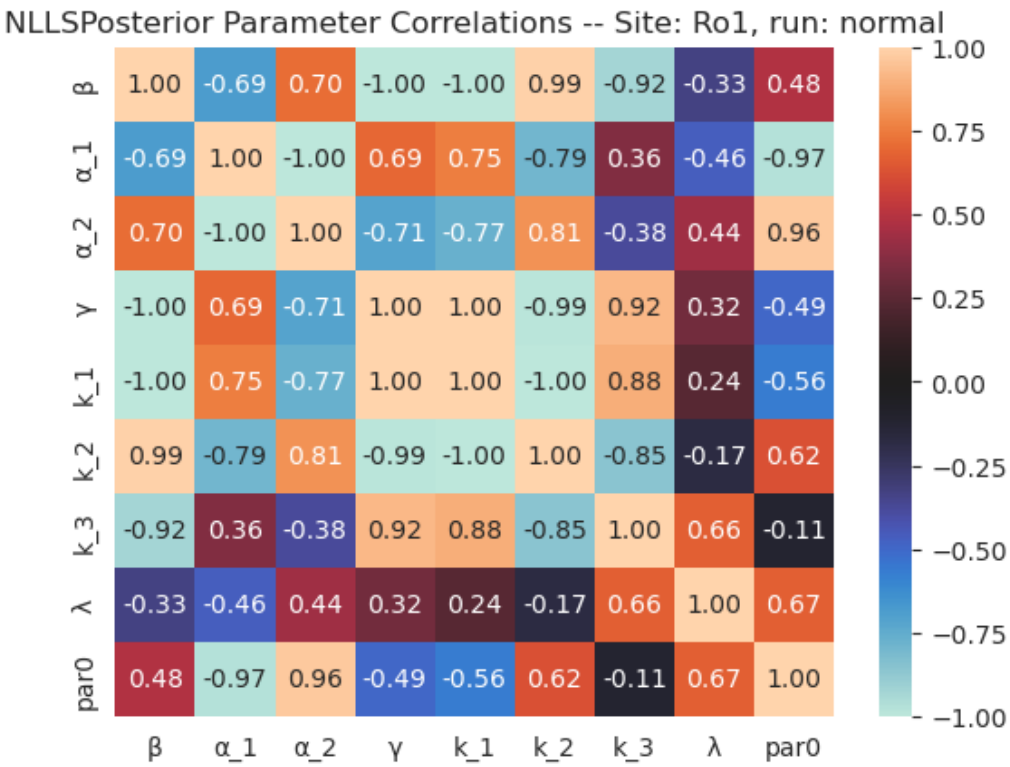

Figure B.23: Same as Figure B.20 but for the Ro1 AmeriFlux site.

B.2.2 ER/GEE Separately

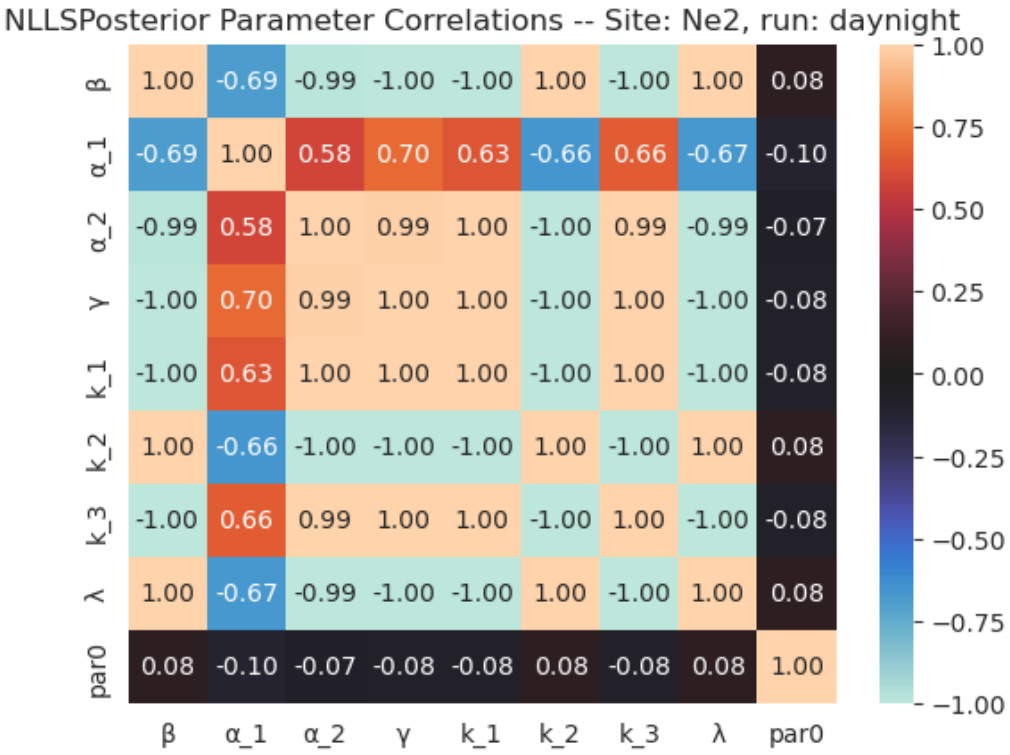

Figure B.24: Same as Figure B.20 but for the NLLS while fitting ER and GEE separately.

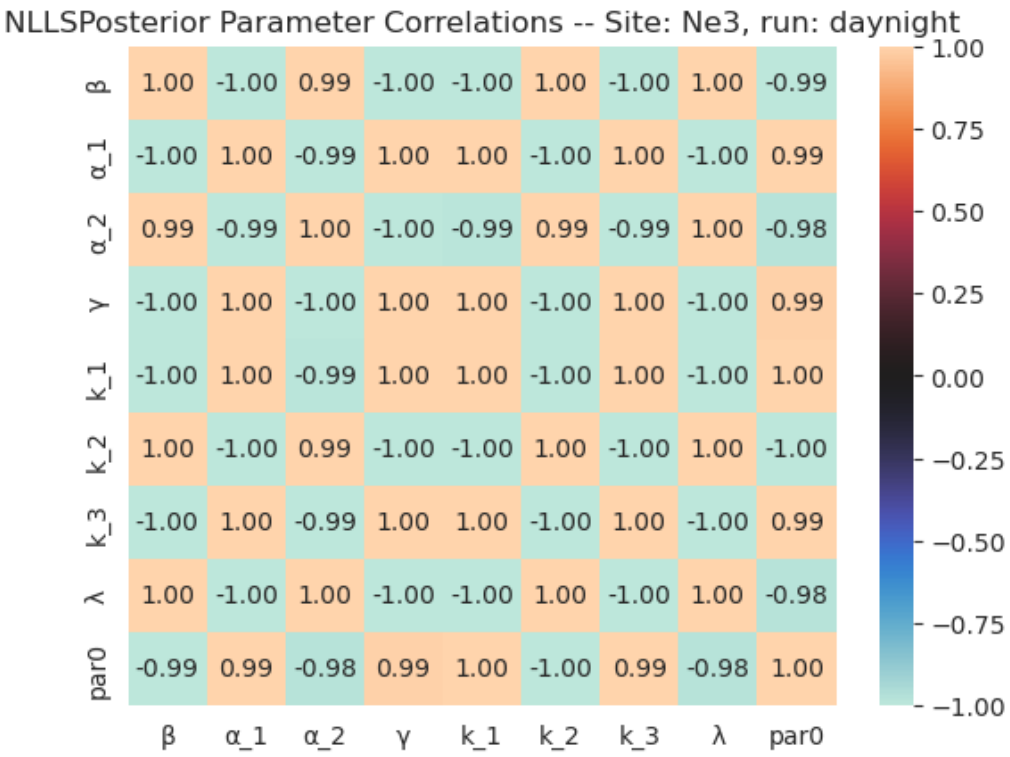

Figure B.25: Same as Figure B.24 but for the Ne3 AmeriFlux site.

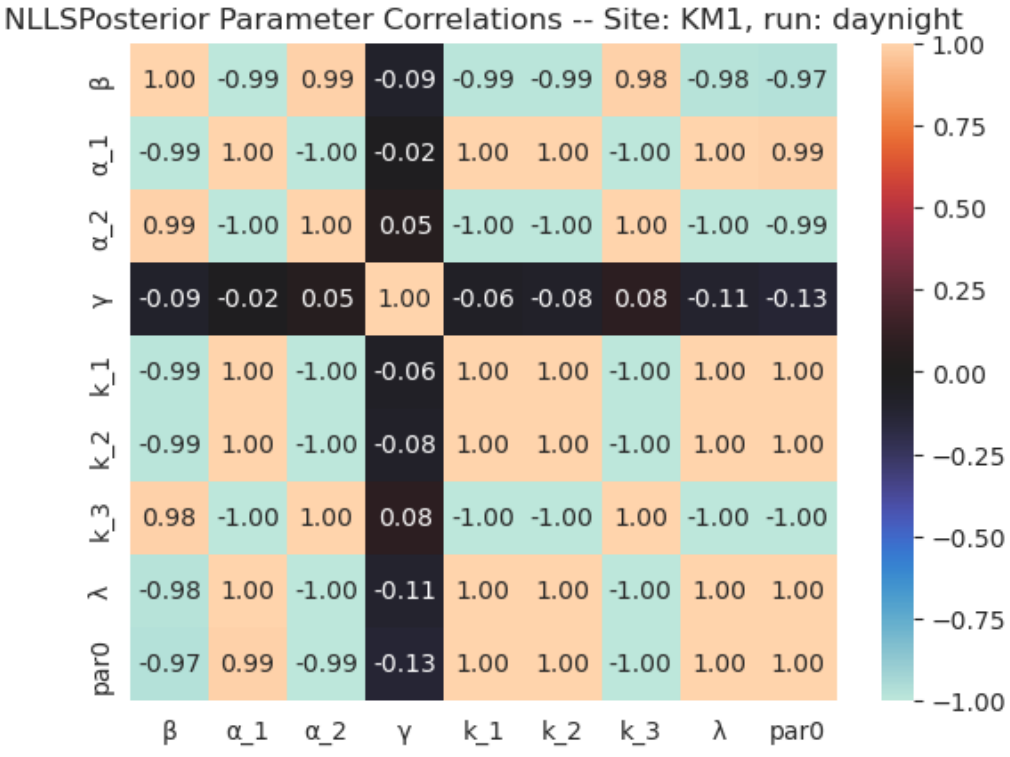

Figure B.26: Same as Figure B.24 but for the KM1 AmeriFlux site.

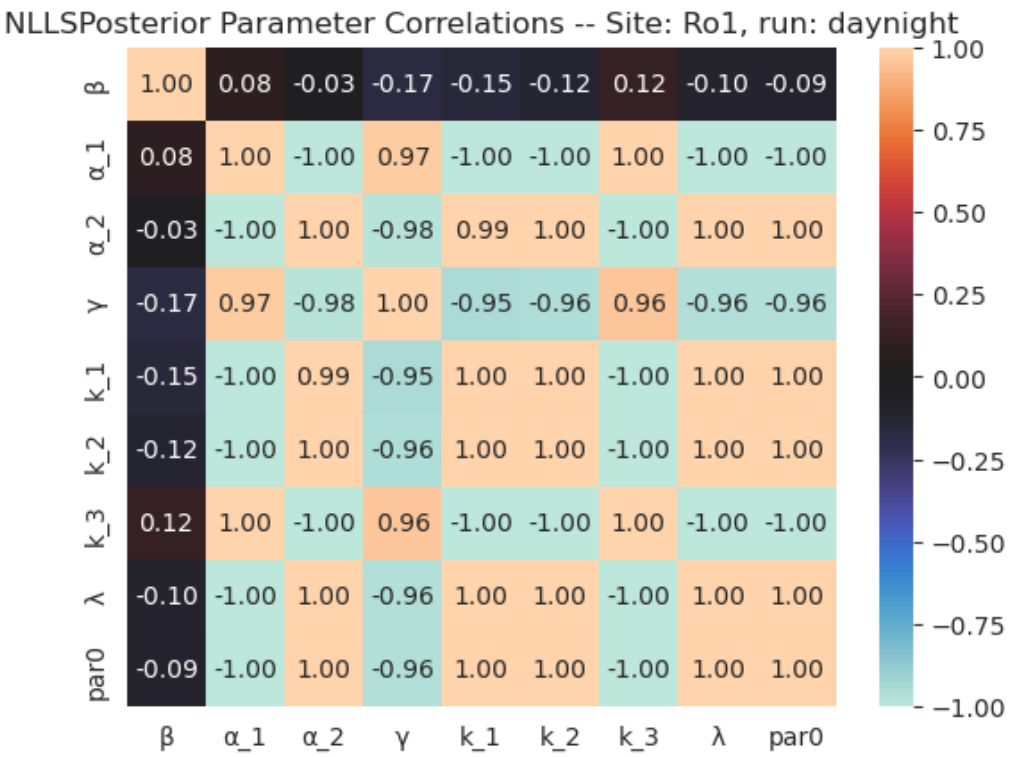

Figure B.27: Same as Figure B.24 but for the Ro1 AmeriFlux site.

B.2.3 α_2 Drop Experiment

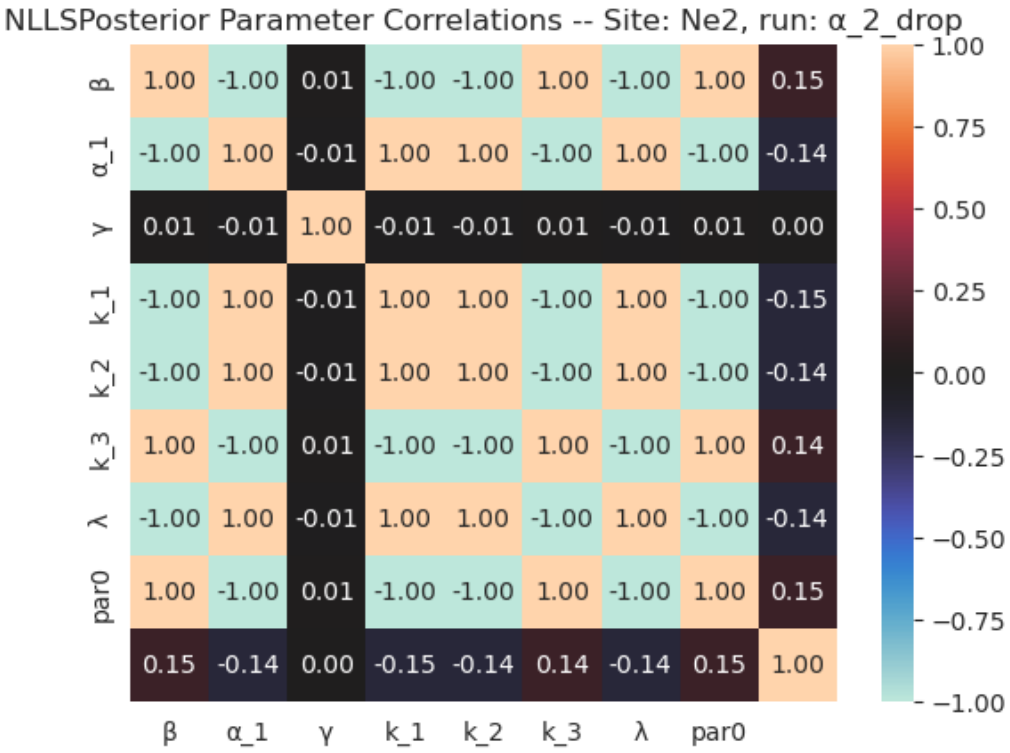

Figure B.28: Same as Figure B.20 but for the NLLS α_2 parameter drop experiment.

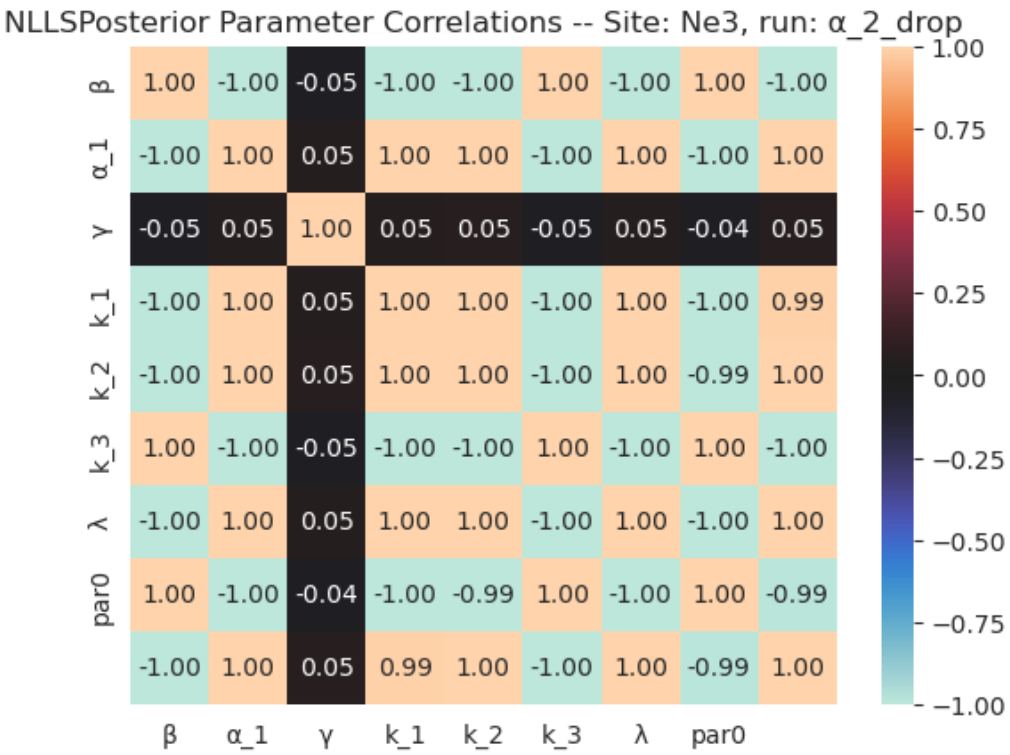

Figure B.29: Same as Figure B.28 but for the Ne3 AmeriFlux site.

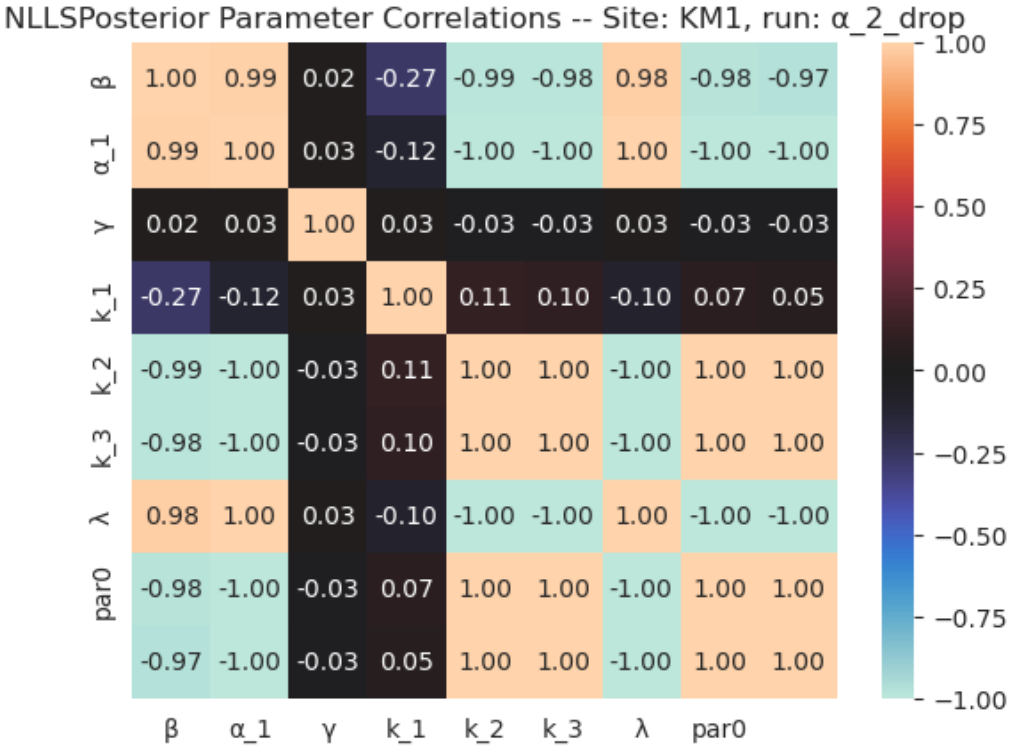

Figure B.30: Same as Figure B.28 but for the KM1 AmeriFlux site.

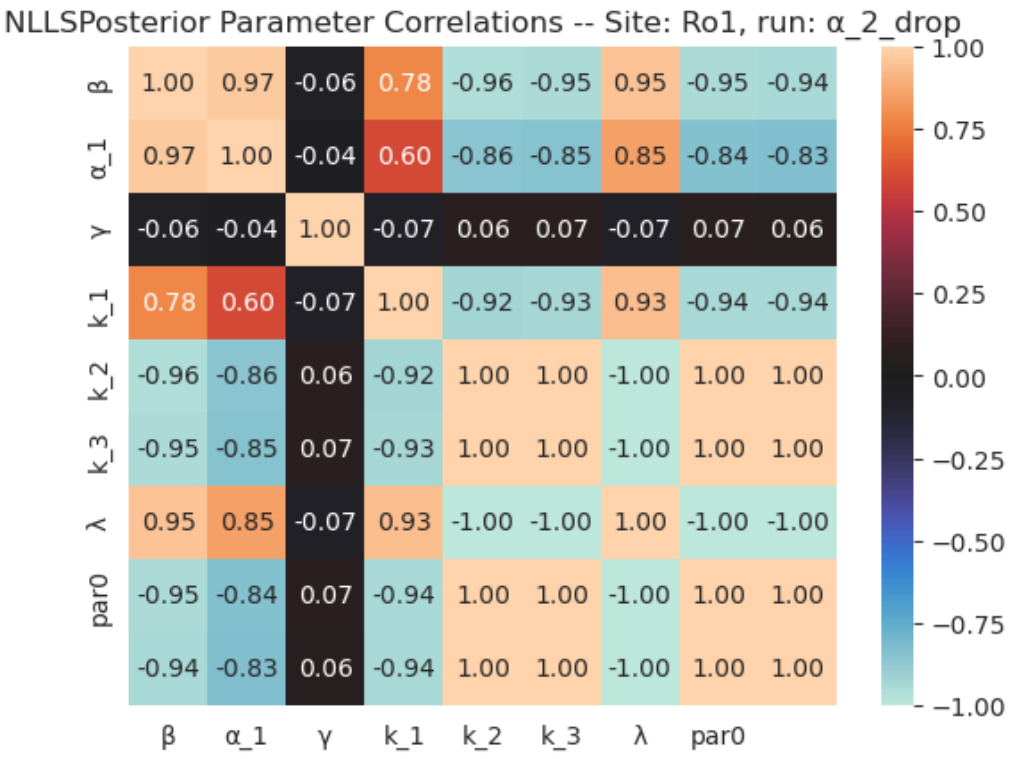

Figure B.31: Same as Figure B.28 but for the Ro1 AmeriFlux site.

B.2.4 k_3 Drop Experiment

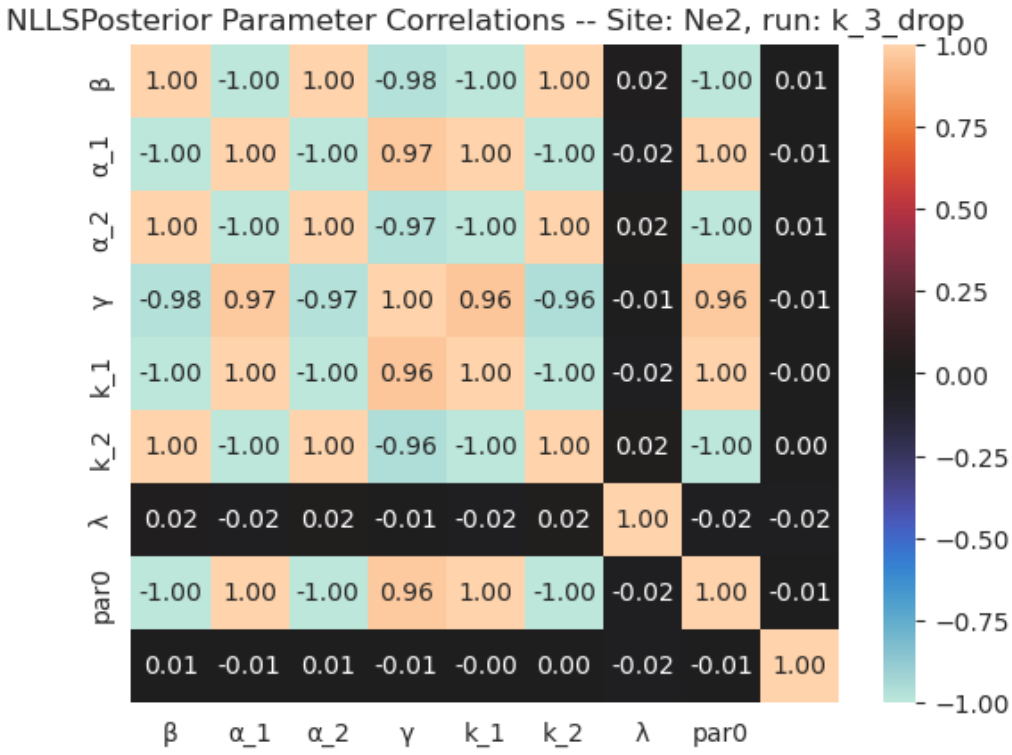

Figure B.32: Same as Figure B.20 but for the NLLS k_3 parameter drop experiment.

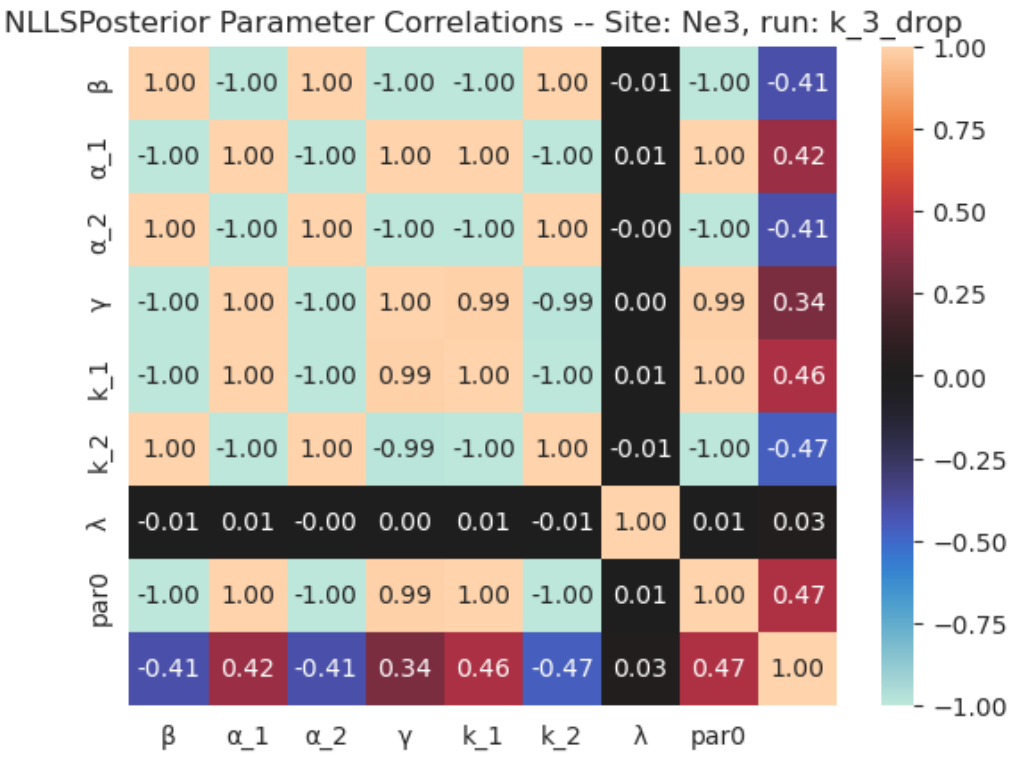

Figure B.33: Same as Figure B.32 but for the Ne3 AmeriFlux site.

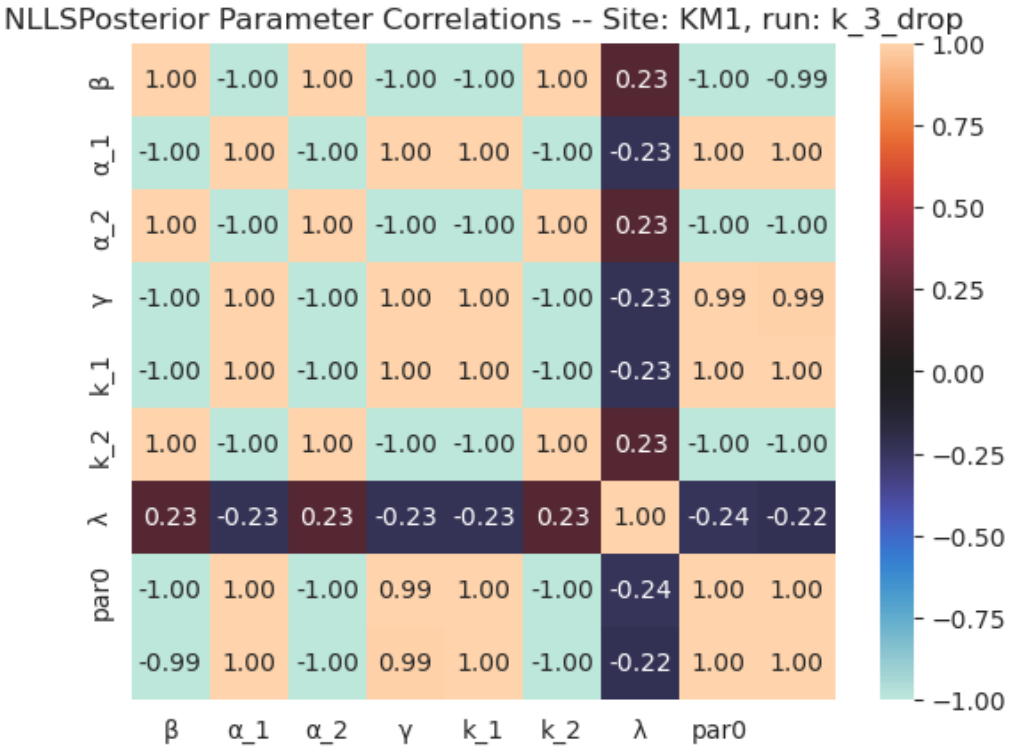

Figure B.34: Same as Figure B.32 but for the KM1 AmeriFlux site.

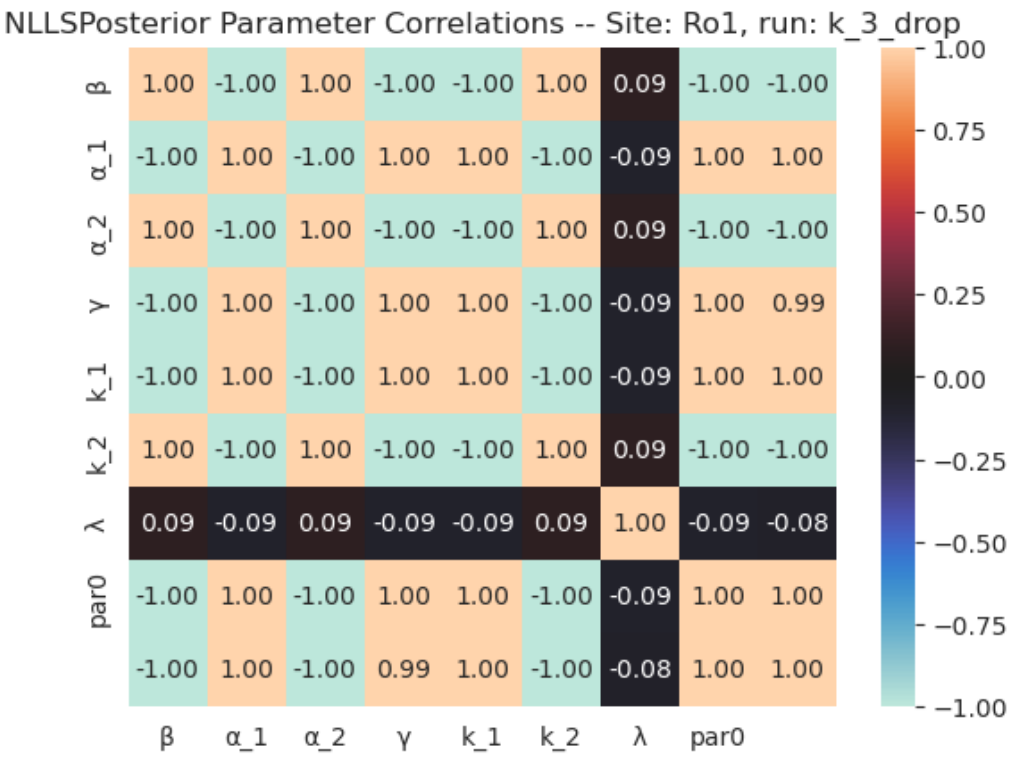

Figure B.35: Same as Figure B.32 but for the Ro1 AmeriFlux site.

B.2.5 λ Drop Experiment

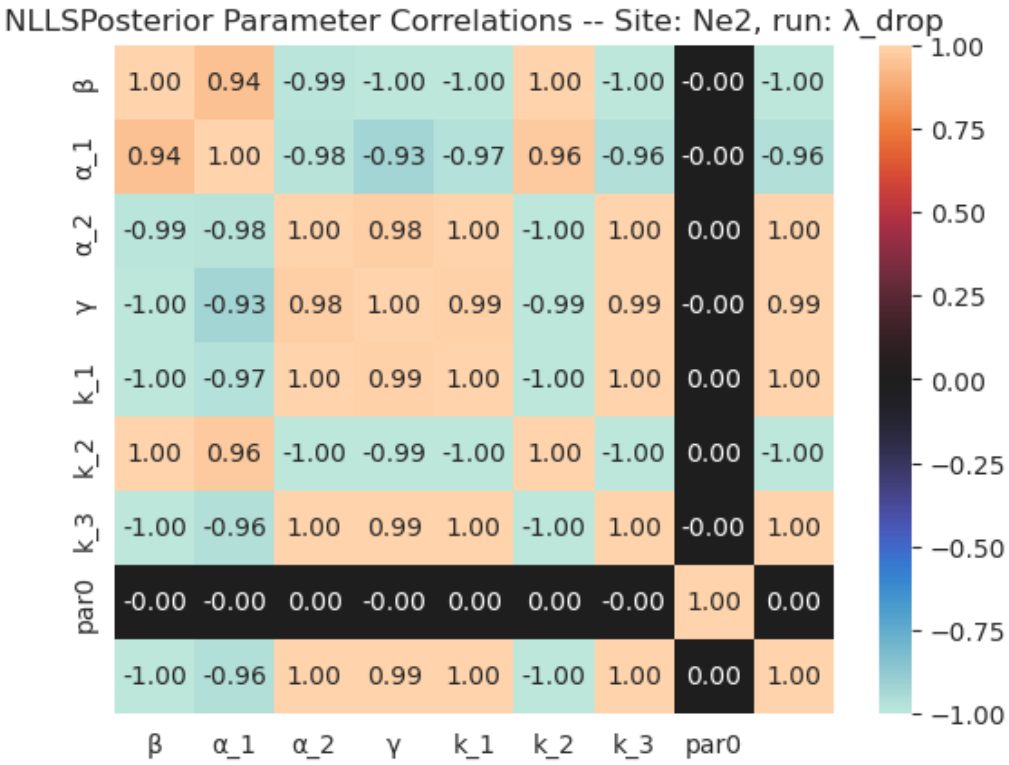

Figure B.36: Same as Figure B.20 but for the NLLS λ parameter drop experiment.

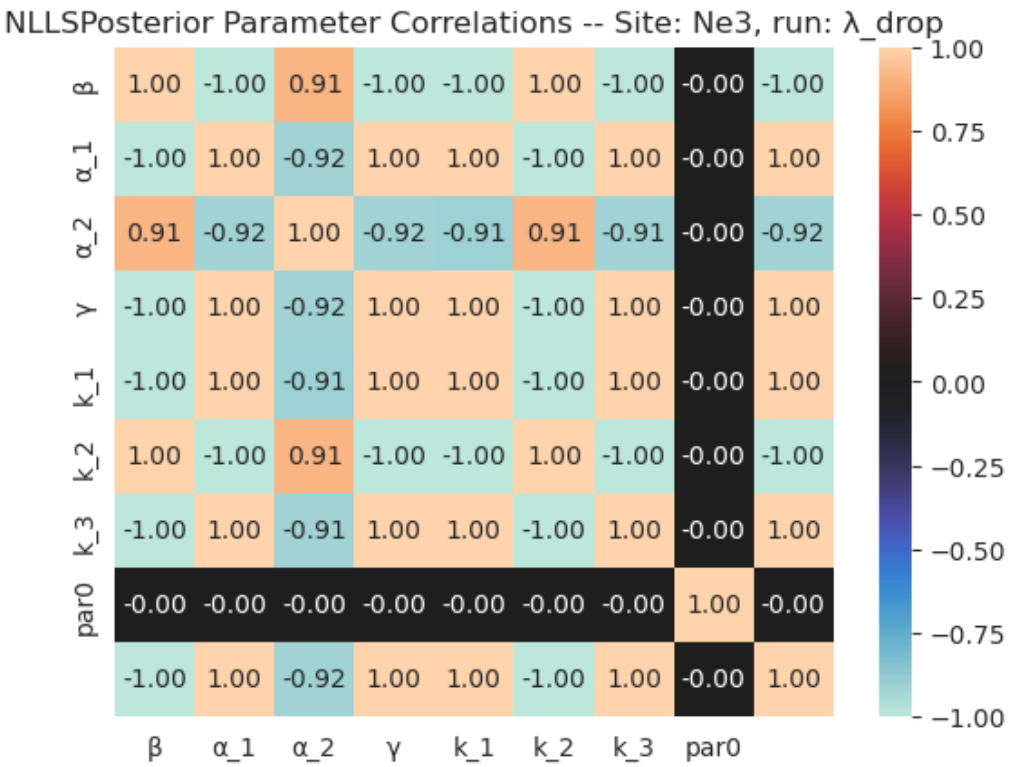

Figure B.37: Same as Figure B.36 but for the Ne3 AmeriFlux site.

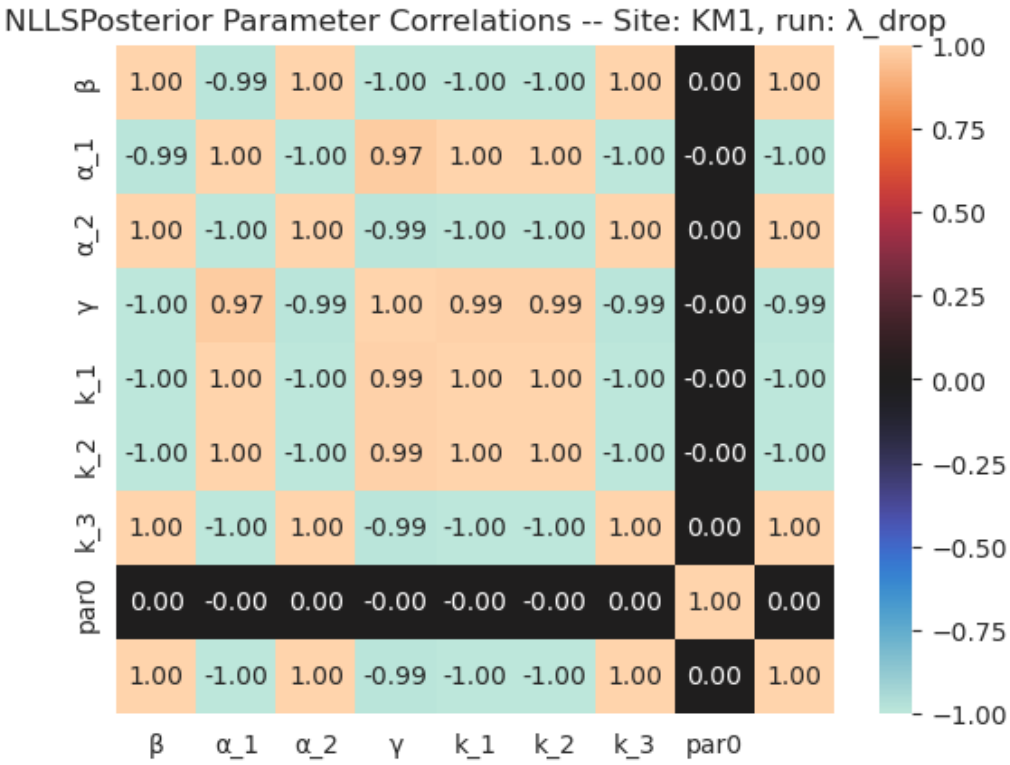

Figure B.38: Same as Figure B.36 but for the KM1 AmeriFlux site.

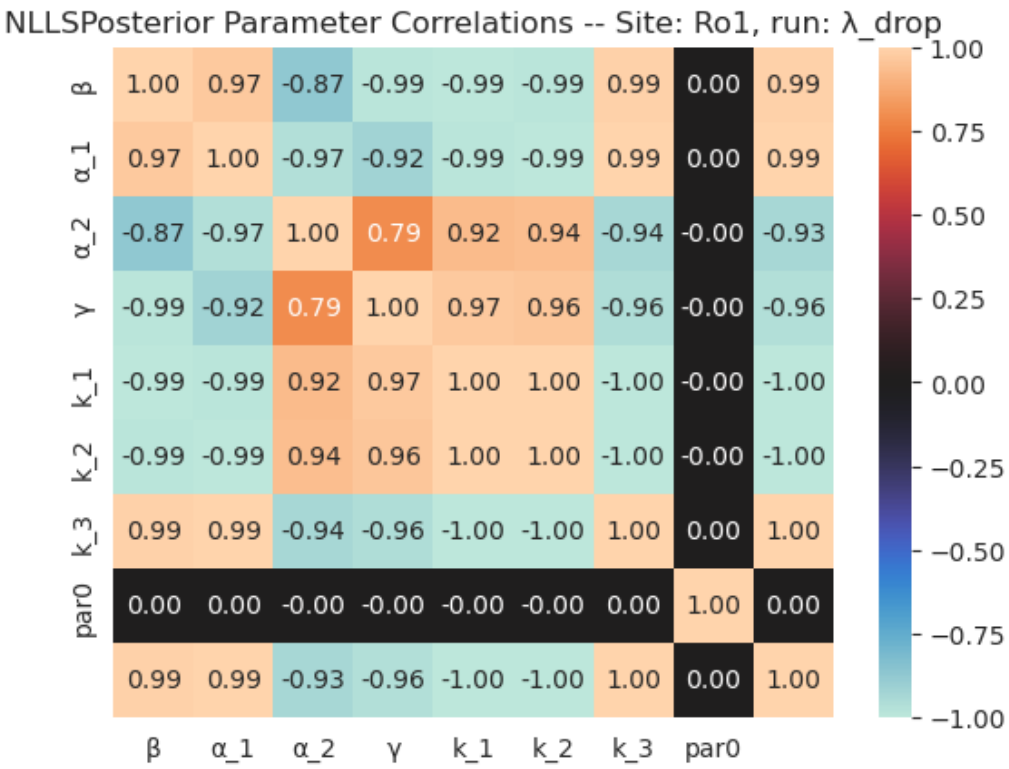

Figure B.39: Same as Figure B.36 but for the Ro1 AmeriFlux site.

B.2.6 PAR_0 Drop Experiment

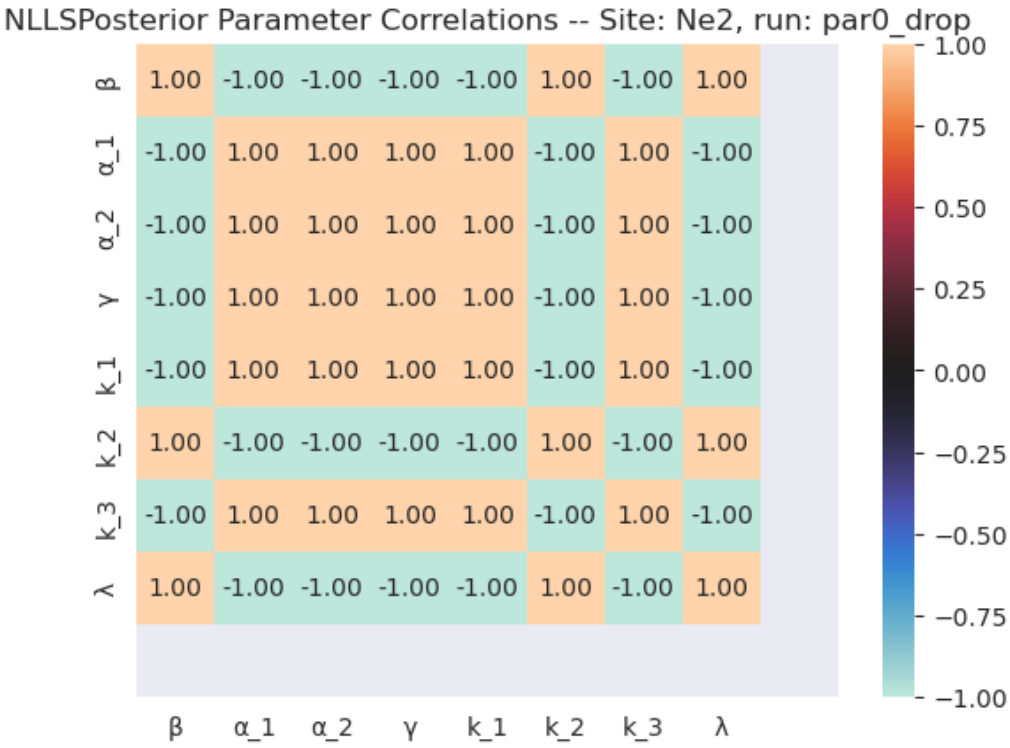

Figure B.40: Same as Figure B.20 but for the NLLS PAR_0 parameter drop experiment.

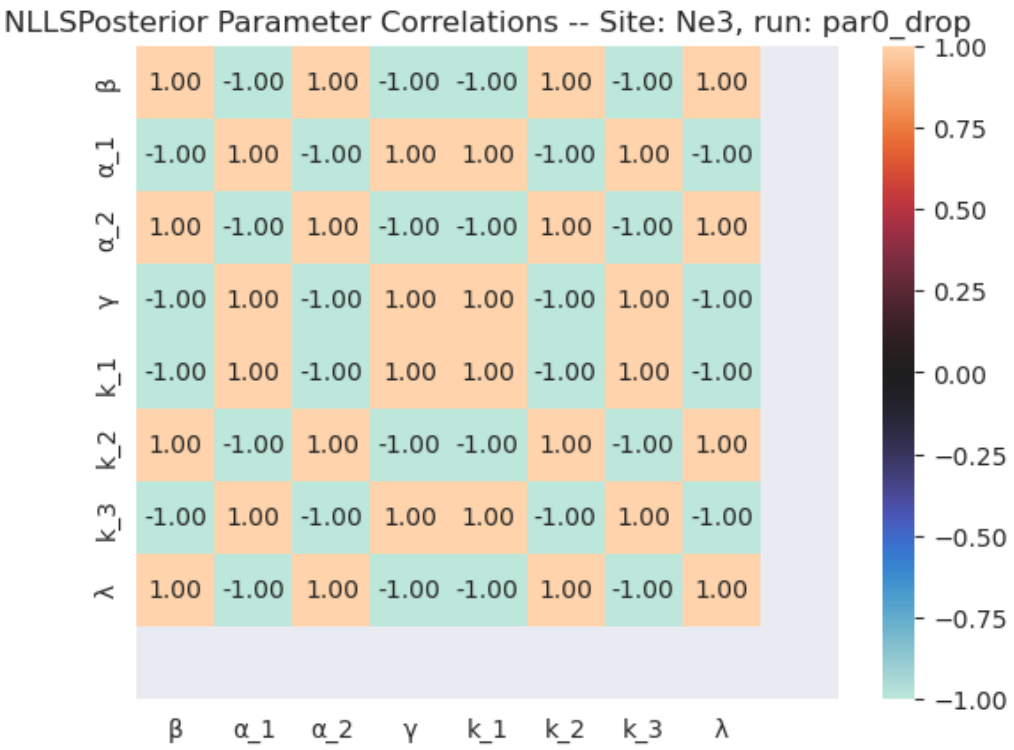

Figure B.41: Same as Figure B.40 but for the Ne3 AmeriFlux site.

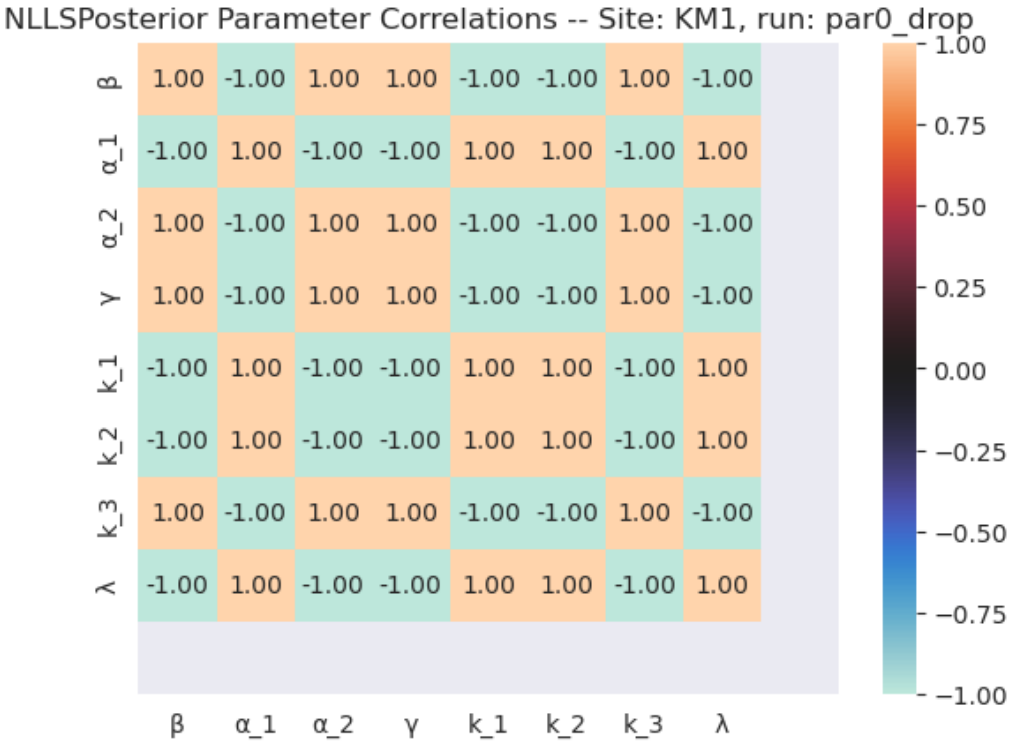

Figure B.42: Same as Figure B.40 but for the KM1 AmeriFlux site.

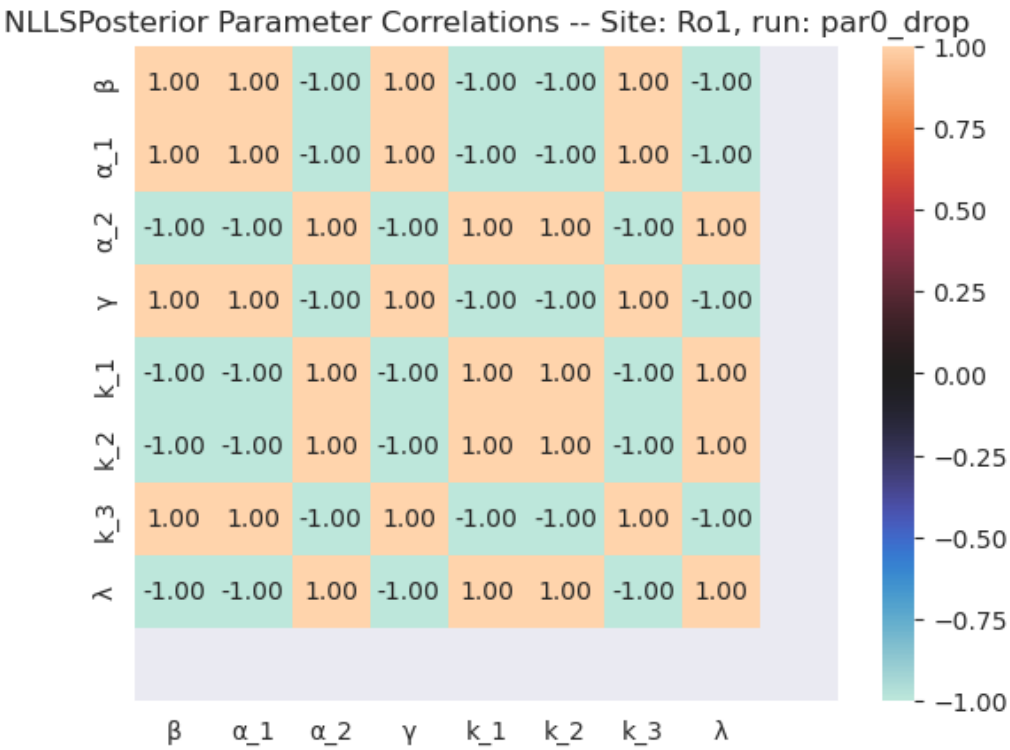

Figure B.43: Same as Figure B.40 but for the Ro1 AmeriFlux site.

Appendix C

Time Series

C.1 Observed Diurnal Cycle

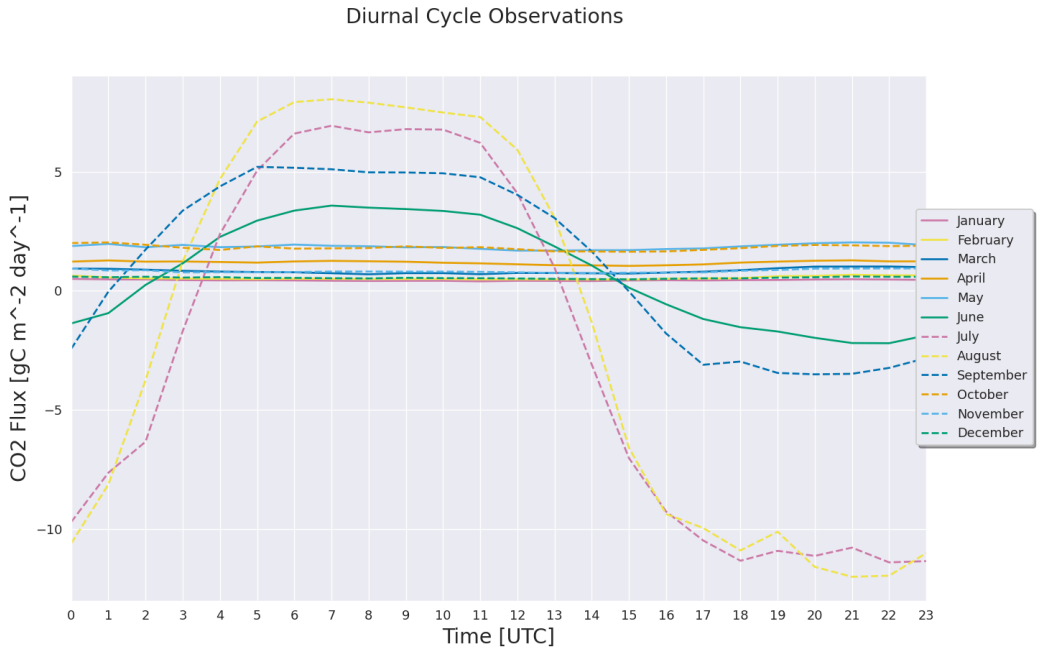

Figure C.1: Same as 4.6 but for the Ne3 AmeriFlux site.

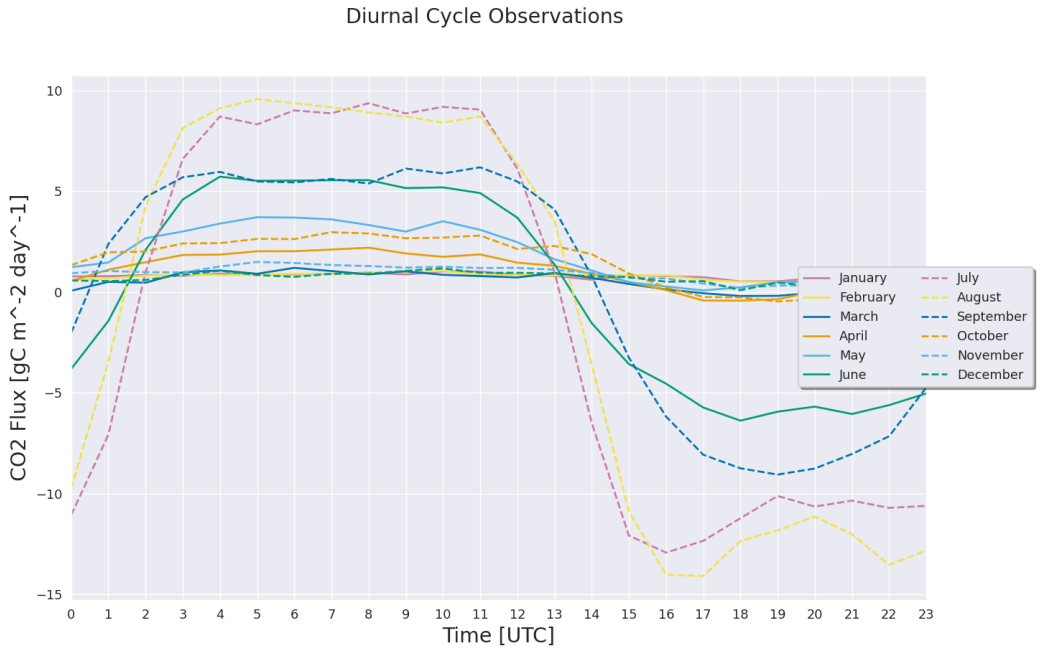

Figure C.2: Same as 4.6 but for the KM1 AmeriFlux site.

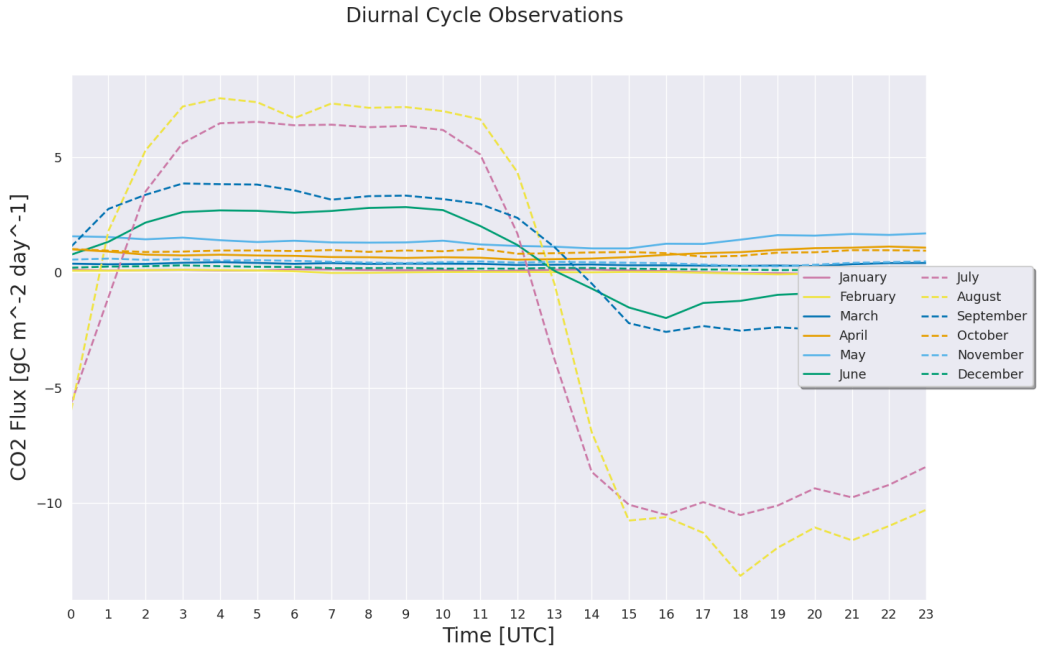

Figure C.3: Same as 4.6 but for the Ro1 AmeriFlux site.

C.2 Full Time Series

C.2.1 Whole Data Set Simultaneously

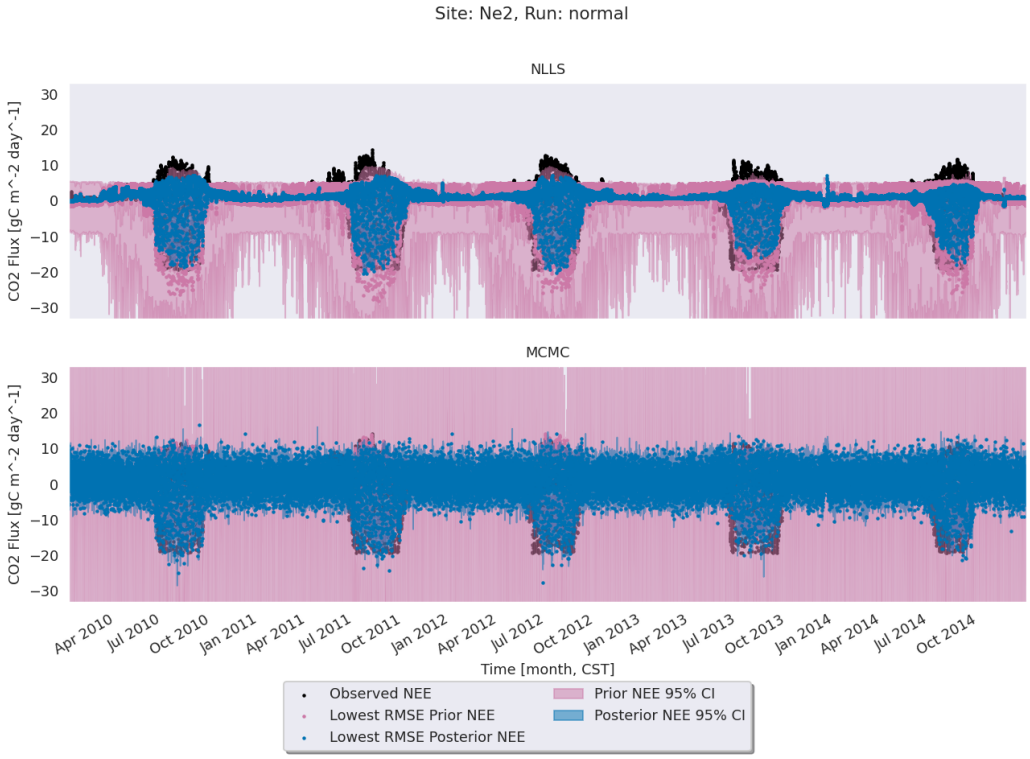

Figure C.4: Same as Figure 3.9 but for the Ne2 AmeriFlux site.

Figure C.5: Same as Figure 3.9 but for the Ne3 AmeriFlux site.

Figure C.6: Same as Figure 3.9 but for the KM1 AmeriFlux site.

C.2.2 ER/GEE Separately

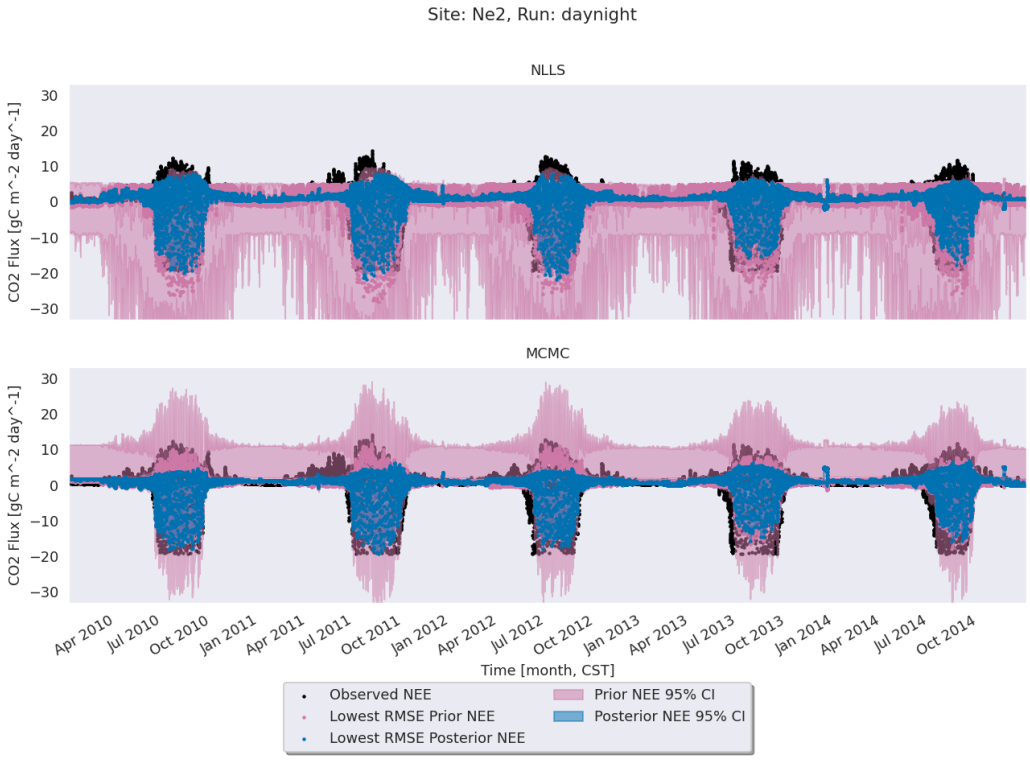

Figure C.7: Same as Figure 3.12 but for the Ne2 AmeriFlux site.

Figure C.8: Same as Figure 3.12 but for the Ne3 AmeriFlux site.

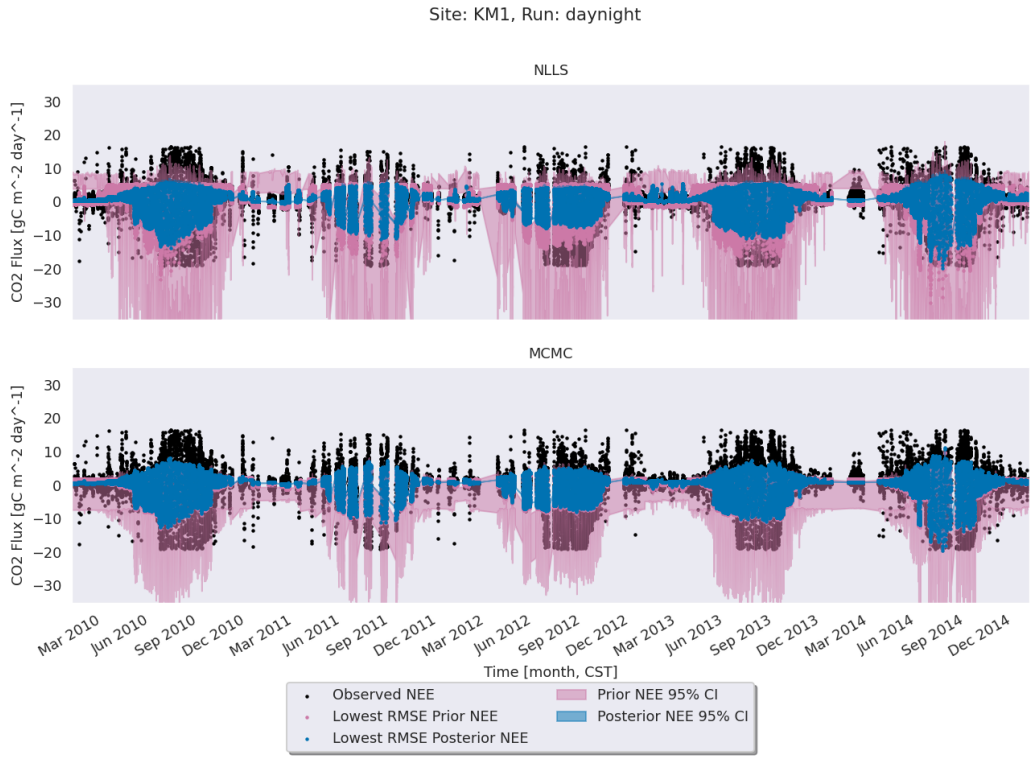

Figure C.9: Same as Figure 3.12 but for the KM1 AmeriFlux site.

C.2.3 α_2 Drop Experiment

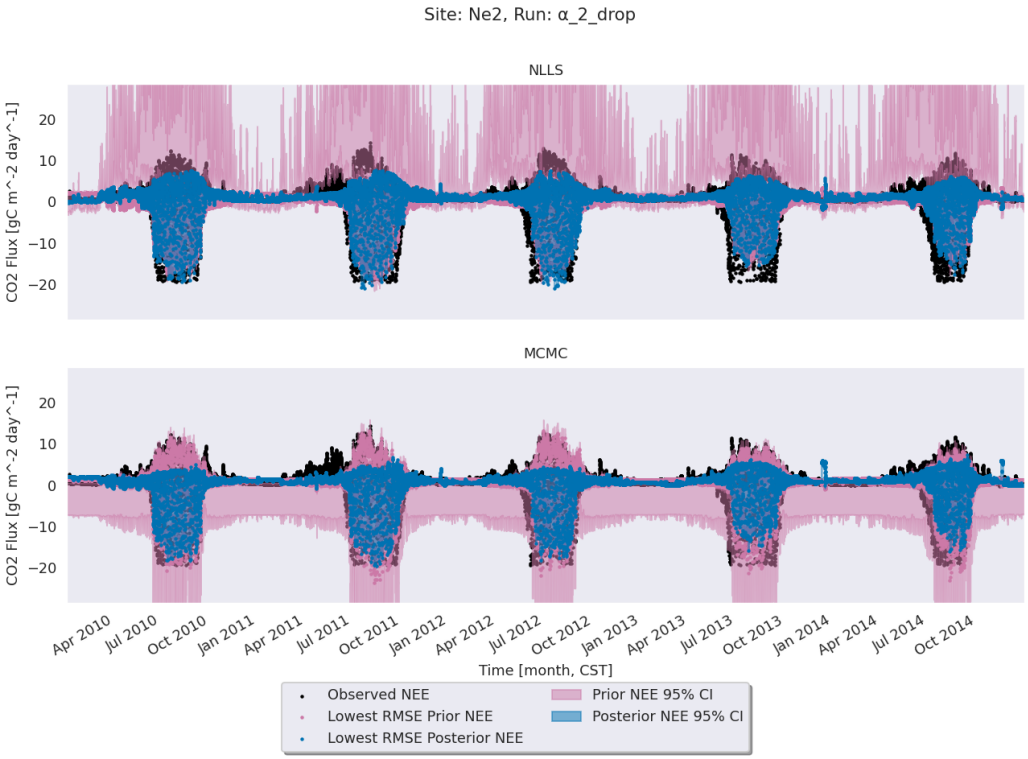

Figure C.10: Same as Figure 3.9 but for the α_2 parameter drop experiment using the Ne2 AmeriFlux site.

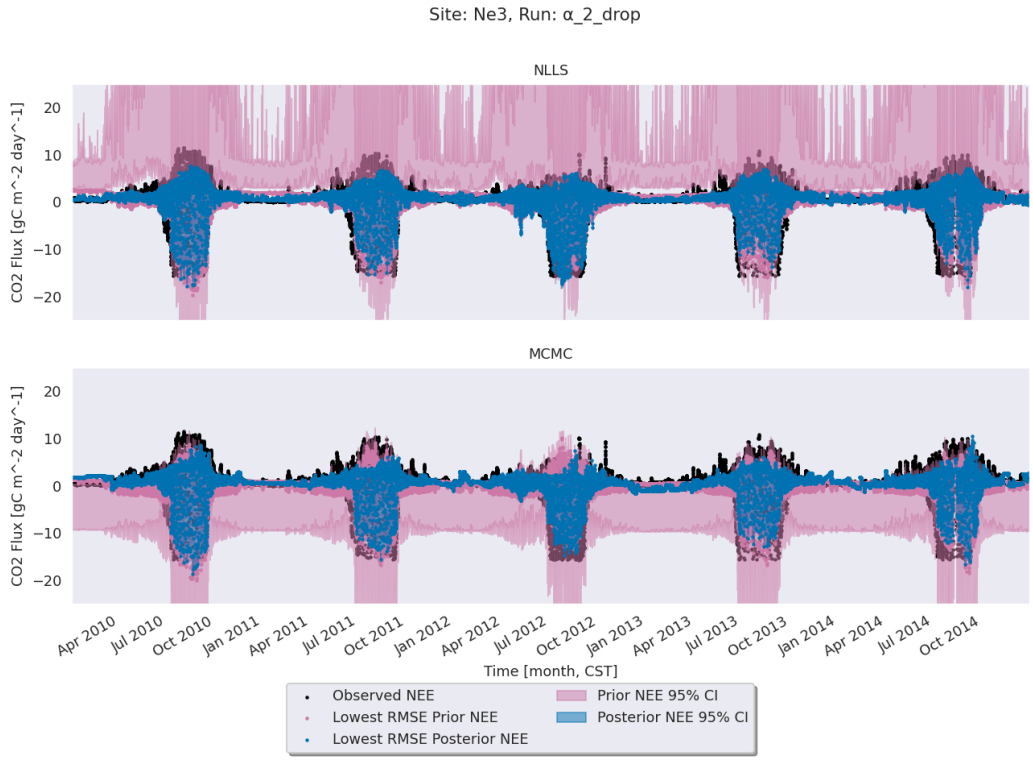

Figure C.11: Same as Figure C.10 but for the Ne3 AmeriFlux site.

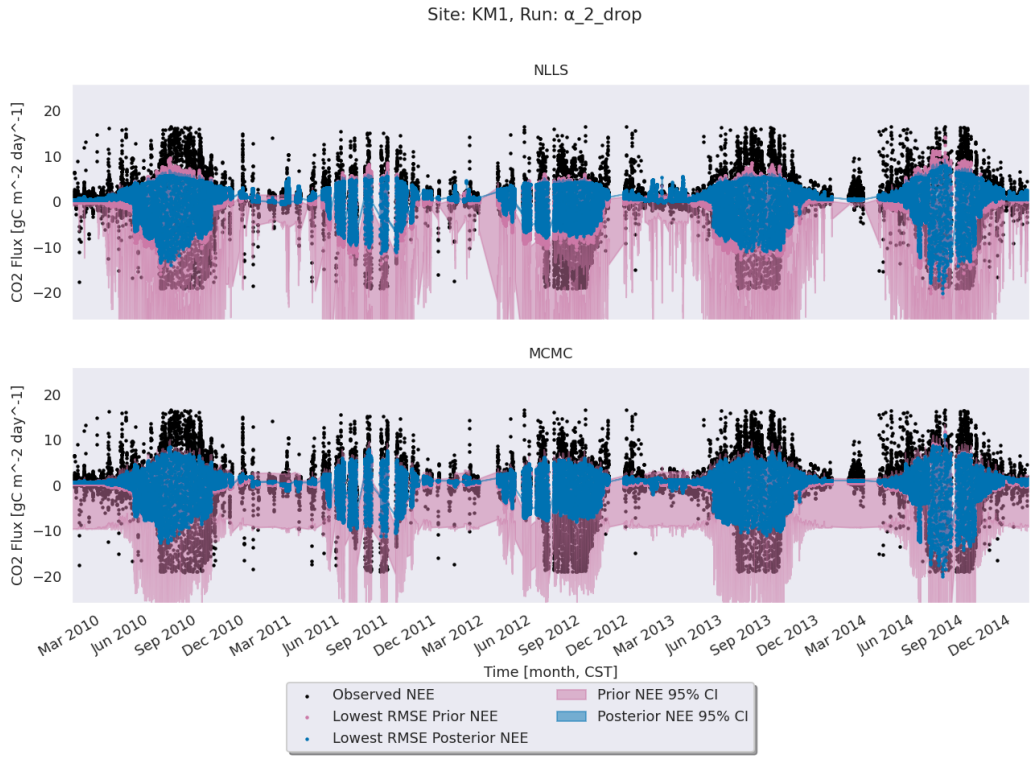

Figure C.12: Same as Figure C.10 but for the KM1 AmeriFlux site.

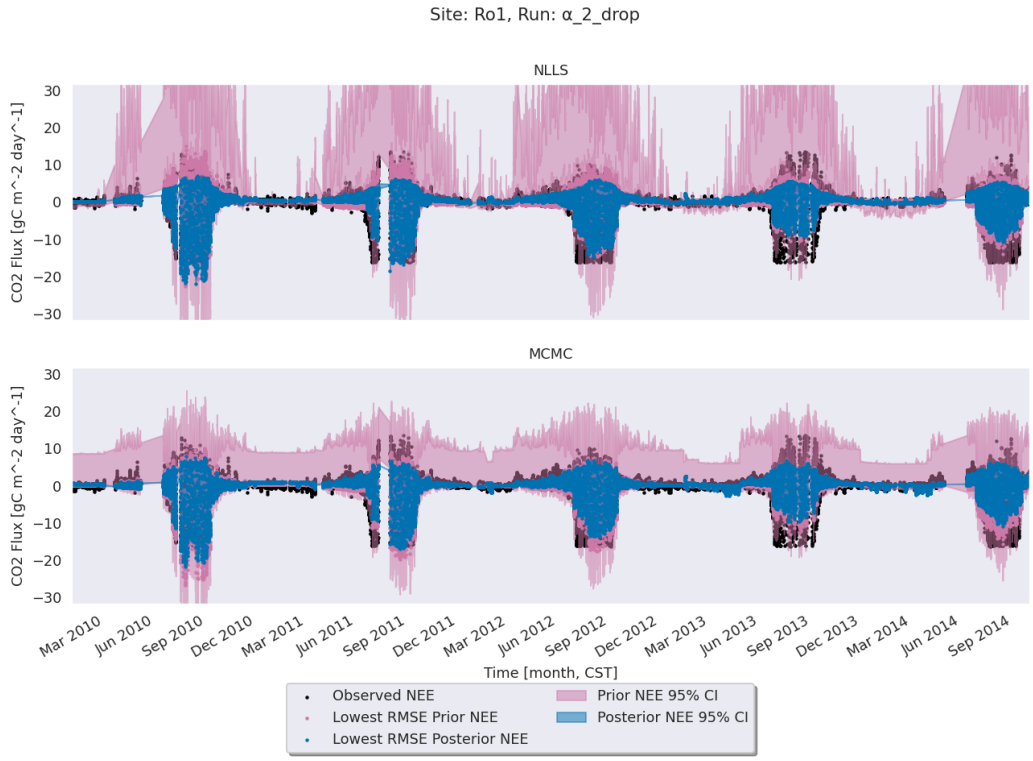

Figure C.13: Same as Figure C.10 but for the Ro1 AmeriFlux site.

C.2.4 k_3 Drop Experiment

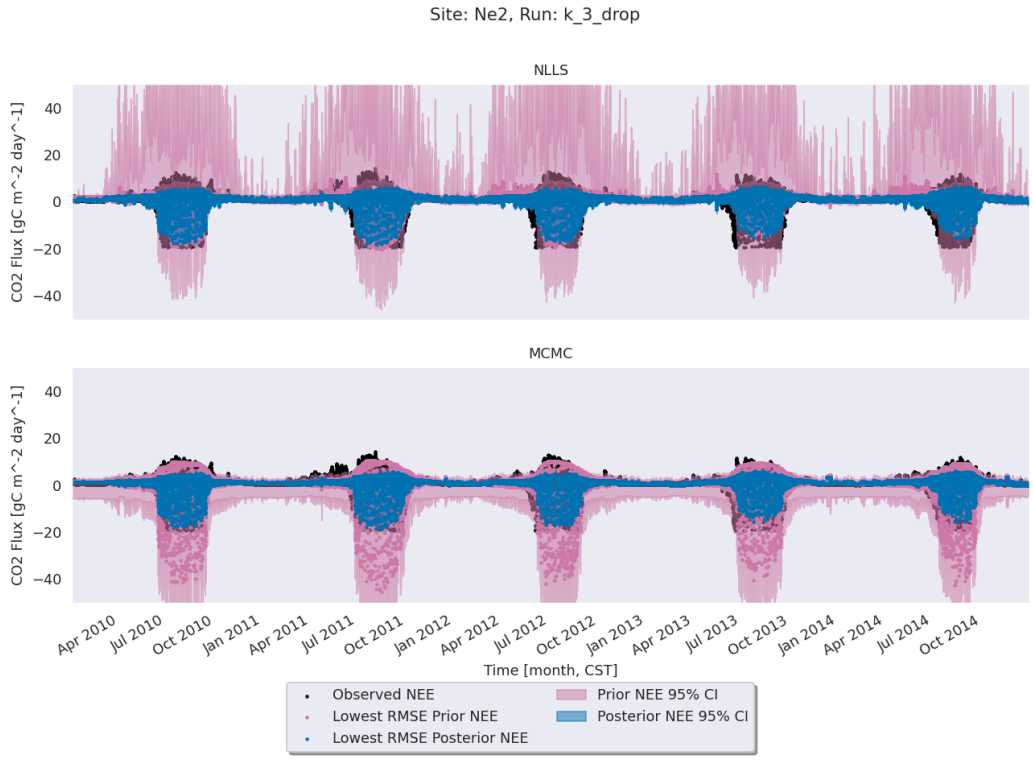

Figure C.14: Same as Figure 3.9 but for the k_3 parameter drop experiment using the Ne2 AmeriFlux site.

Figure C.15: Same as Figure C.14 but for the Ne3 AmeriFlux site.

Figure C.16: Same as Figure C.14 but for the KM1 AmeriFlux site.

Figure C.17: Same as Figure C.14 but for the Ro1 AmeriFlux site.

C.2.5 λ Drop Experiment

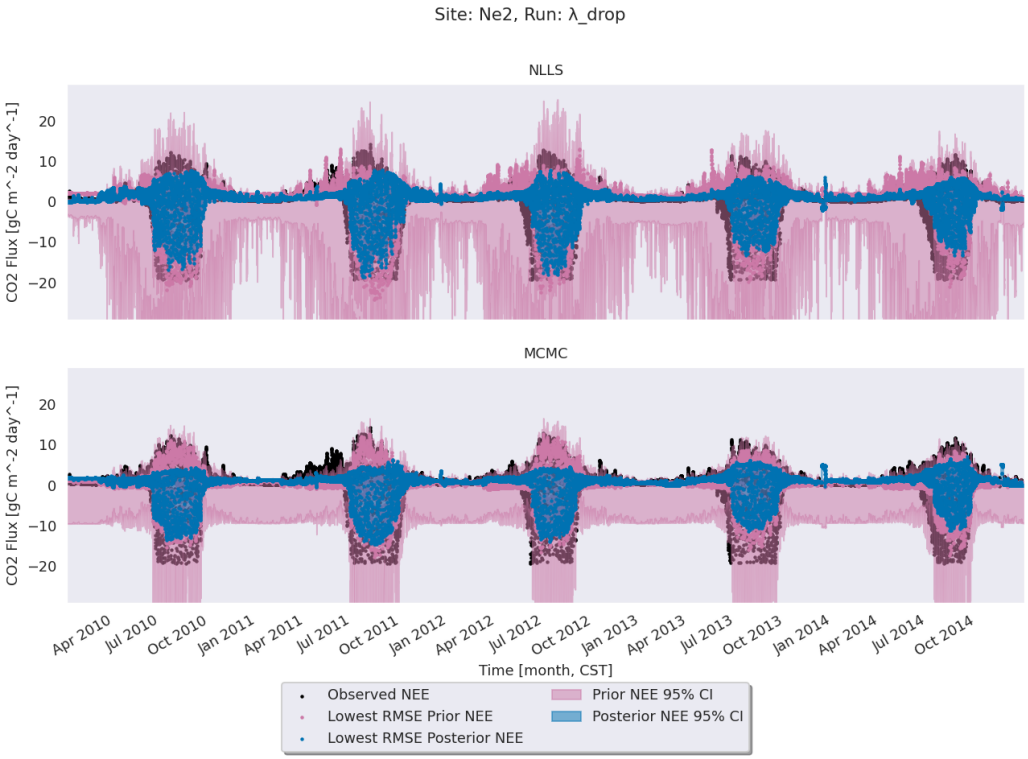

Figure C.18: Same as Figure 3.9 but for the λ parameter drop experiment using the Ne2 AmeriFlux site.

Figure C.19: Same as Figure C.18 but for the Ne3 AmeriFlux site.

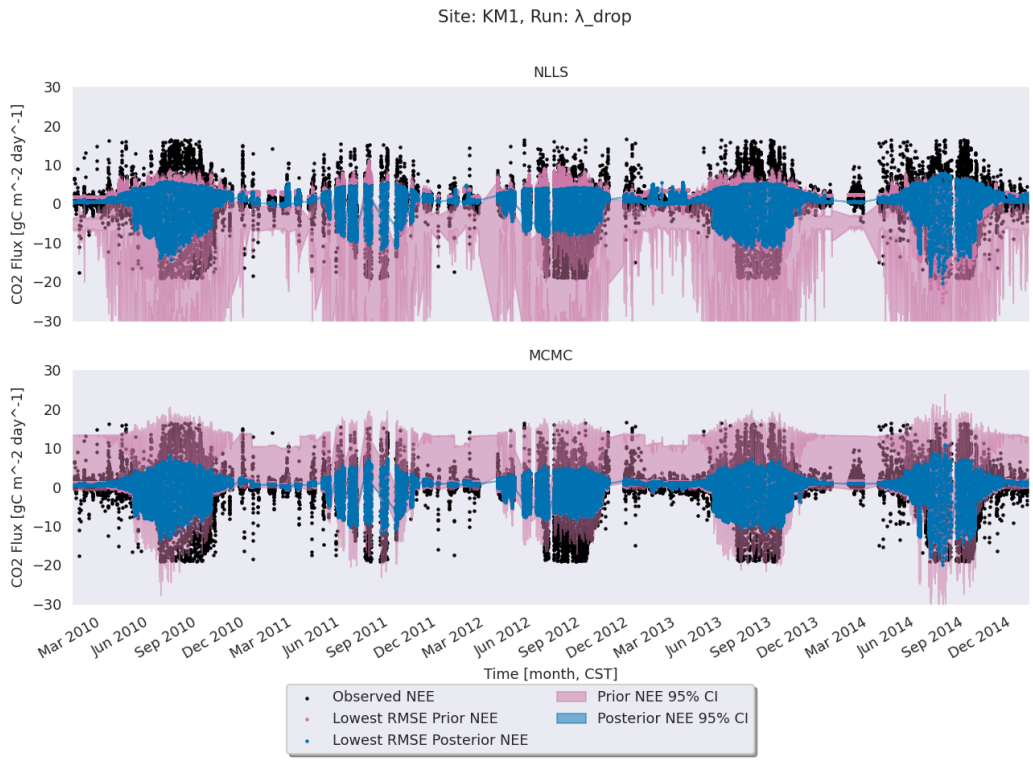

Figure C.20: Same as Figure C.18 but for the KM1 AmeriFlux site.

C.2.6 PAR_0 Drop Experiment

Figure C.21: Same as Figure 3.9 but for the PAR_0 parameter drop experiment using the Ne2 AmeriFlux site.

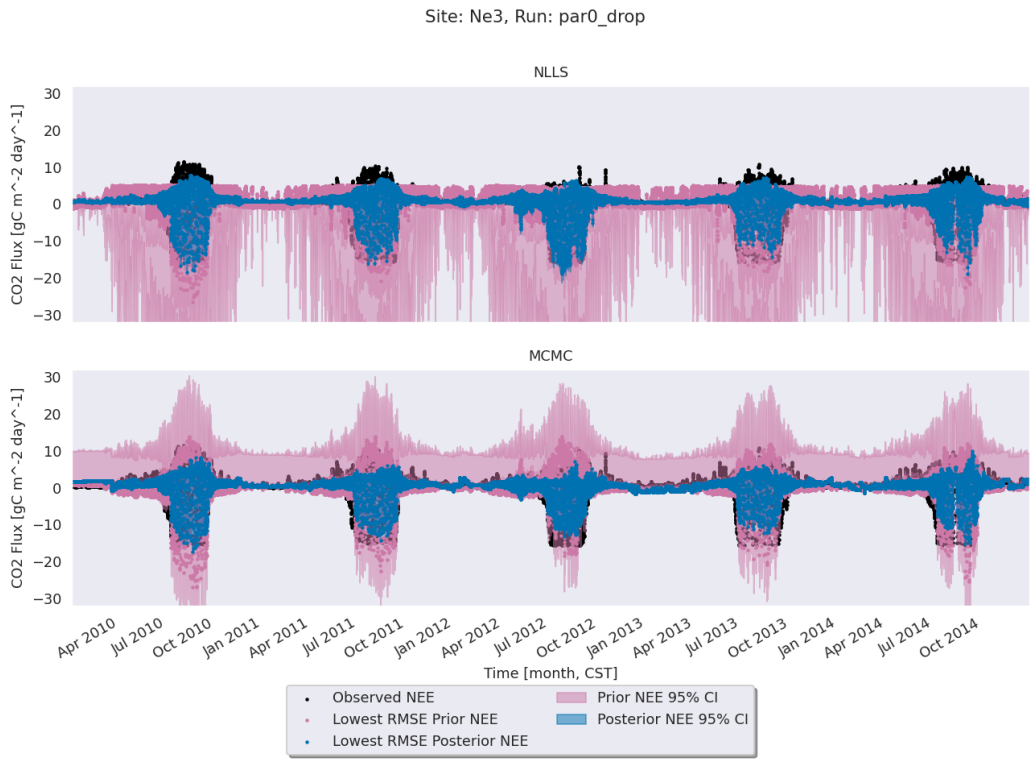

Figure C.22: Same as Figure C.21 but for the Ne3 AmeriFlux site.

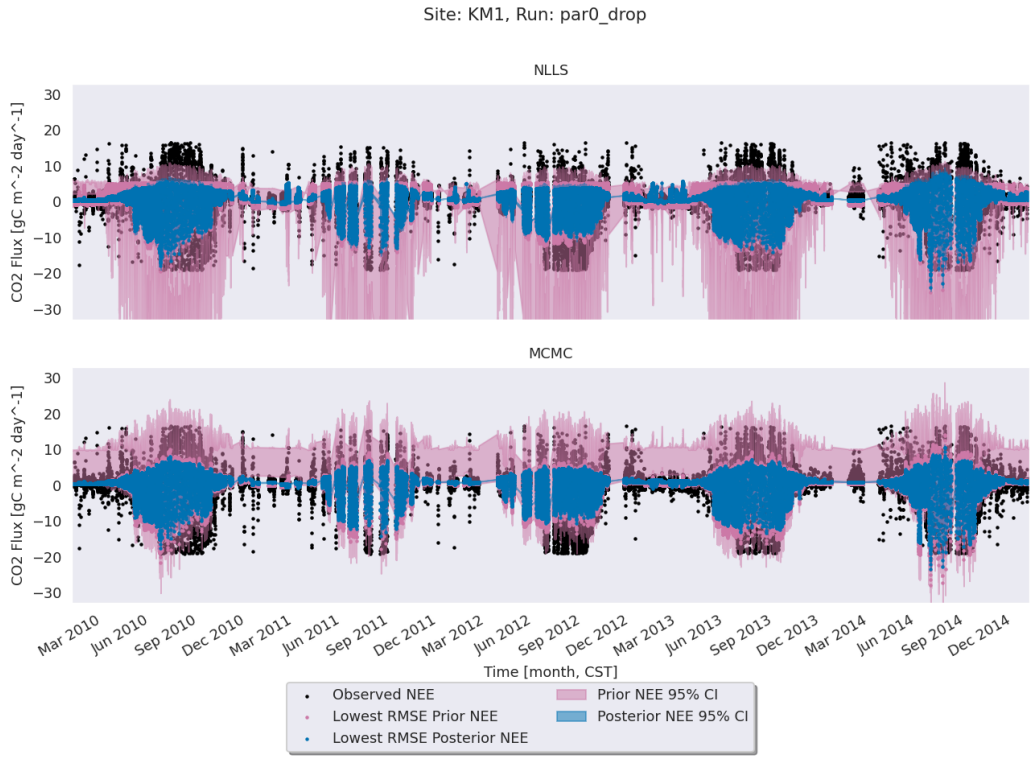

Figure C.23: Same as Figure C.21 but for the KM1 AmeriFlux site.

C.3 Residual Time Series

C.3.1 Whole Data Set Simultaneously

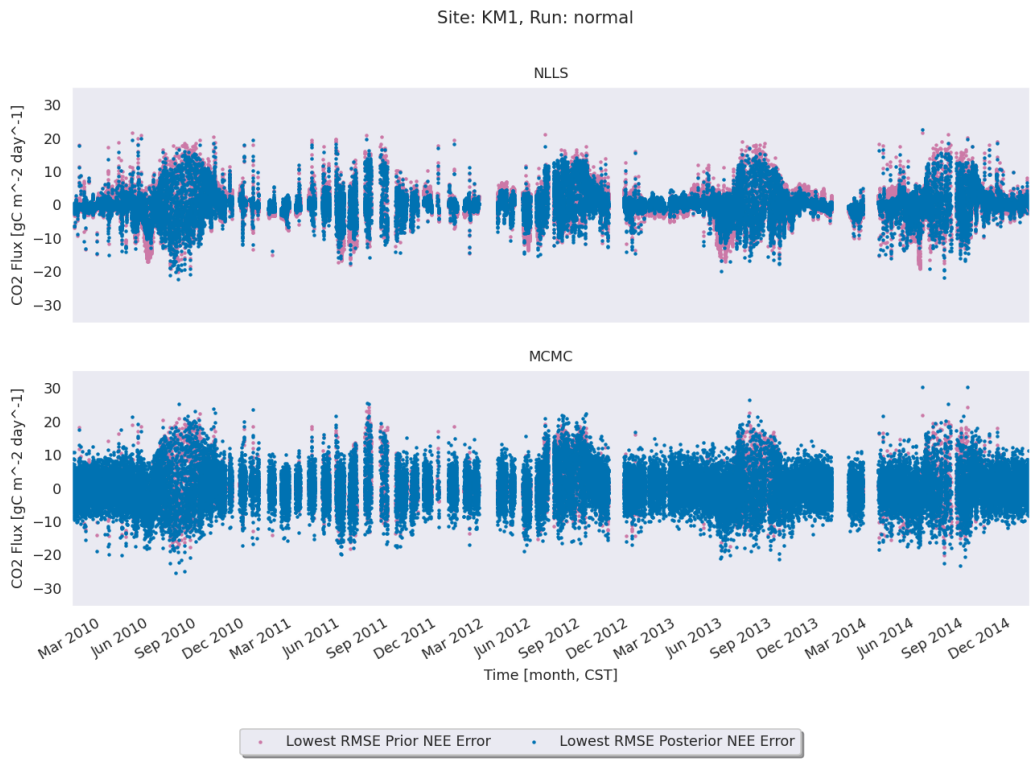

Figure C.24: Same as Figure 3.10 but for the KM1 AmeriFlux site.

C.3.2 ER/GEE Separately

Figure C.25: Same as Figure 3.10 but for the Ne2 AmeriFlux site when fitting ER and GEE separately.

Figure C.26: Same as Figure C.25 but for the Ne3 AmeriFlux site.

Figure C.27: Same as Figure C.25 but for the KM1 AmeriFlux site.

C.3.3 α_2 Drop Experiment

Figure C.28: Same as Figure 3.10 but for the α_2 parameter drop experiment using the Ne2 AmeriFlux site.

Figure C.29: Same as Figure C.28 but for the Ne3 AmeriFlux site.

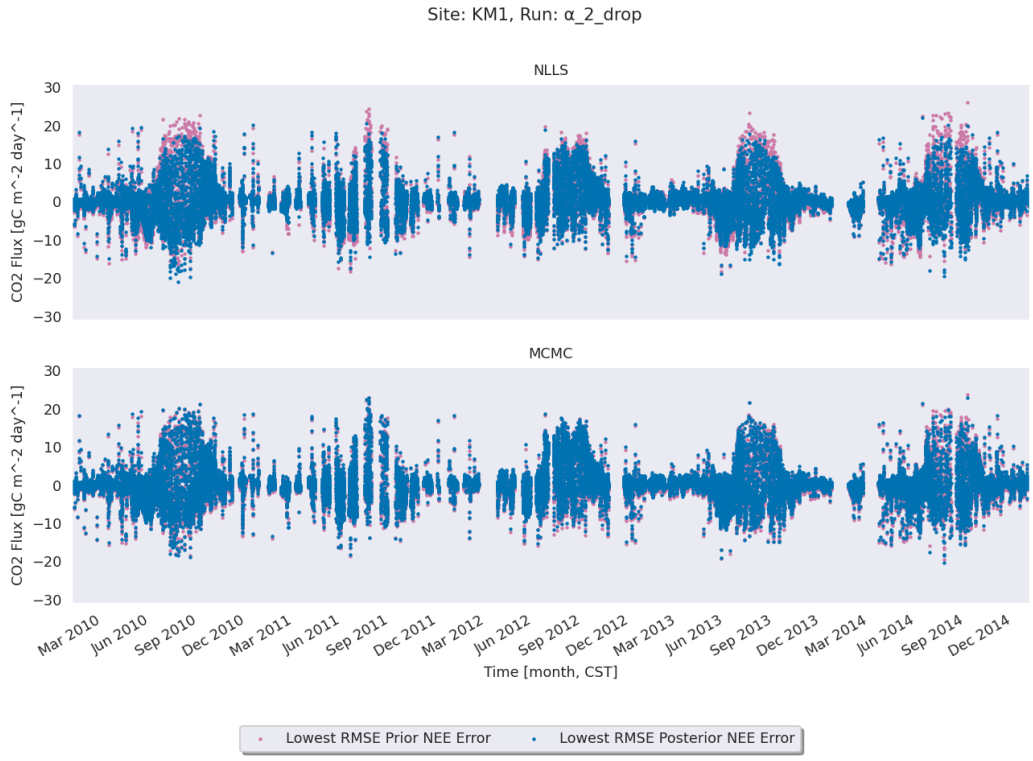

Figure C.30: Same as Figure C.28 but for the KM1 AmeriFlux site.

Figure C.31: Same as Figure C.28 but for the Ro1 AmeriFlux site.

C.3.4 k_3 Drop Experiment

Figure C.32: Same as Figure 3.10 but for the k_3 parameter drop experiment using the Ne2 AmeriFlux site.

Figure C.33: Same as Figure C.32 but for the Ne3 AmeriFlux site.

Figure C.34: Same as Figure C.32 but for the KM1 AmeriFlux site.

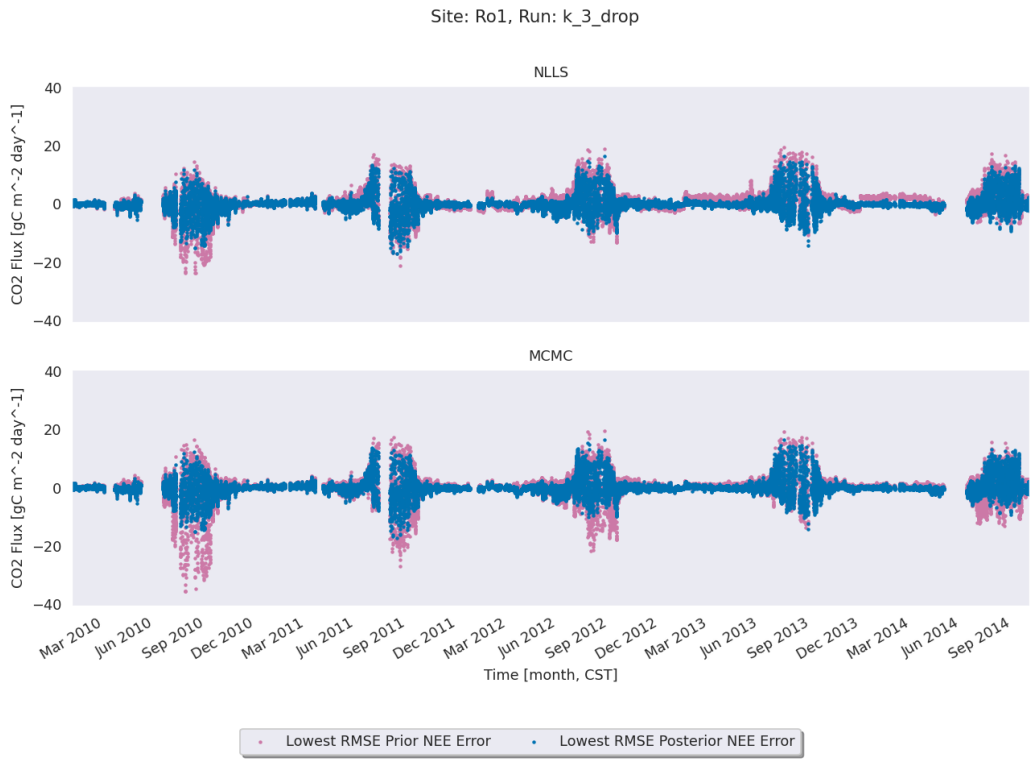

Figure C.35: Same as Figure C.32 but for the Ro1 AmeriFlux site.

C.3.5 λ Drop Experiment

Figure C.36: Same as Figure 3.10 but for the λ parameter drop experiment using the Ne2 AmeriFlux site.

Figure C.37: Same as Figure C.36 but for the Ne3 AmeriFlux site.

Figure C.38: Same as Figure C.36 but for the KM1 AmeriFlux site.

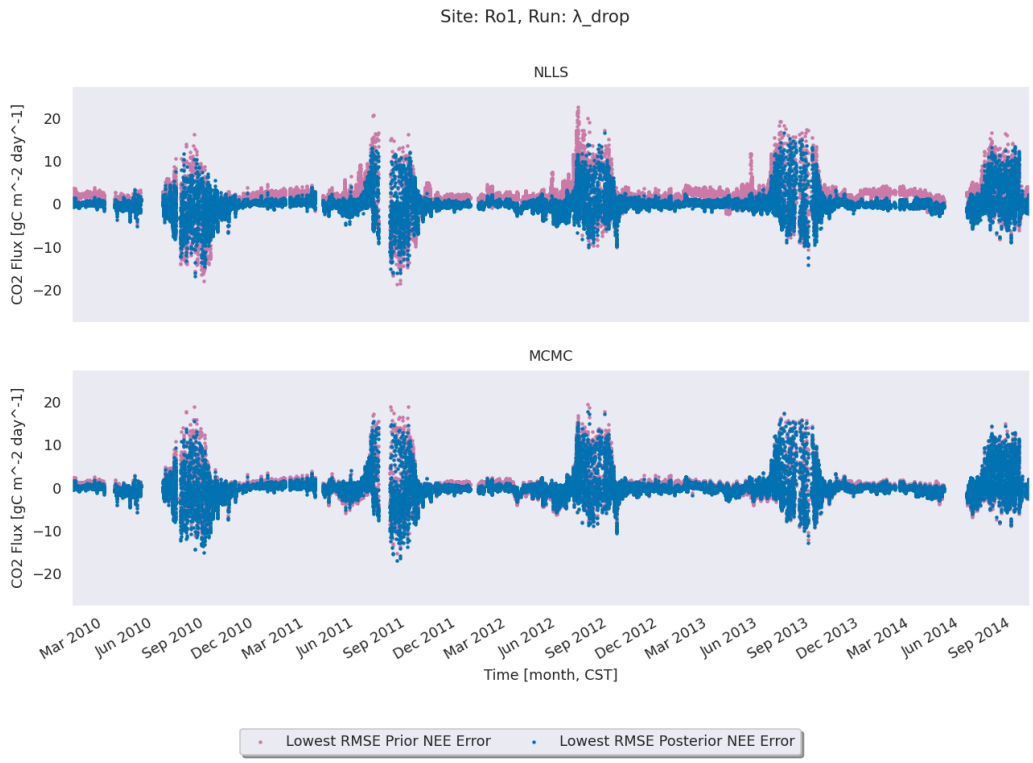

Figure C.39: Same as Figure C.36 but for the Ro1 AmeriFlux site.

C.3.6 PAR_0 Drop Experiment

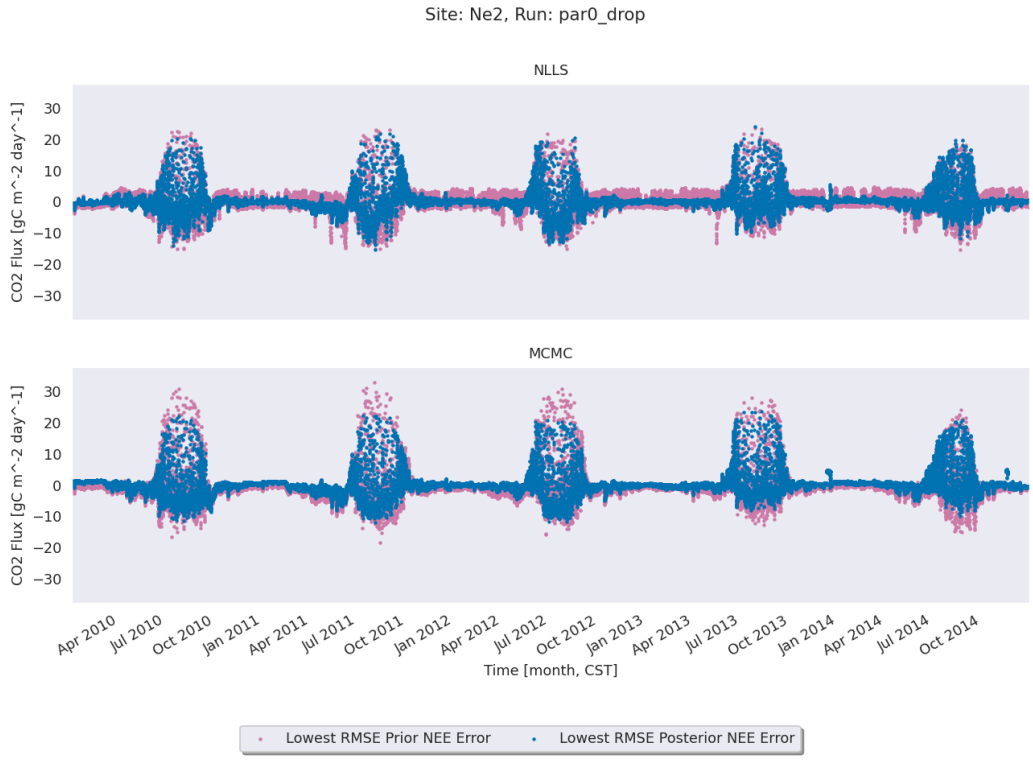

Figure C.40: Same as Figure 3.10 but for the PAR_0 parameter drop experiment using the Ne2 AmeriFlux site.

Figure C.41: Same as Figure C.40 but for the Ne3 AmeriFlux site.

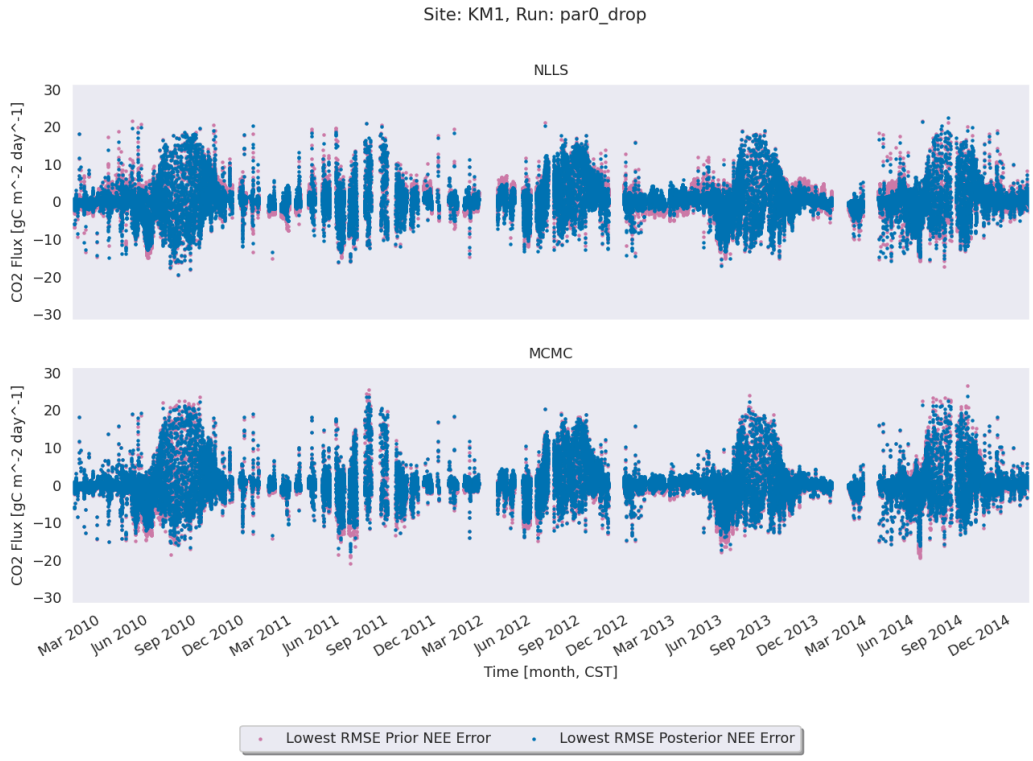

Figure C.42: Same as Figure C.40 but for the KM1 AmeriFlux site.

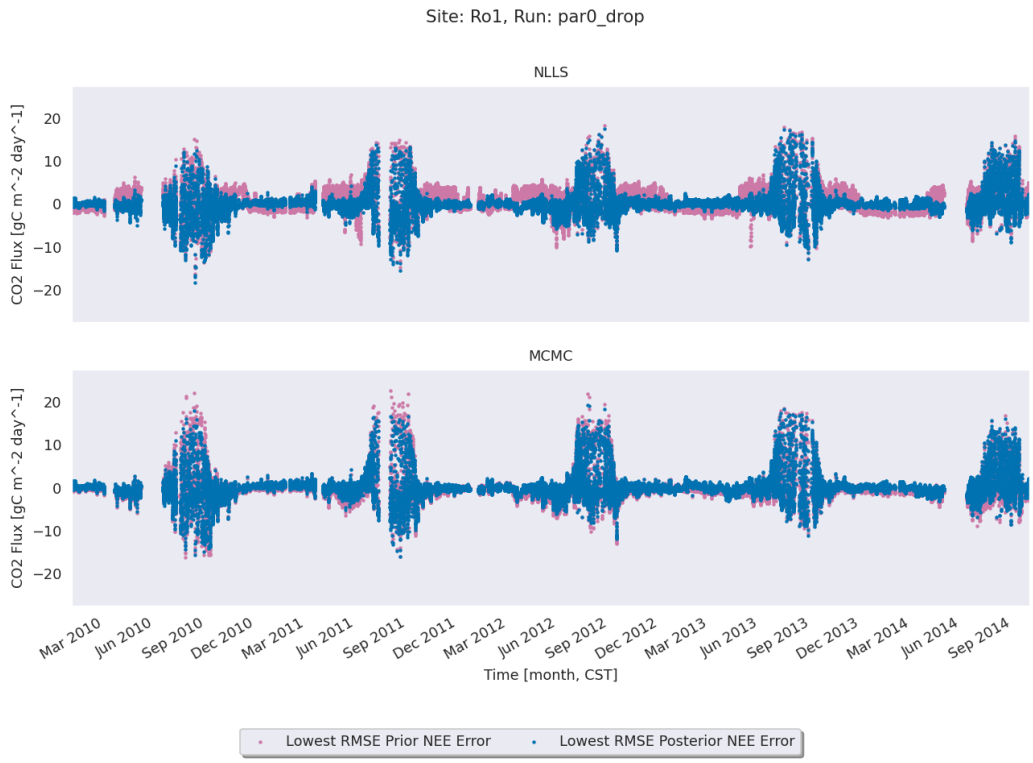

Figure C.43: Same as Figure C.40 but for the Ro1 AmeriFlux site.

C.4 Monthly Average Analysis

C.4.1 Whole Data Set Simultaneously

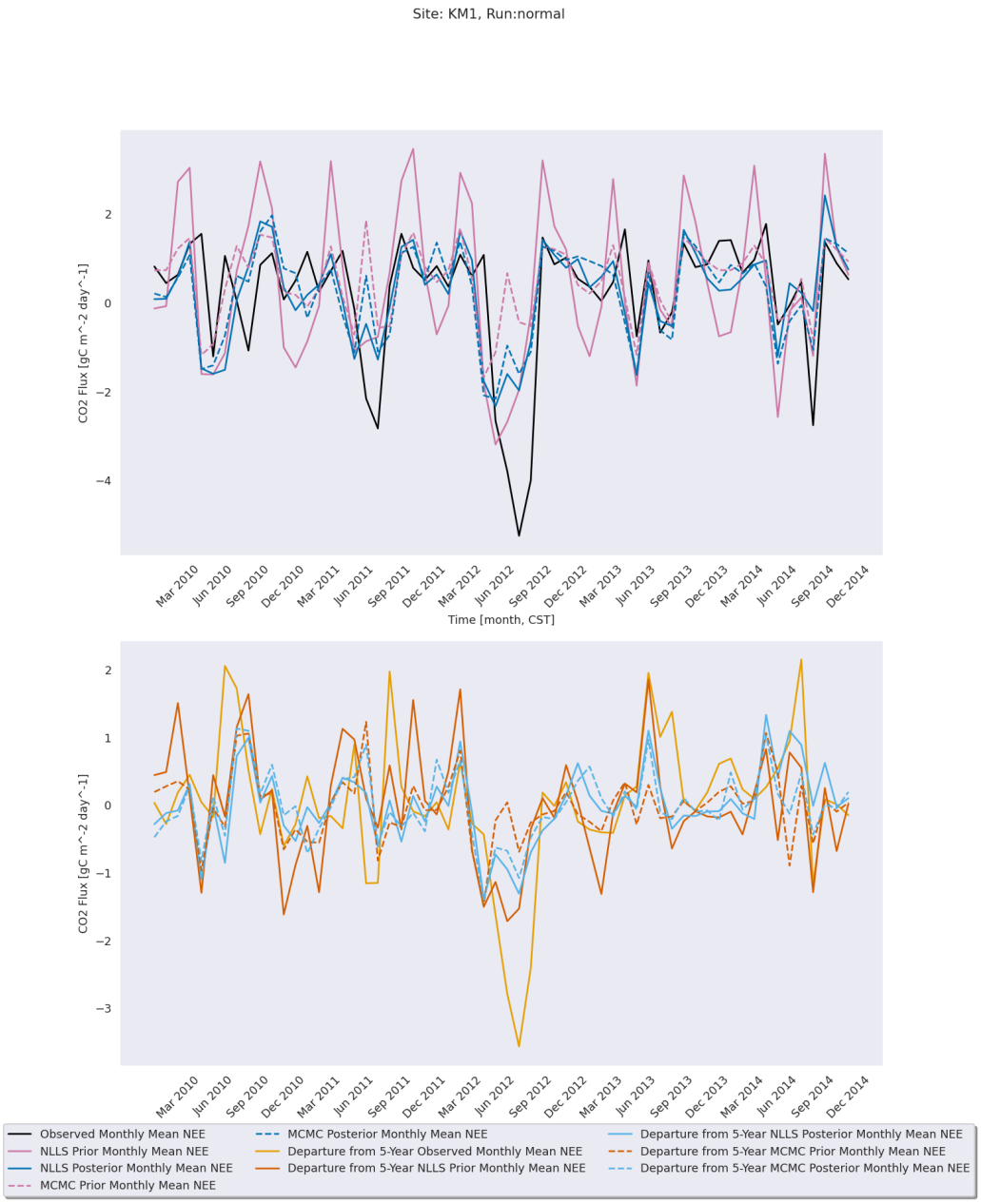

Figure C.44: Same as Figure 4.1 but for the KM1 AmeriFlux site.

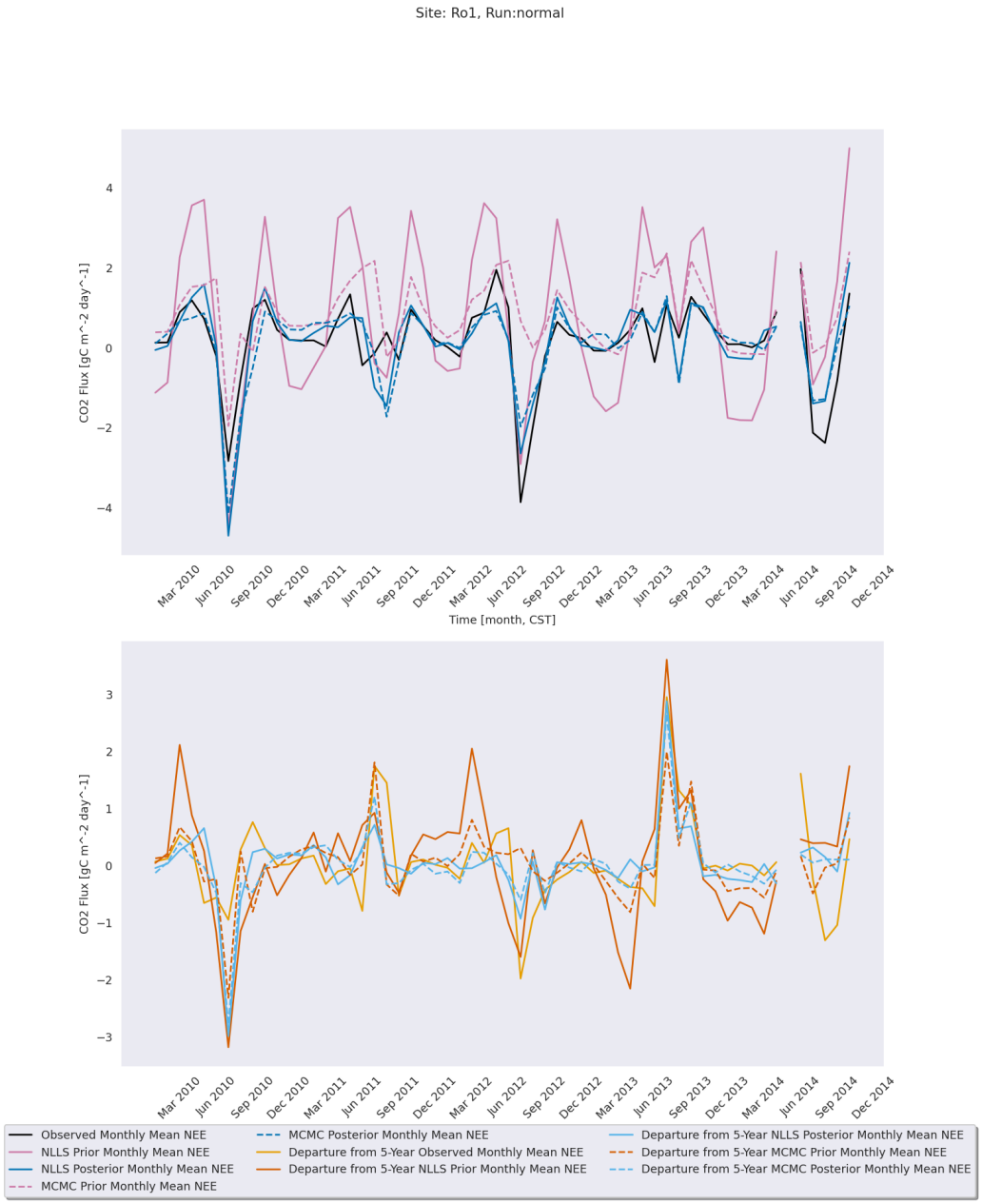

Figure C.45: Same as Figure 4.1 but for the Ro1 AmeriFlux site.

C.4.2 ER/GEE Separately

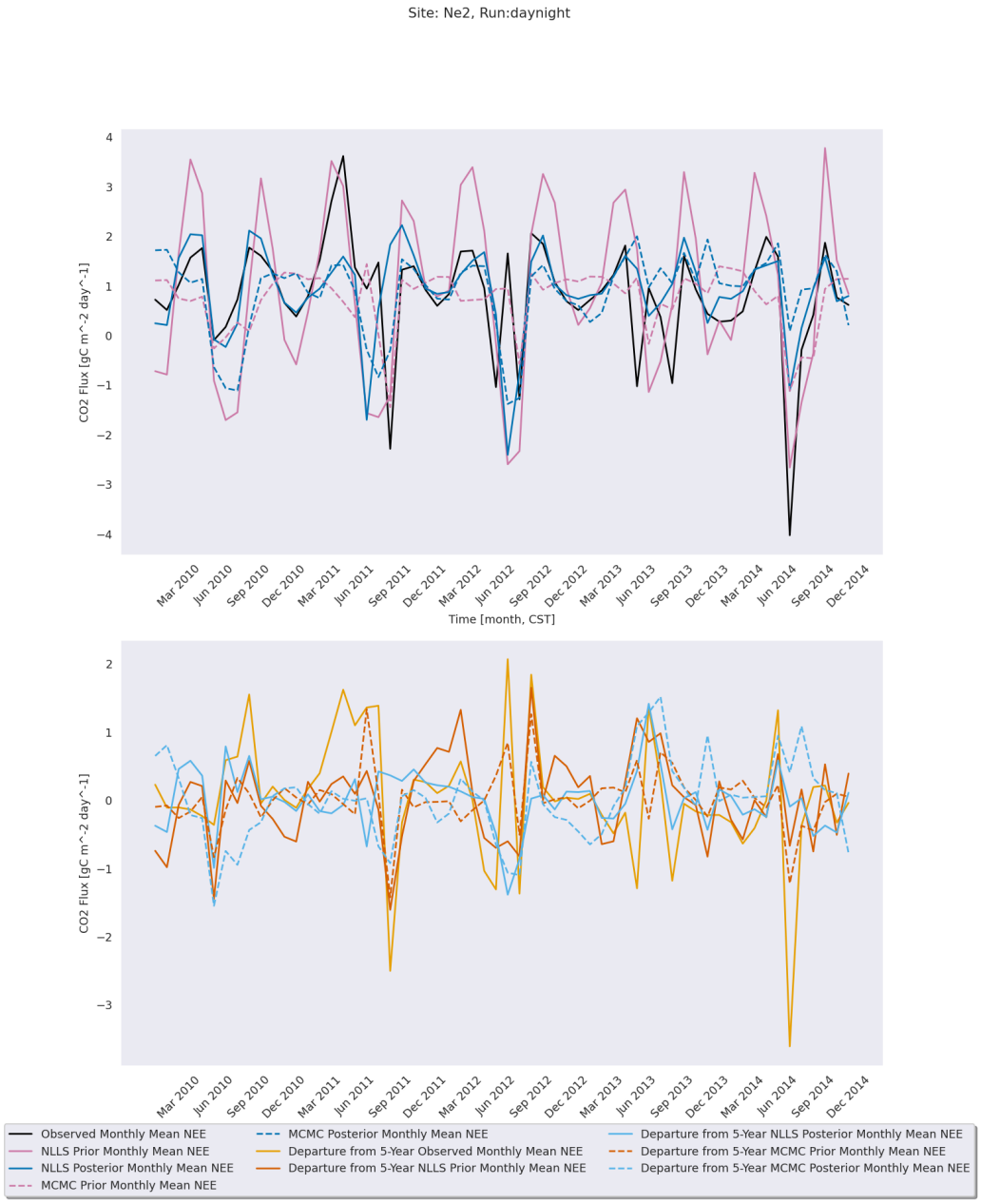

Figure C.46: Same as Figure 4.1 but for fitting ER and GEE separately.

Figure C.47: Same as Figure C.46 but for the Ne3 AmeriFlux site.

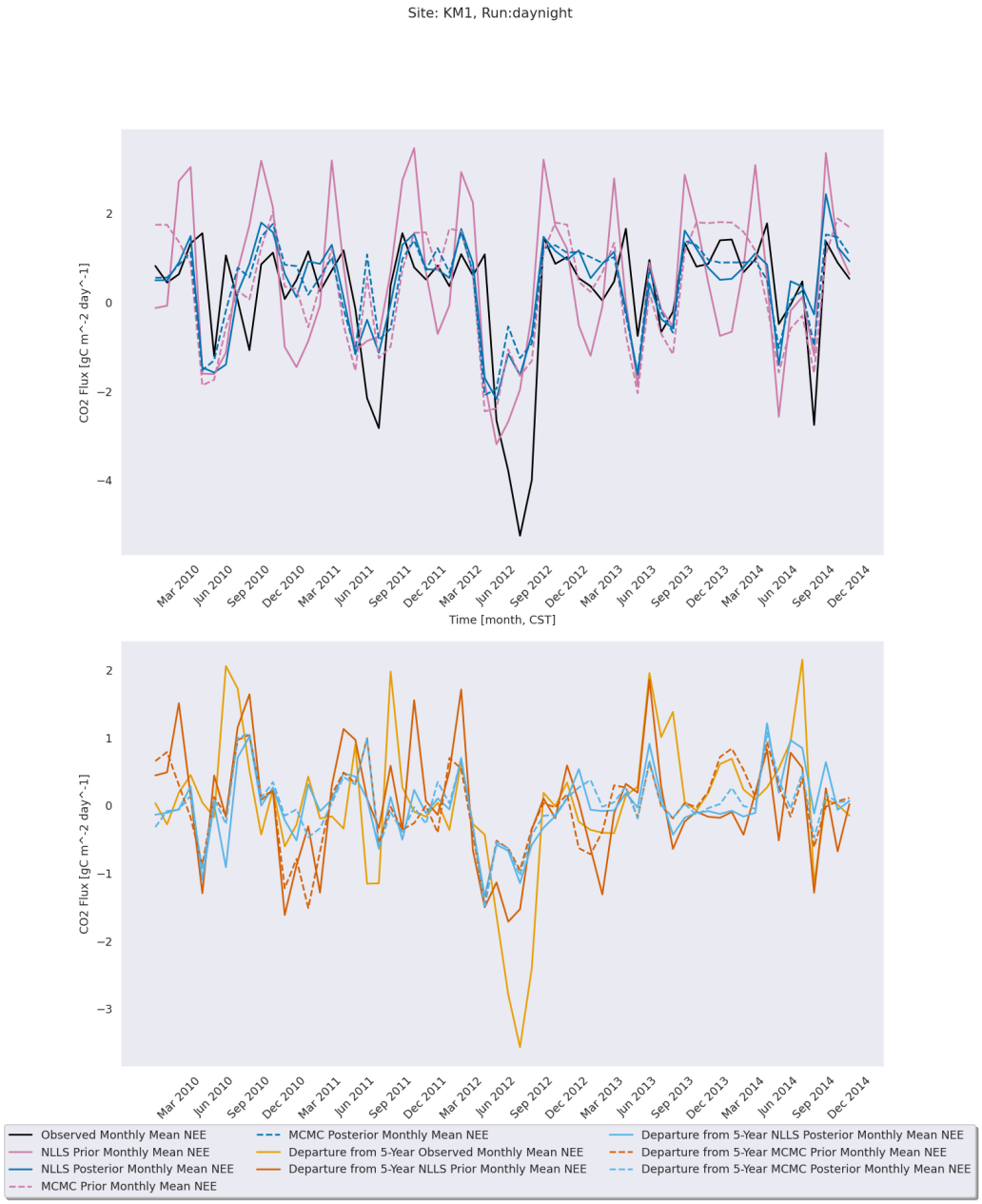

Figure C.48: Same as Figure C.46 but for the KM1 AmeriFlux site.

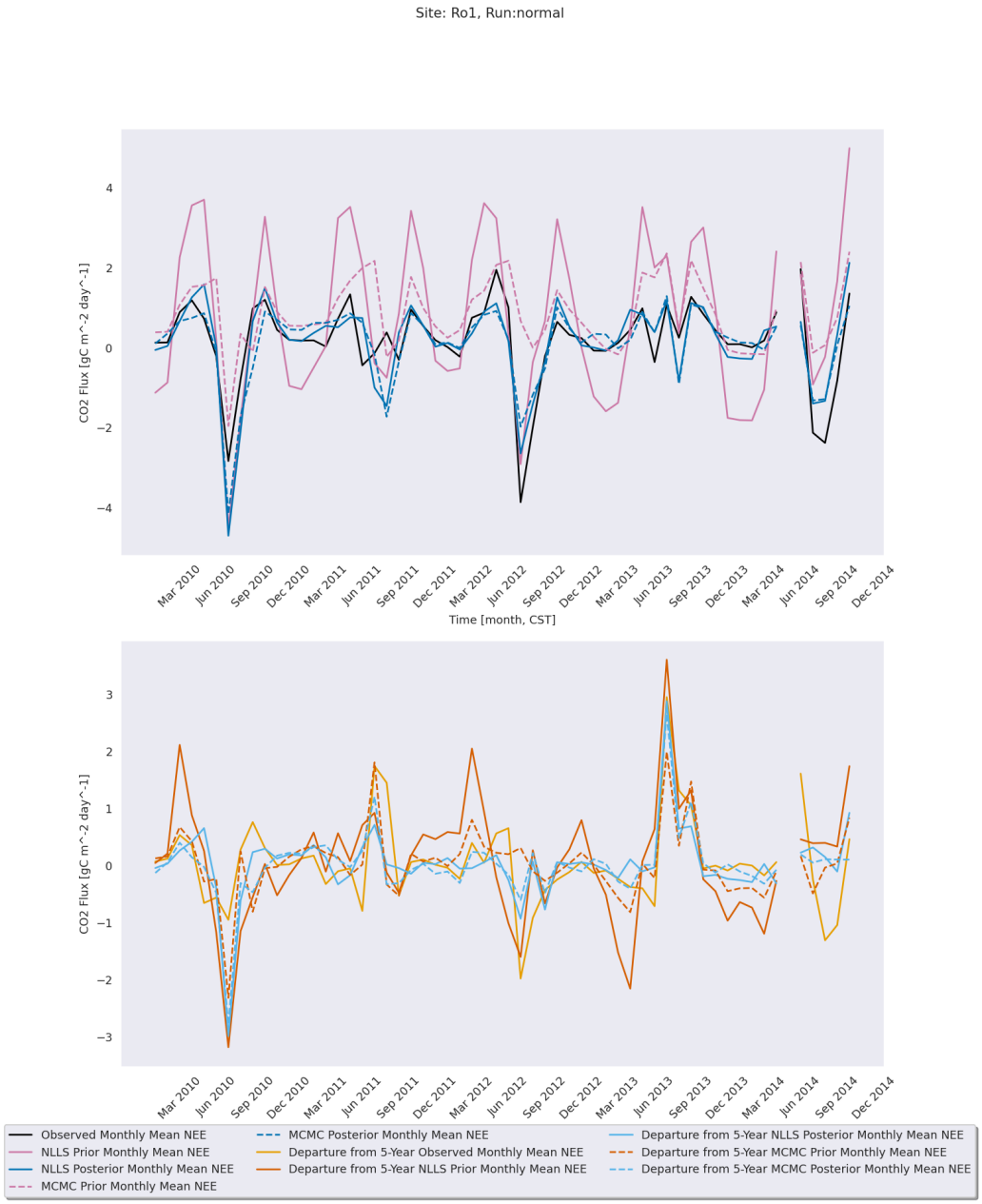

Figure C.49: Same as Figure C.46 but for the Ro1 AmeriFlux site.

C.4.3 α_2 Drop Experiment

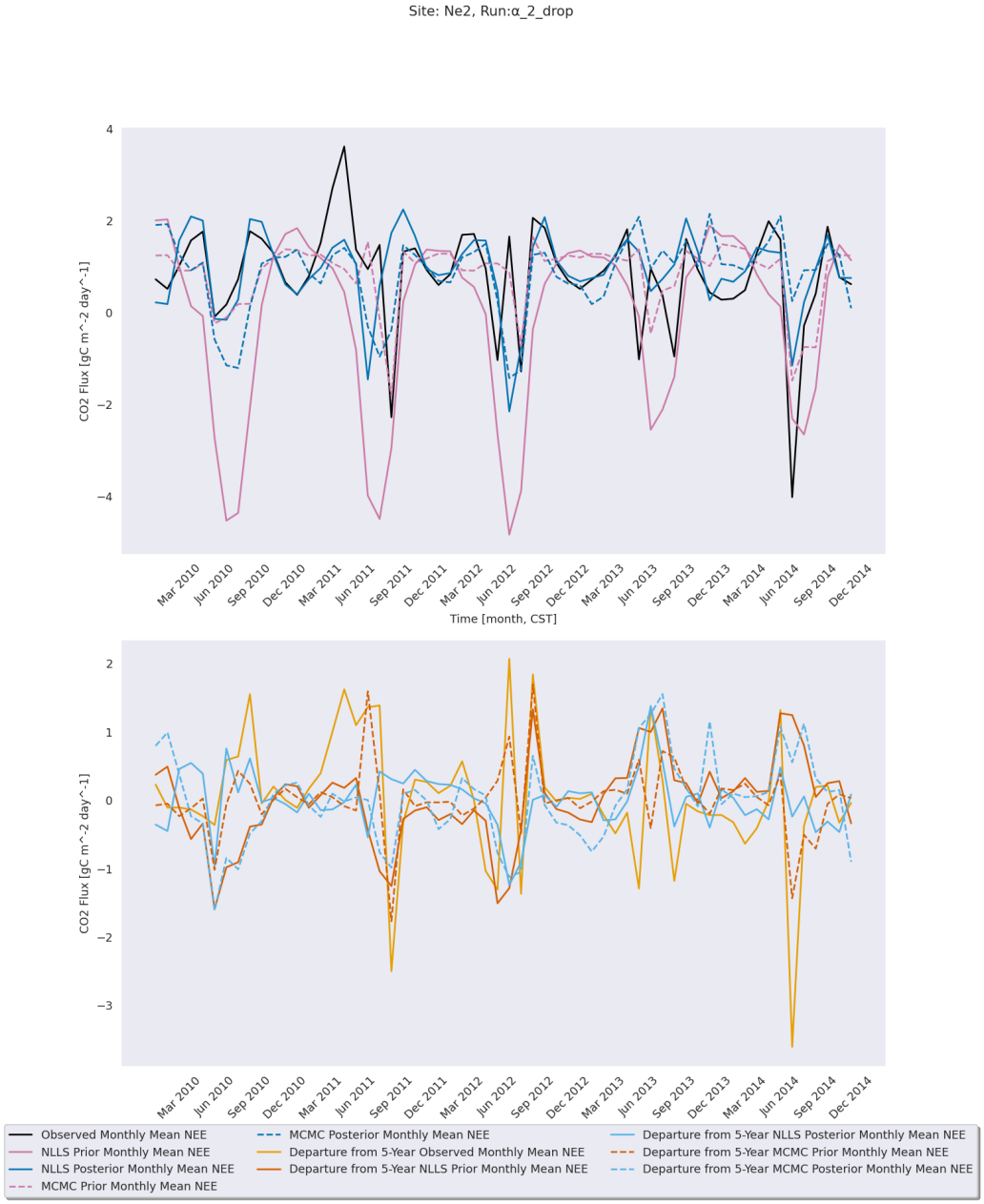

Figure C.50: Same as Figure 4.1 but for the α_2 parameter drop experiment.

Figure C.51: Same as Figure C.50 but for the Ne3 AmeriFlux site.

Figure C.52: Same as Figure C.50 but for the KM1 AmeriFlux site.

Figure C.53: Same as Figure C.50 but for the Ro1 AmeriFlux site.

C.4.4 k_3 Drop Experiment

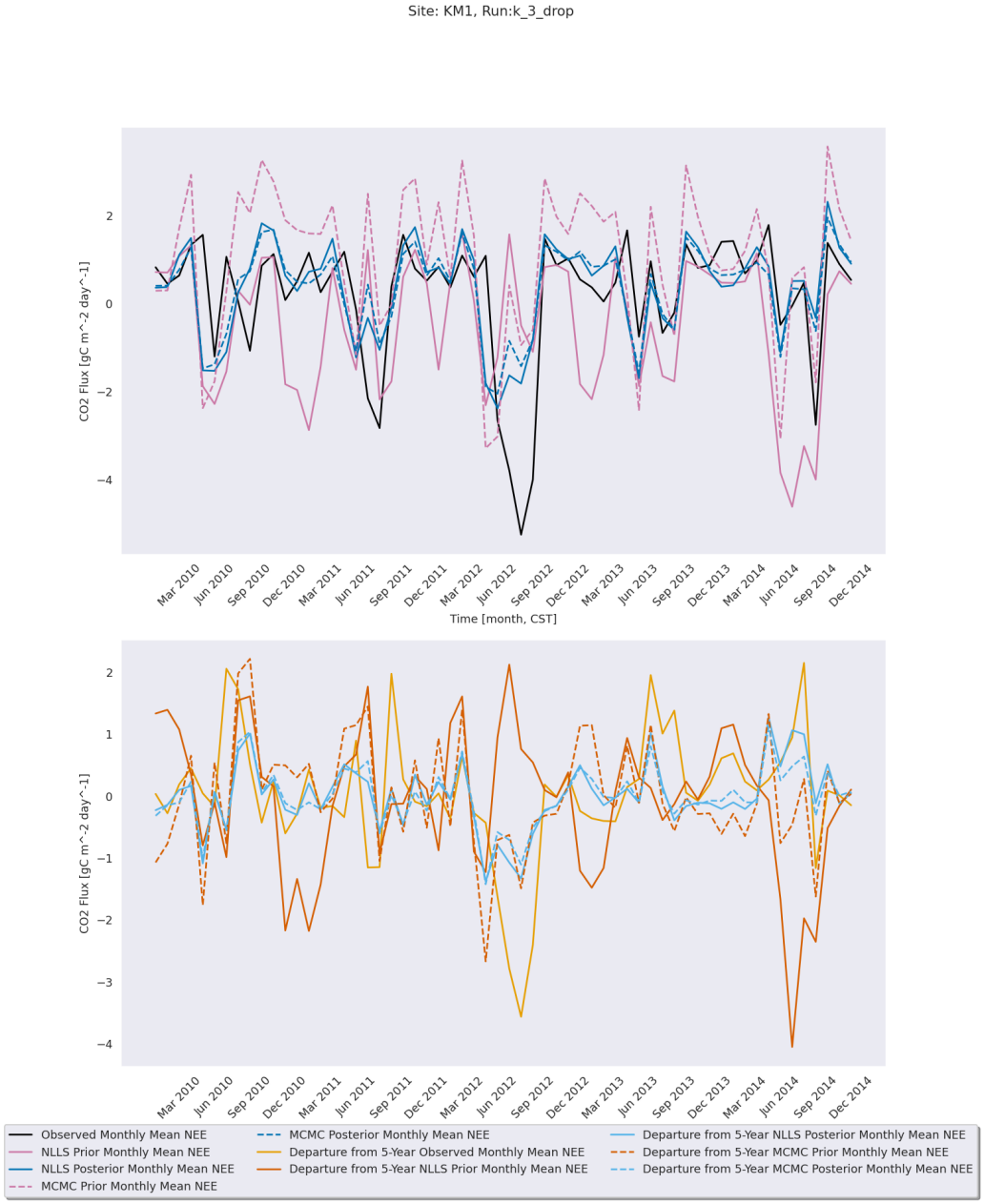

Figure C.54: Same as Figure 4.2 but for the KM1 AmeriFlux site.

Figure C.55: Same as Figure 4.2 but for the Ro1 AmeriFlux site.

C.4.5 λ Drop Experiment

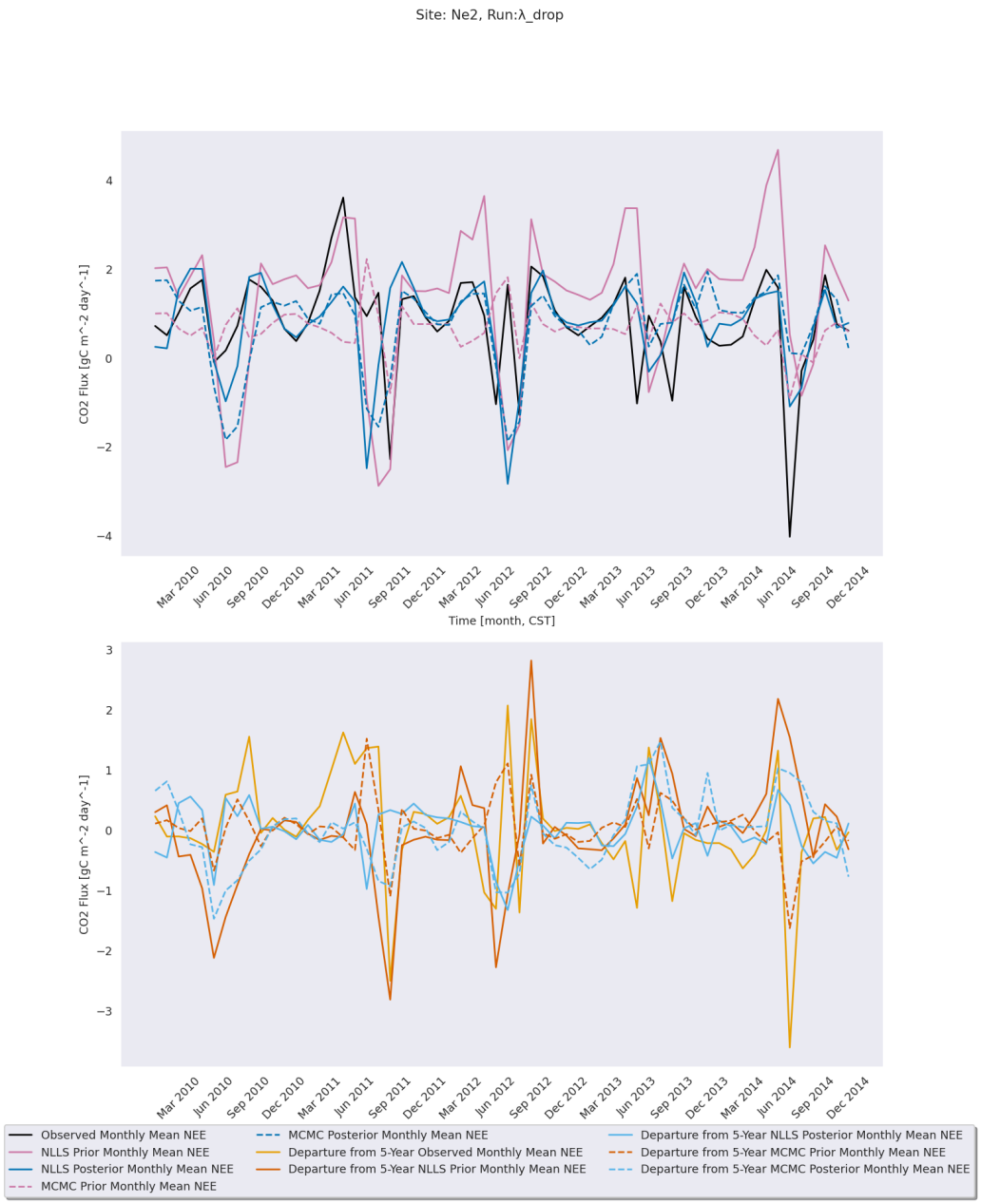

Figure C.56: Same as Figure 4.1 but for the λ parameter drop experiment.

Figure C.57: Same as Figure C.56 but for the Ne3 AmeriFlux site.

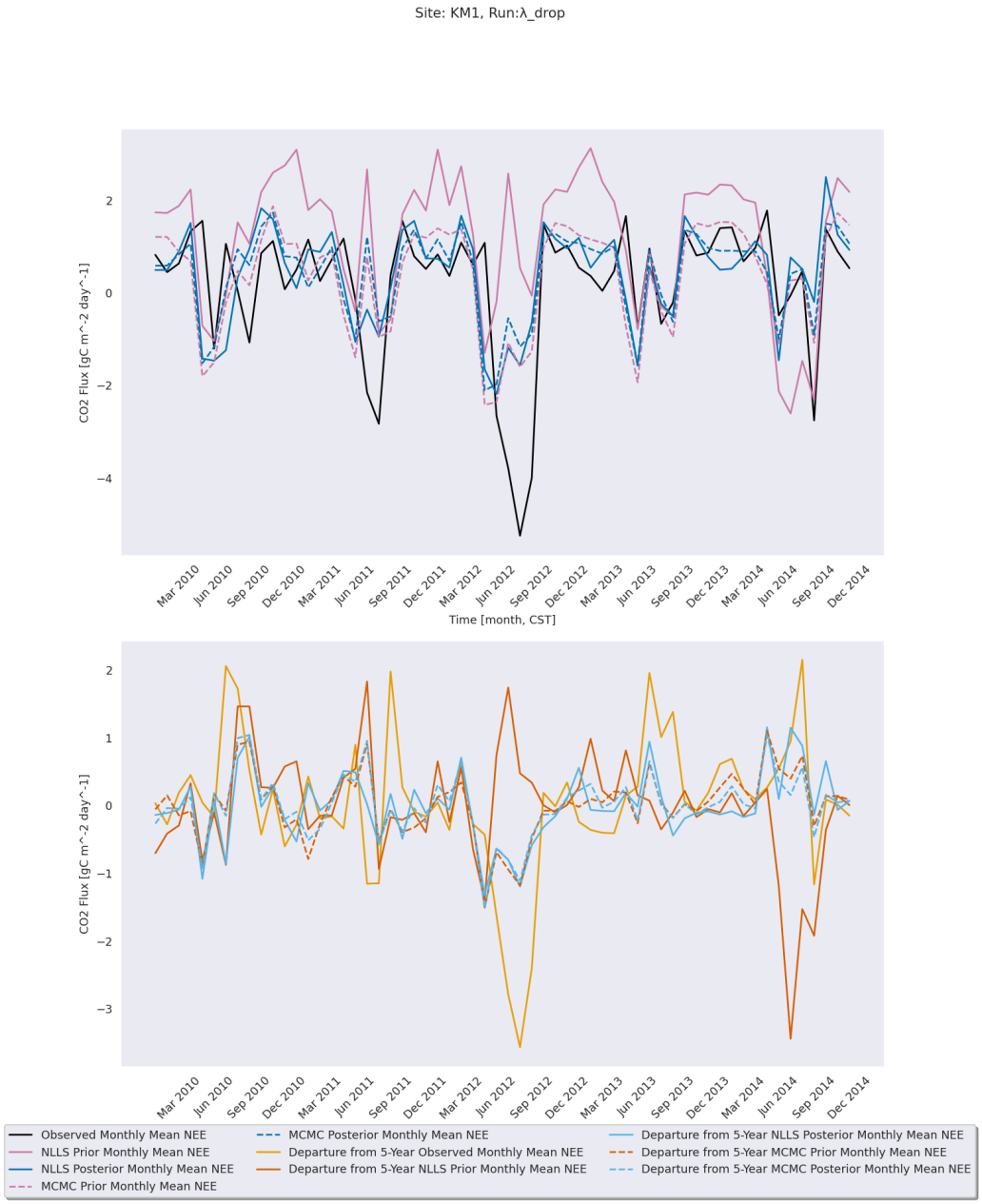

Figure C.58: Same as Figure C.56 but for the KM1 AmeriFlux site.

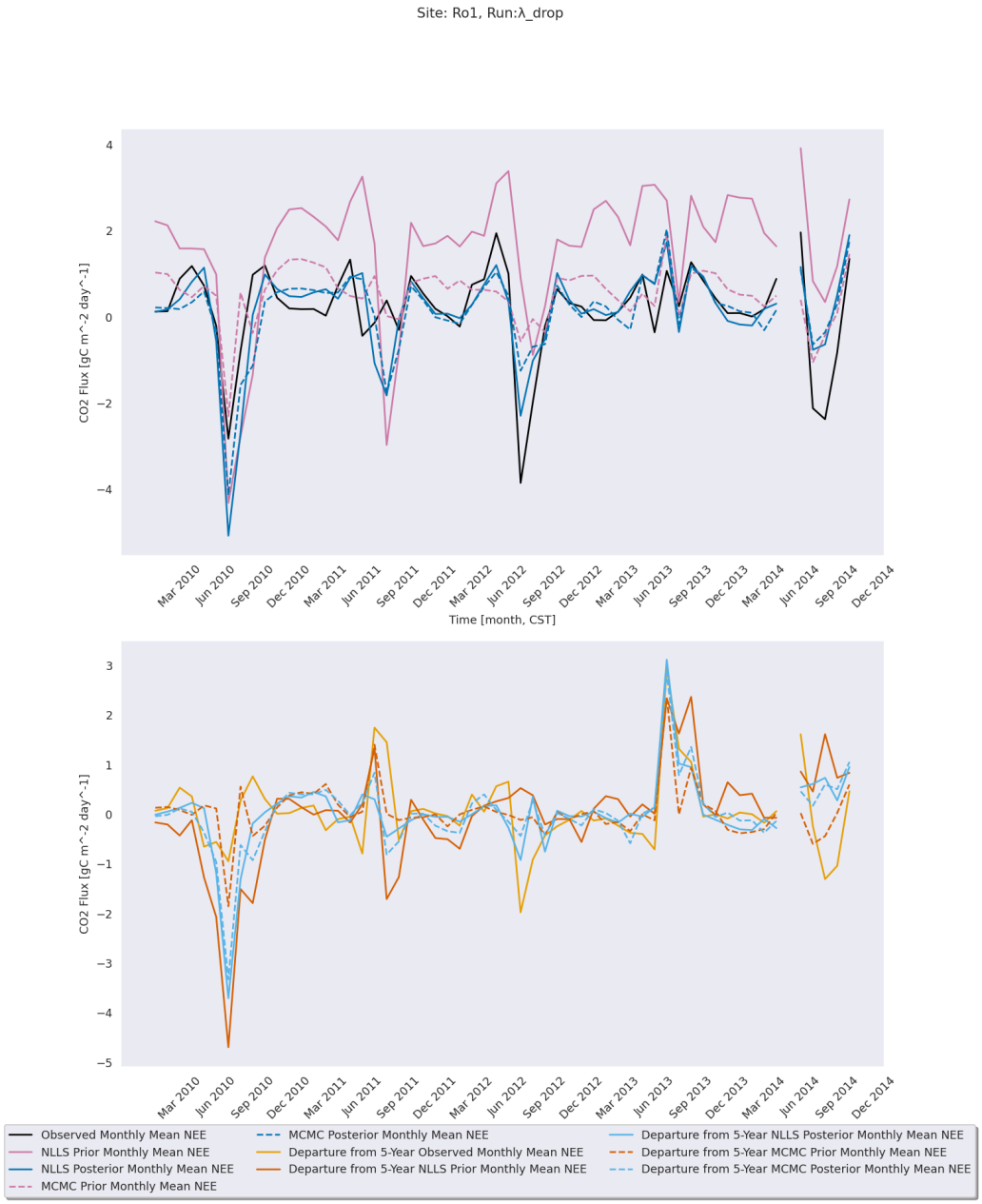

Figure C.59: Same as Figure C.56 but for the Ro1 AmeriFlux site.

C.4.6 PAR_0 Drop Experiment

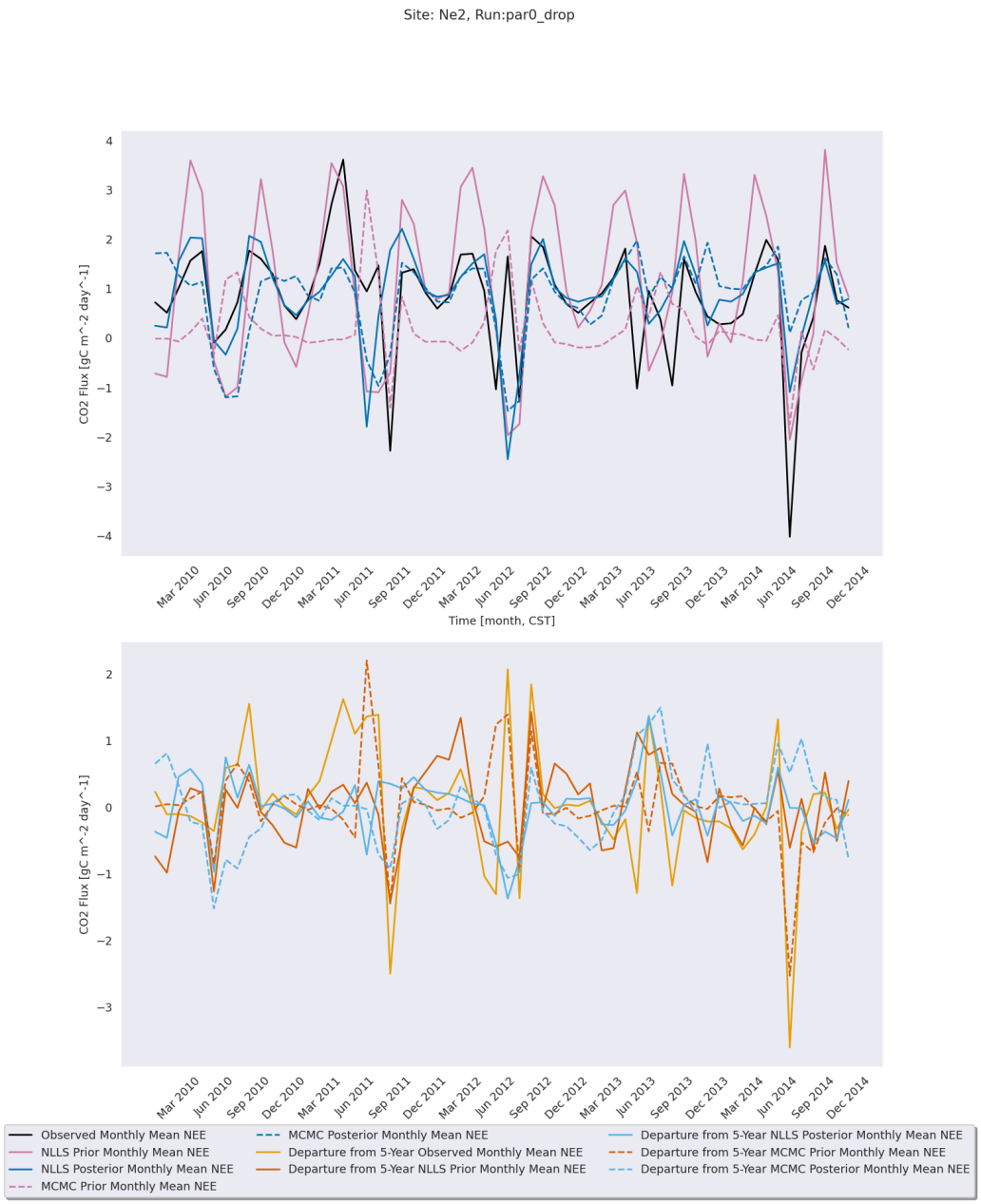

Figure C.60: Same as Figure 4.1 but for the PAR_0 parameter drop experiment.

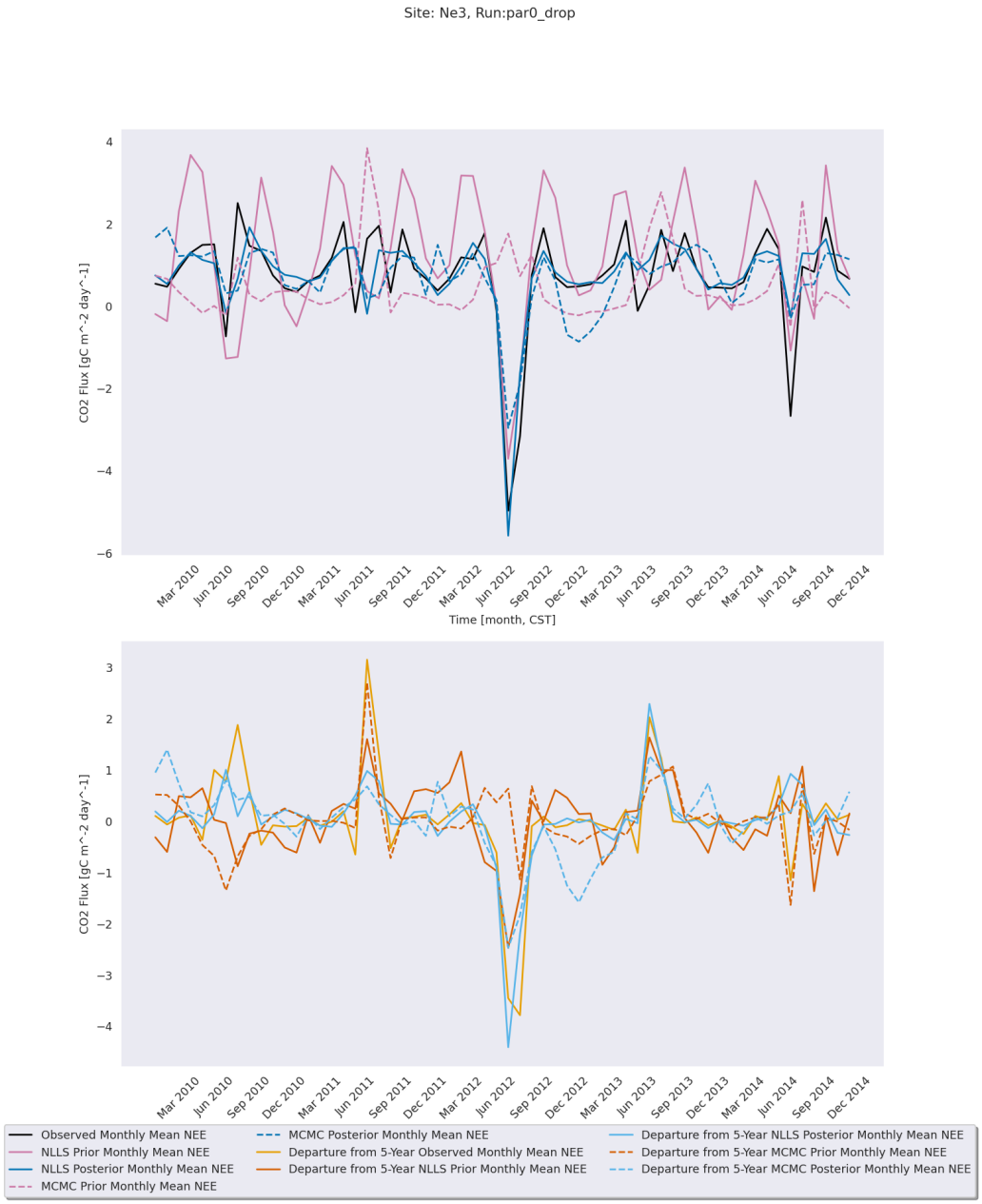

Figure C.61: Same as Figure C.60 but for the Ne3 AmeriFlux site.

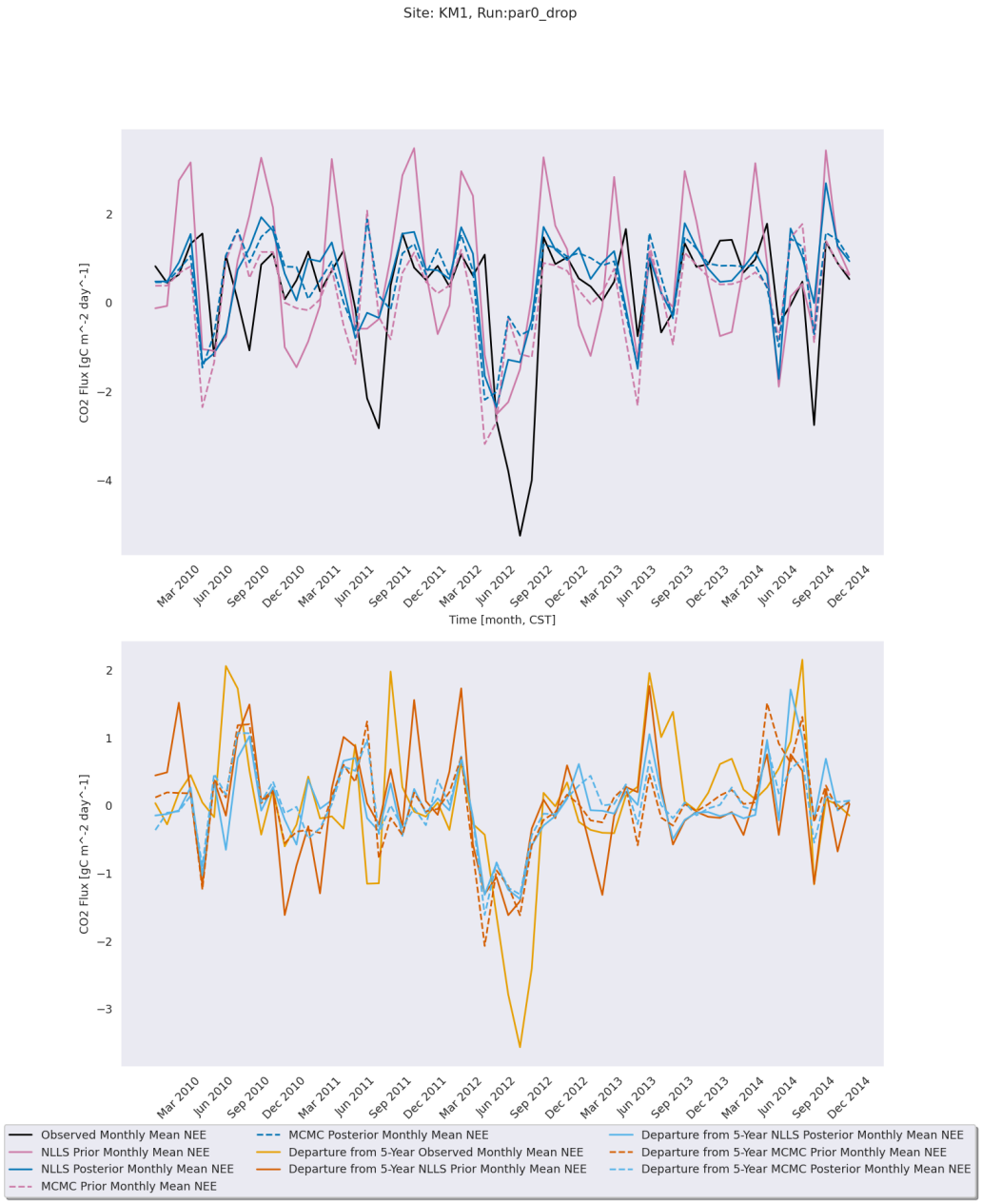

Figure C.62: Same as Figure C.60 but for the KM1 AmeriFlux site.

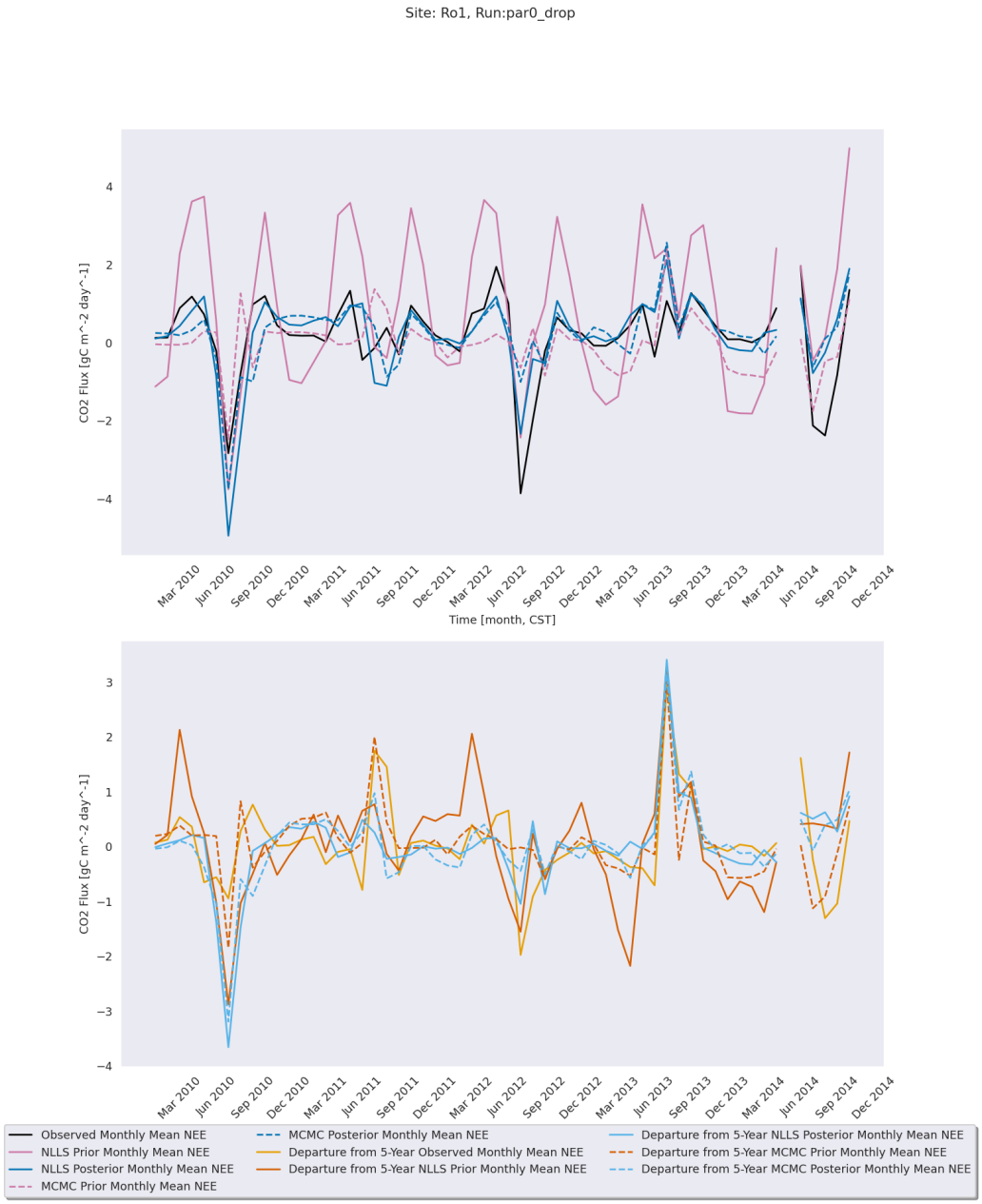

Figure C.63: Same as Figure C.60 but for the Ro1 AmeriFlux site.

Appendix D

Seasonal Analysis

D.1 Whole Data Set Simultaneously

D.1.1 Winter (DJF)

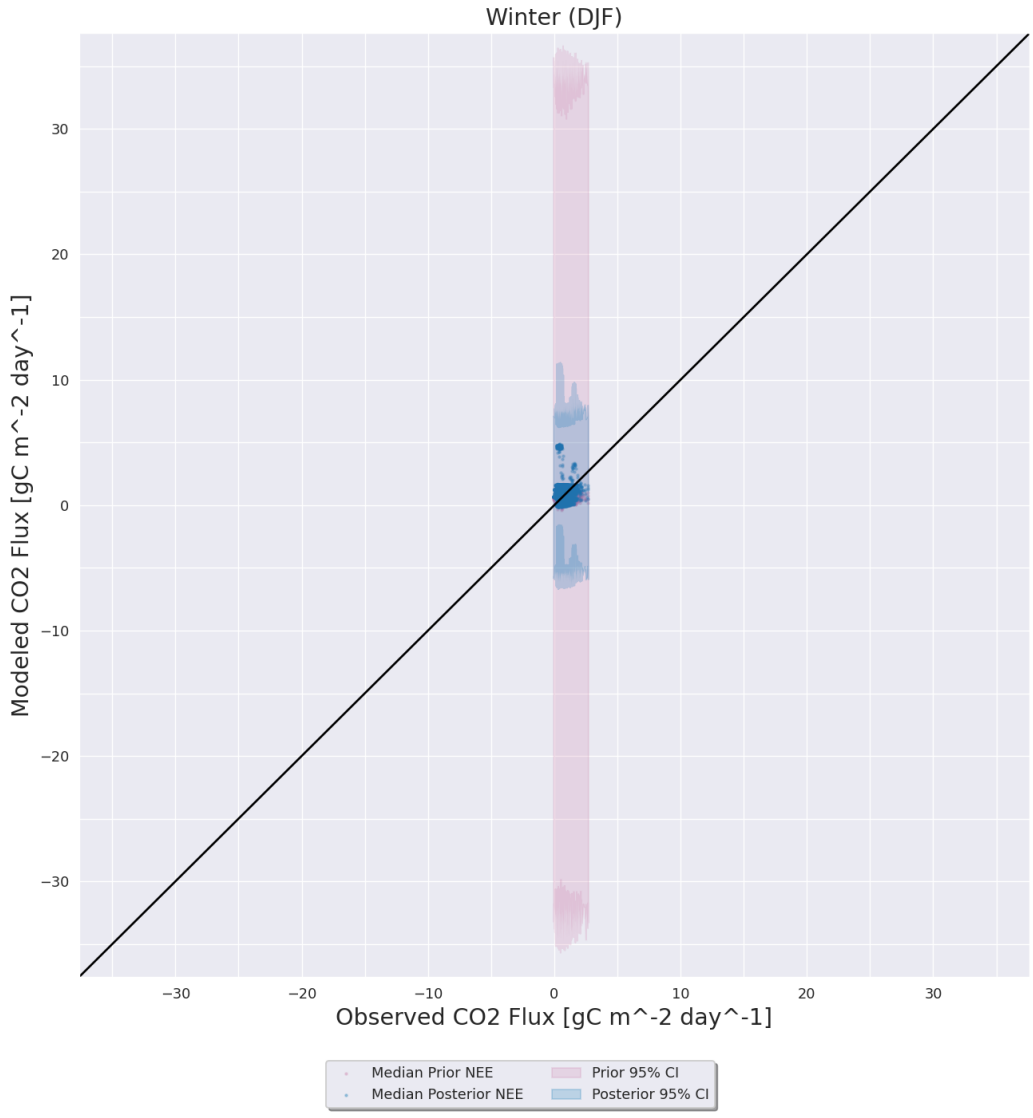

Figure D.1: Same as 4.4 except for during the winter (DJF) months.

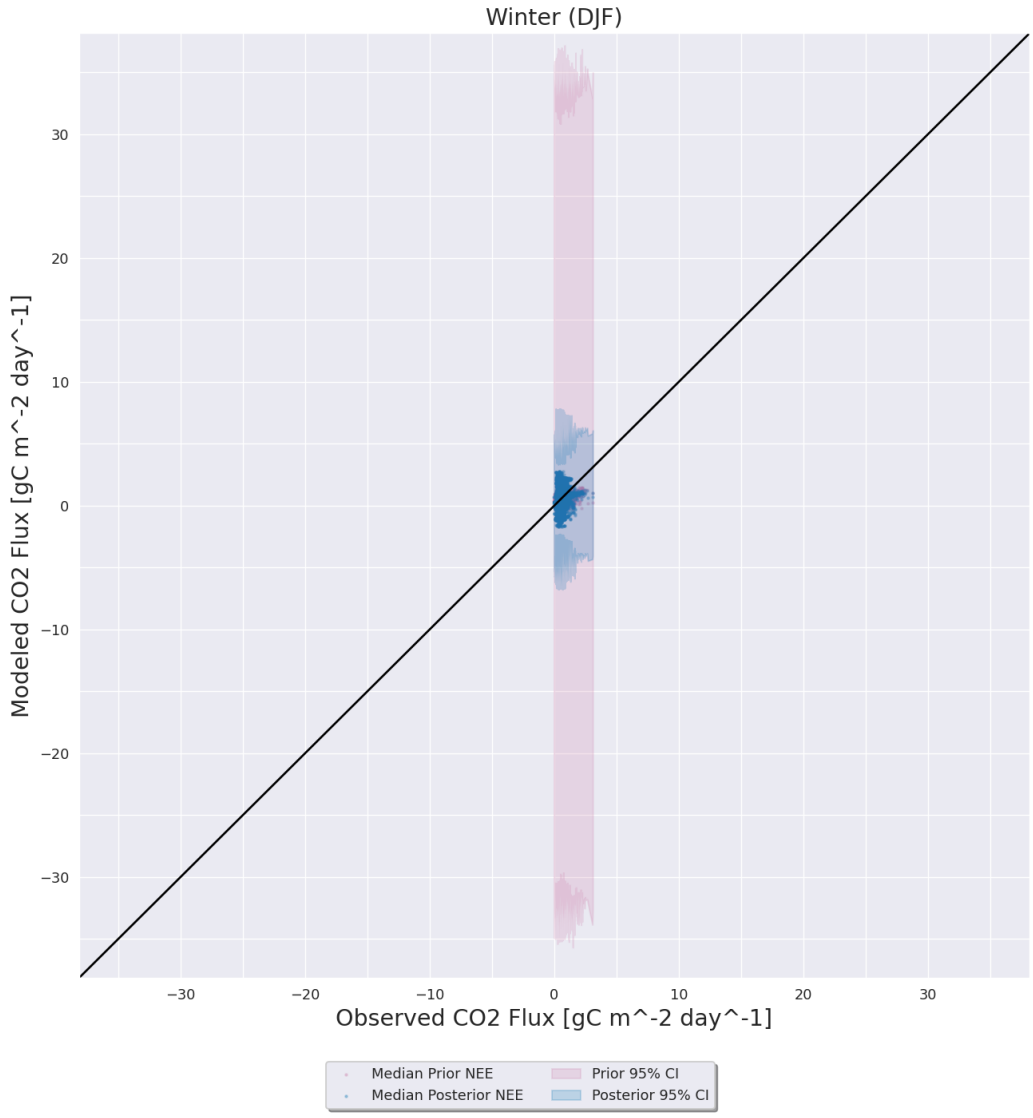

Figure D.2: Same as D.1 except for the Ne3 AmeriFlux site.

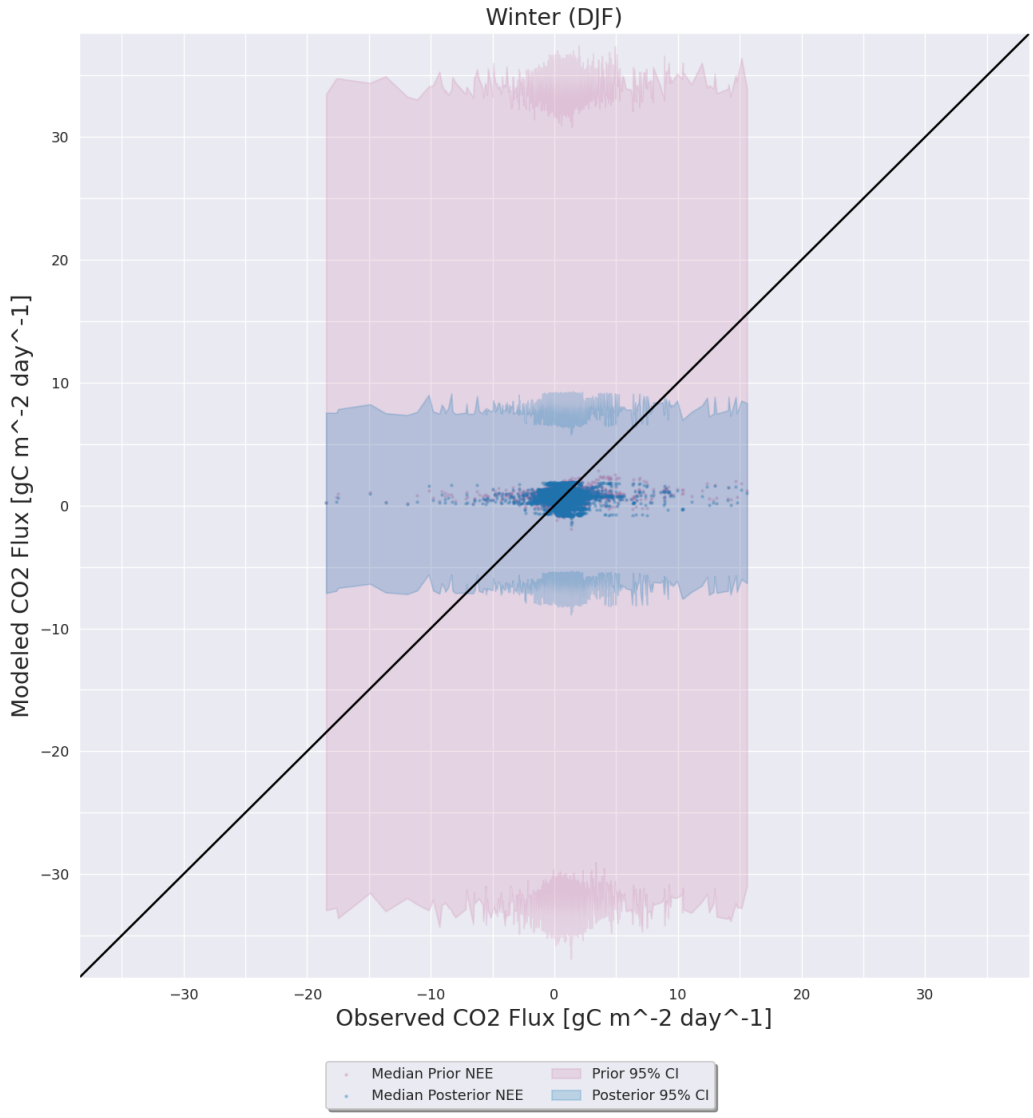

Figure D.3: Same as D.1 except for the KM1 AmeriFlux site.

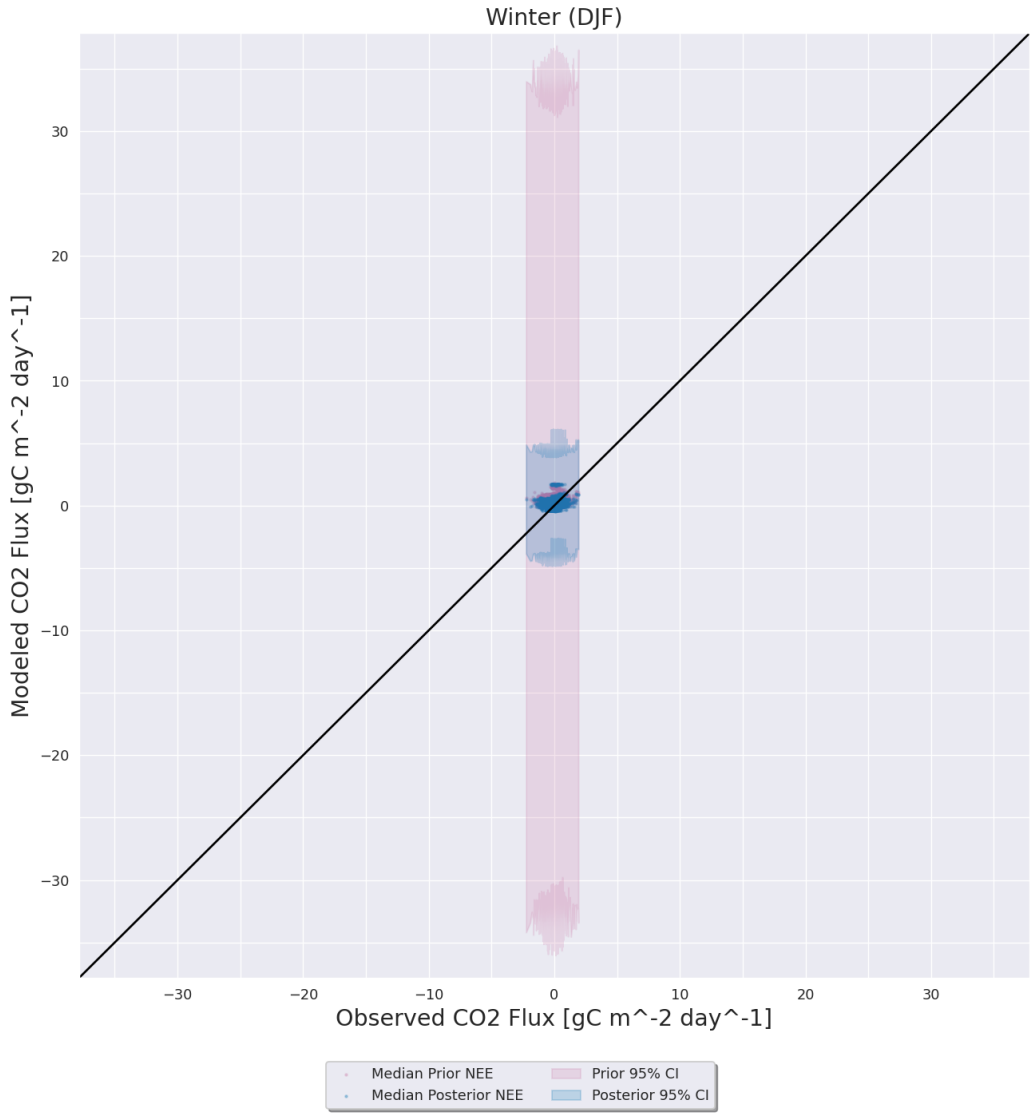

Figure D.4: Same as D.1 except for the Ro1 AmeriFlux site.

D.1.2 Spring (MAM)

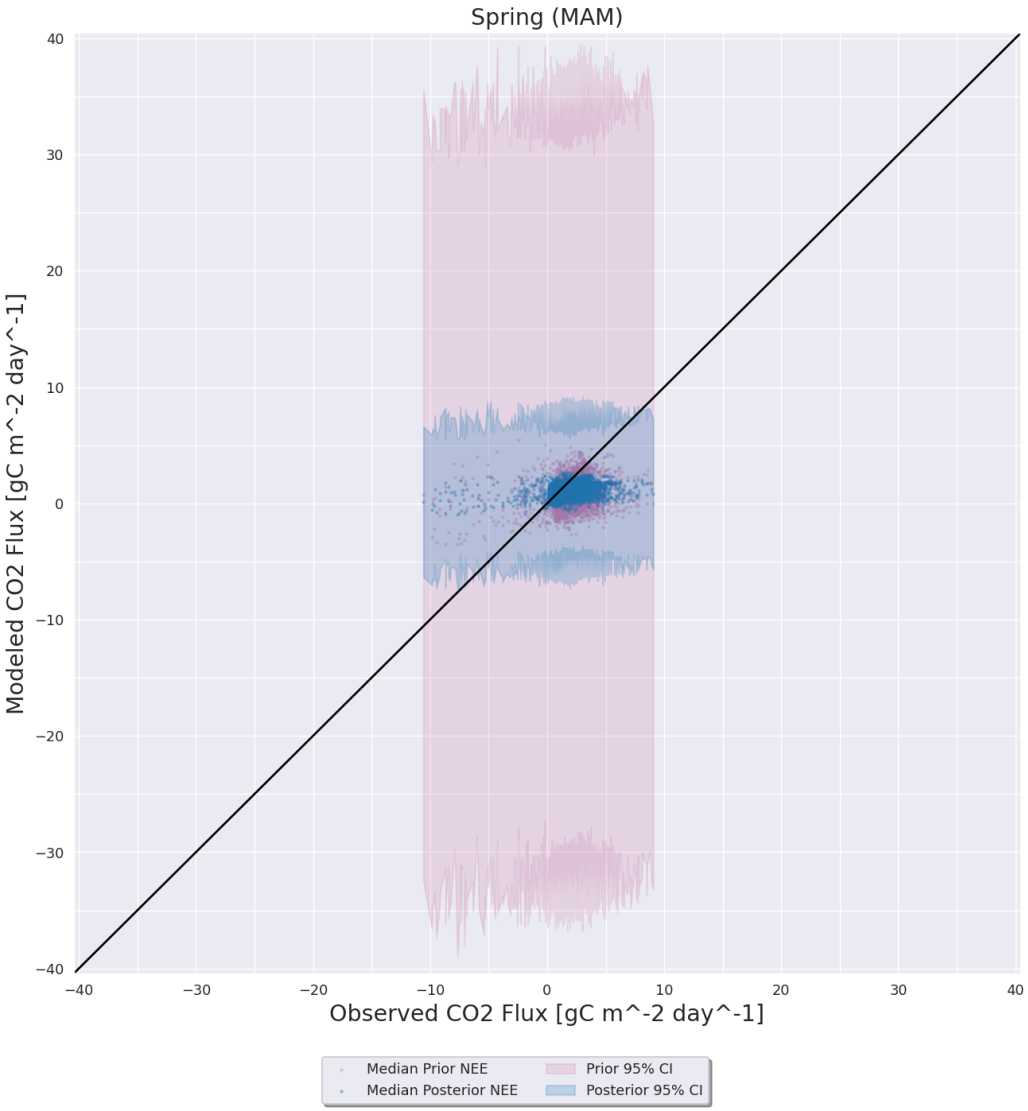

Figure D.5: Same as 4.4 except for during the spring (MAM) months.

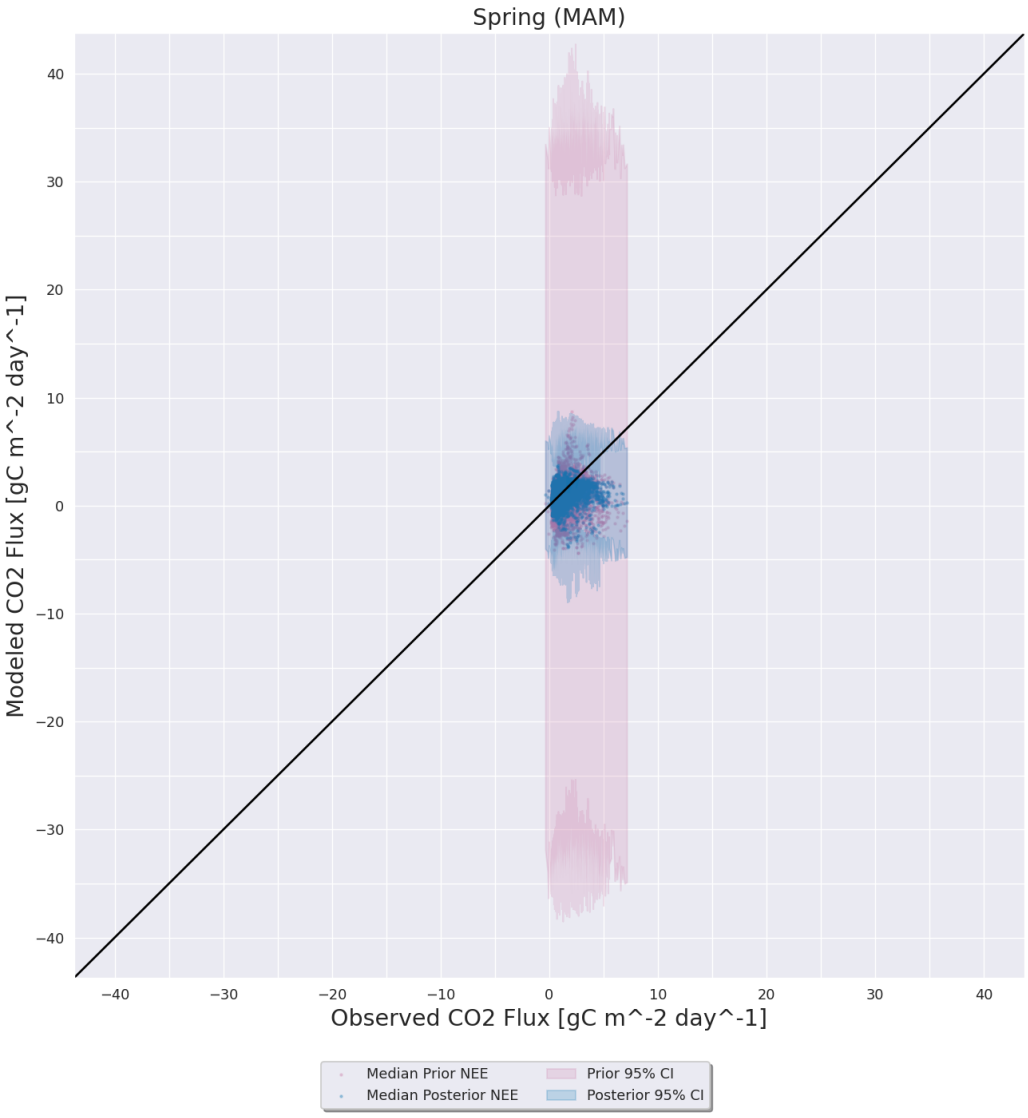

Figure D.6: Same as D.5 except for the Ne3 AmeriFlux site.

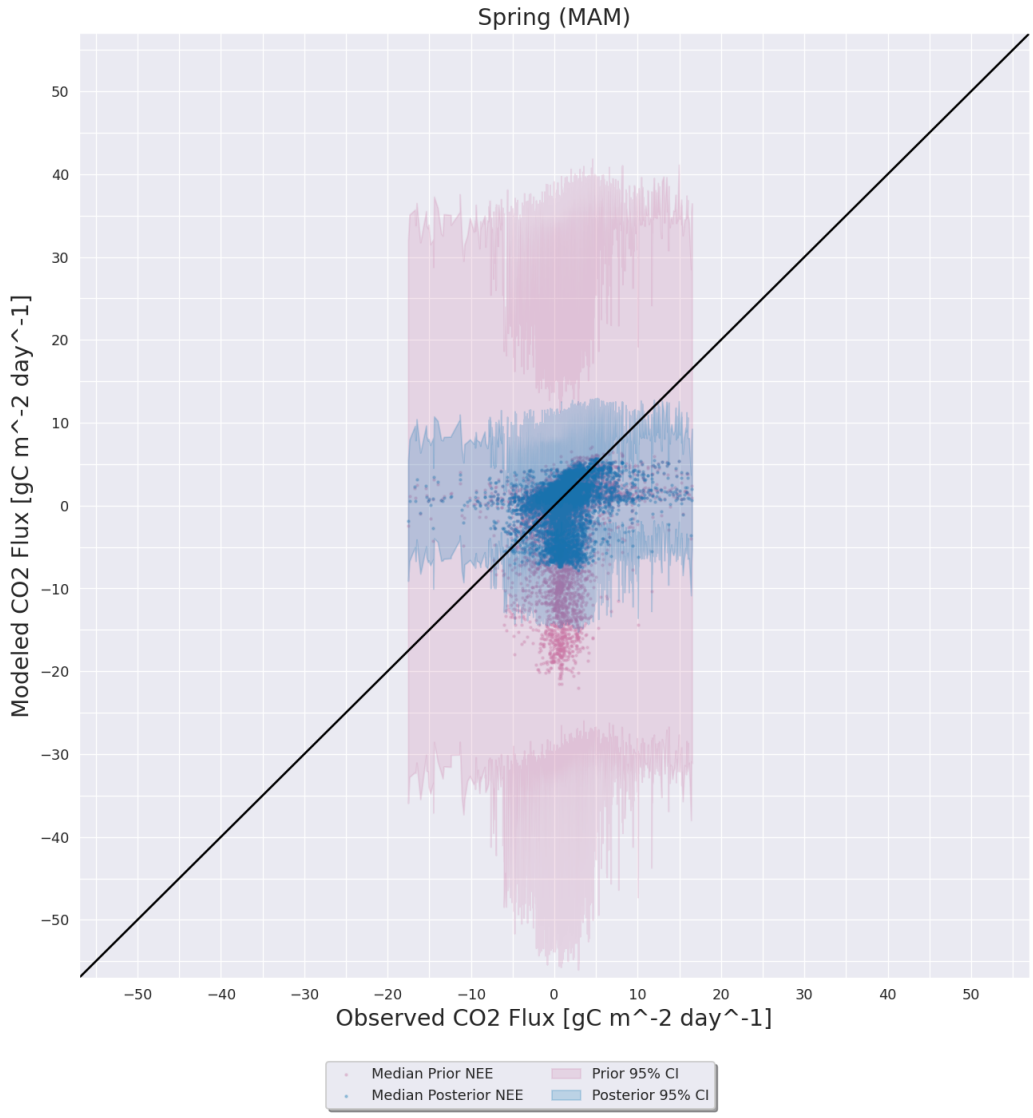

Figure D.7: Same as D.5 except for the KM1 AmeriFlux site.

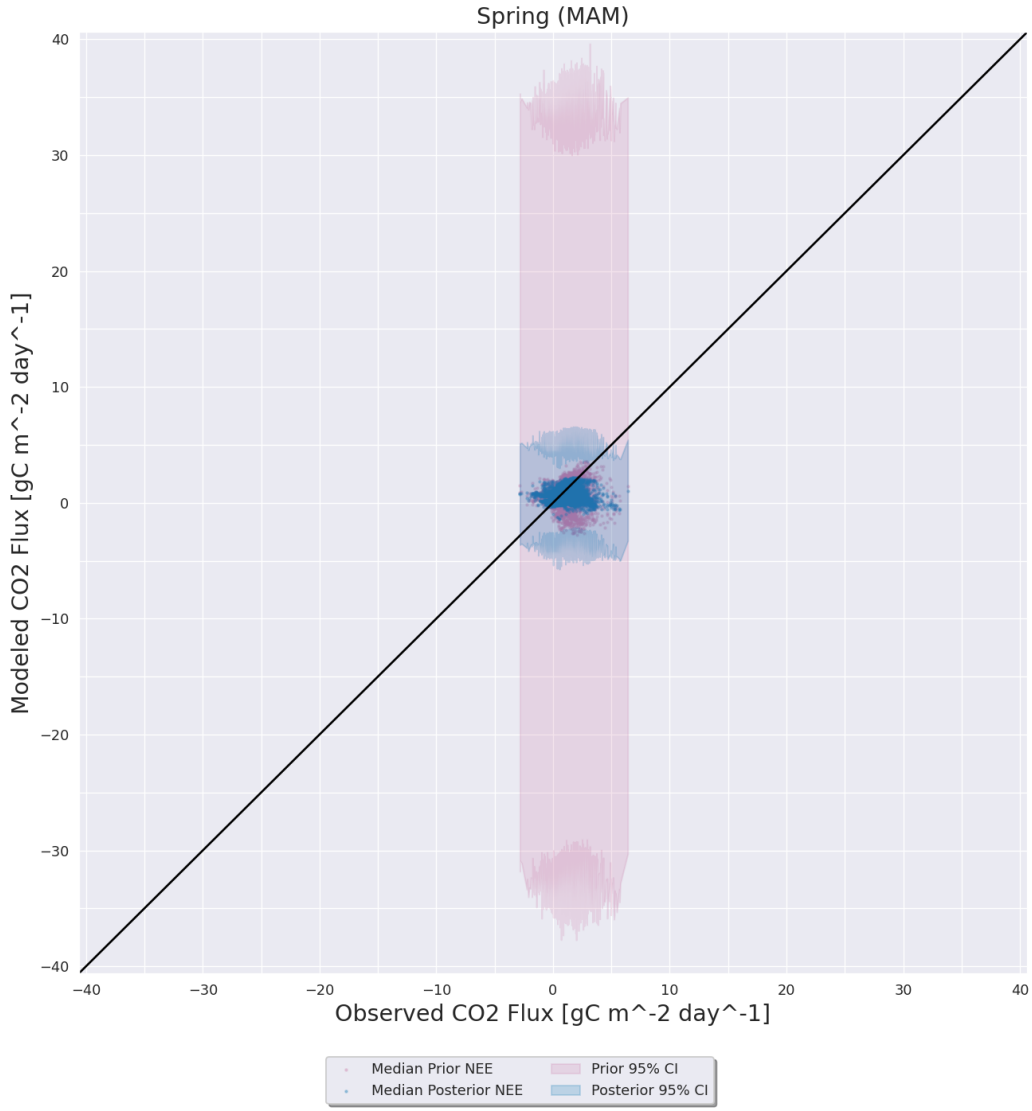

Figure D.8: Same as D.5 except for the Ro1 AmeriFlux site.

D.1.3 Summer (JJA)

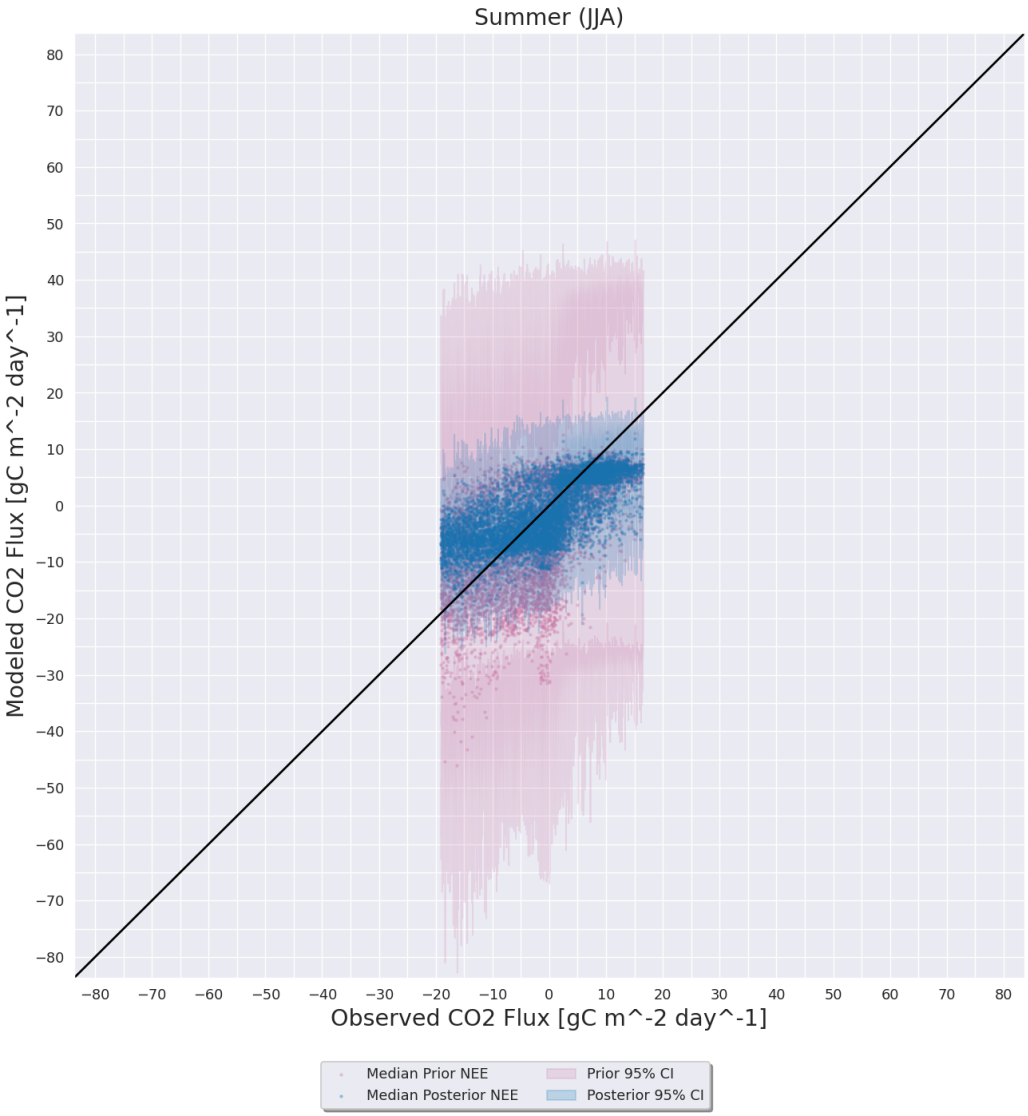

Figure D.9: Same as 4.4 except for the KM1 AmeriFlux site.

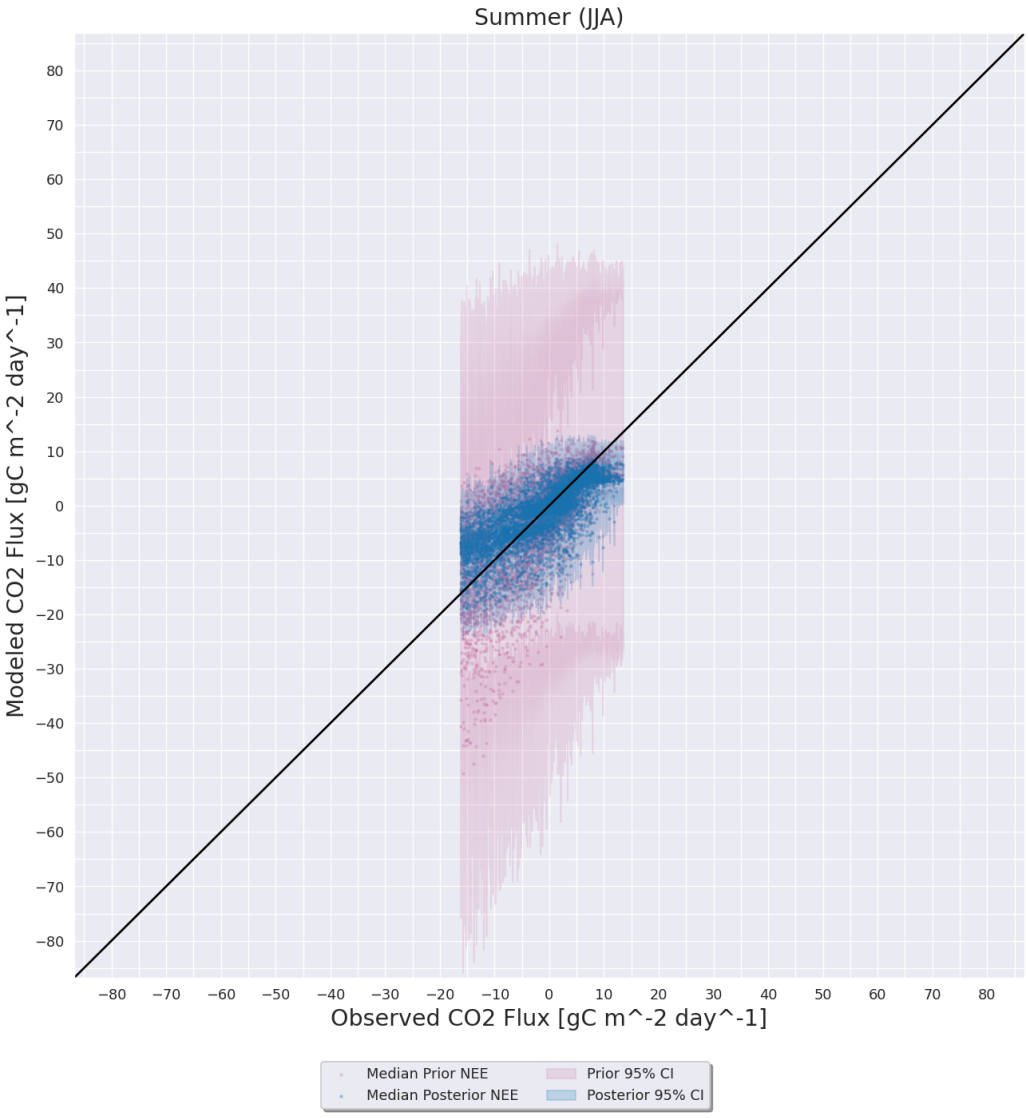

Figure D.10: Same as 4.4 except for the Ro1 AmeriFlux site.

D.1.4 Autumn (SON)

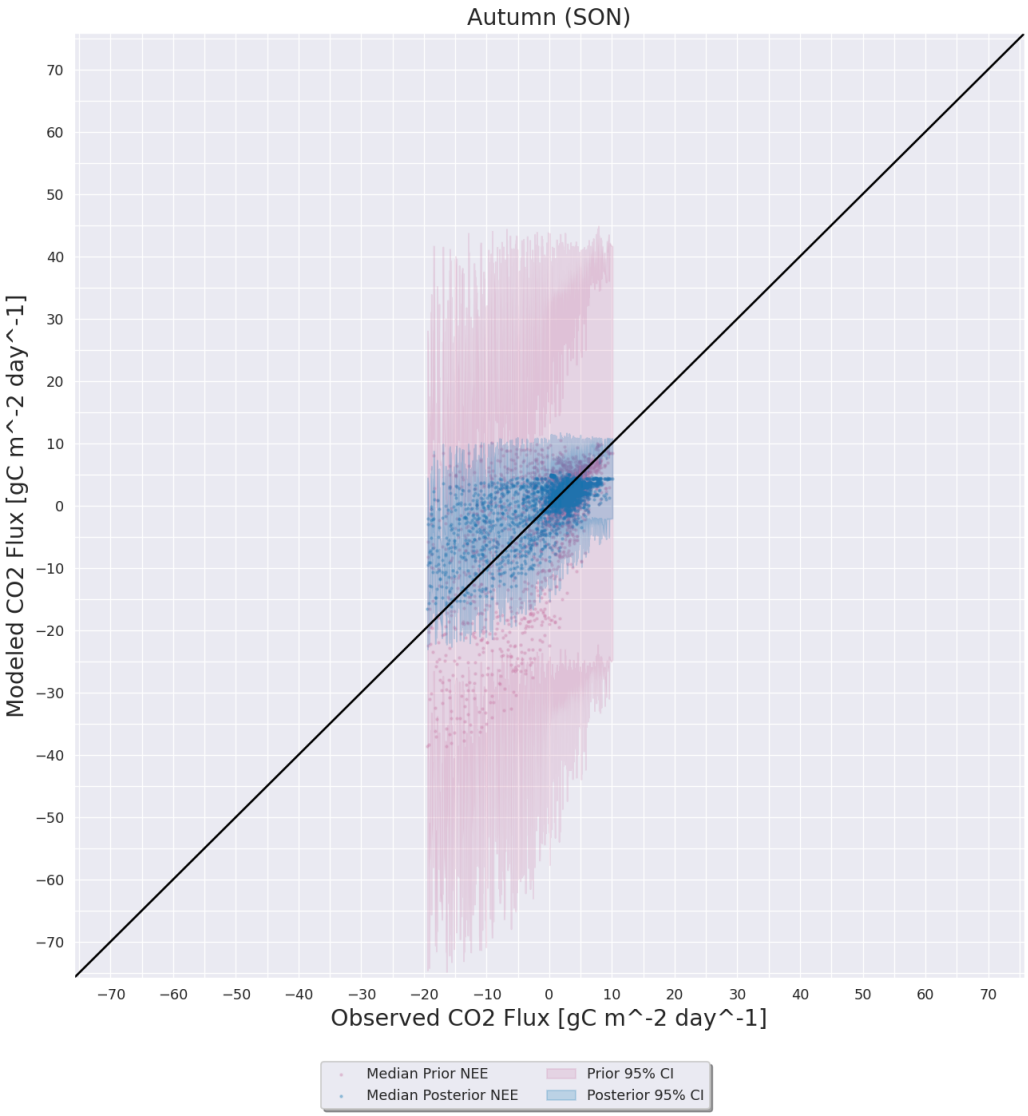

Figure D.11: Same as 4.4 except for during the autumn (SON) months.

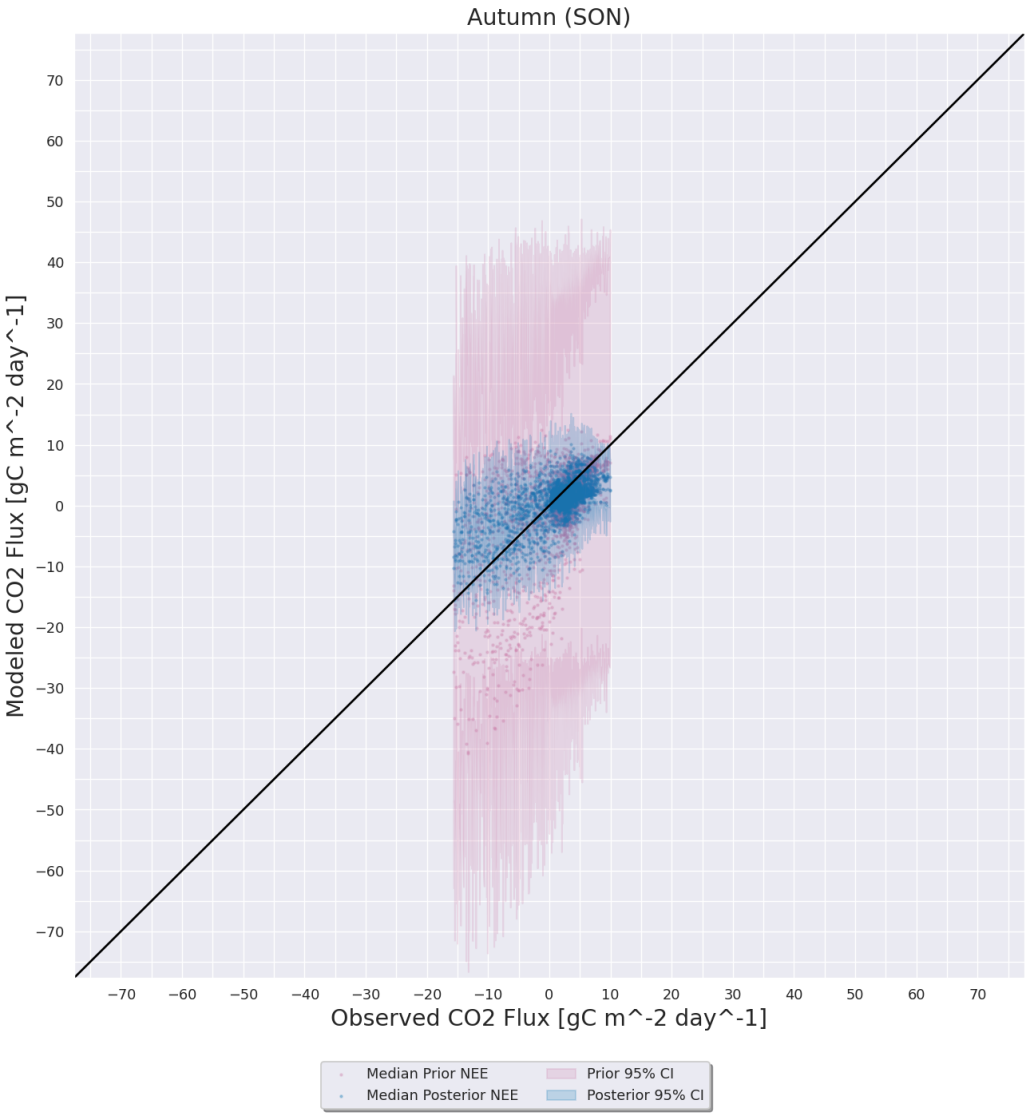

Figure D.12: Same as D.11 except for the Ne3 AmeriFlux site.

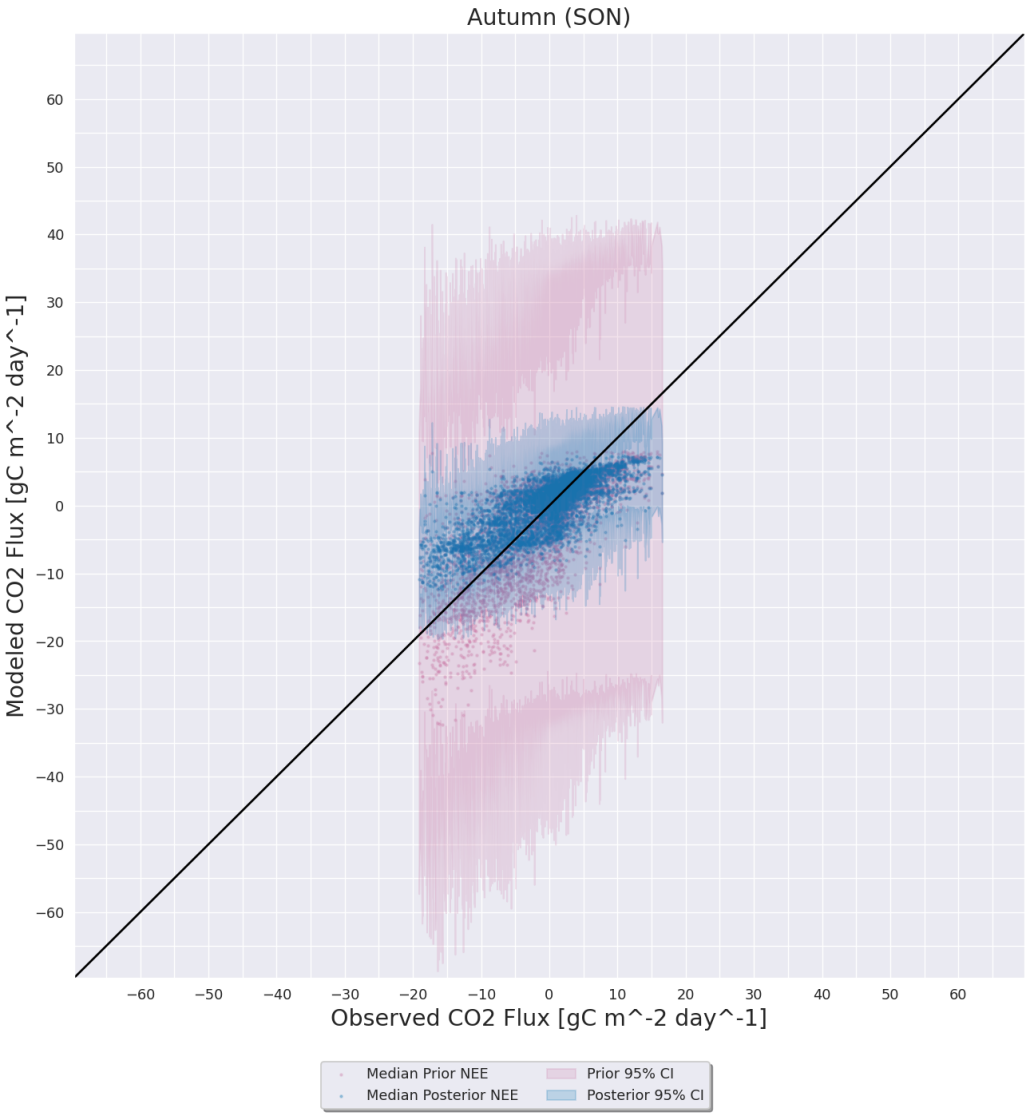

Figure D.13: Same as D.11 except for the KM1 AmeriFlux site.

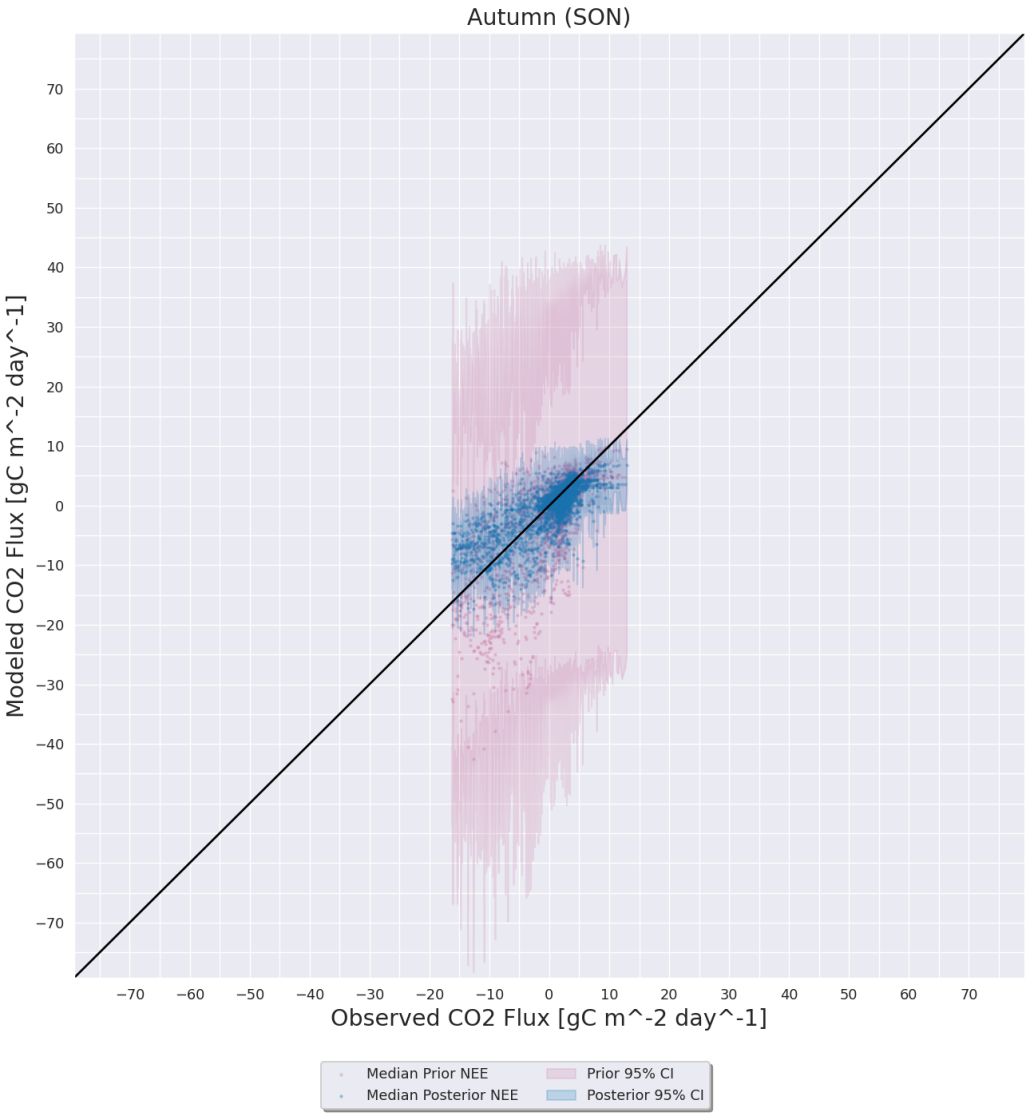

Figure D.14: Same as D.11 except for the Ro1 AmeriFlux site.

D.2 ER/GEE Separately

D.2.1 Winter (DJF)

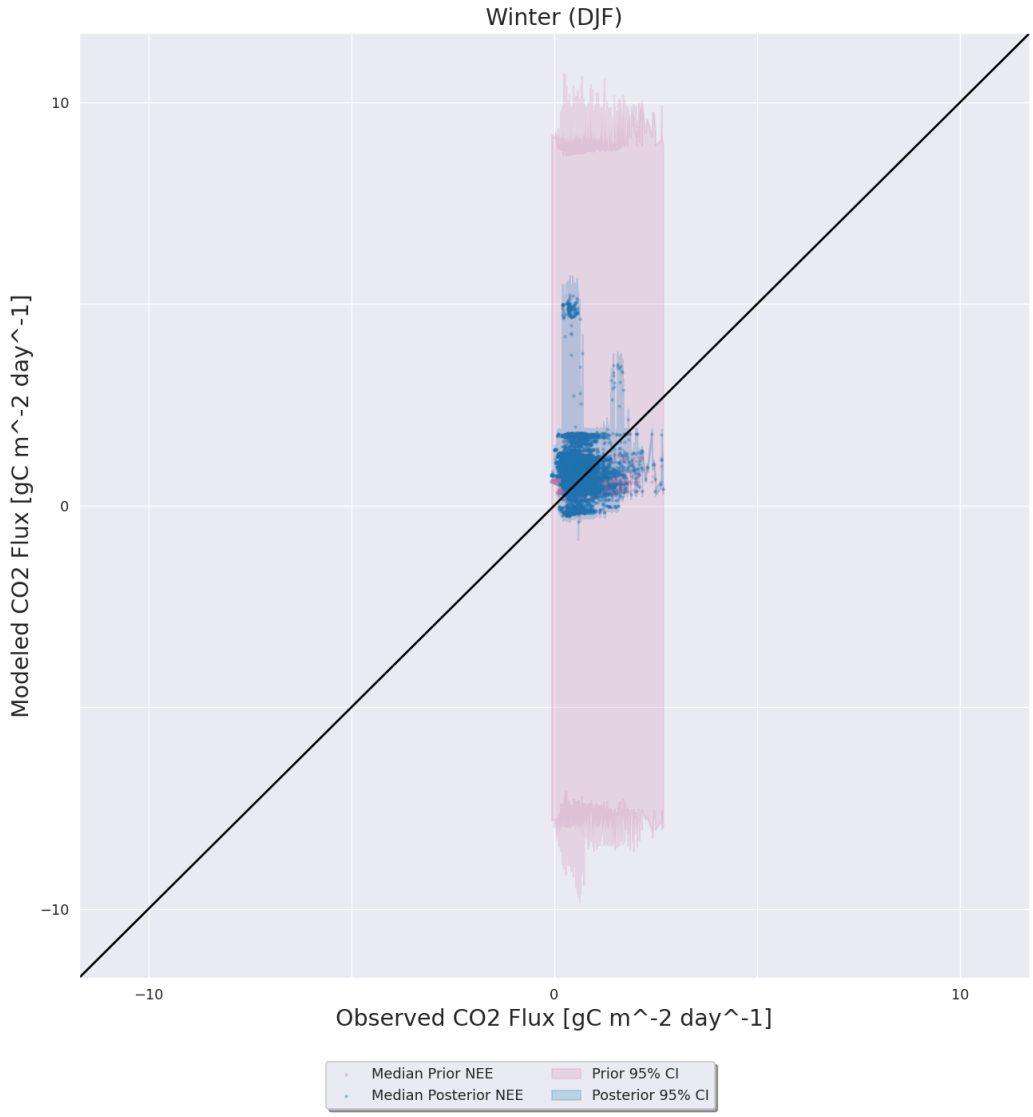

Figure D.15: Same as D.1 except for fitting ER and GEE separately.

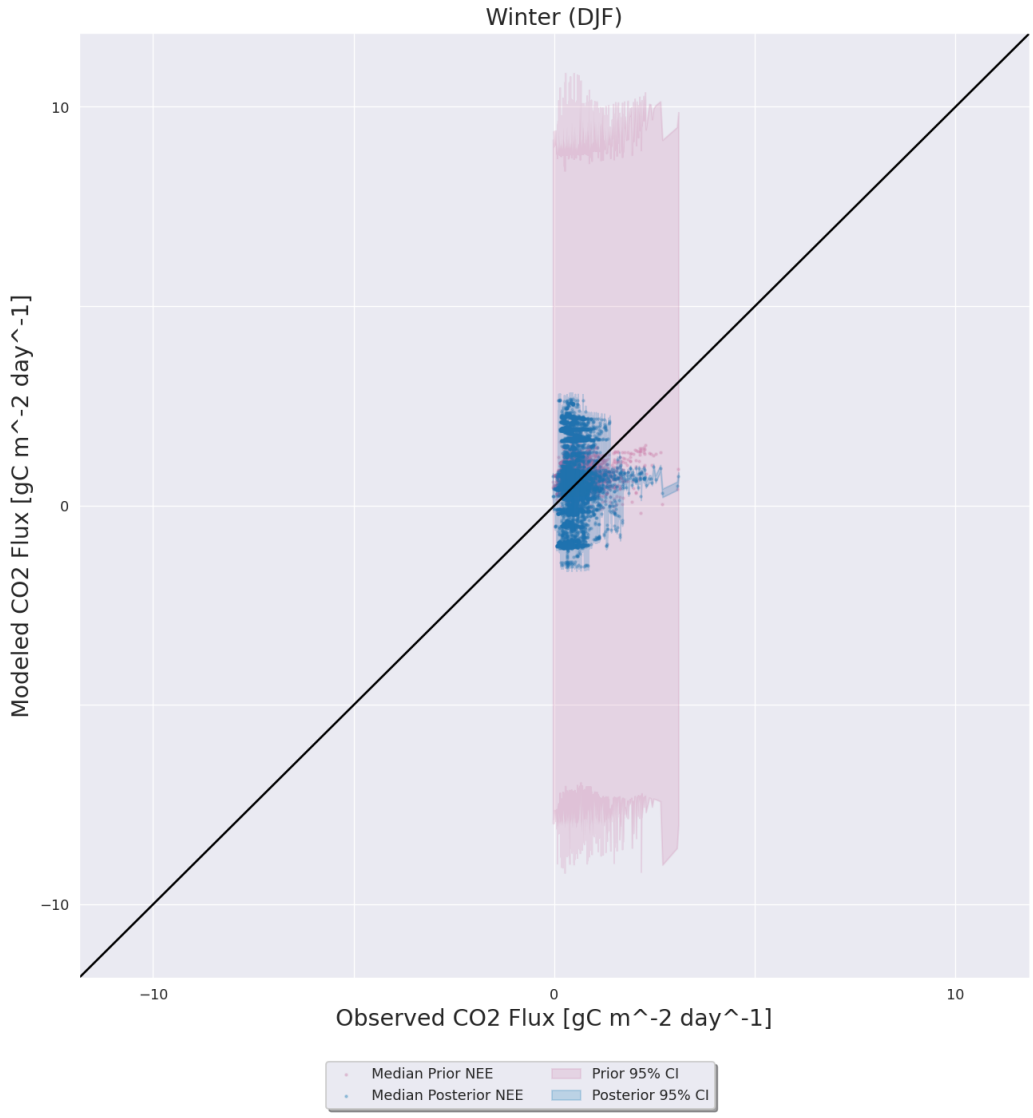

Figure D.16: Same as D.15 except for the Ne3 AmeriFlux site.

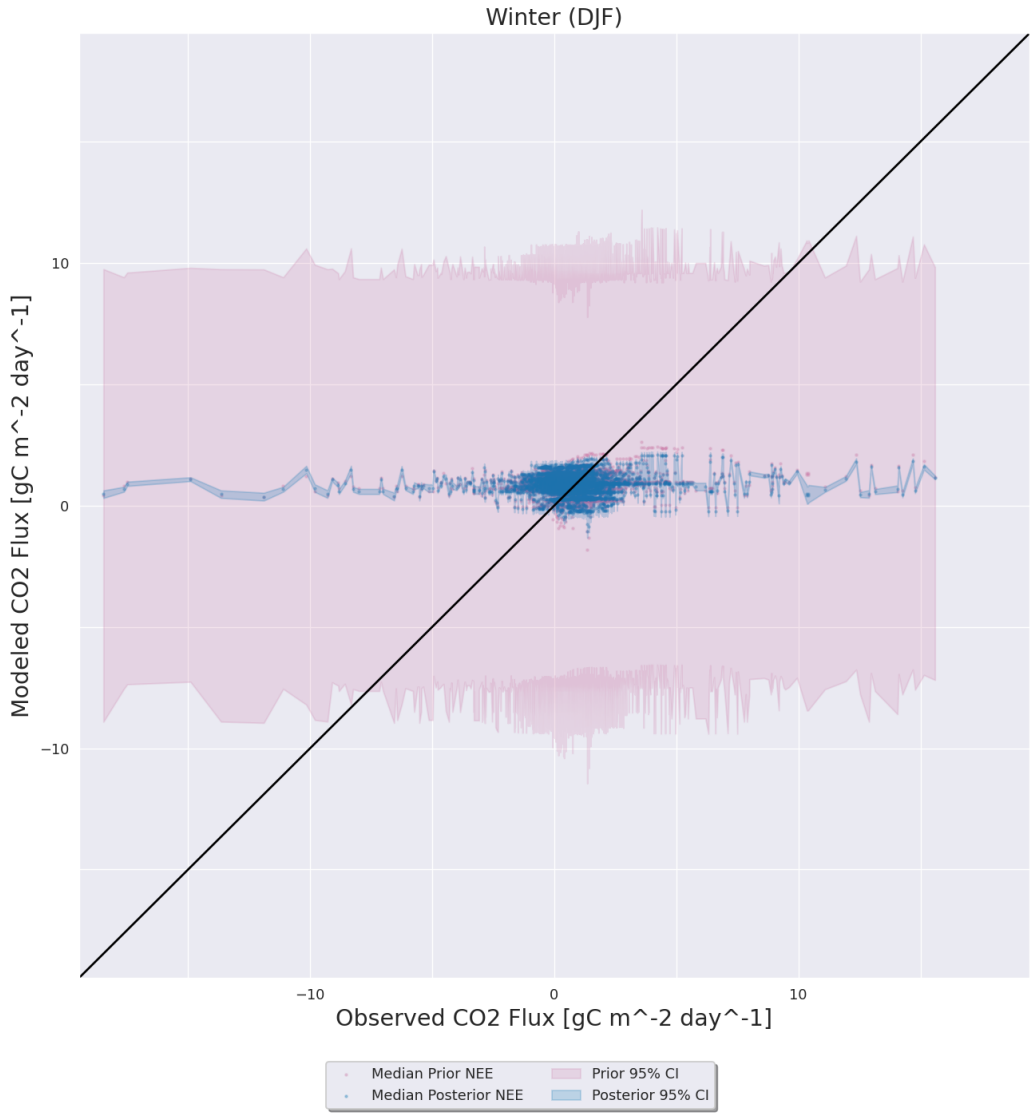

Figure D.17: Same as D.15 except for the KM1 AmeriFlux site.

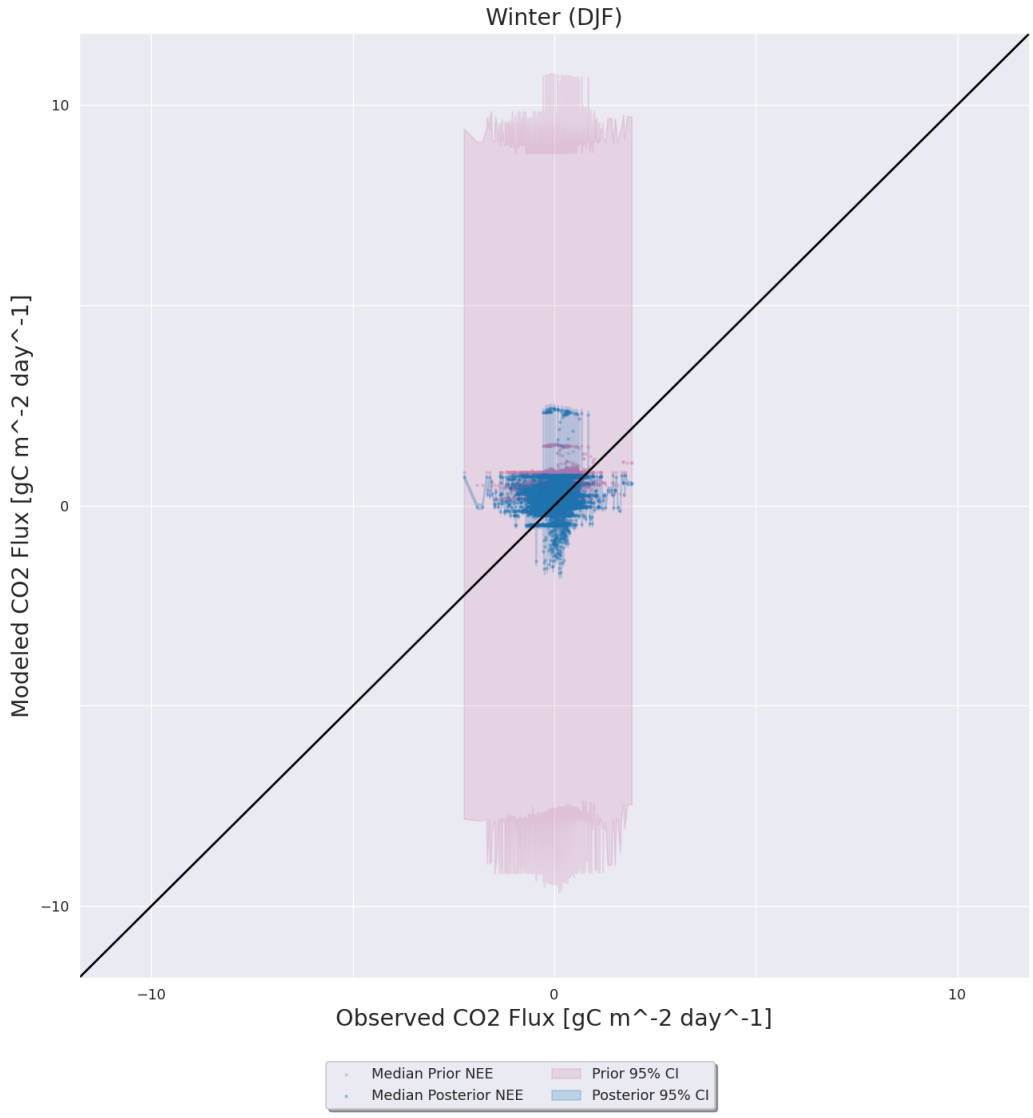

Figure D.18: Same as D.15 except for the Ro1 AmeriFlux site.

D.2.2 Spring (MAM)

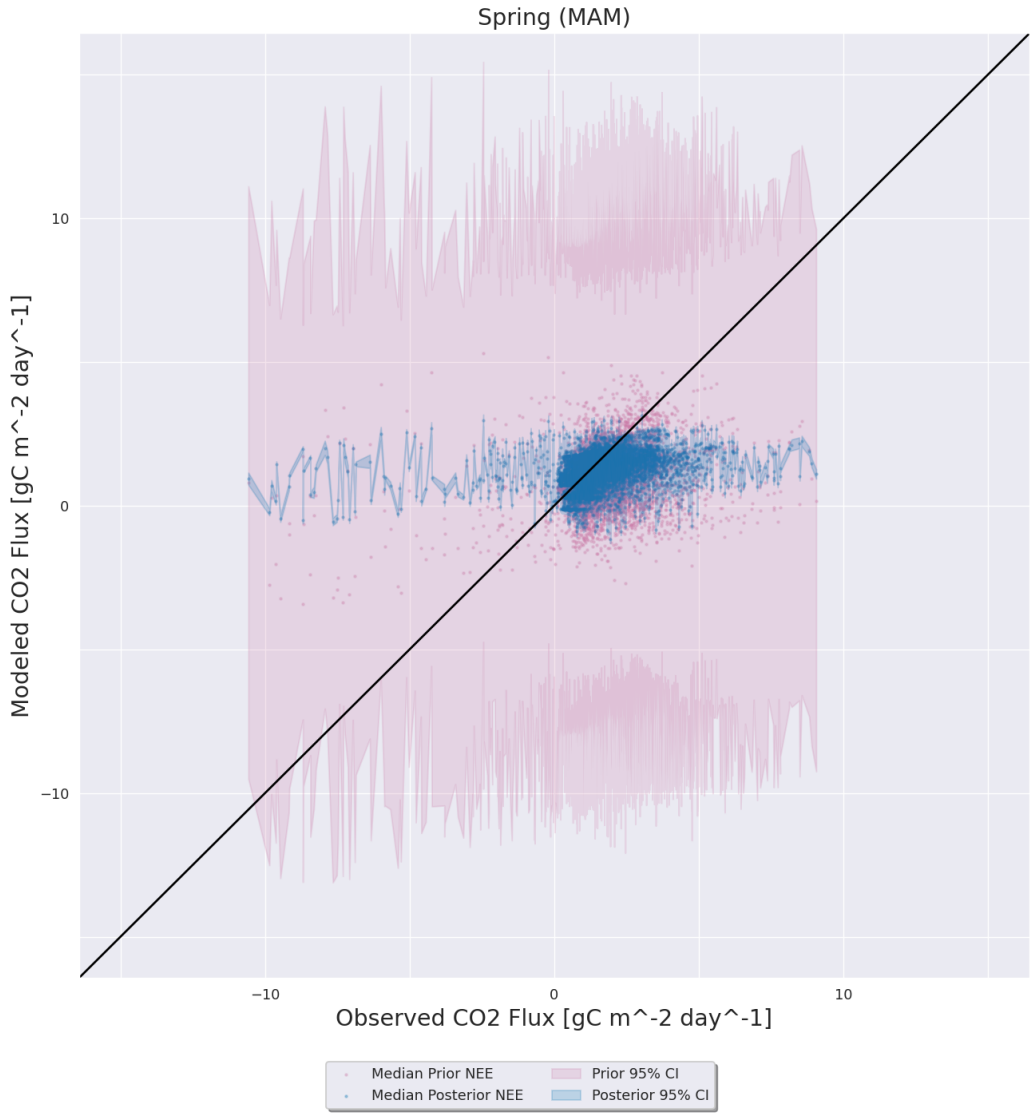

Figure D.19: Same as D.15 except for during the spring (MAM) months.

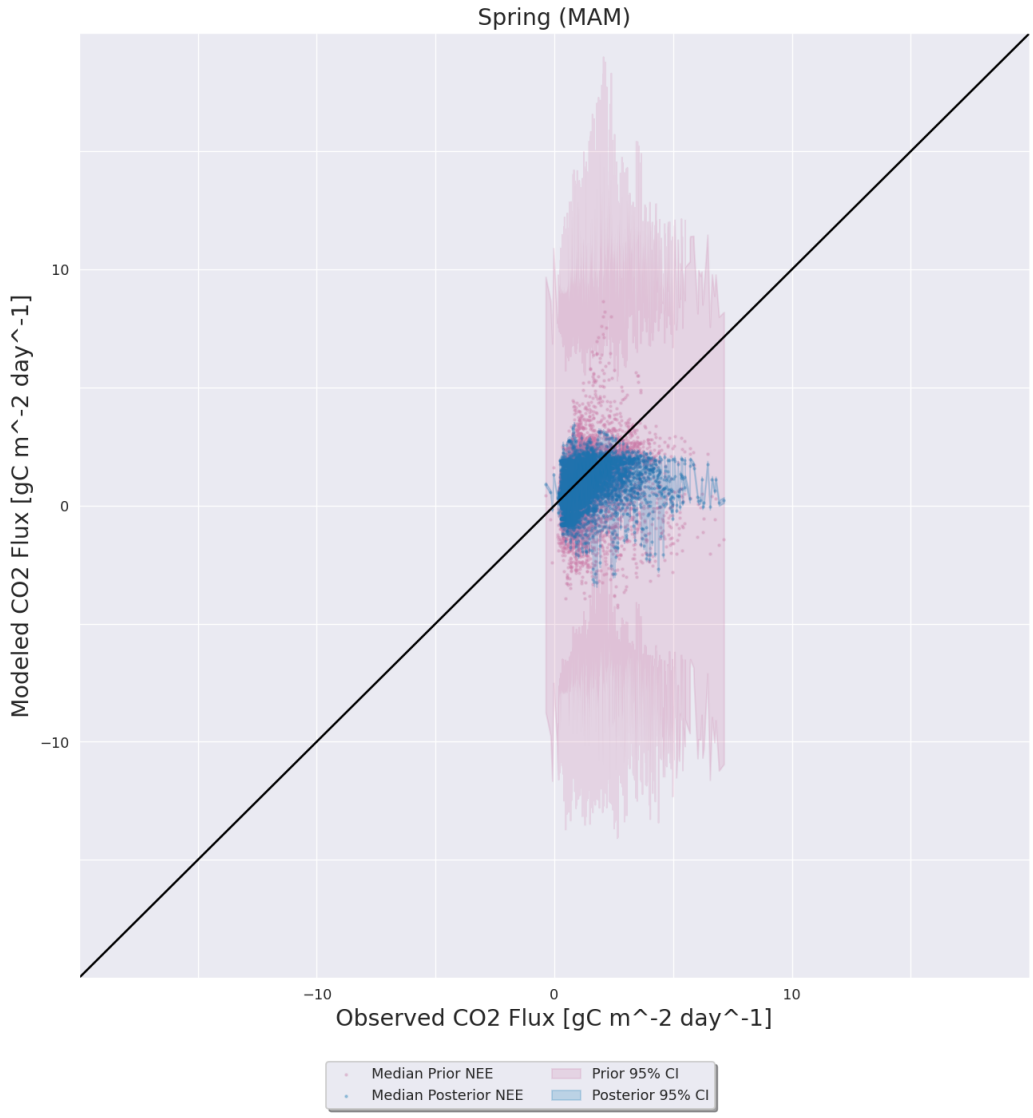

Figure D.20: Same as D.19 except for the Ne3 AmeriFlux site.

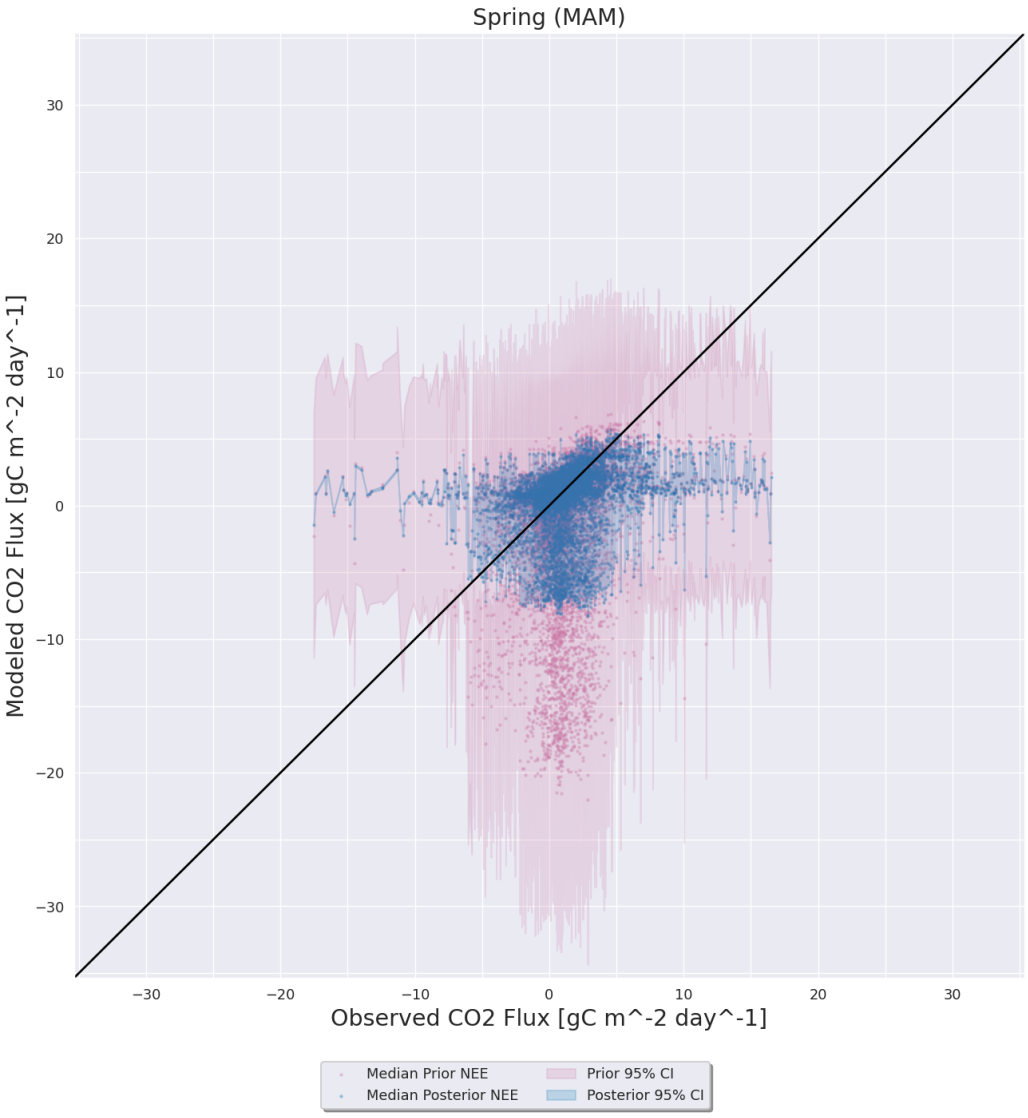

Figure D.21: Same as D.19 except for the KM1 AmeriFlux site.

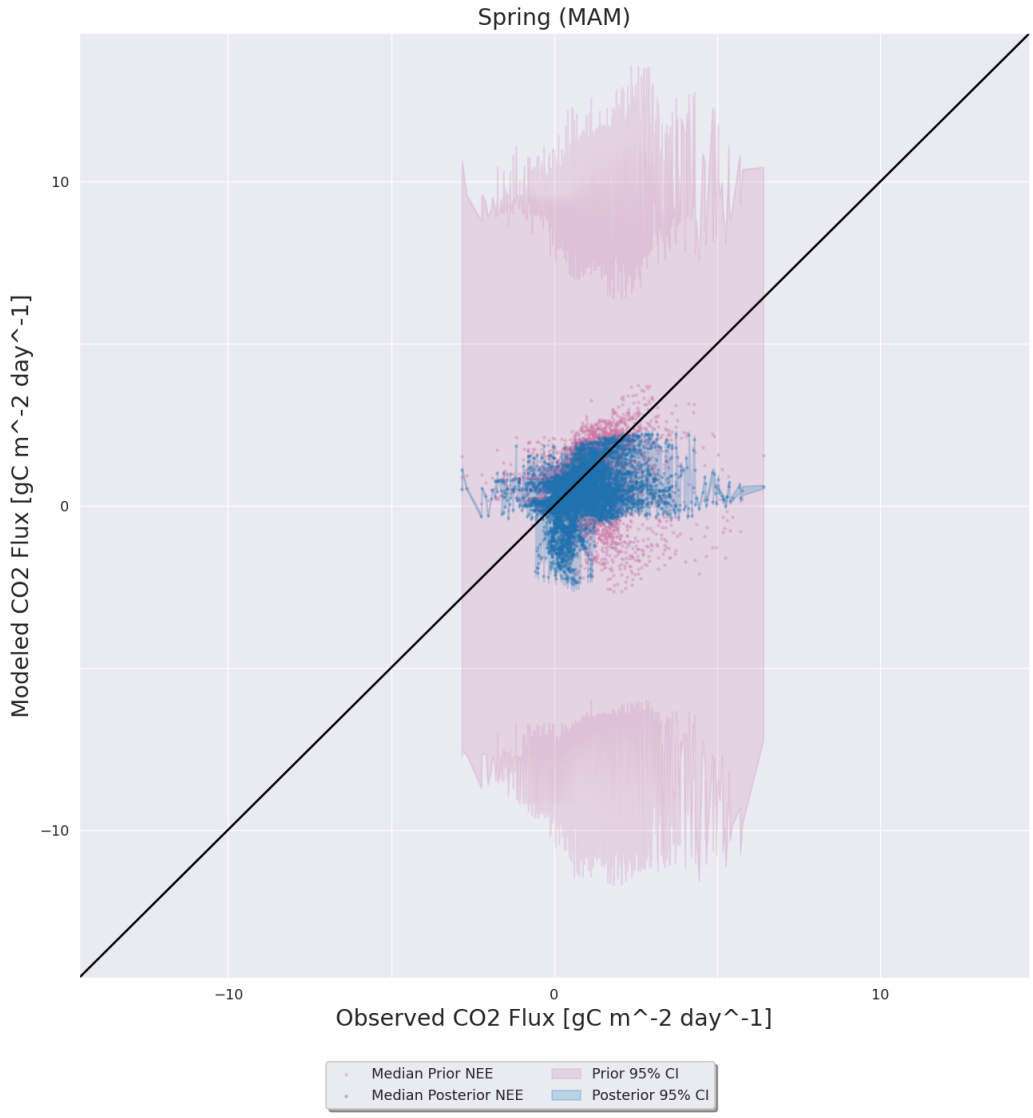

Figure D.22: Same as D.19 except for the Ro1 AmeriFlux site.

D.2.3 Summer (JJA)

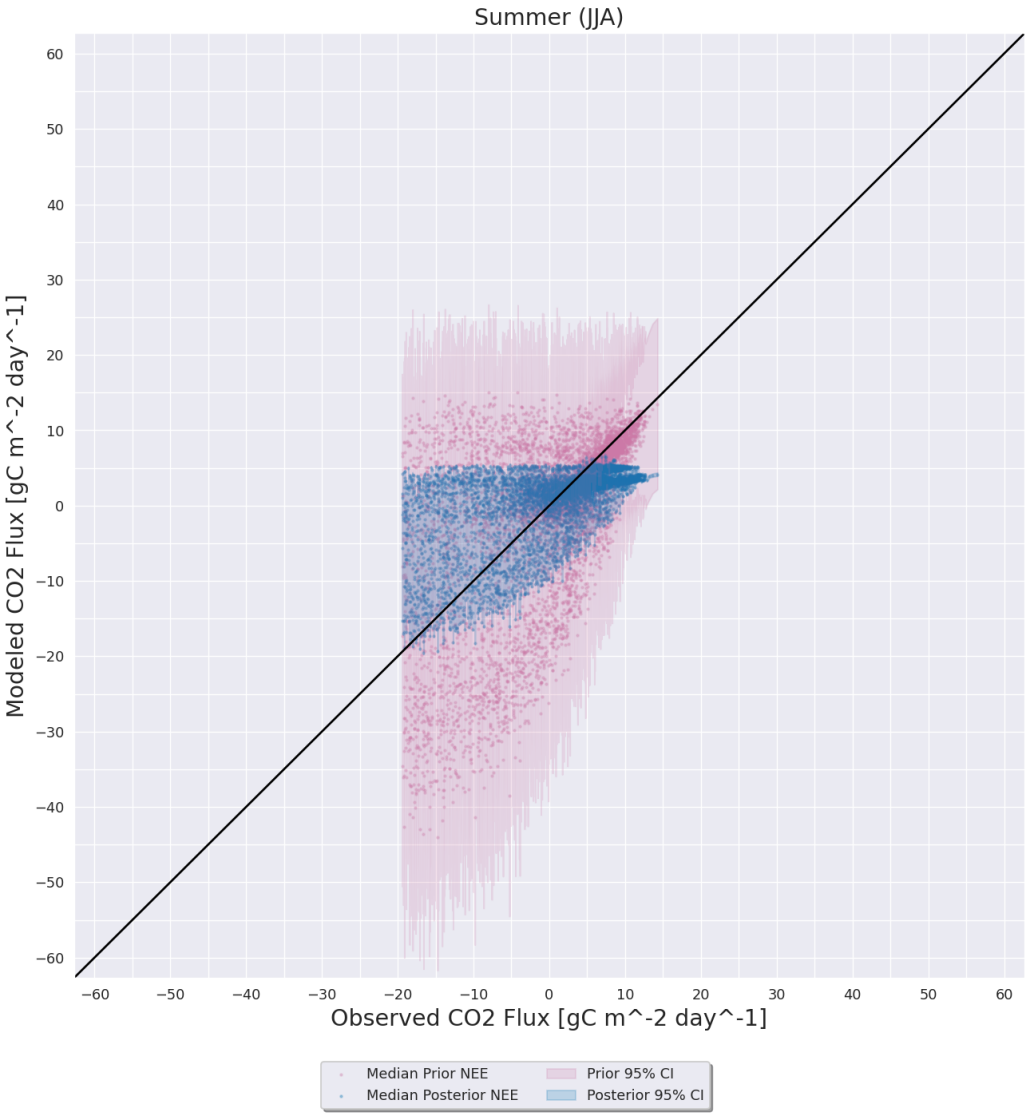

Figure D.23: Same as D.15 except for during the summer (JJA) months.

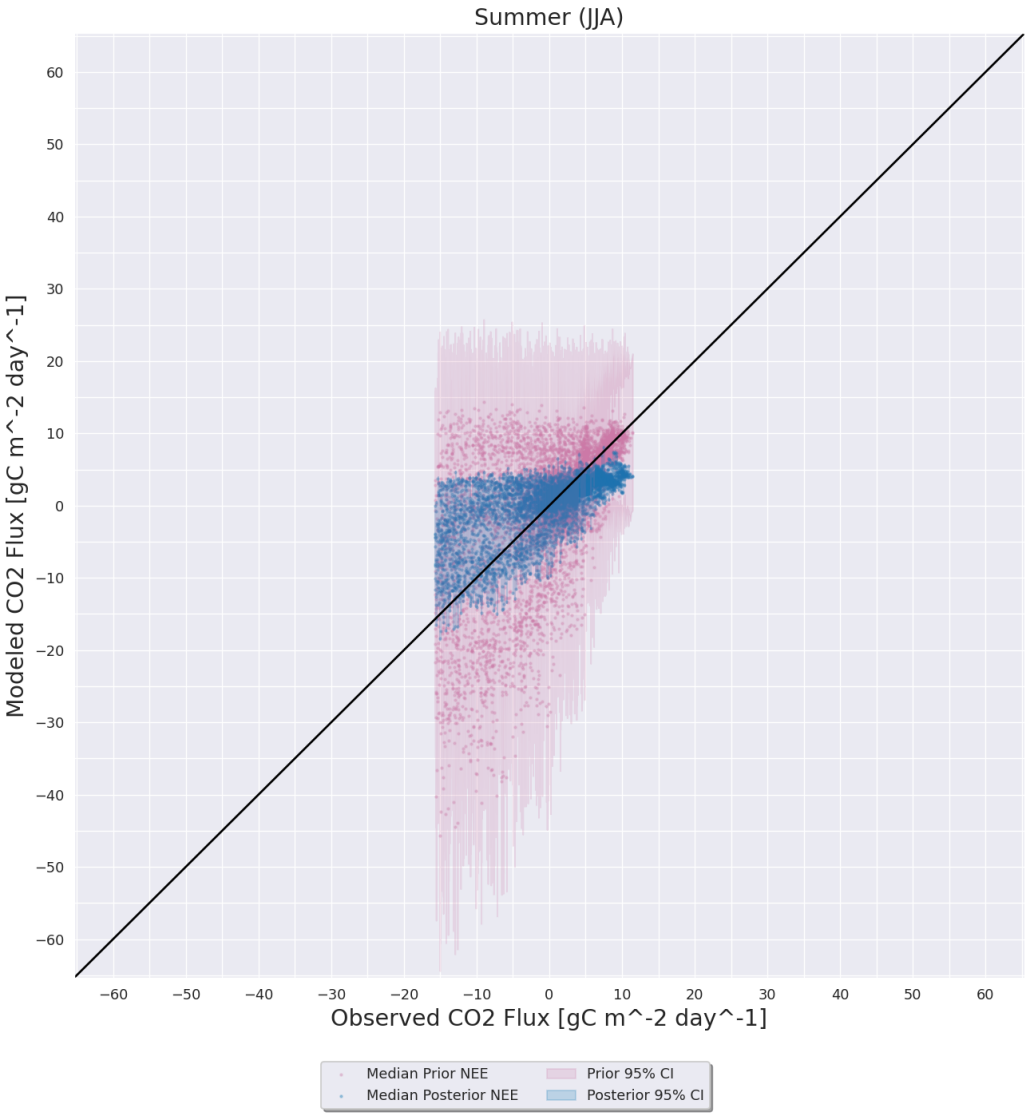

Figure D.24: Same as D.23 except for the Ne3 AmeriFlux site.

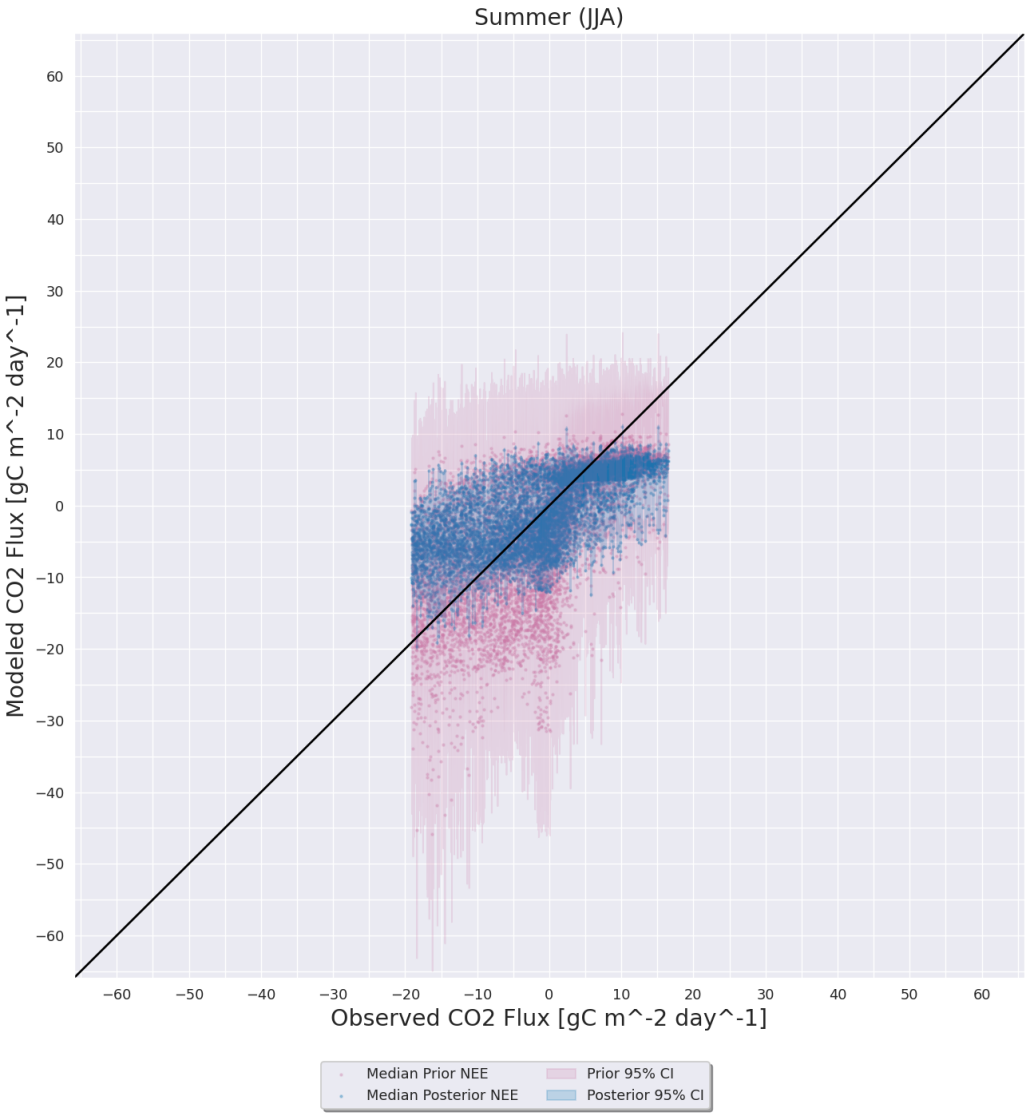

Figure D.25: Same as D.23 except for the KM1 AmeriFlux site.

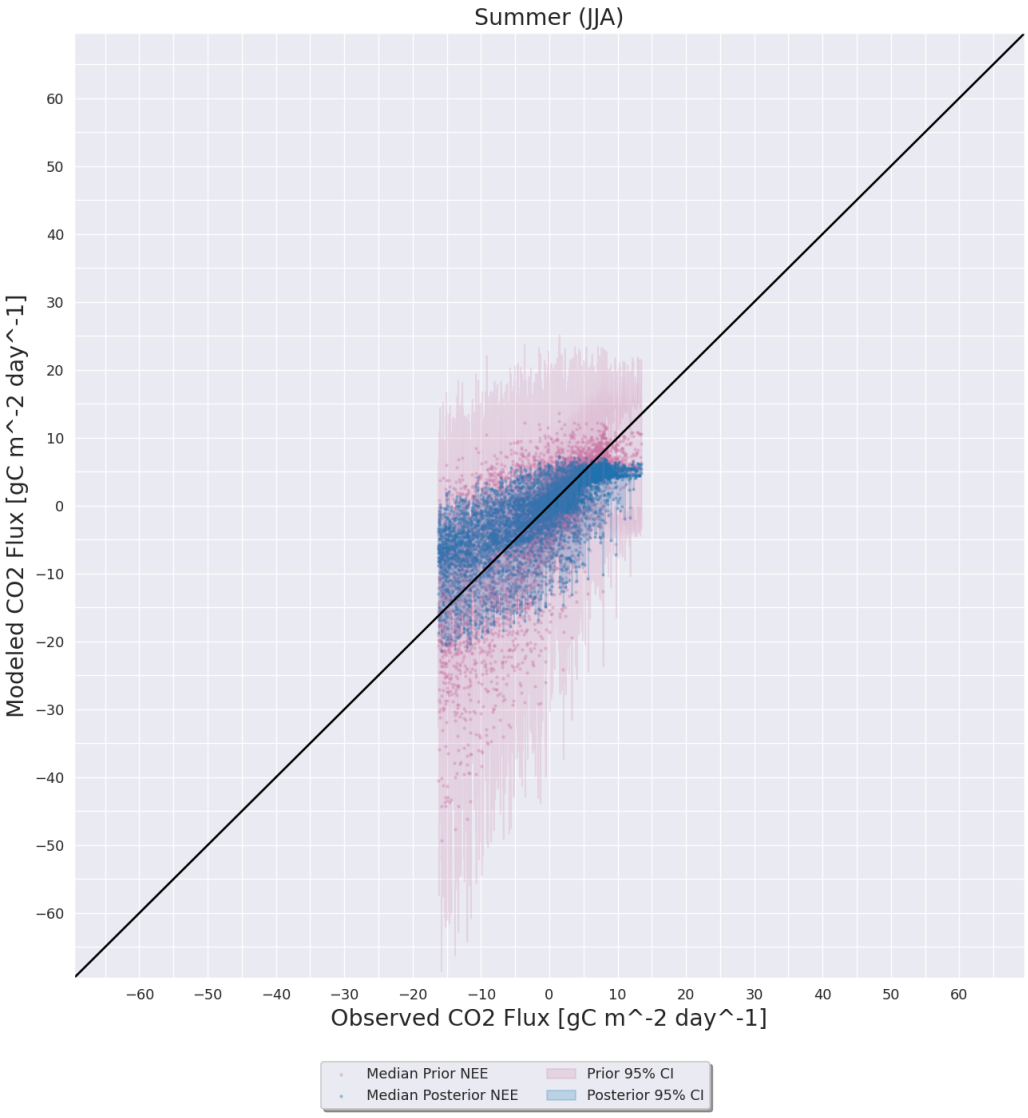

Figure D.26: Same as D.23 except for the Ro1 AmeriFlux site.

D.2.4 Autumn (SON)

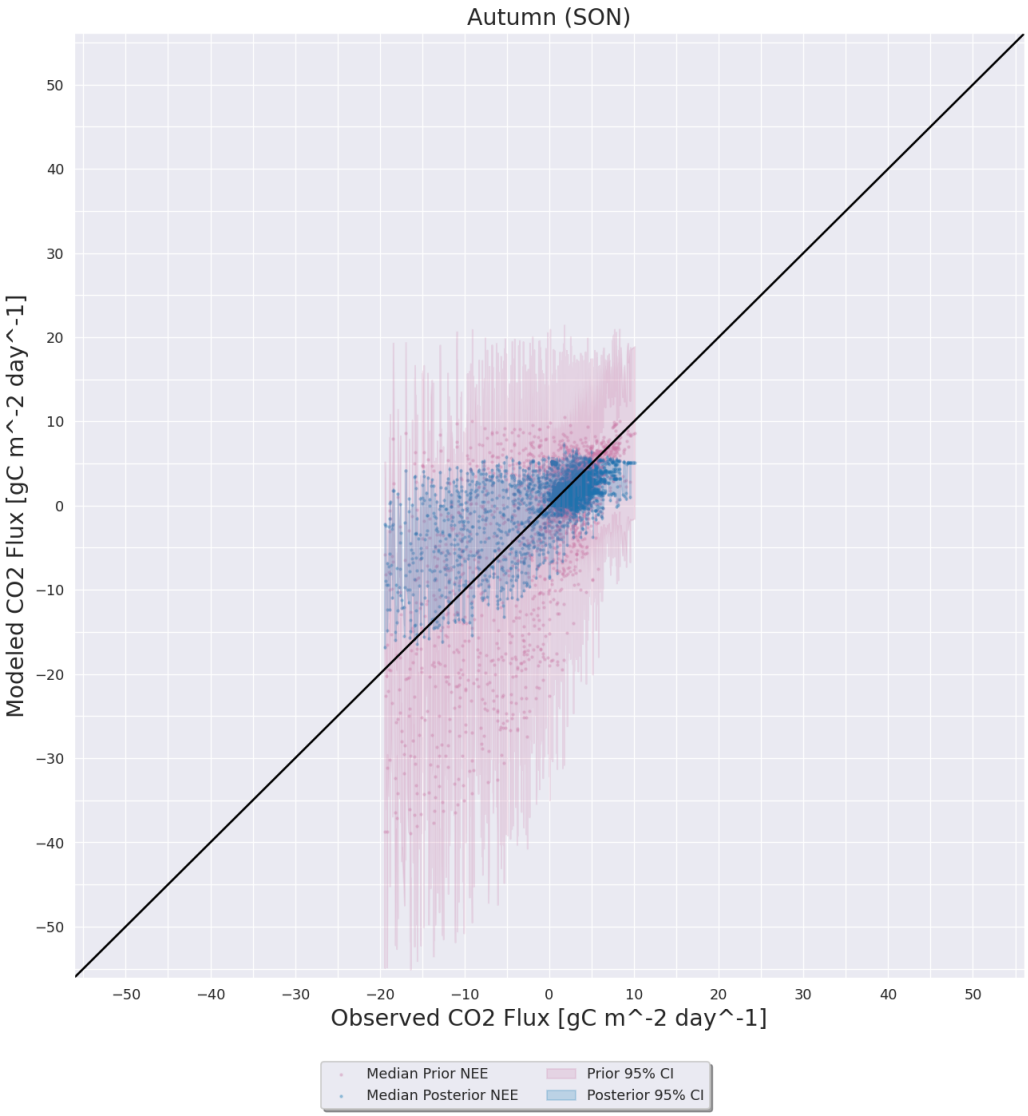

Figure D.27: Same as D.15 except for during the autumn (SON) months.

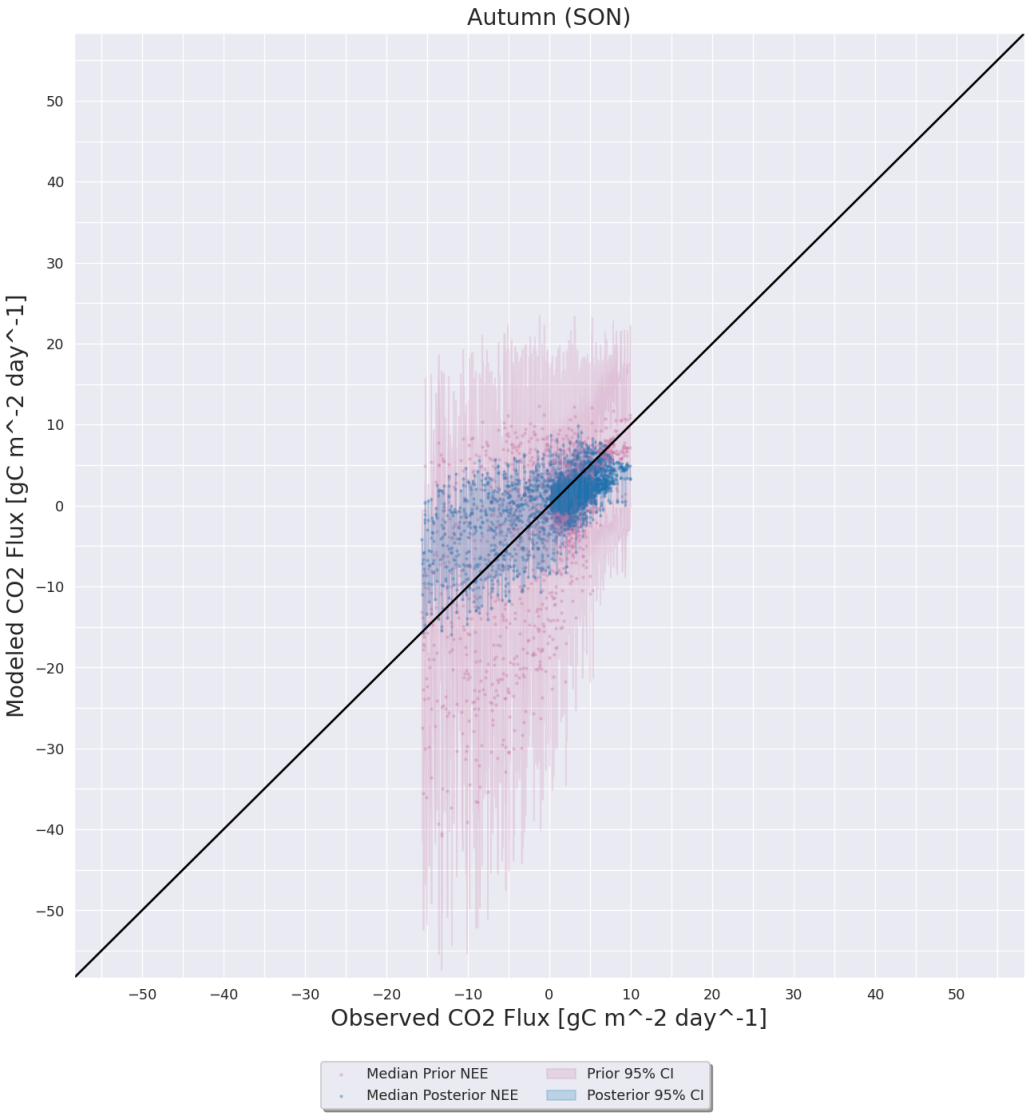

Figure D.28: Same as D.27 except for the Ne3 AmeriFlux site.

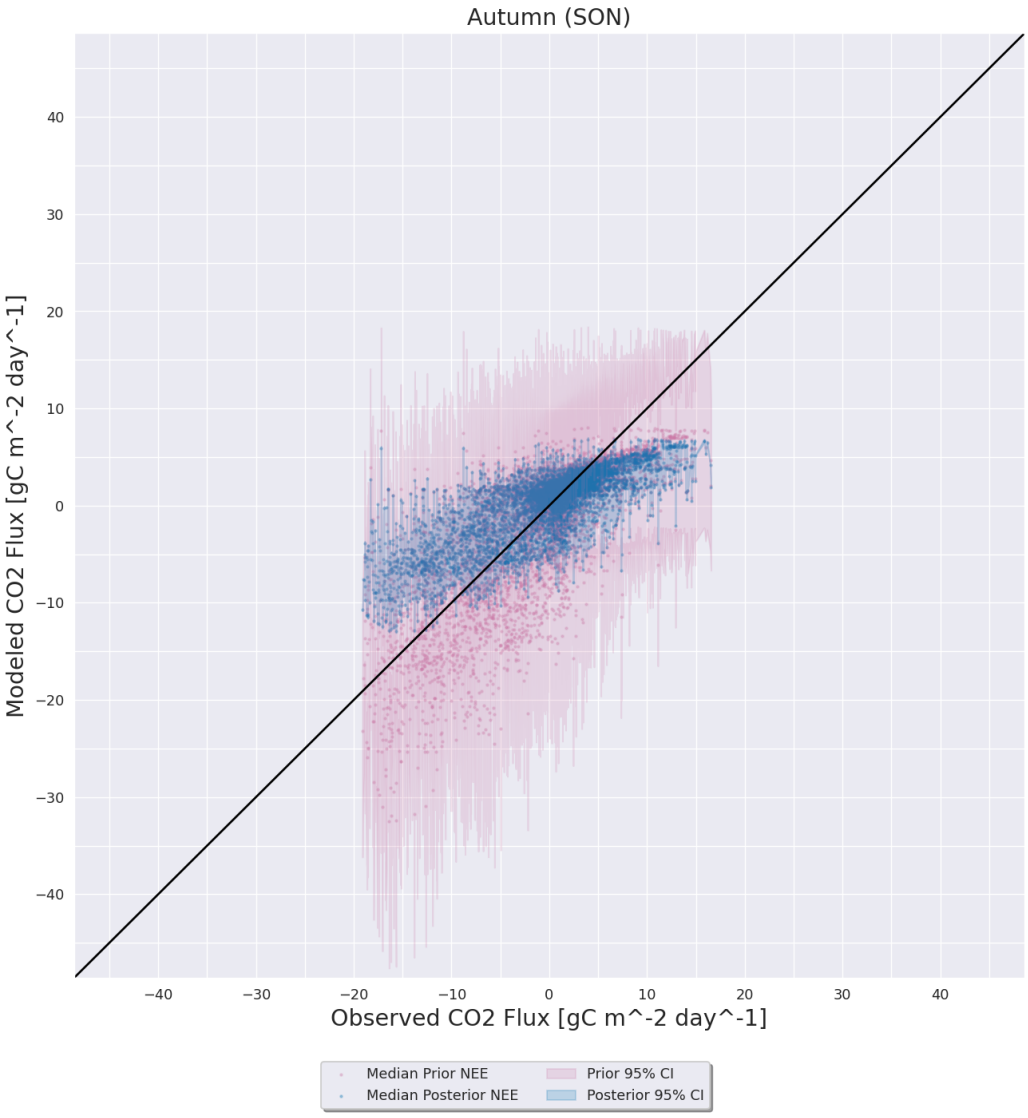

Figure D.29: Same as D.27 except for the KM1 AmeriFlux site.

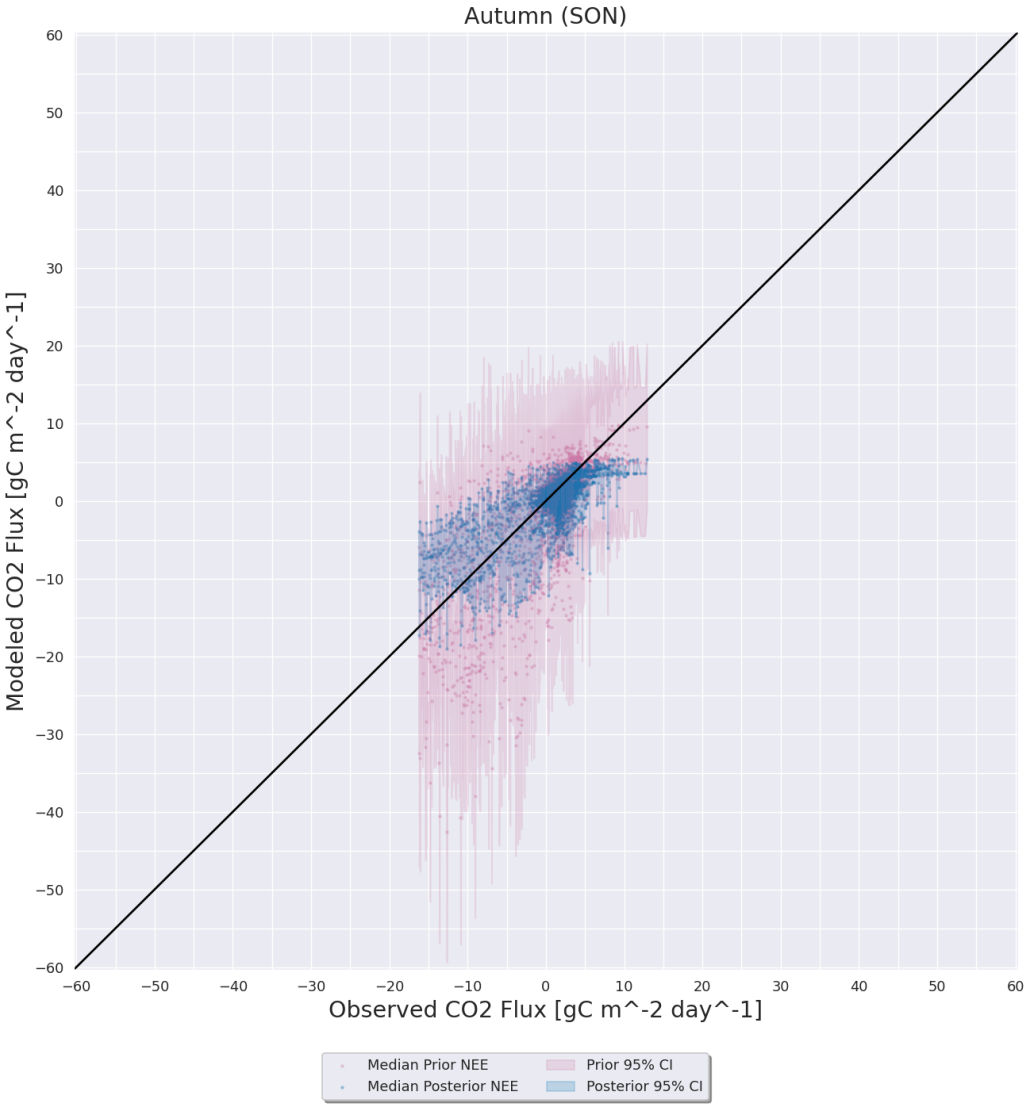

Figure D.30: Same as D.27 except for the Ro1 AmeriFlux site.

D.3 α_2 Drop Experiment

D.3.1 Winter (DJF)

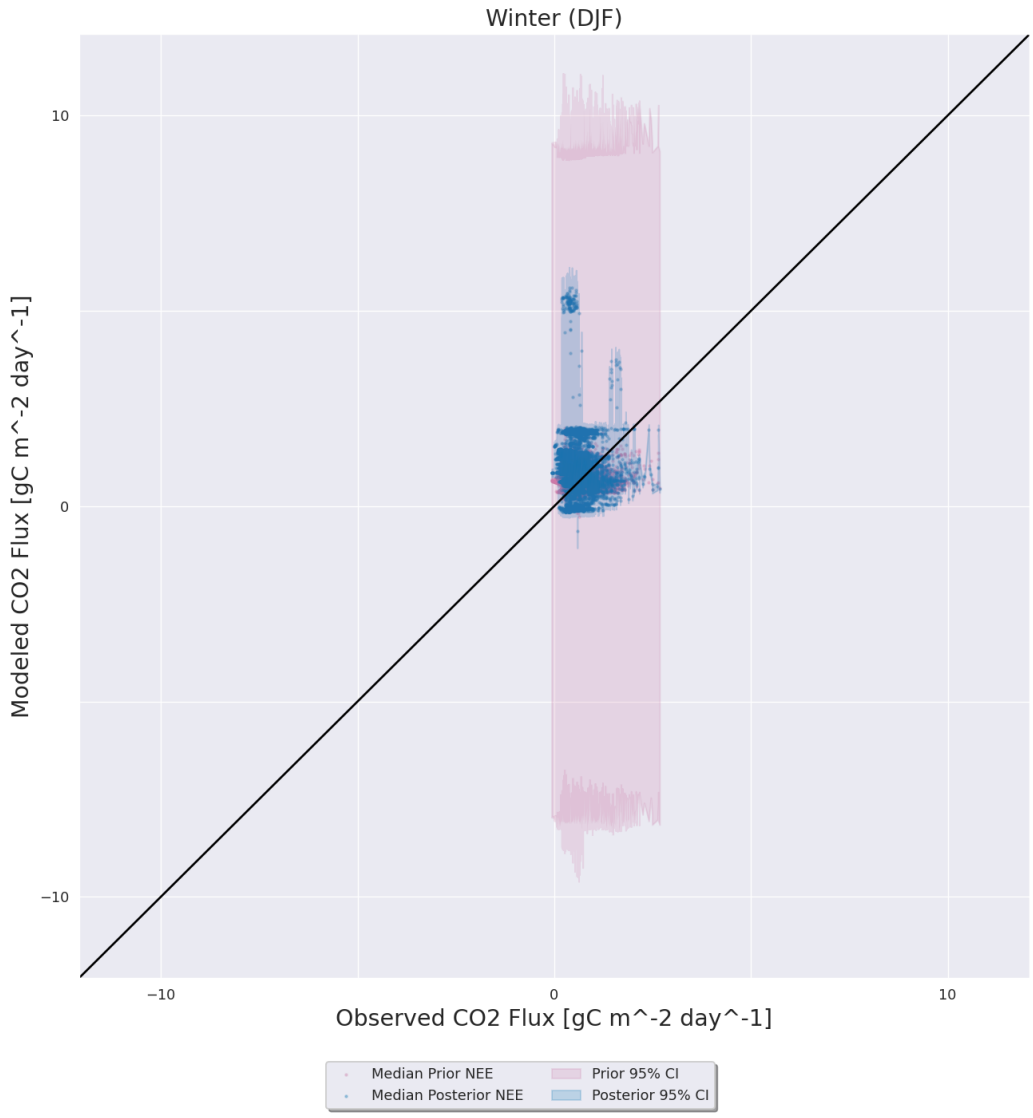

Figure D.31: Same as D.1 except for the α_2 parameter drop experiment.

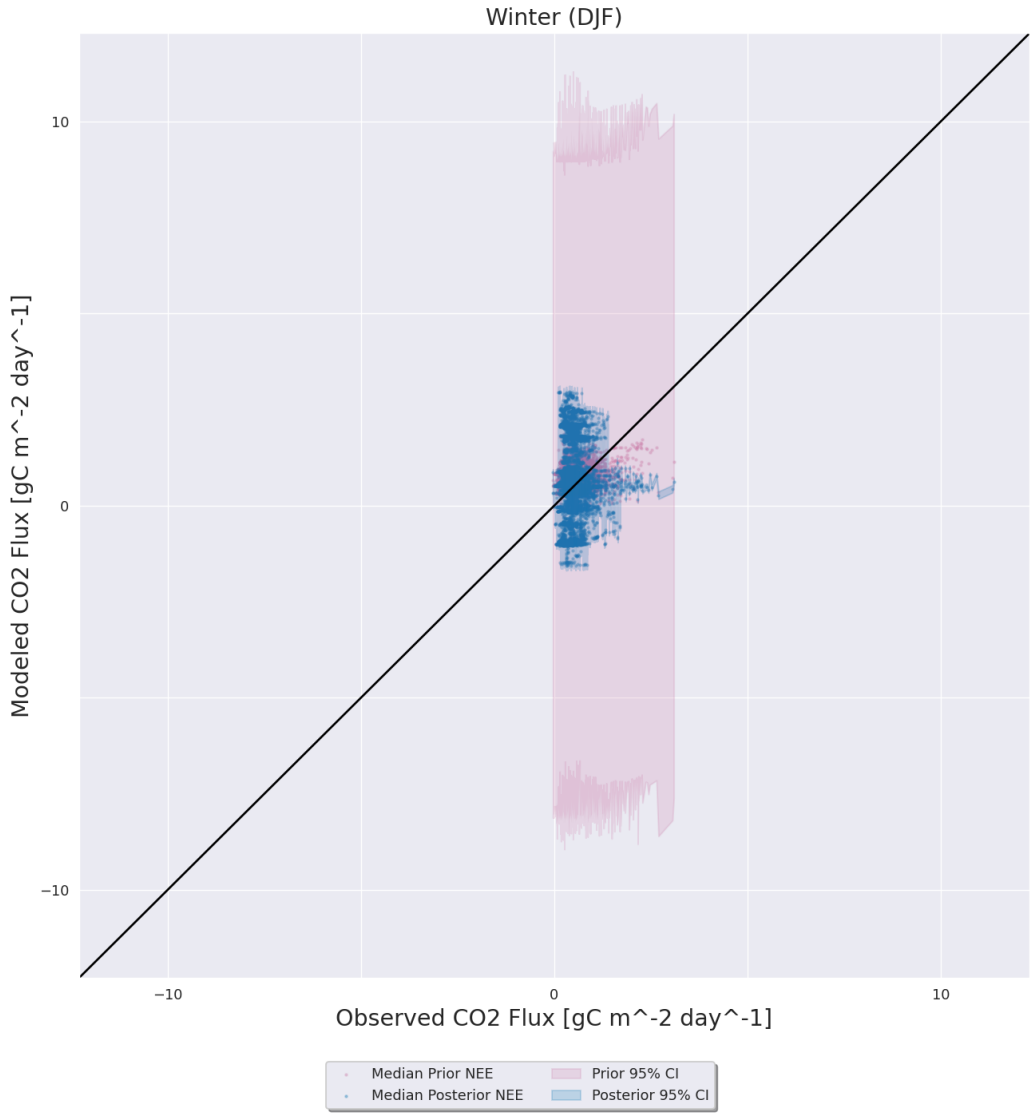

Figure D.32: Same as D.31 except for the Ne3 AmeriFlux site.

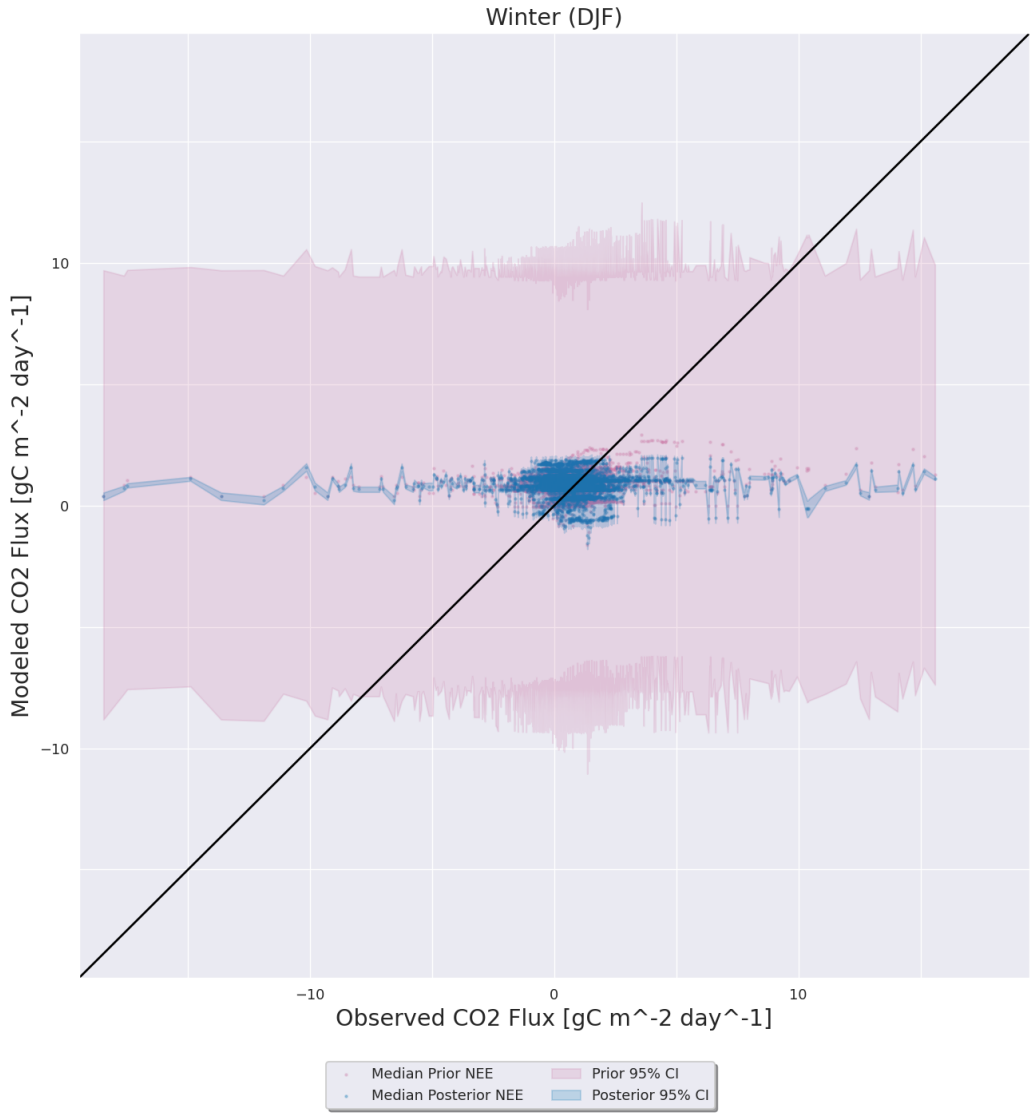

Figure D.33: Same as D.31 except for the KM1 AmeriFlux site.

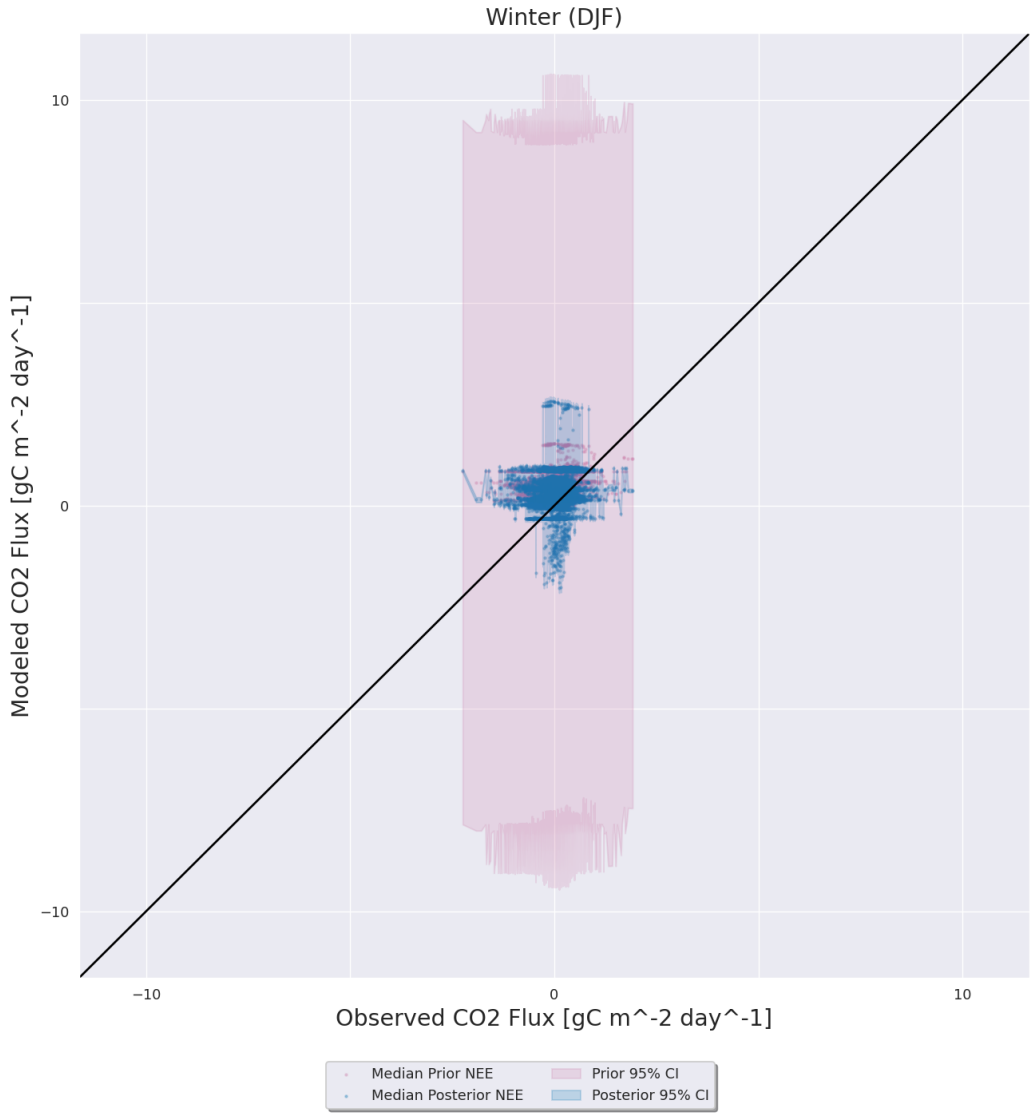

Figure D.34: Same as D.31 except for the Ro1 AmeriFlux site.

D.3.2 Spring (MAM)

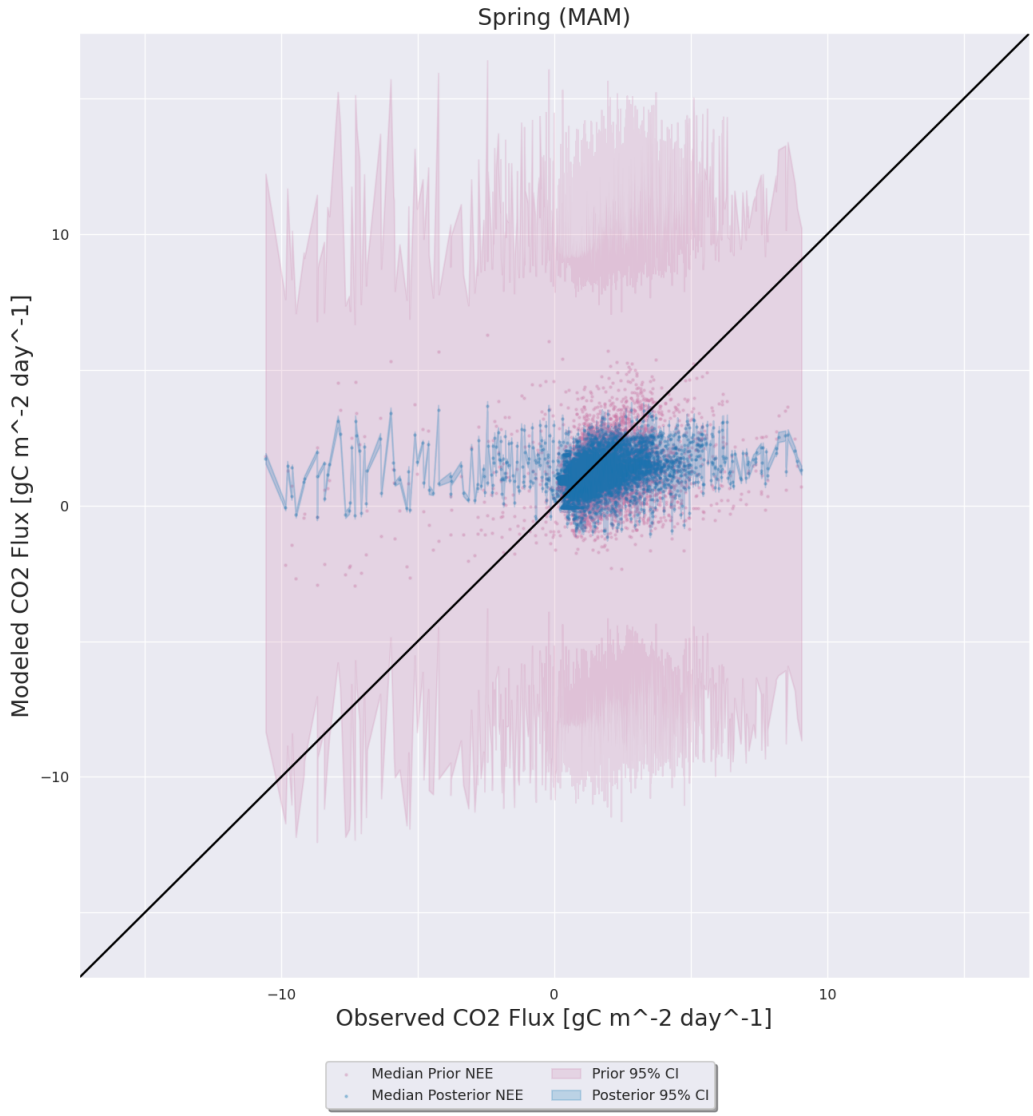

Figure D.35: Same as D.31 except for during the spring (MAM) months.

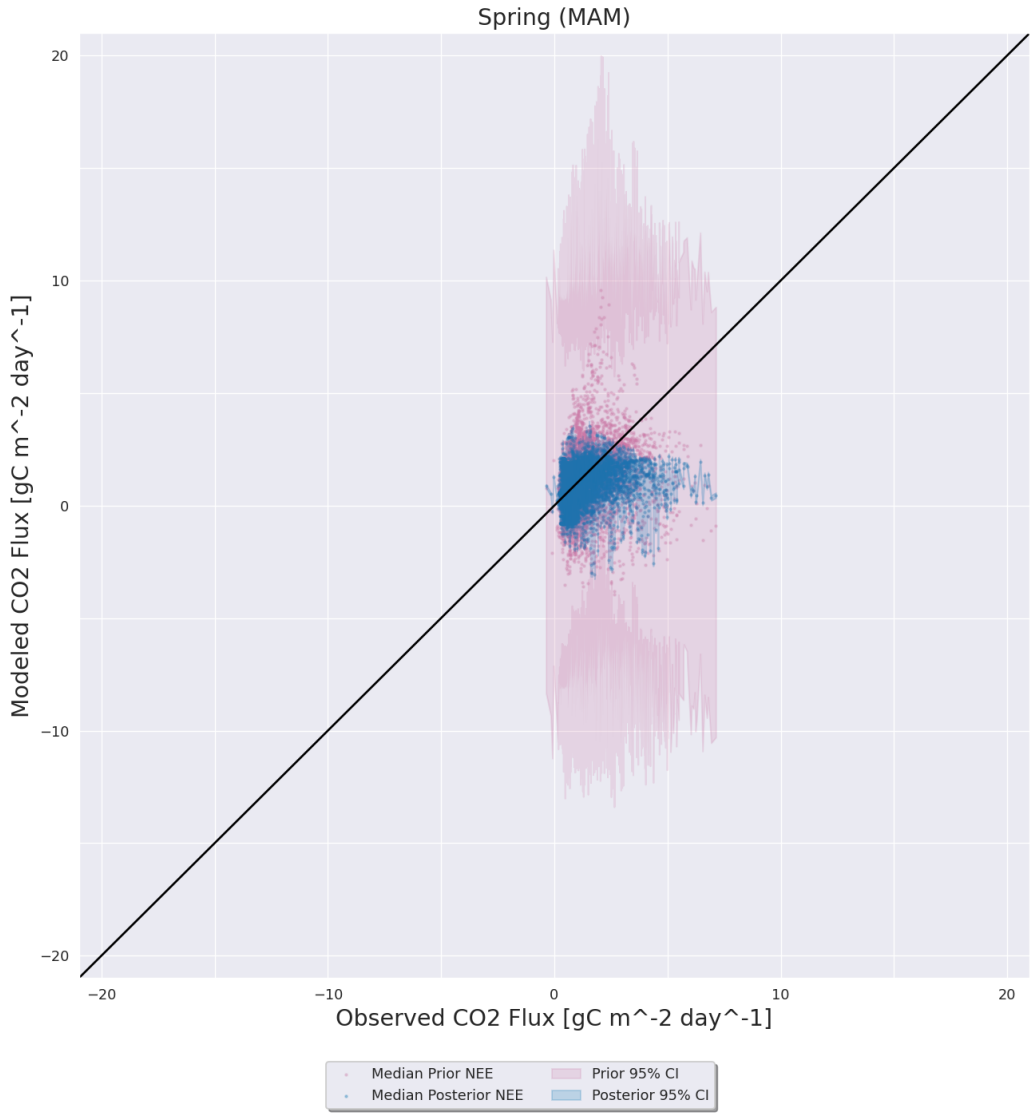

Figure D.36: Same as D.35 except for the Ne3 AmeriFlux site.

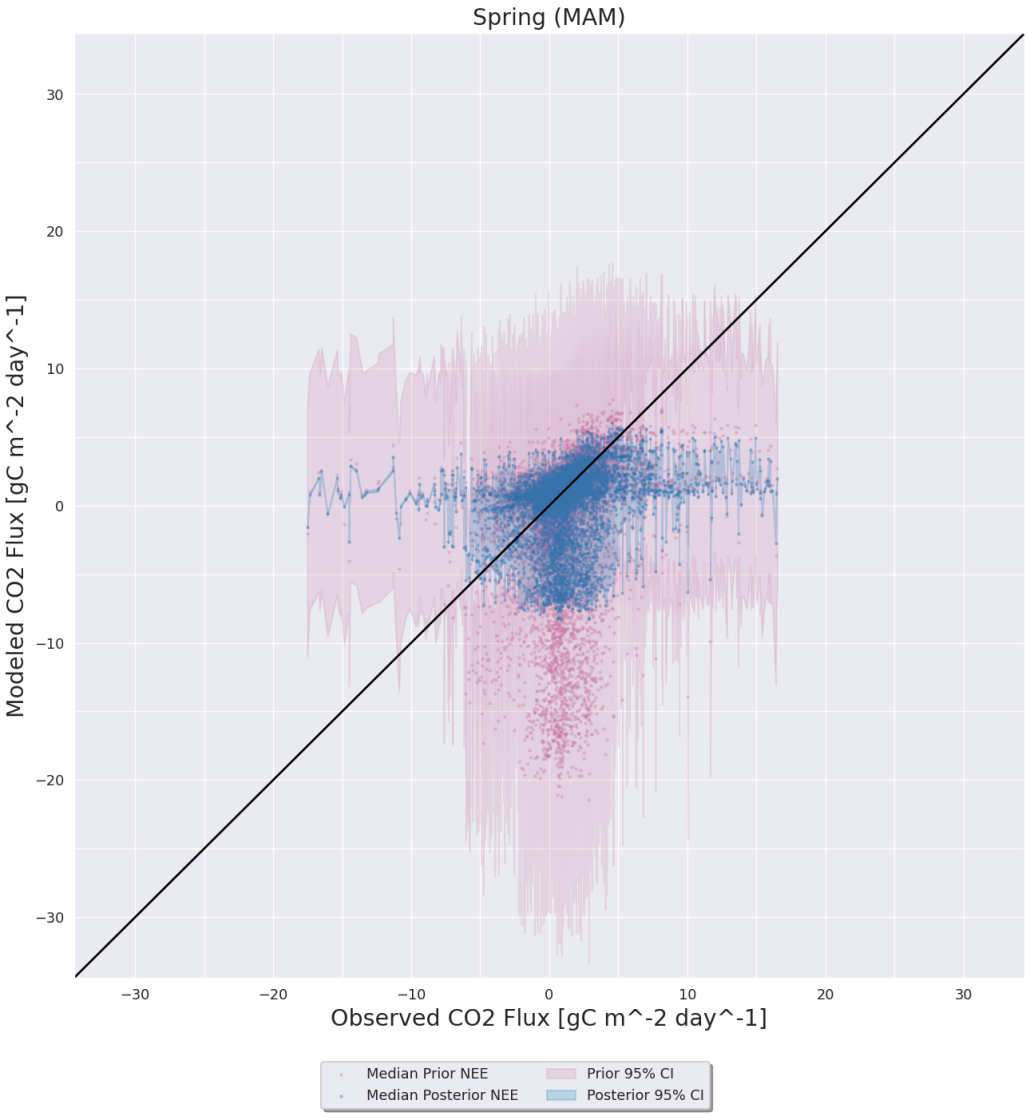

Figure D.37: Same as D.35 except for the KM1 AmeriFlux site.

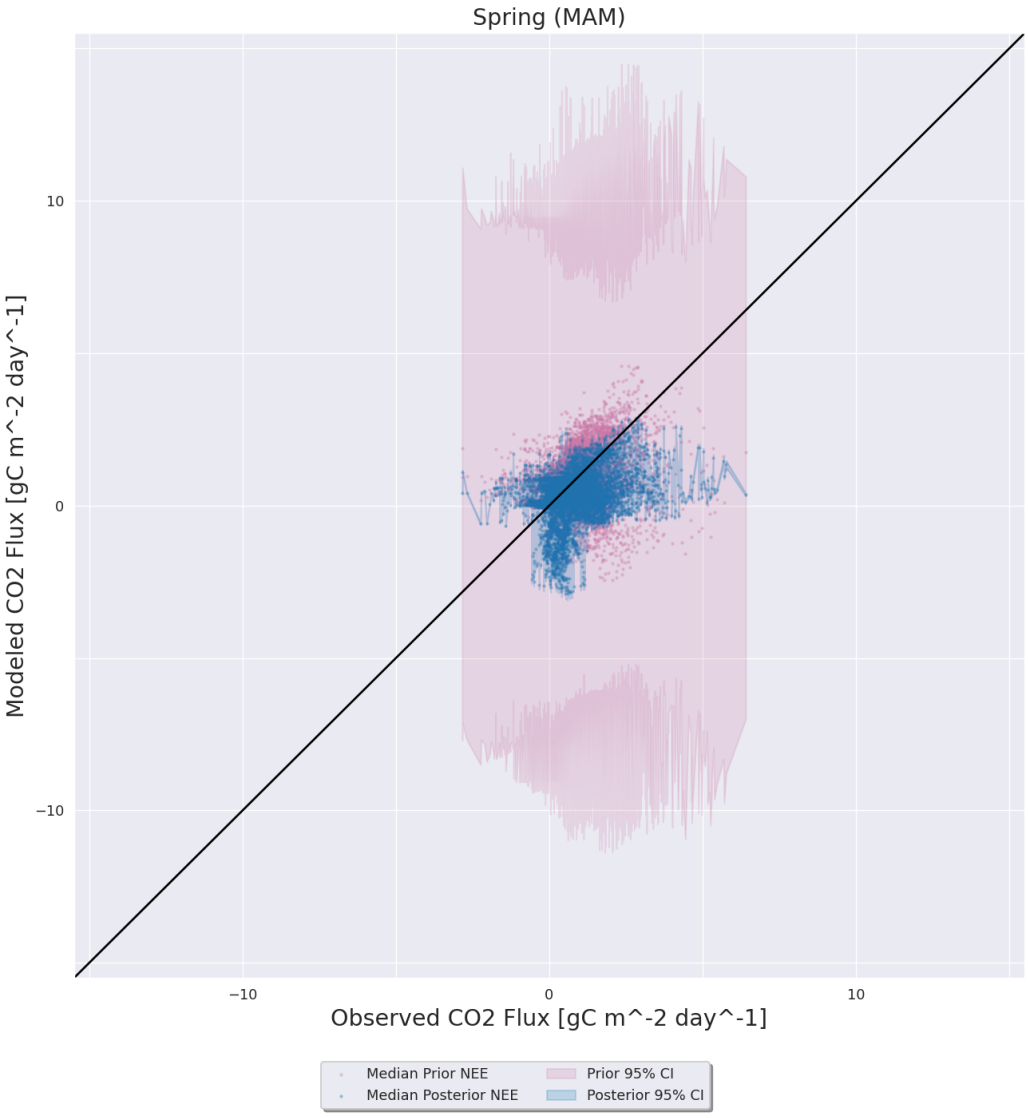

Figure D.38: Same as D.35 except for the Ro1 AmeriFlux site.

D.3.3 Summer (JJA)

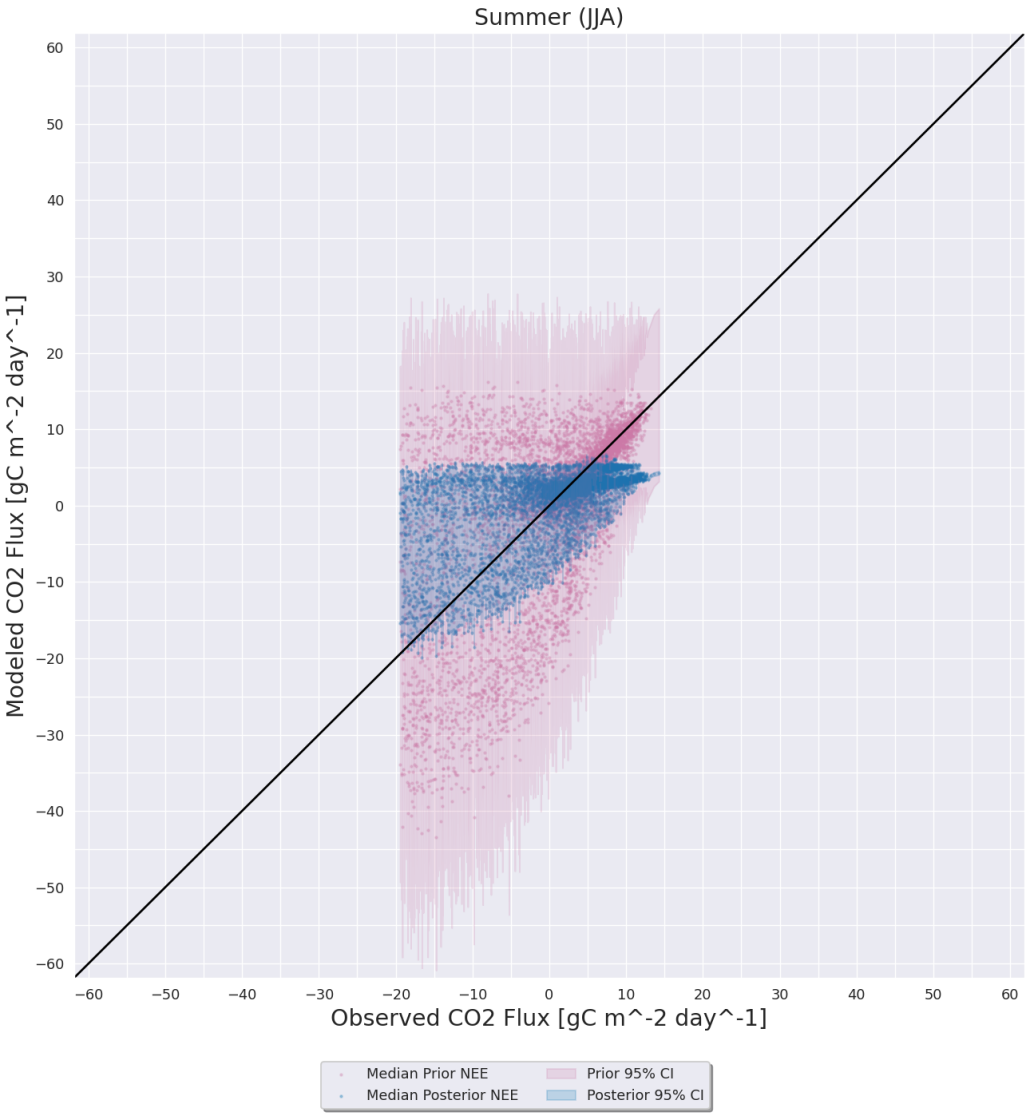

Figure D.39: Same as D.31 except for during the summer (JJA) months.

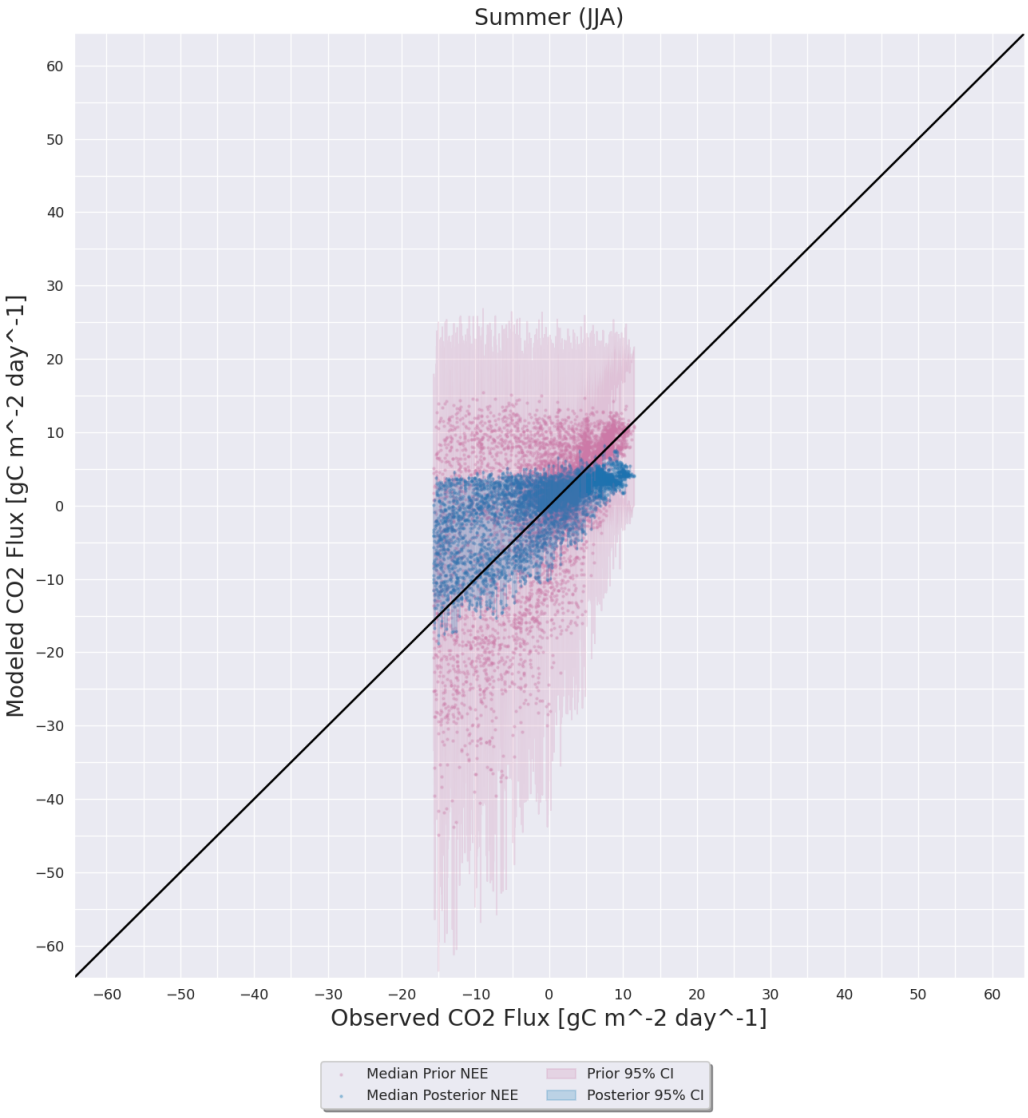

Figure D.40: Same as D.39 except for the Ne3 AmeriFlux site.

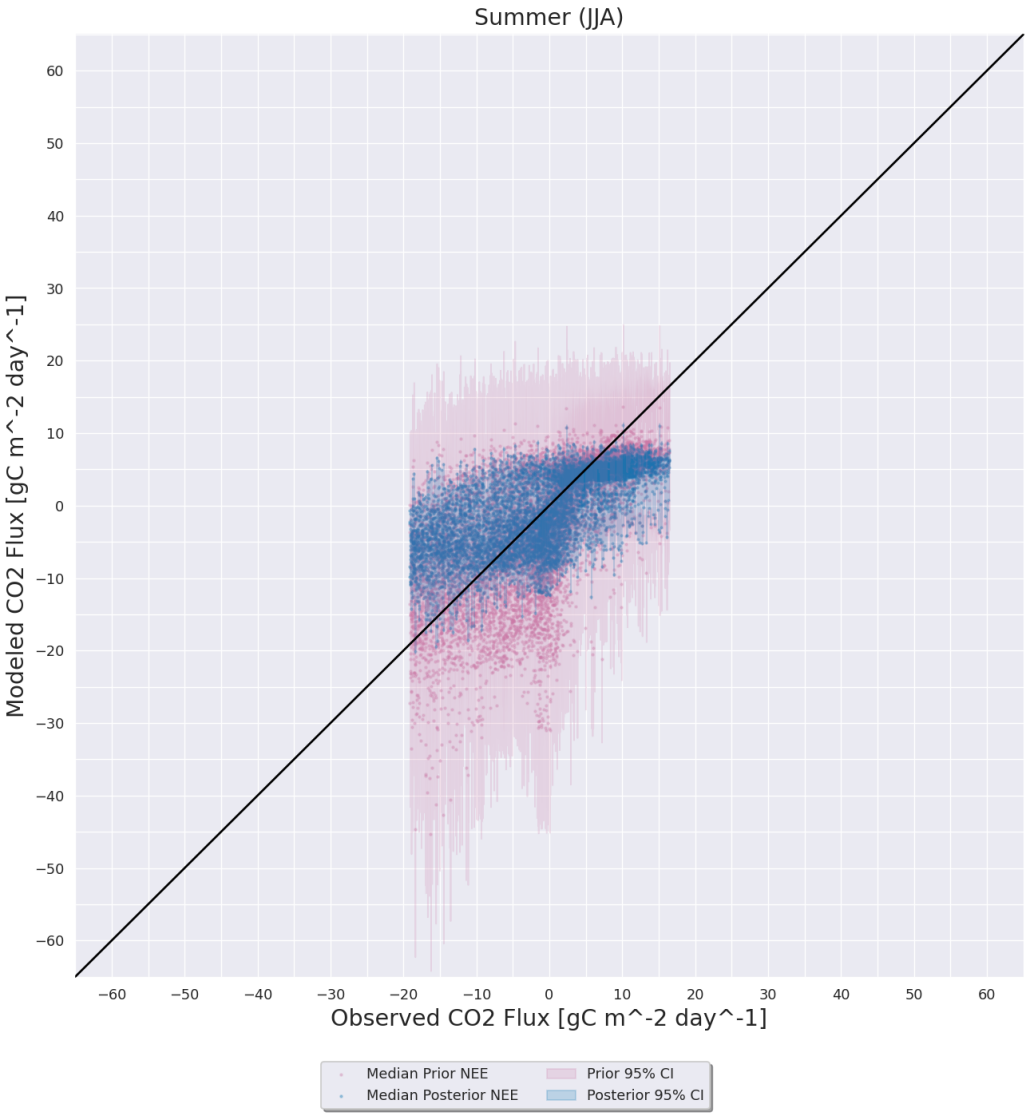

Figure D.41: Same as D.39 except for the KM1 AmeriFlux site.

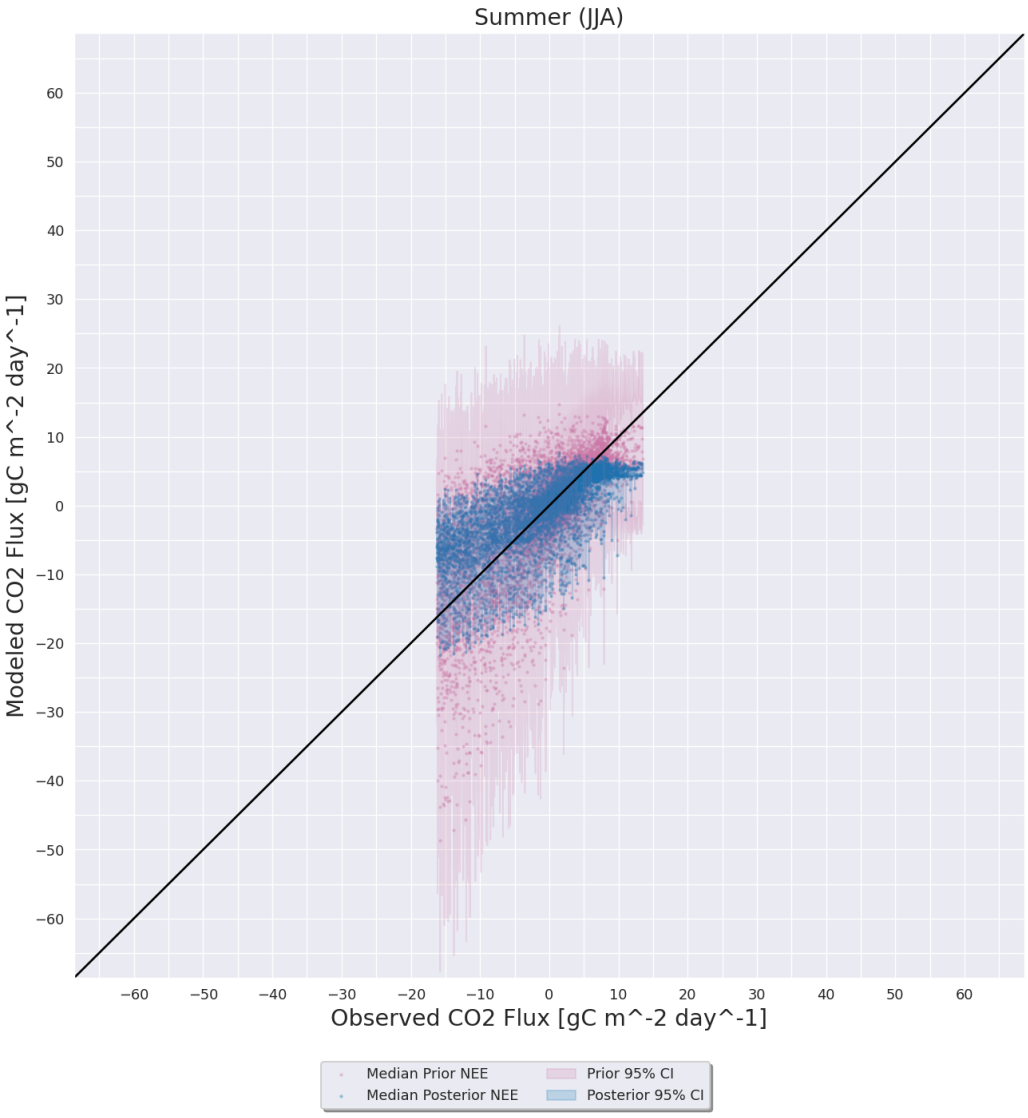

Figure D.42: Same as D.39 except for the Ro1 AmeriFlux site.

D.3.4 Autumn (SON)

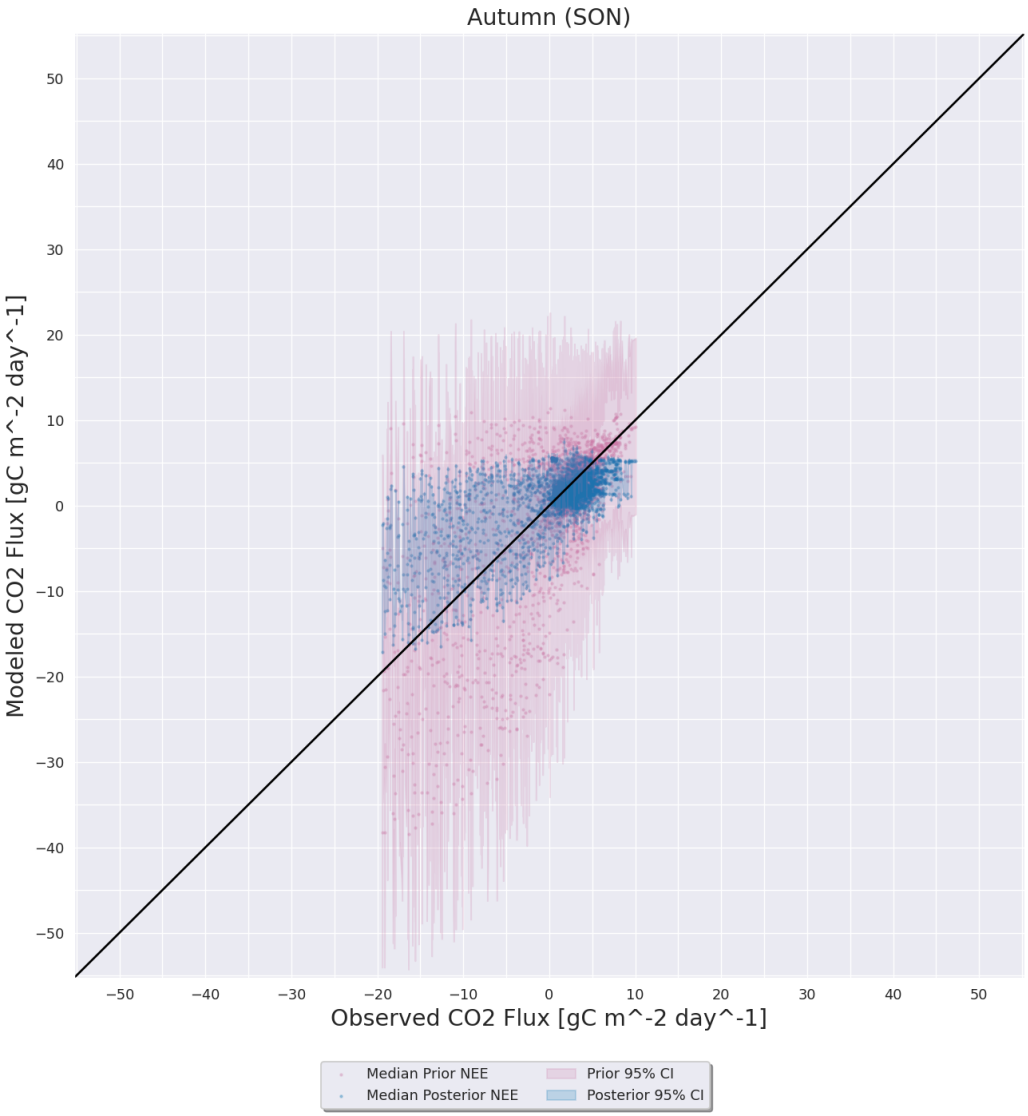

Figure D.43: Same as D.31 except for during the autumn (SON) months.

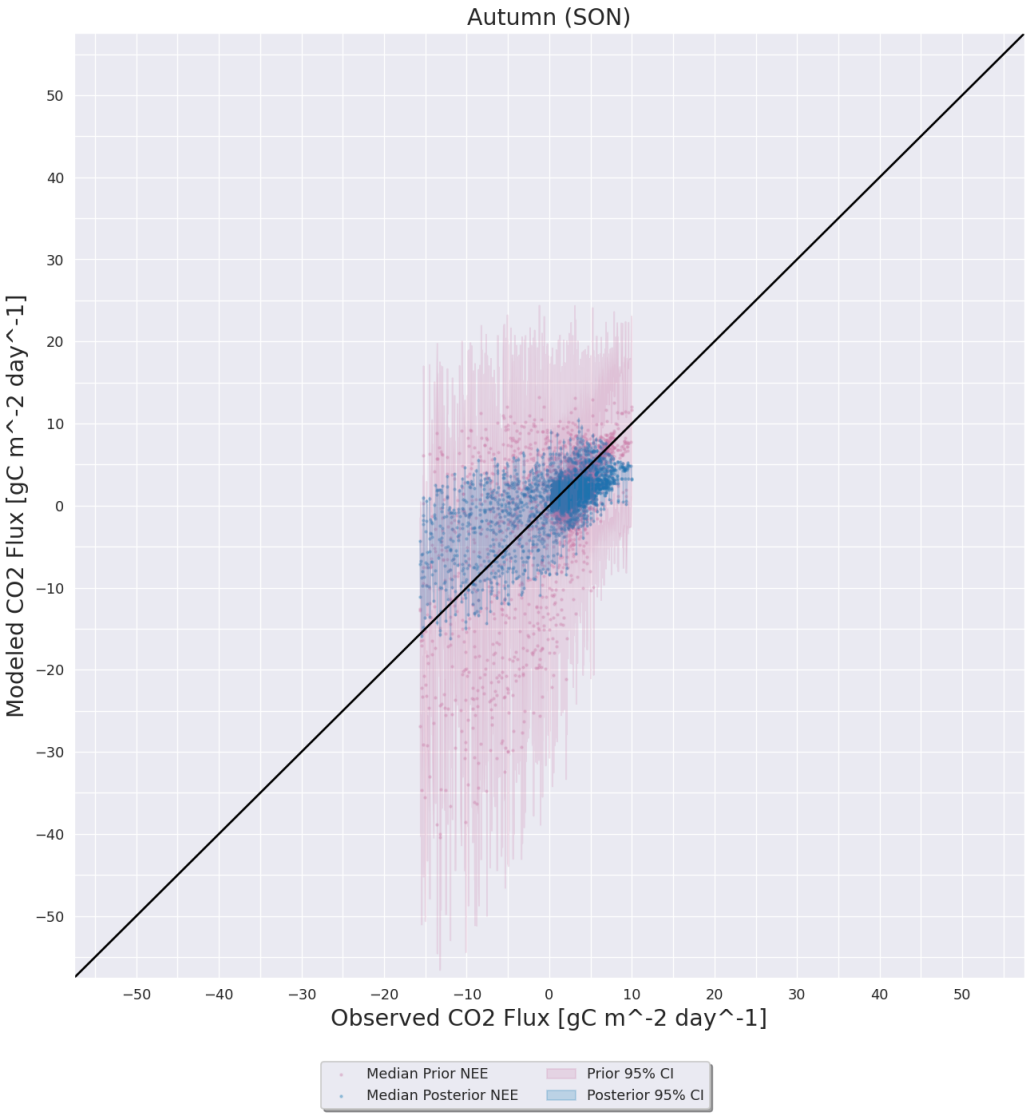

Figure D.44: Same as D.43 except for the Ne3 AmeriFlux site.

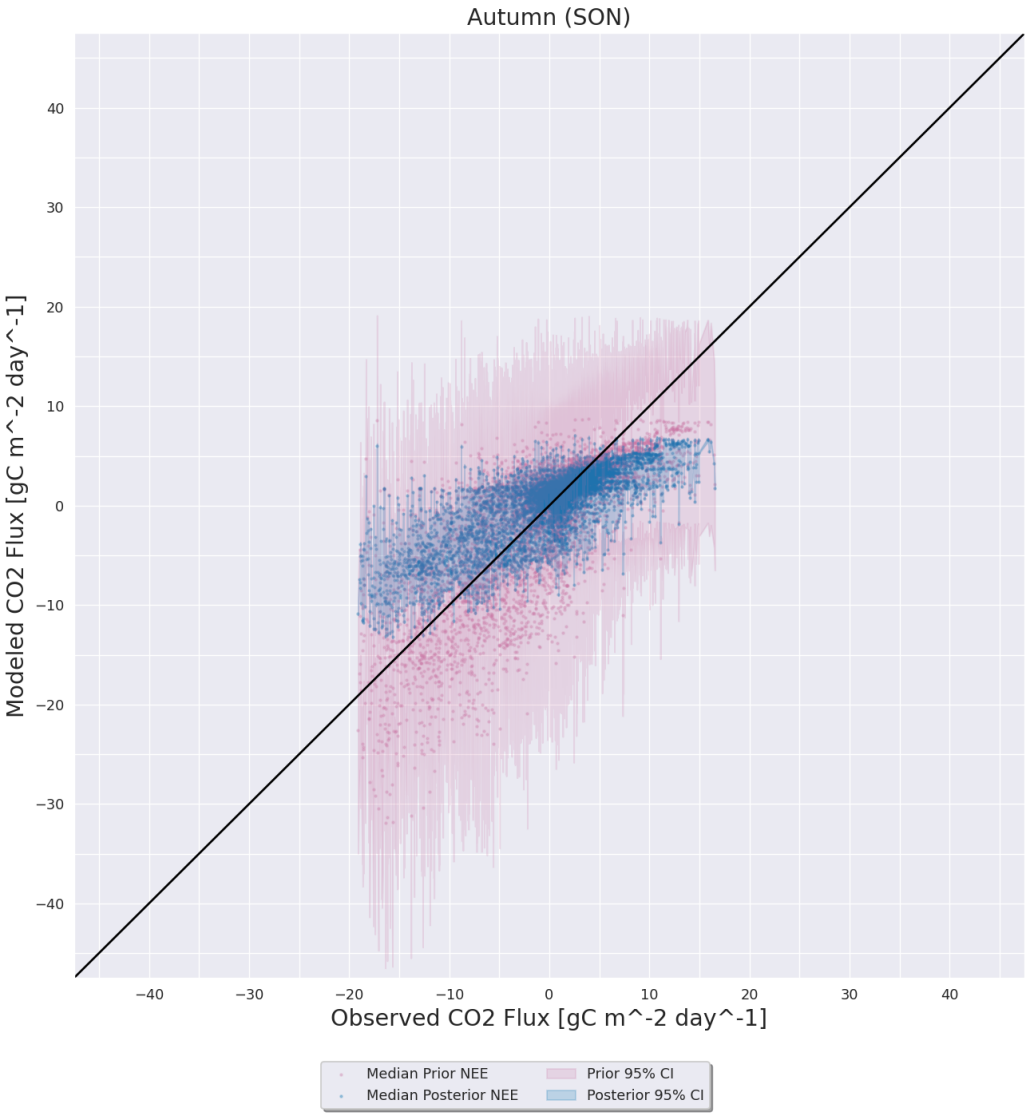

Figure D.45: Same as D.43 except for the KM1 AmeriFlux site.

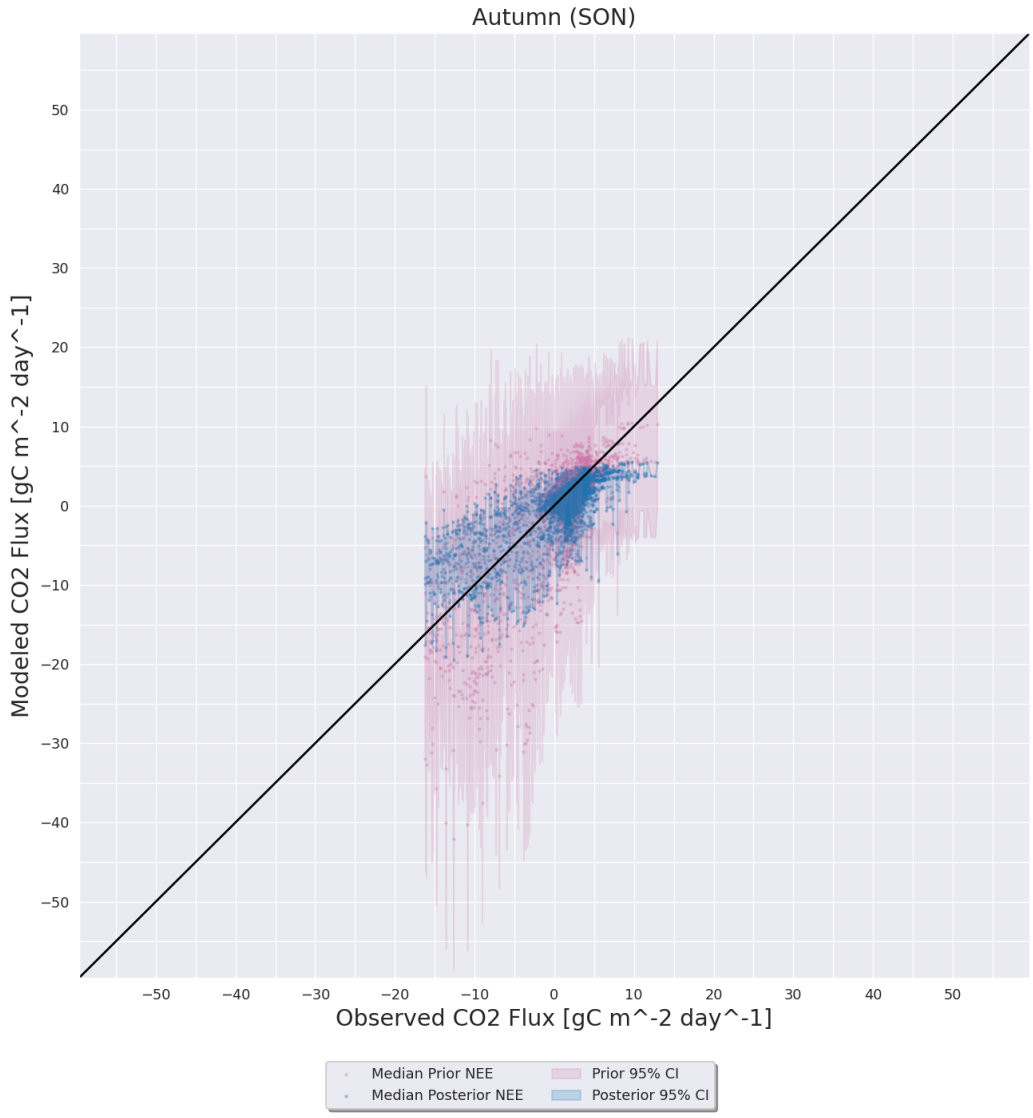

Figure D.46: Same as D.43 except for the Ro1 AmeriFlux site.

D.4 k_3 Drop Experiment

D.4.1 Winter (DJF)

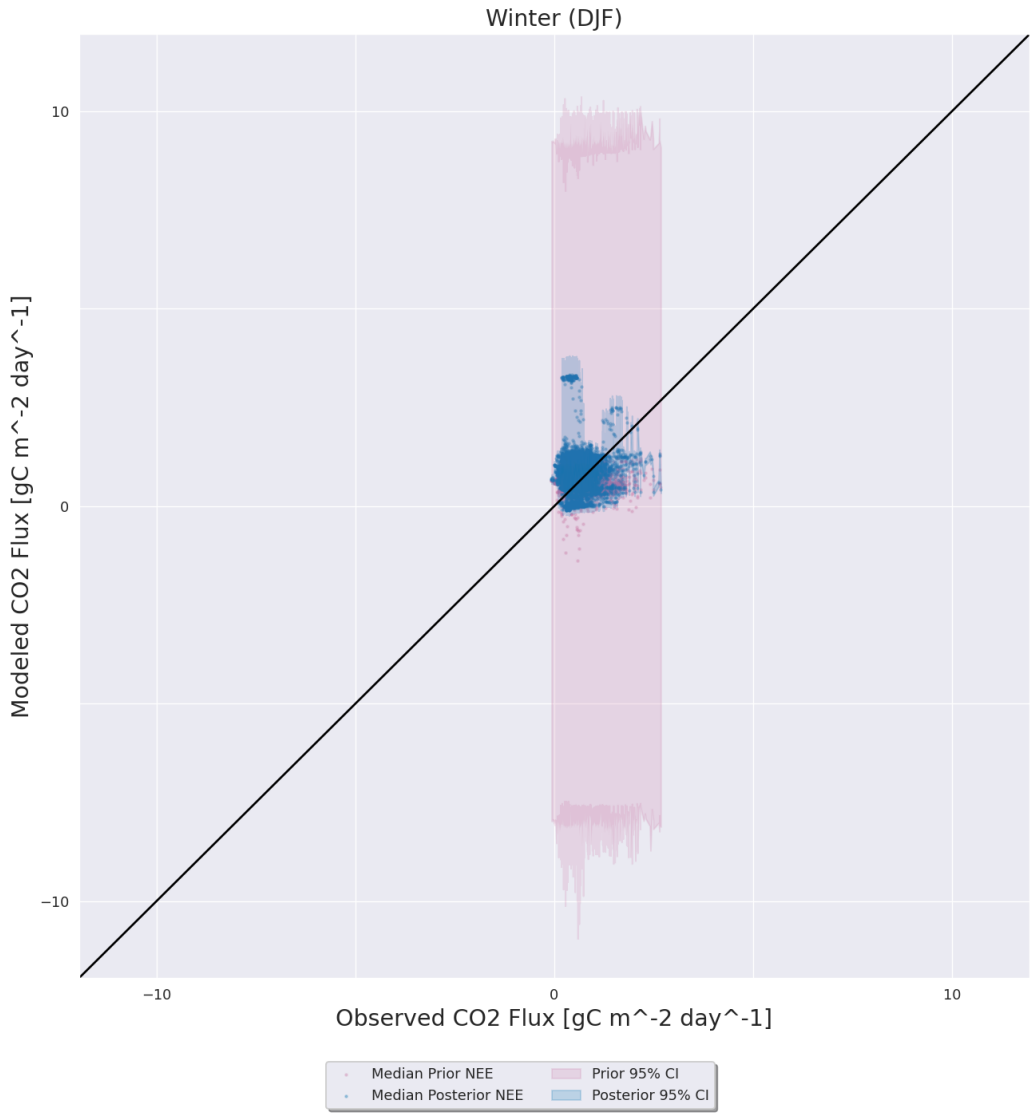

Figure D.47: Same as D.1 except for the k_3 parameter drop experiment.

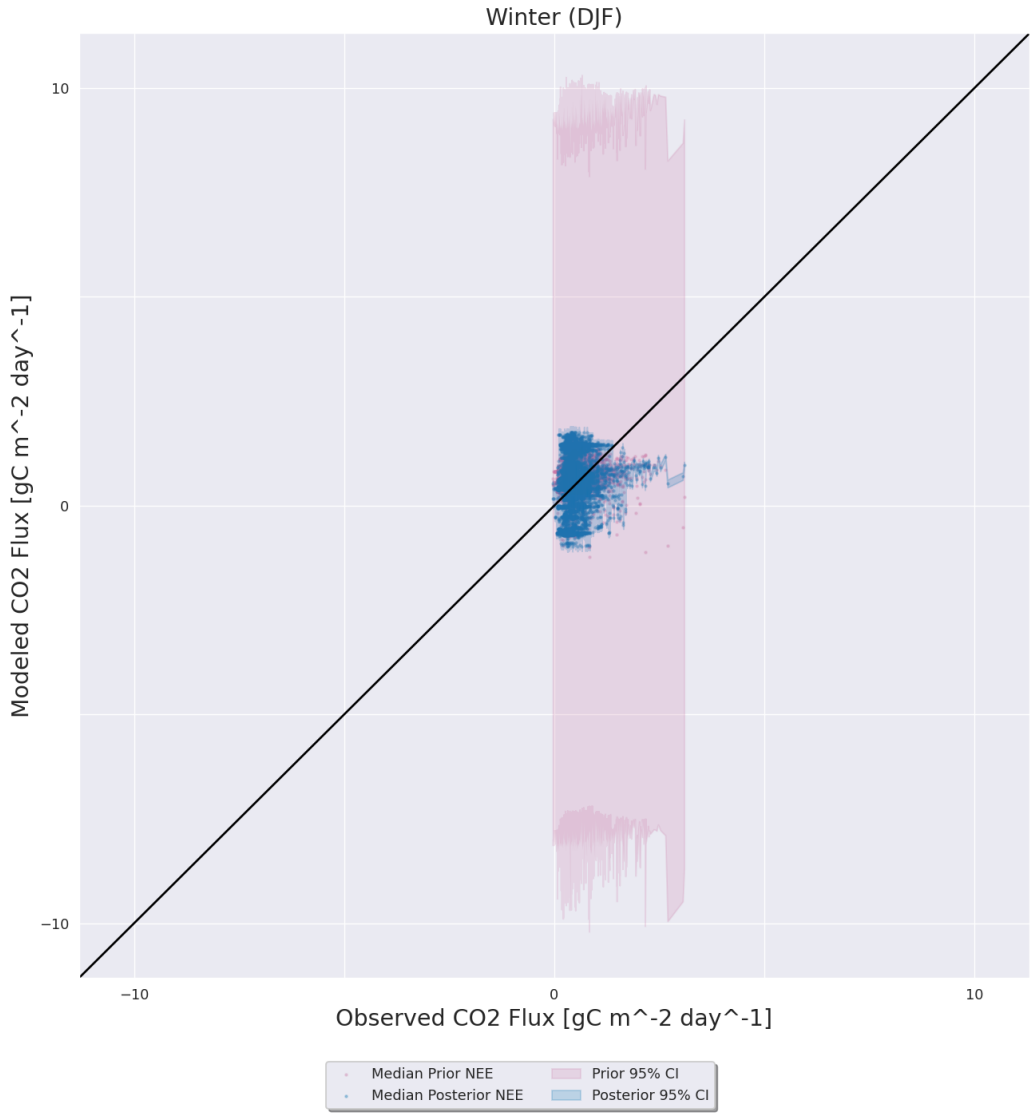

Figure D.48: Same as D.47 except for the Ne3 AmeriFlux site.

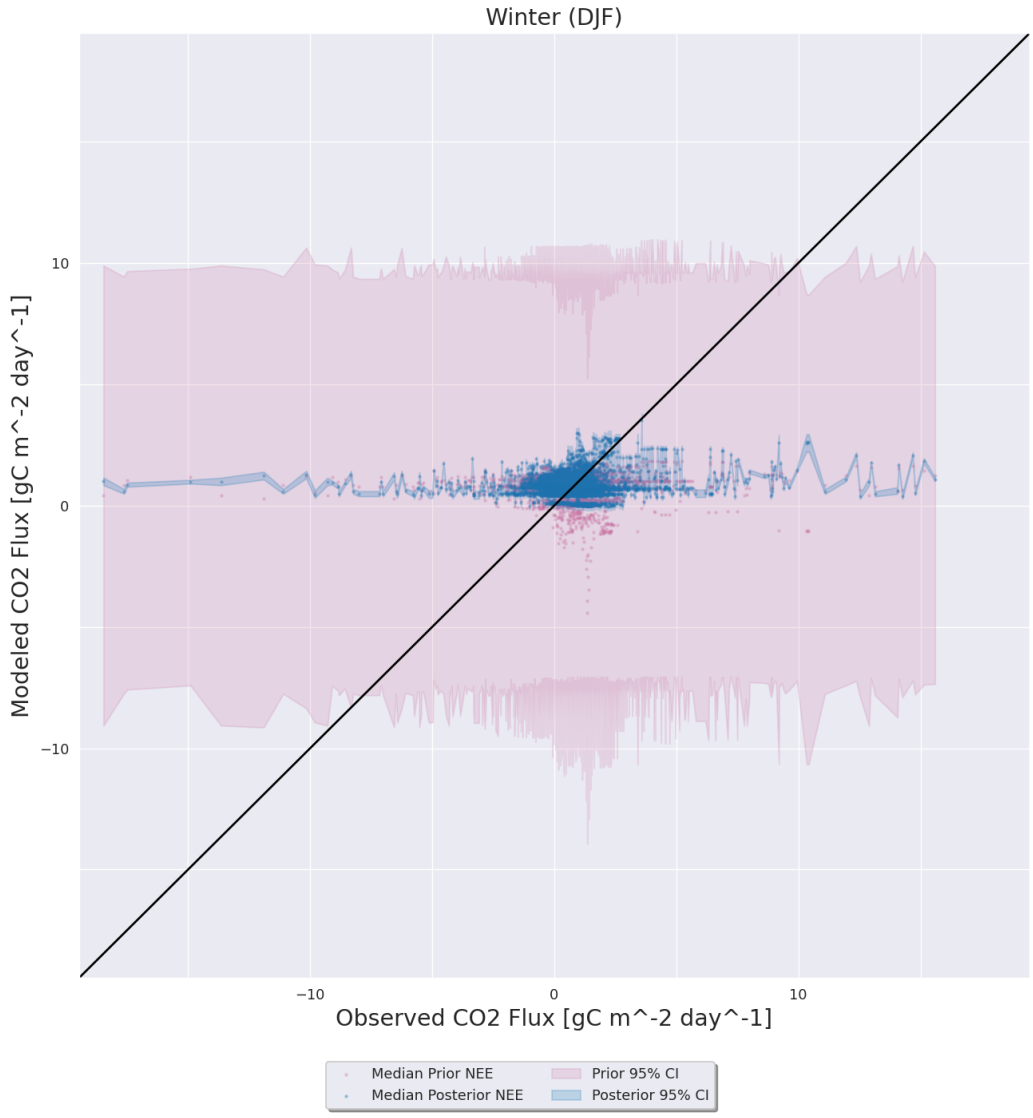

Figure D.49: Same as D.47 except for the KM1 AmeriFlux site.

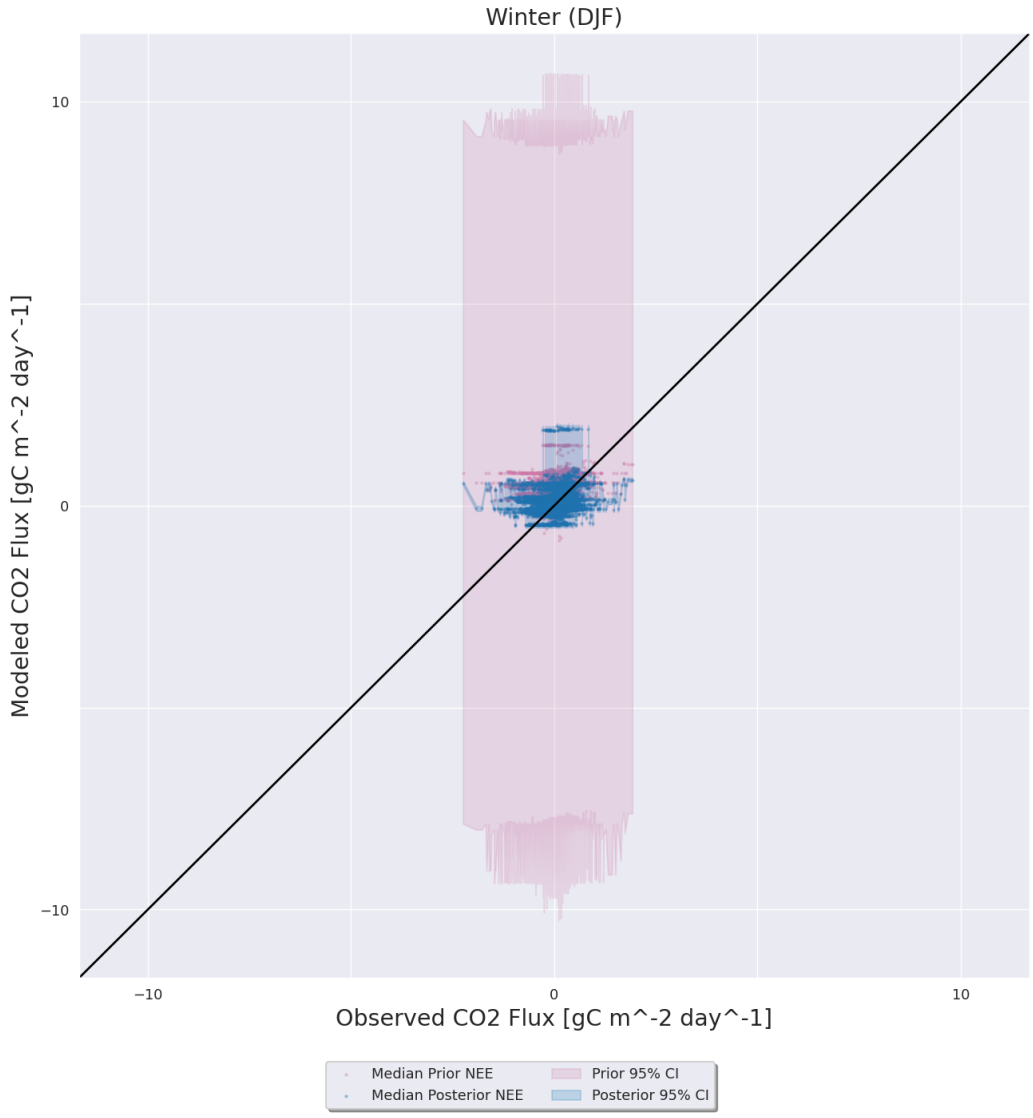

Figure D.50: Same as D.47 except for the Ro1 AmeriFlux site.

D.4.2 Spring (MAM)

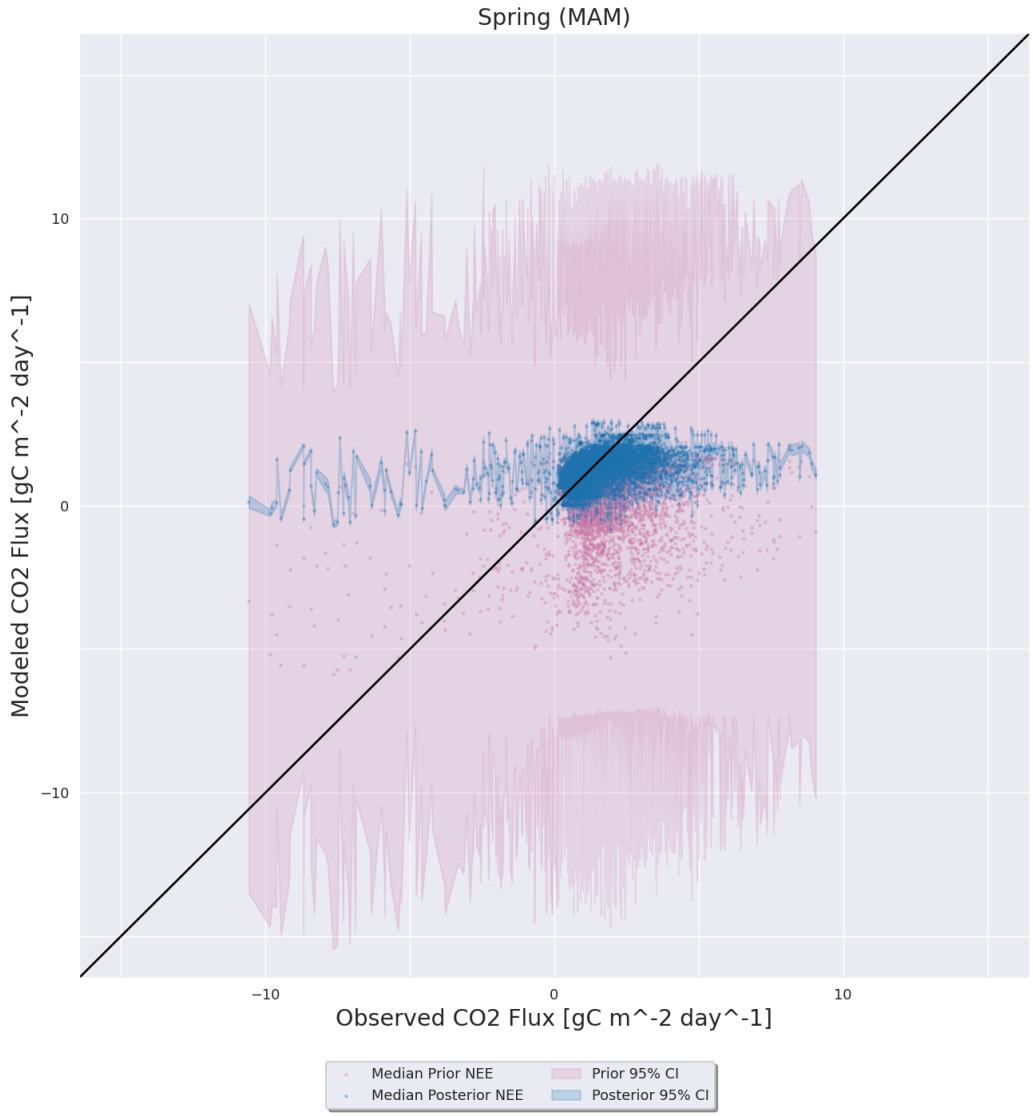

Figure D.51: Same as D.47 except for during the spring (MAM) months.

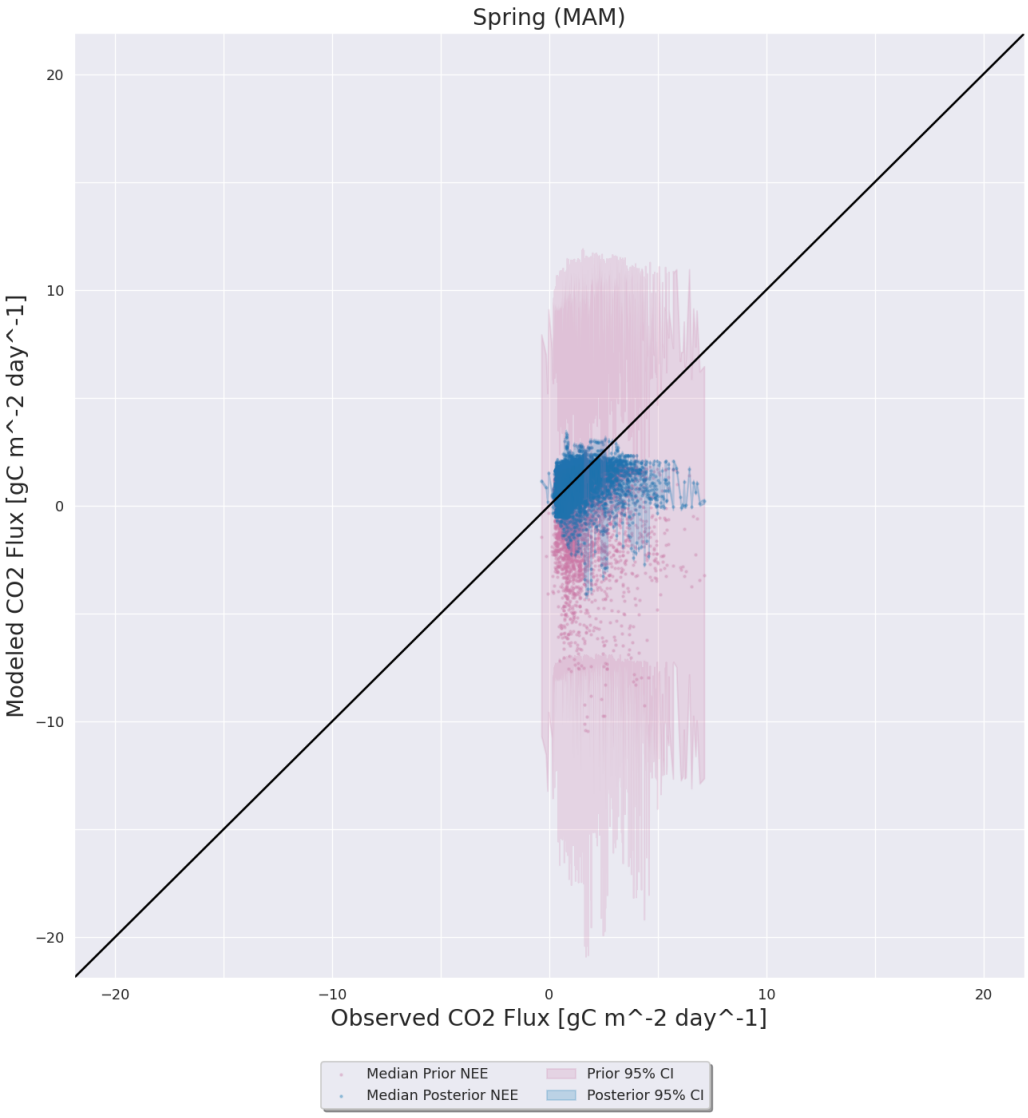

Figure D.52: Same as D.51 except for the Ne3 AmeriFlux site.

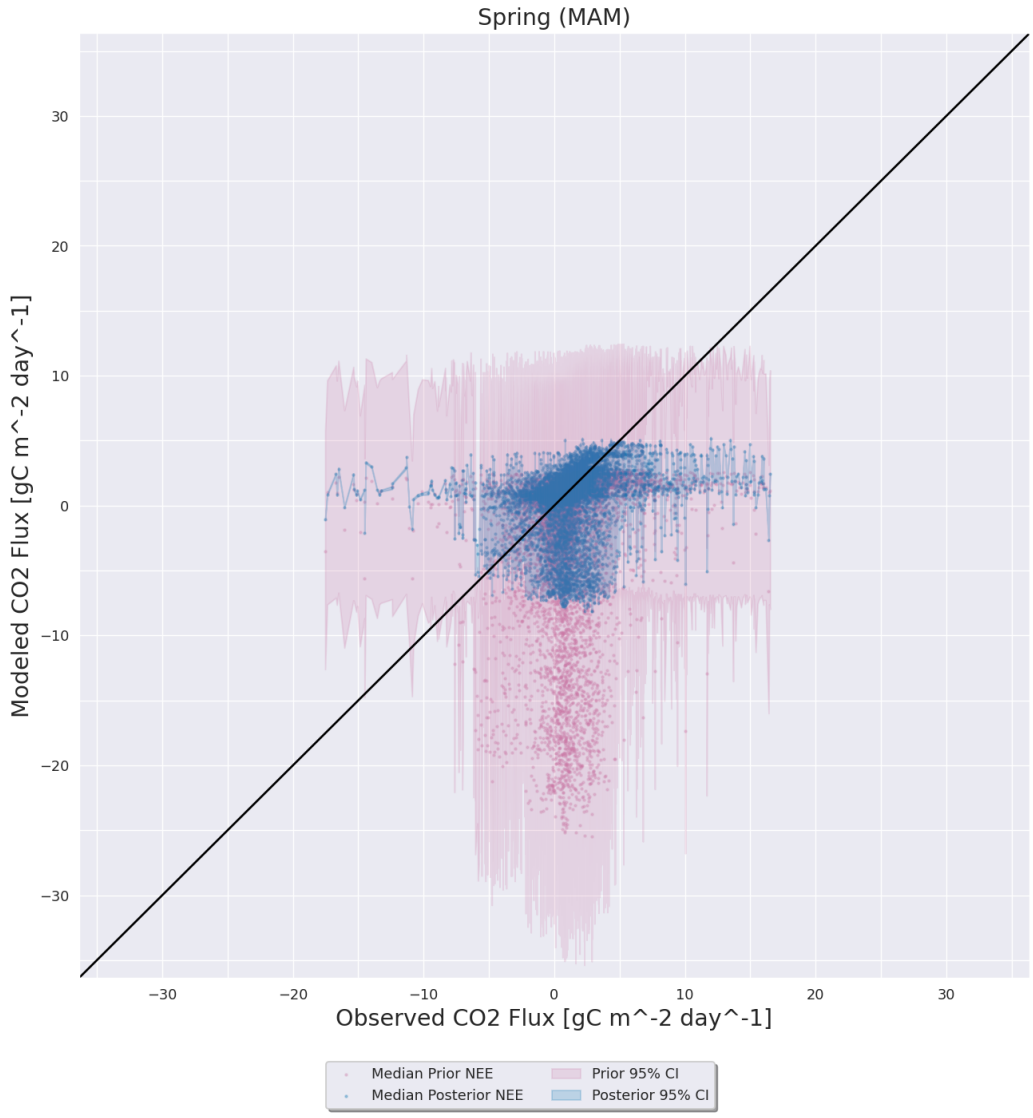

Figure D.53: Same as D.51 except for the KM1 AmeriFlux site.

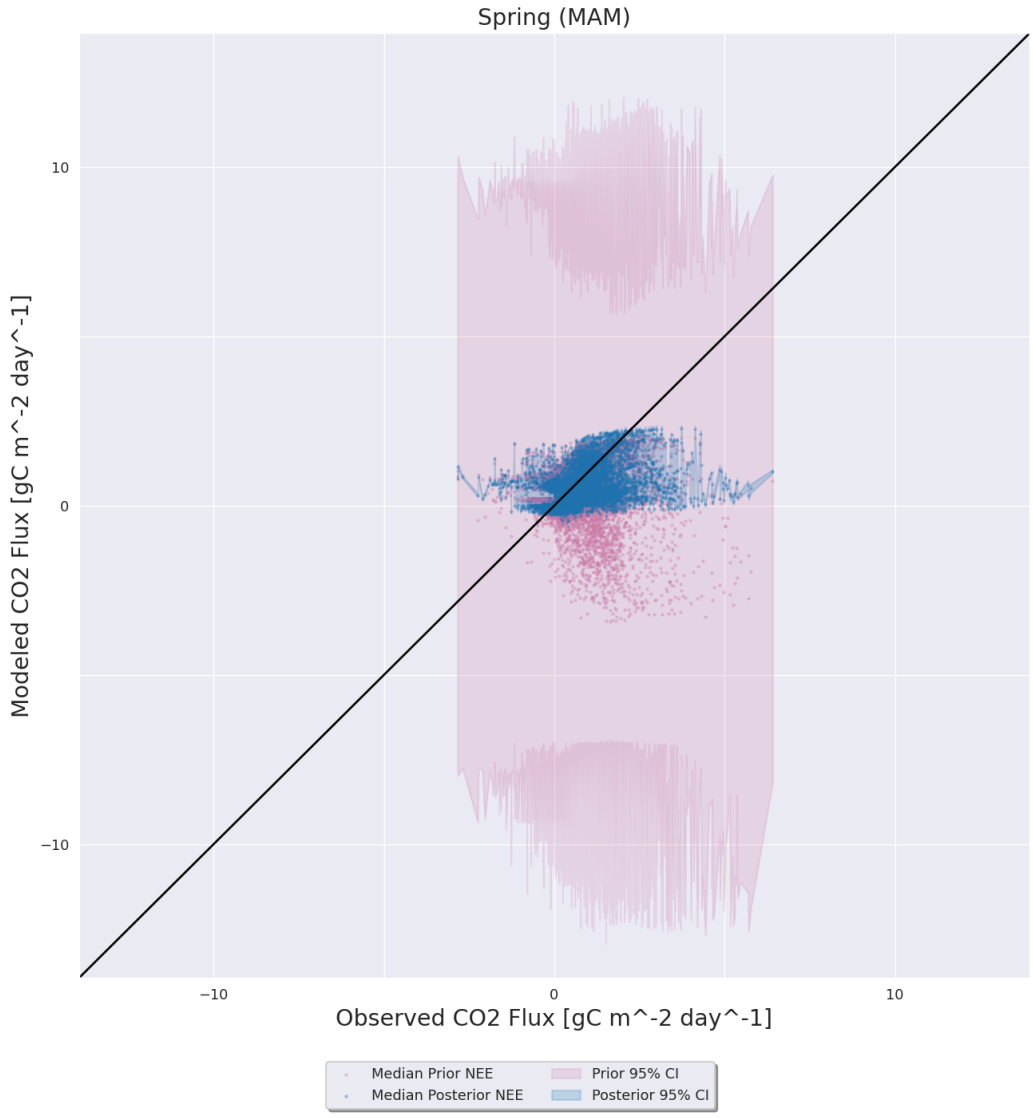

Figure D.54: Same as D.51 except for the Ro1 AmeriFlux site.

D.4.3 Summer (JJA)

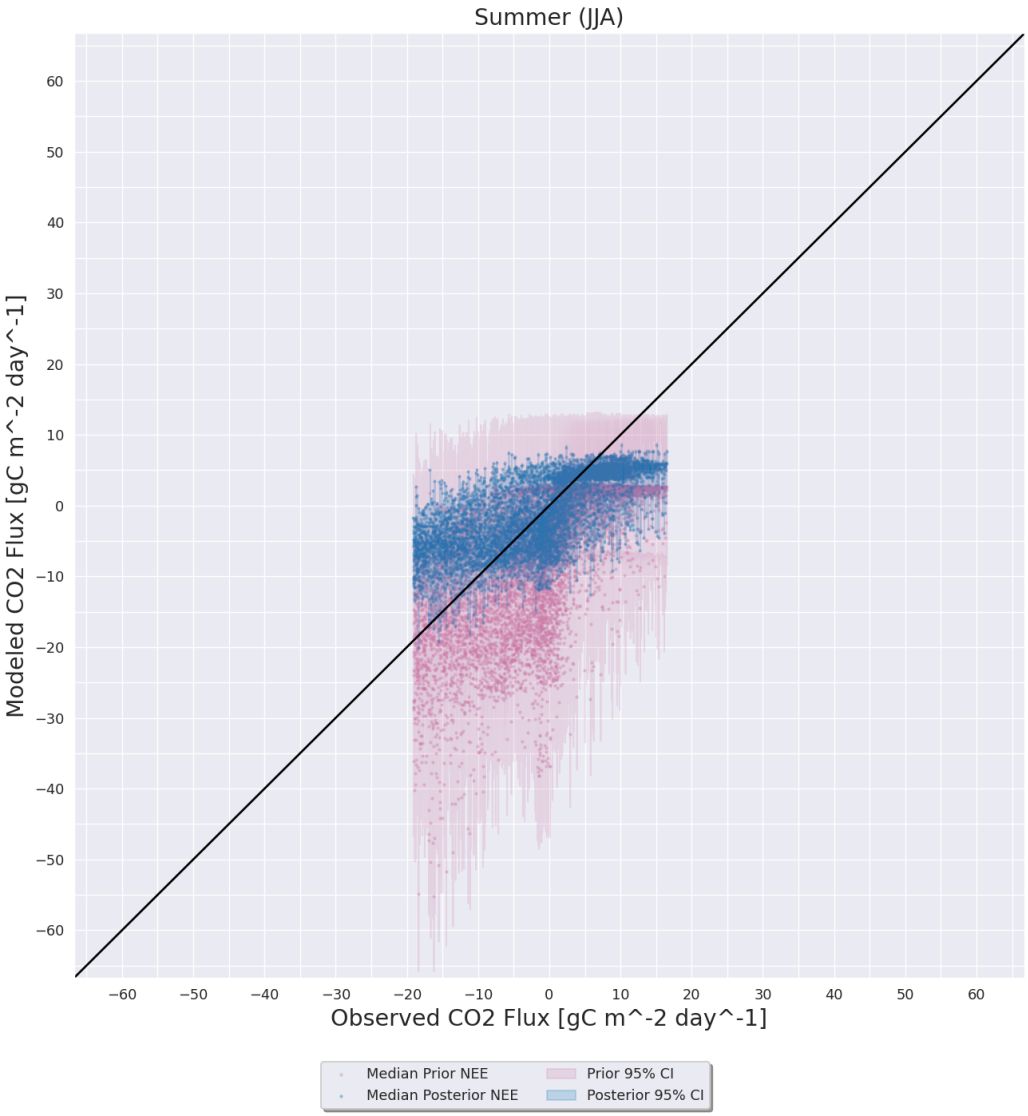

Figure D.55: Same as 4.5 except for the KM1 AmeriFlux site.

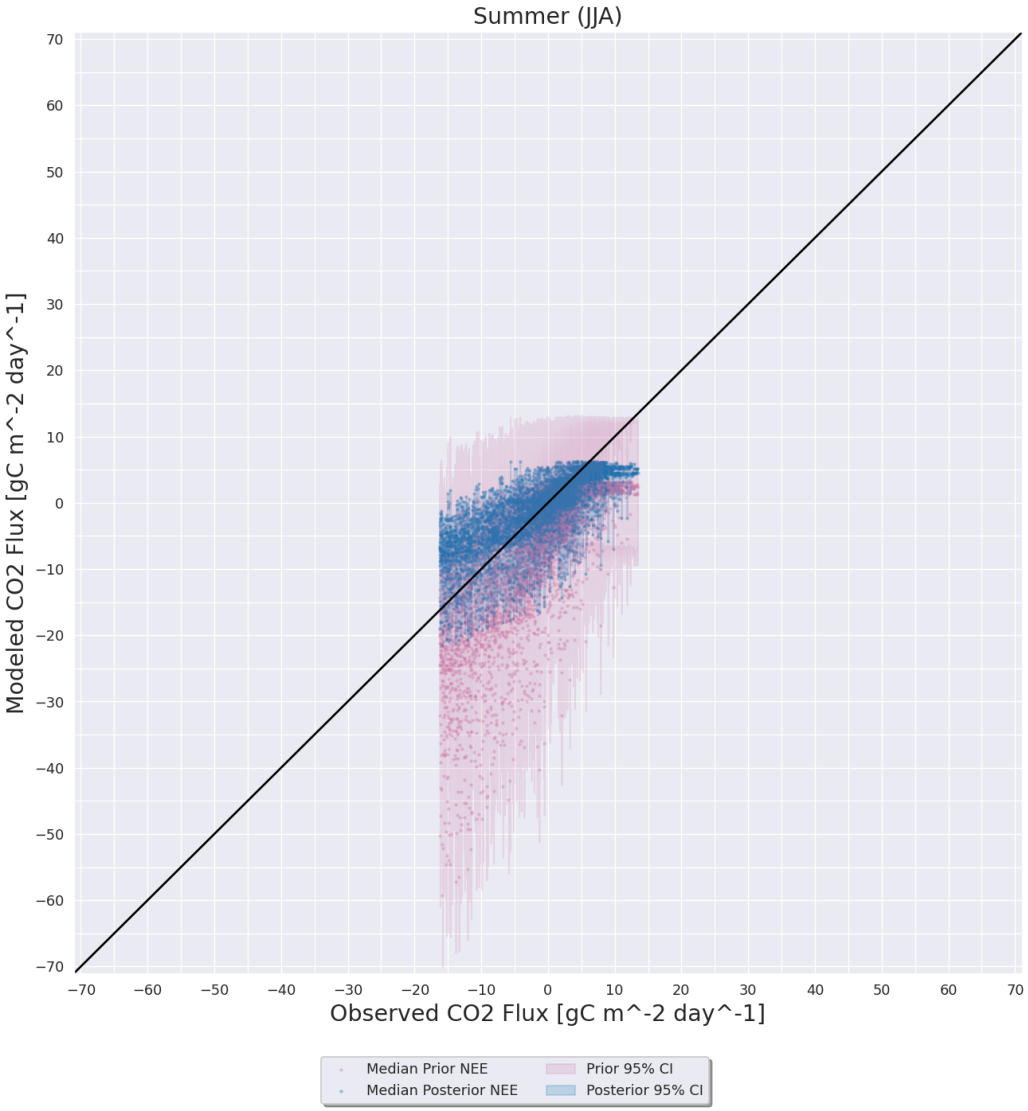

Figure D.56: Same as 4.5 except for the Ro1 AmeriFlux site.

D.4.4 Autumn (SON)

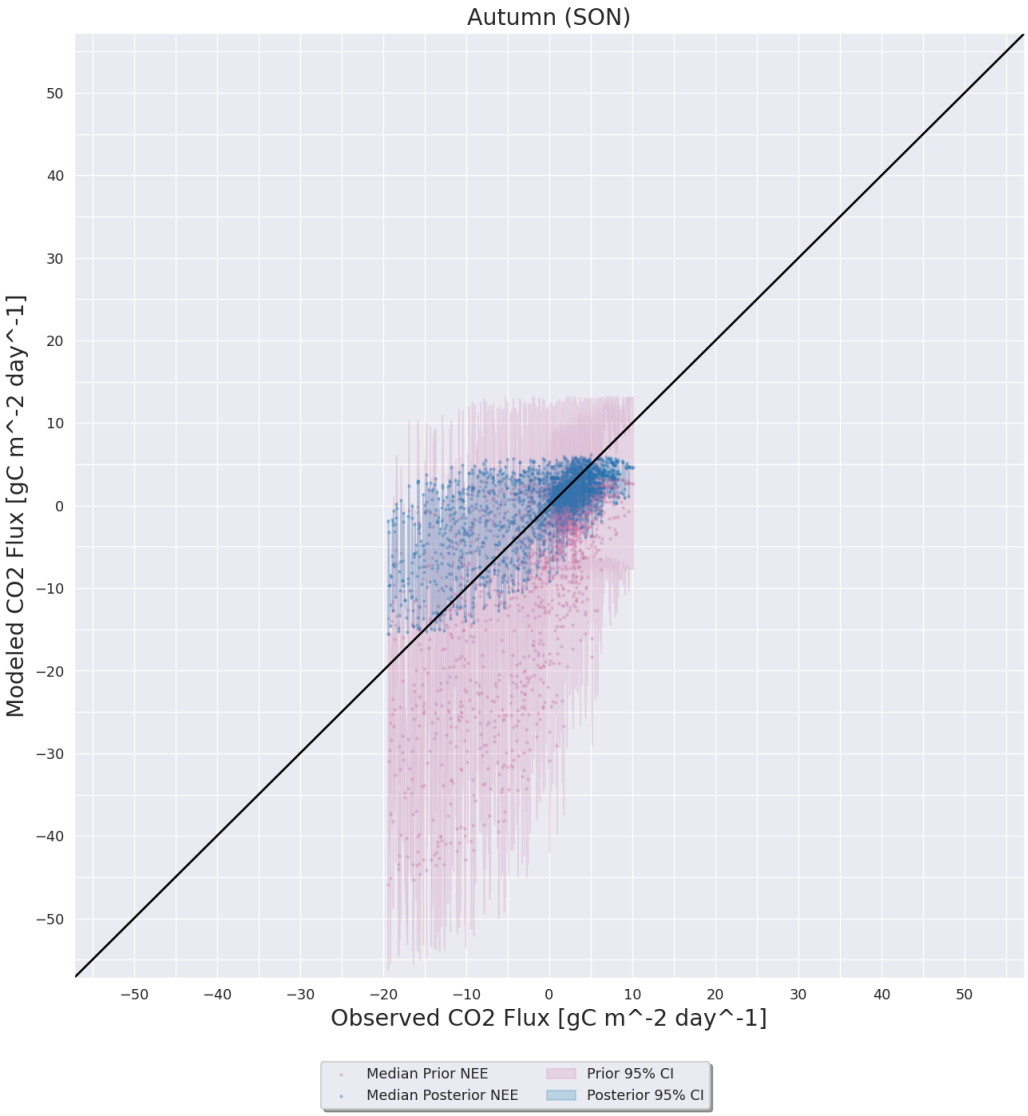

Figure D.57: Same as D.47 except for during the autumn (SON) months.

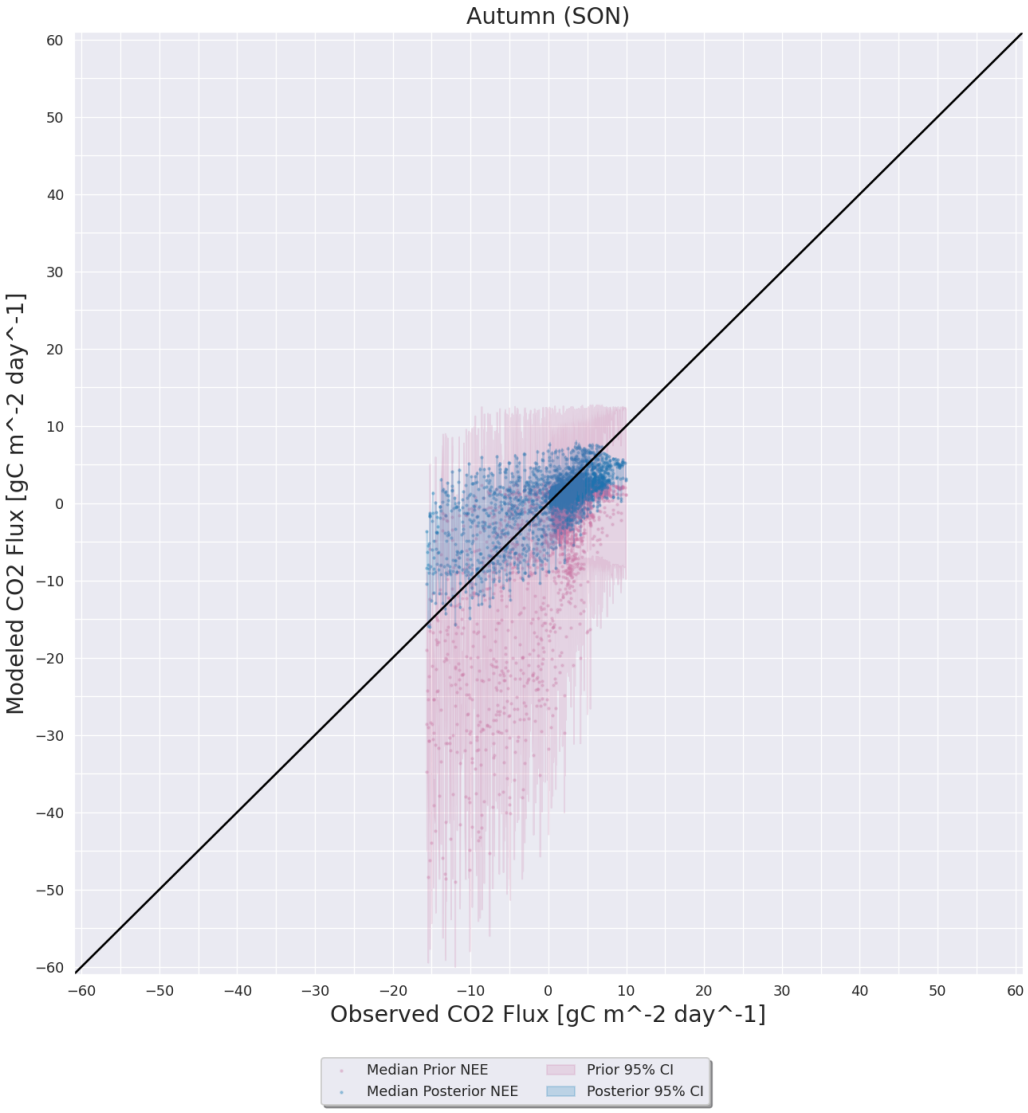

Figure D.58: Same as D.57 except for the Ne3 AmeriFlux site.

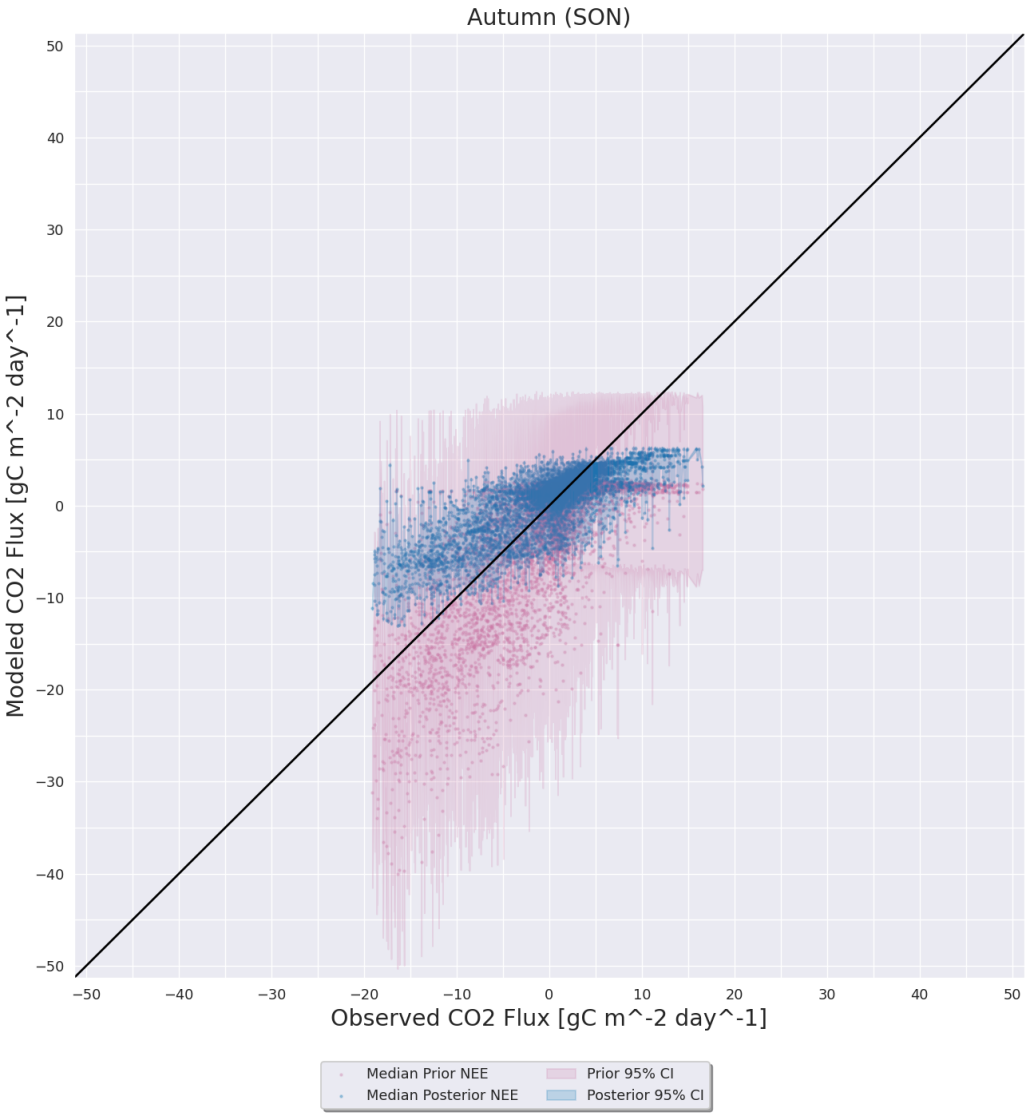

Figure D.59: Same as D.57 except for the KM1 AmeriFlux site.

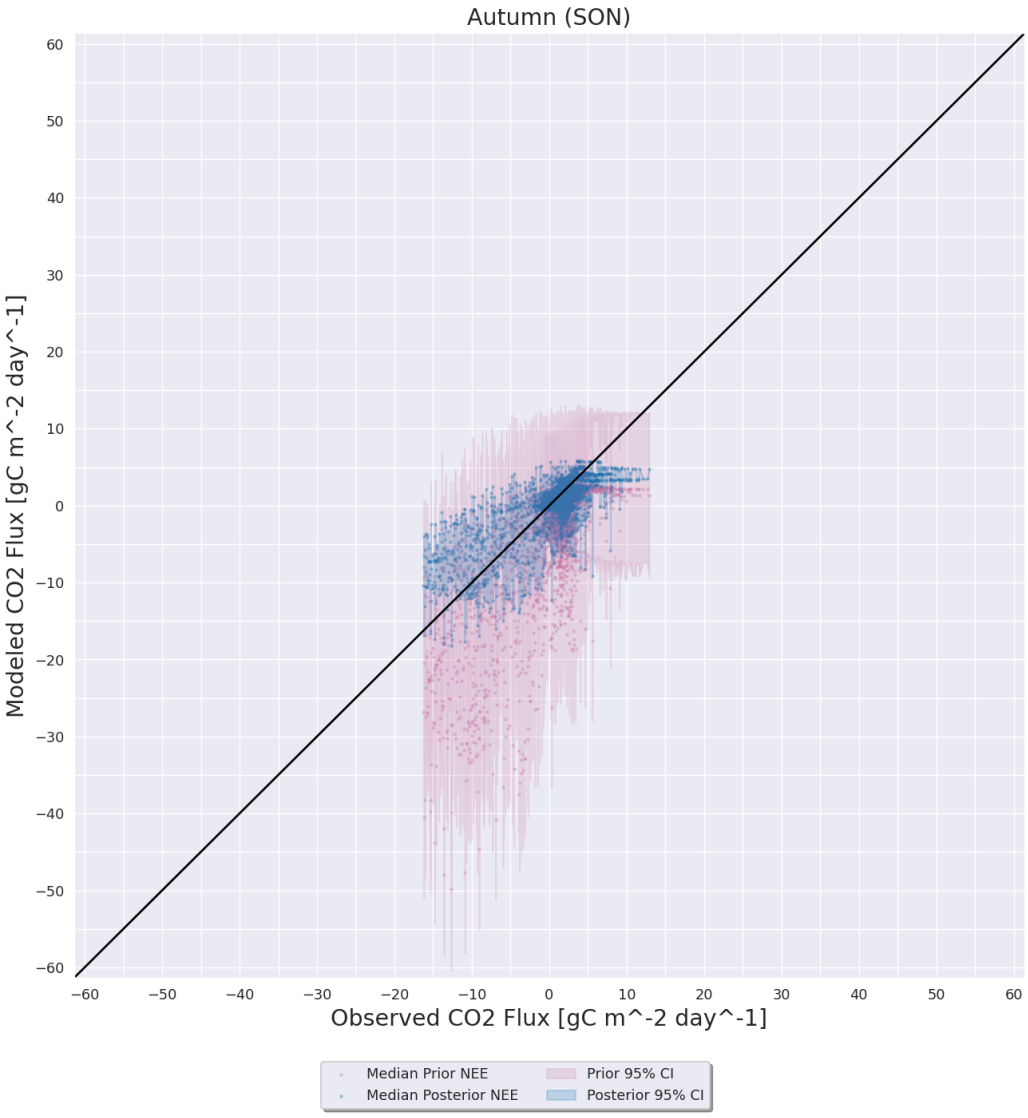

Figure D.60: Same as D.57 except for the Ro1 AmeriFlux site.

D.5 λ Drop Experiment

D.5.1 Winter (DJF)

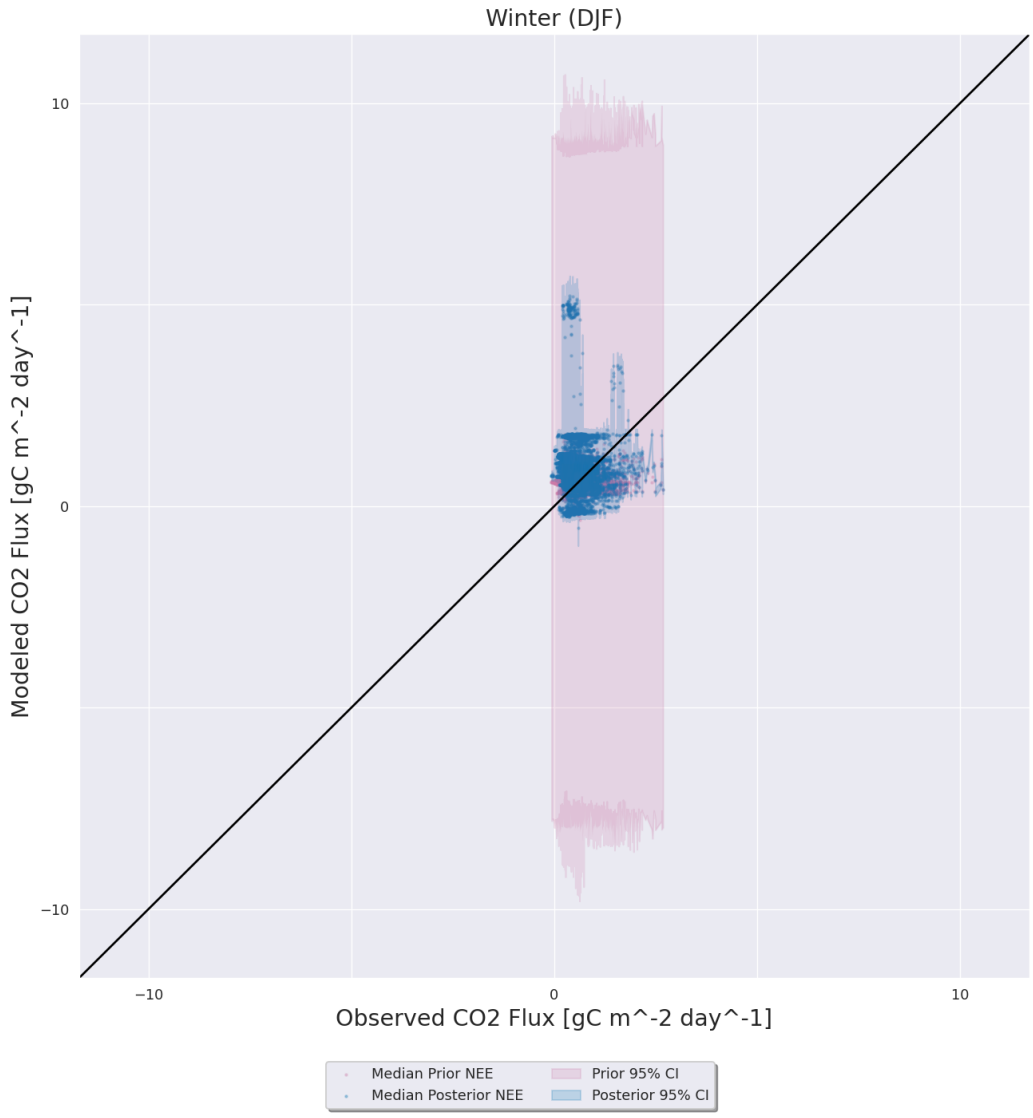

Figure D.61: Same as D.1 except for the λ parameter drop experiment.

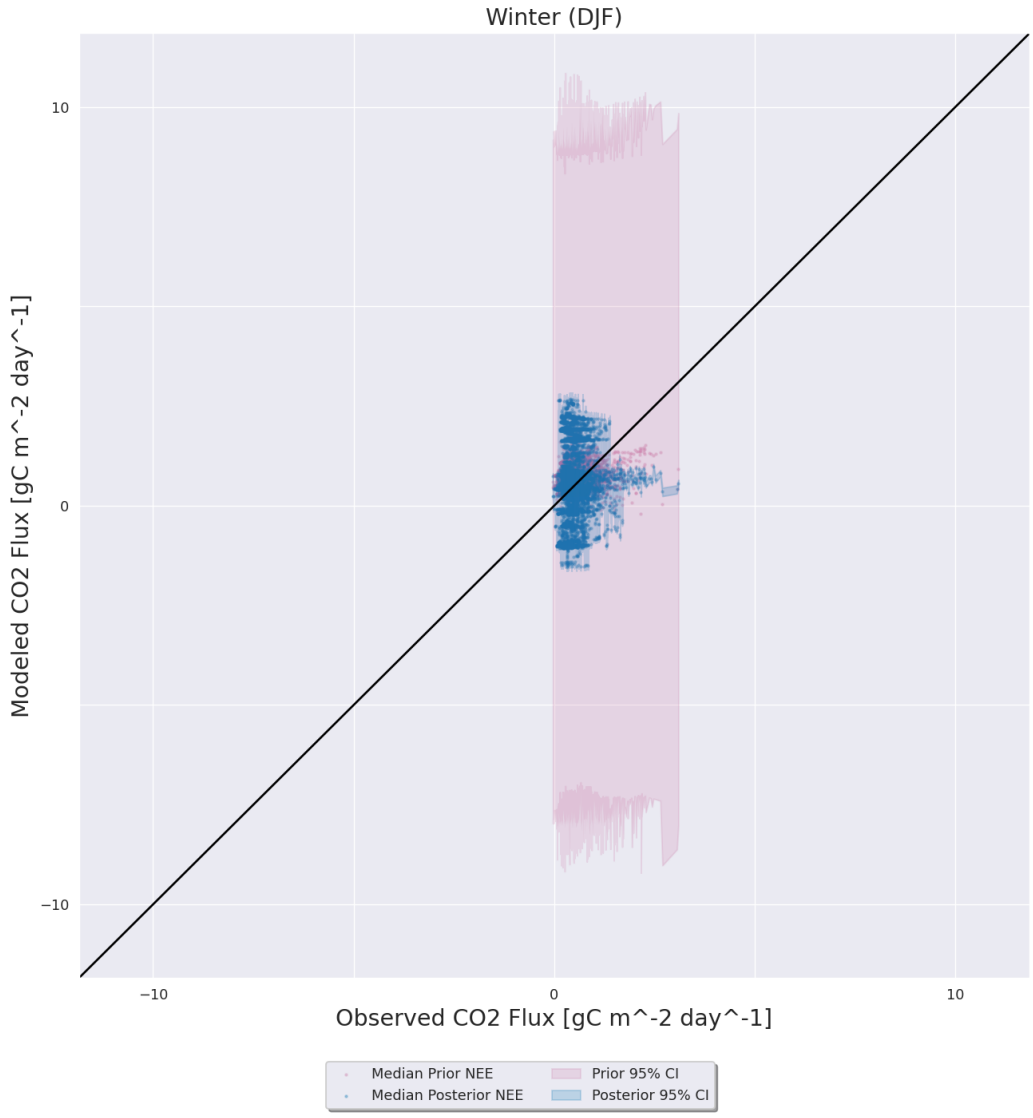

Figure D.62: Same as D.61 except for the Ne3 AmeriFlux site.

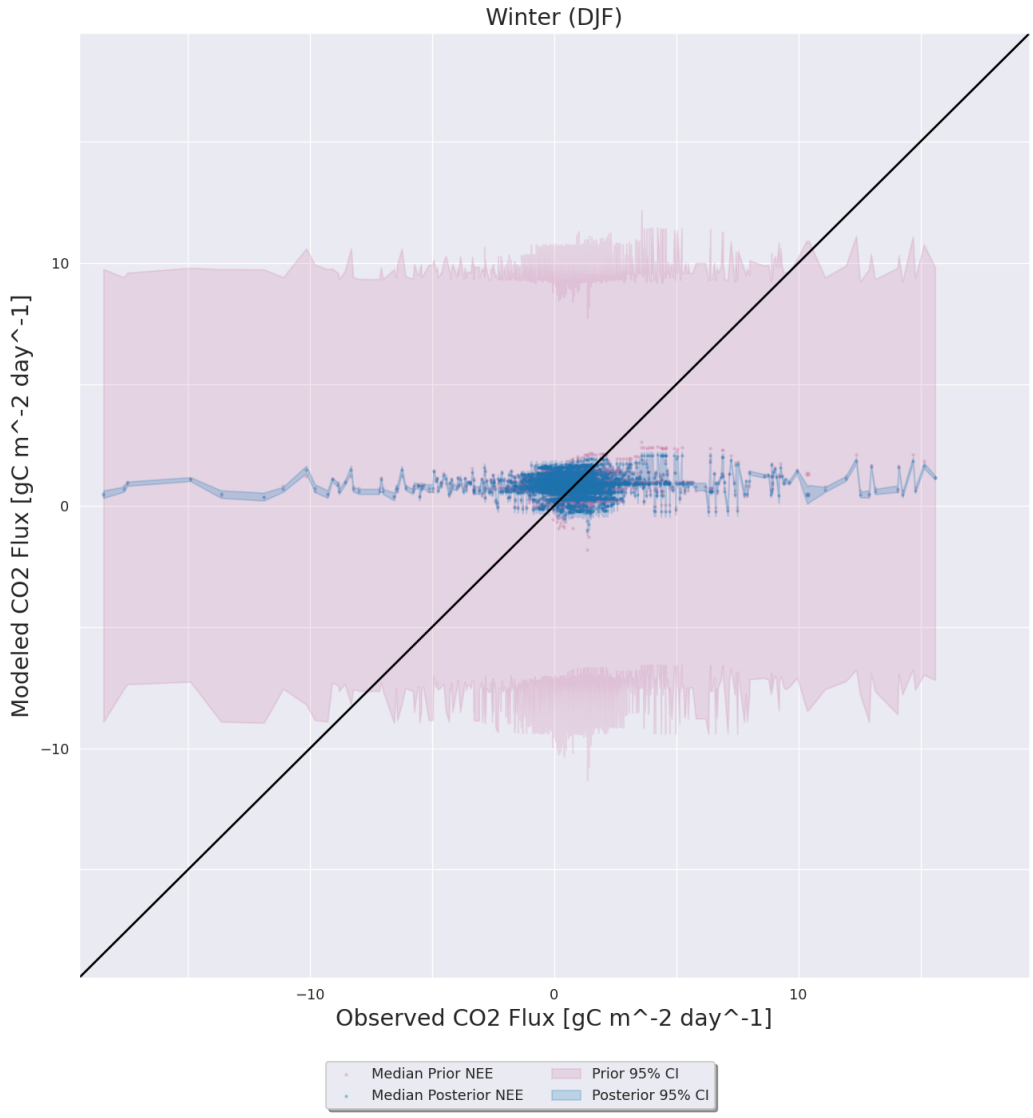

Figure D.63: Same as D.61 except for the KM1 AmeriFlux site.

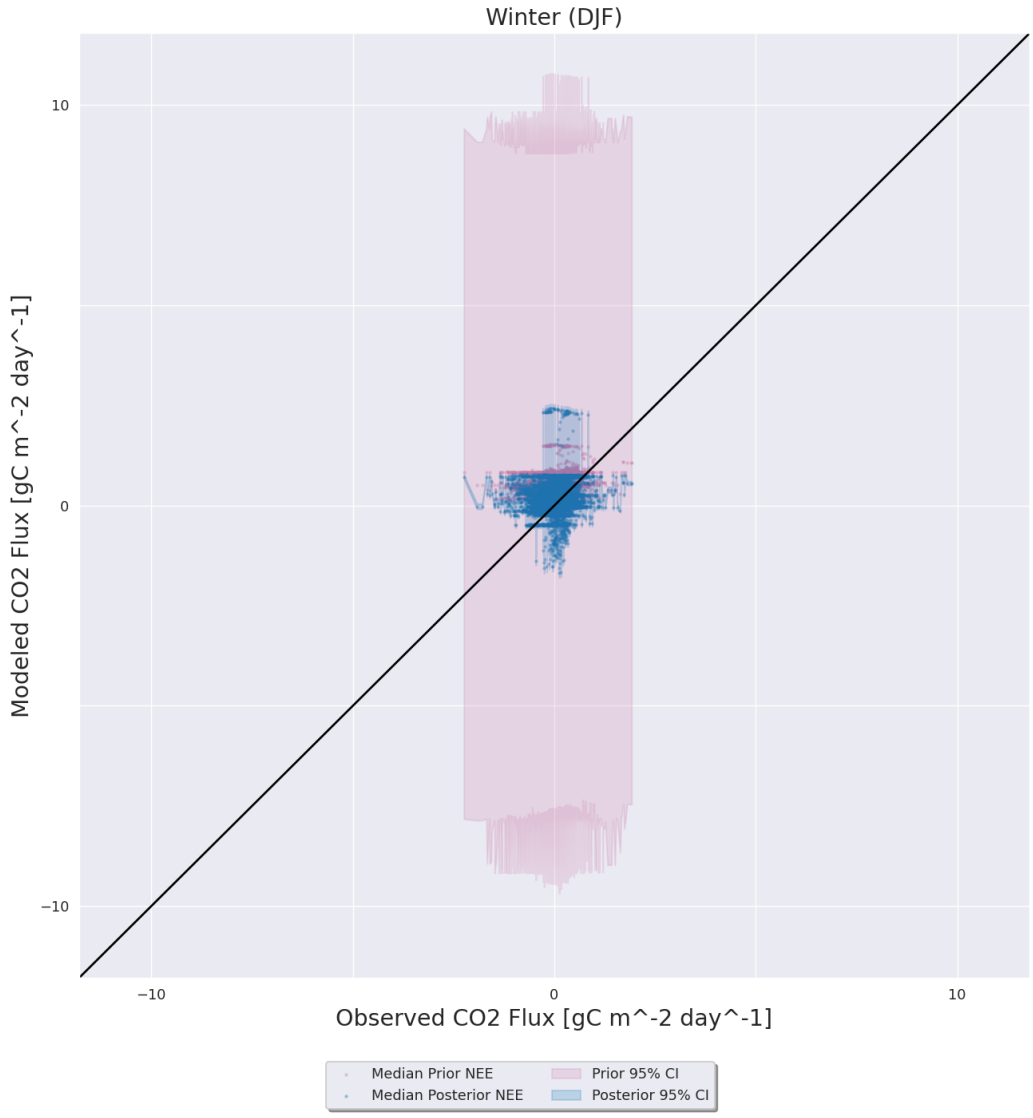

Figure D.64: Same as D.61 except for the Ro1 AmeriFlux site.

D.5.2 Spring (MAM)

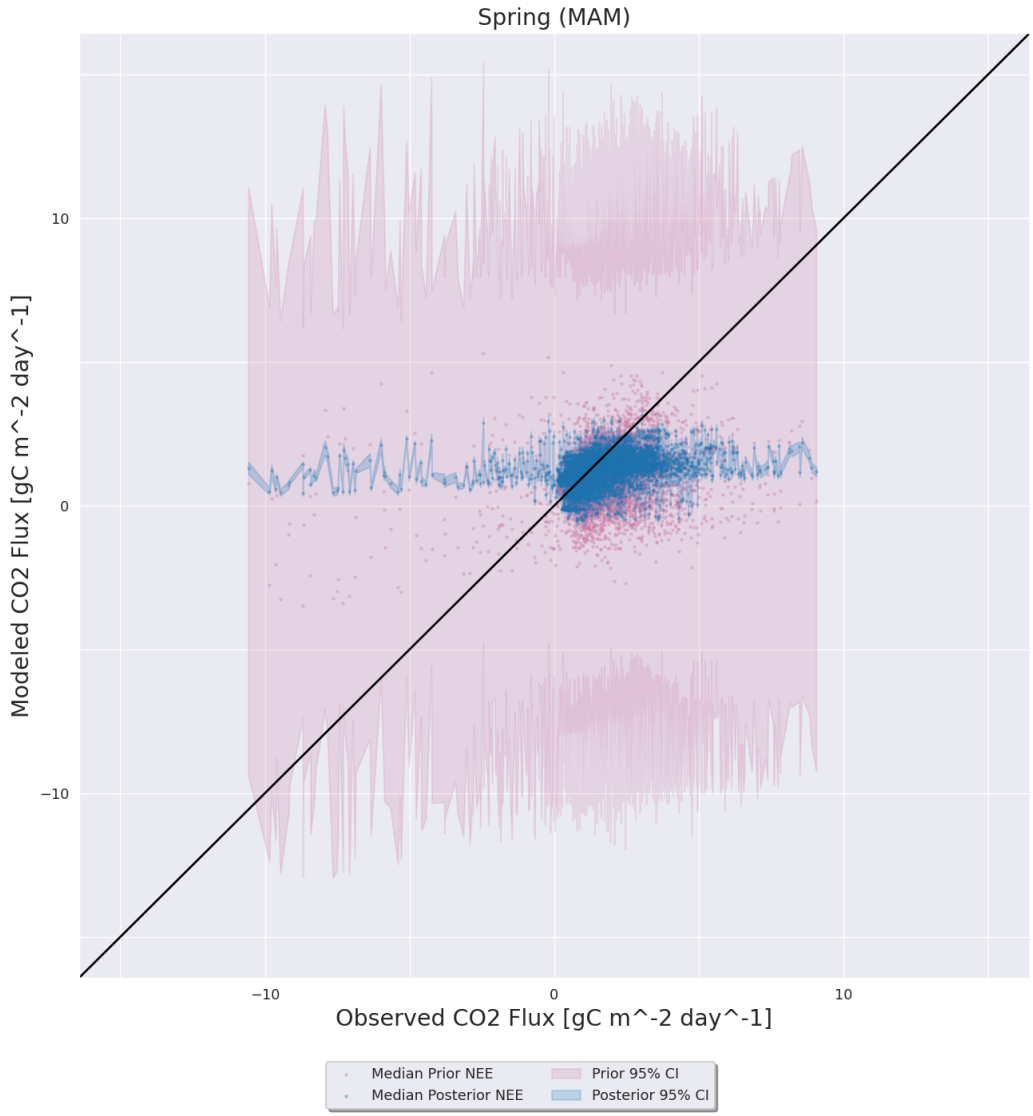

Figure D.65: Same as D.61 except for during the spring (MAM) months.

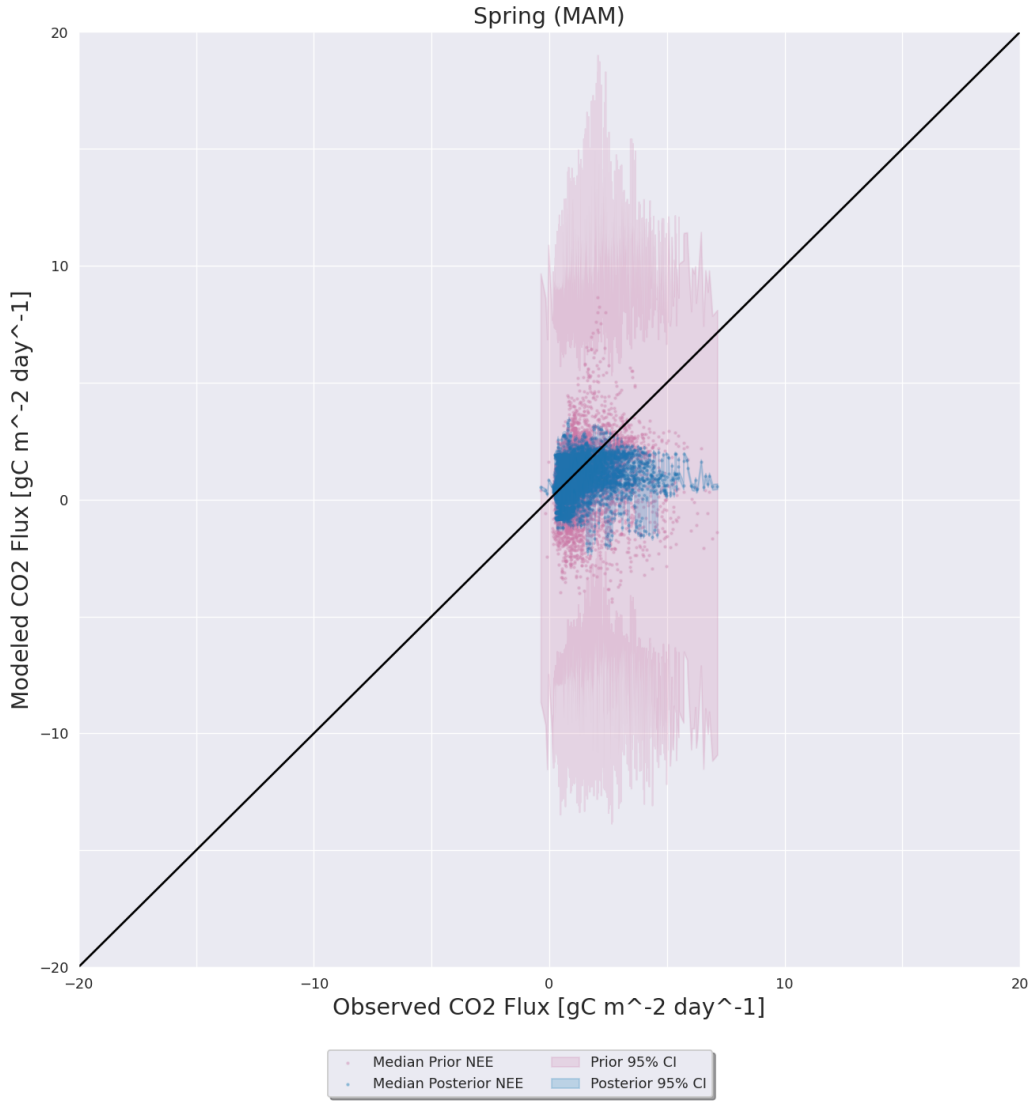

Figure D.66: Same as D.65 except for the Ne3 AmeriFlux site.

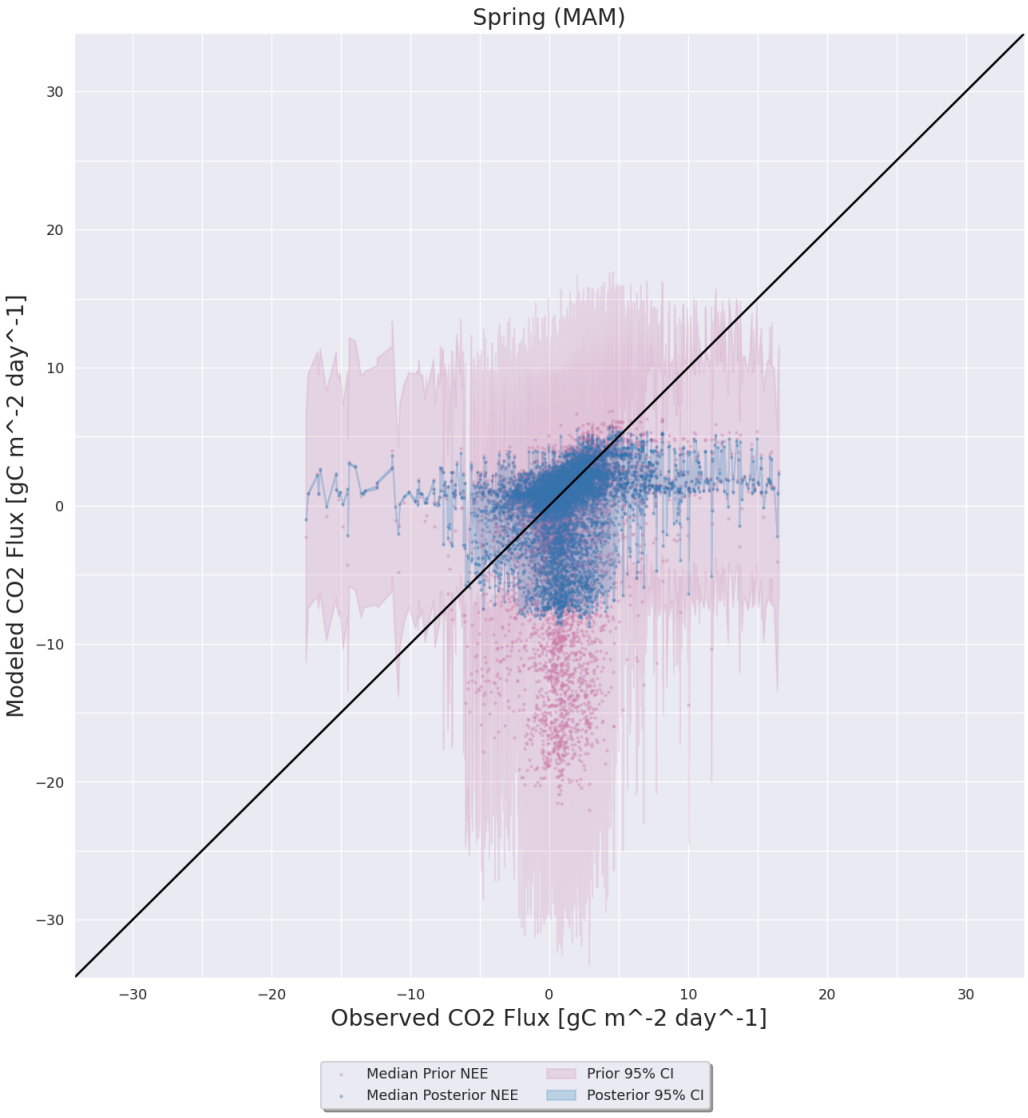

Figure D.67: Same as D.65 except for the KM1 AmeriFlux site.

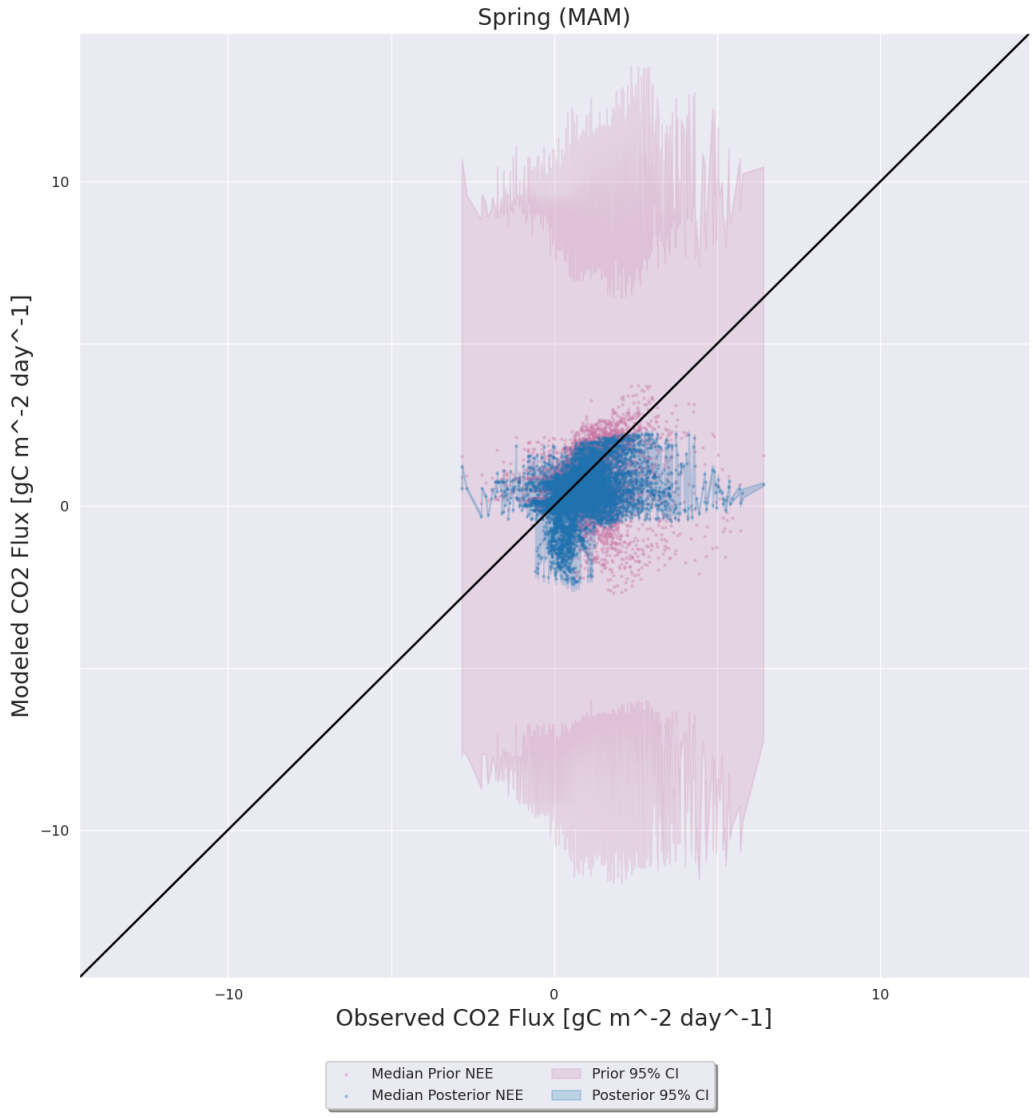

Figure D.68: Same as D.65 except for the Ro1 AmeriFlux site.

D.5.3 Summer (JJA)

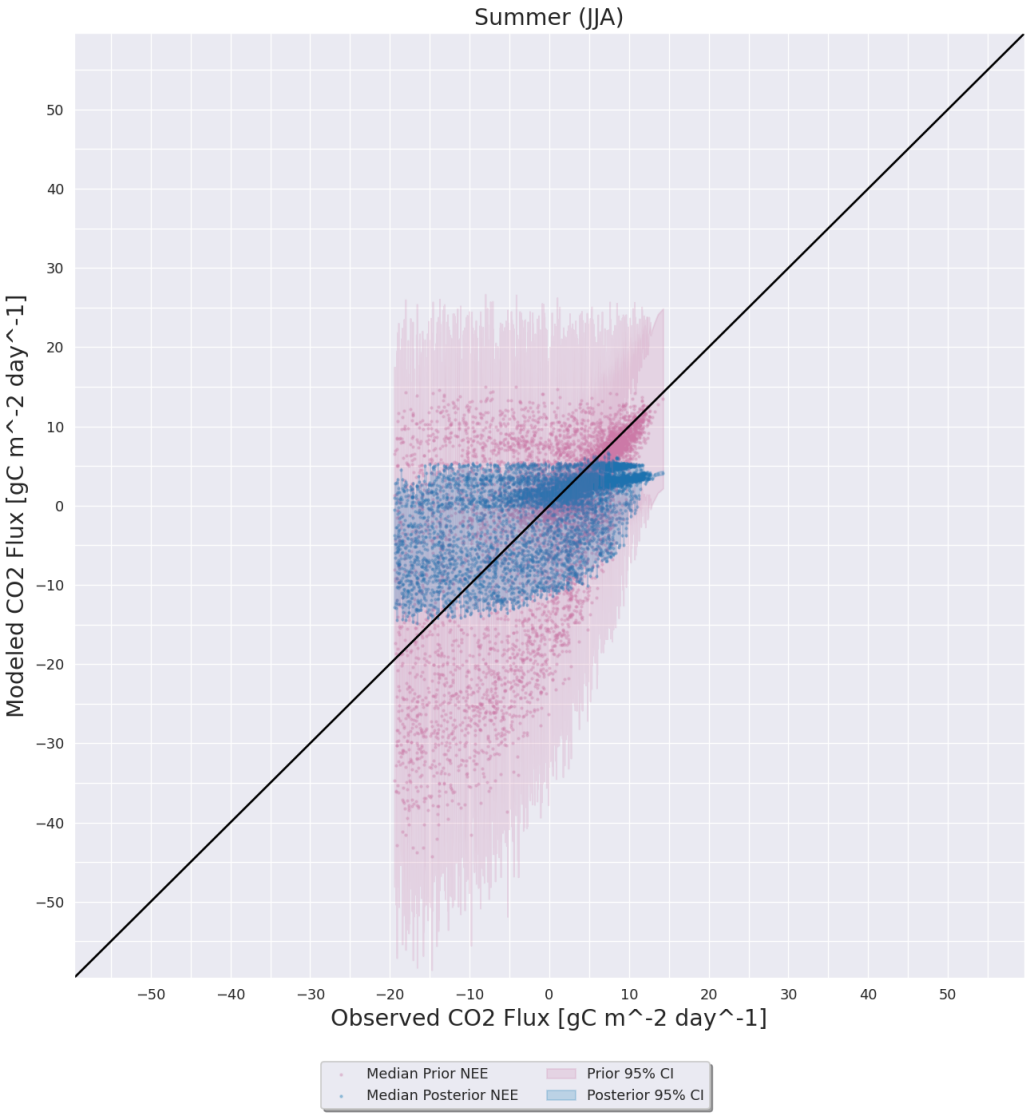

Figure D.69: Same as D.61 except for during the summer (JJA) months.

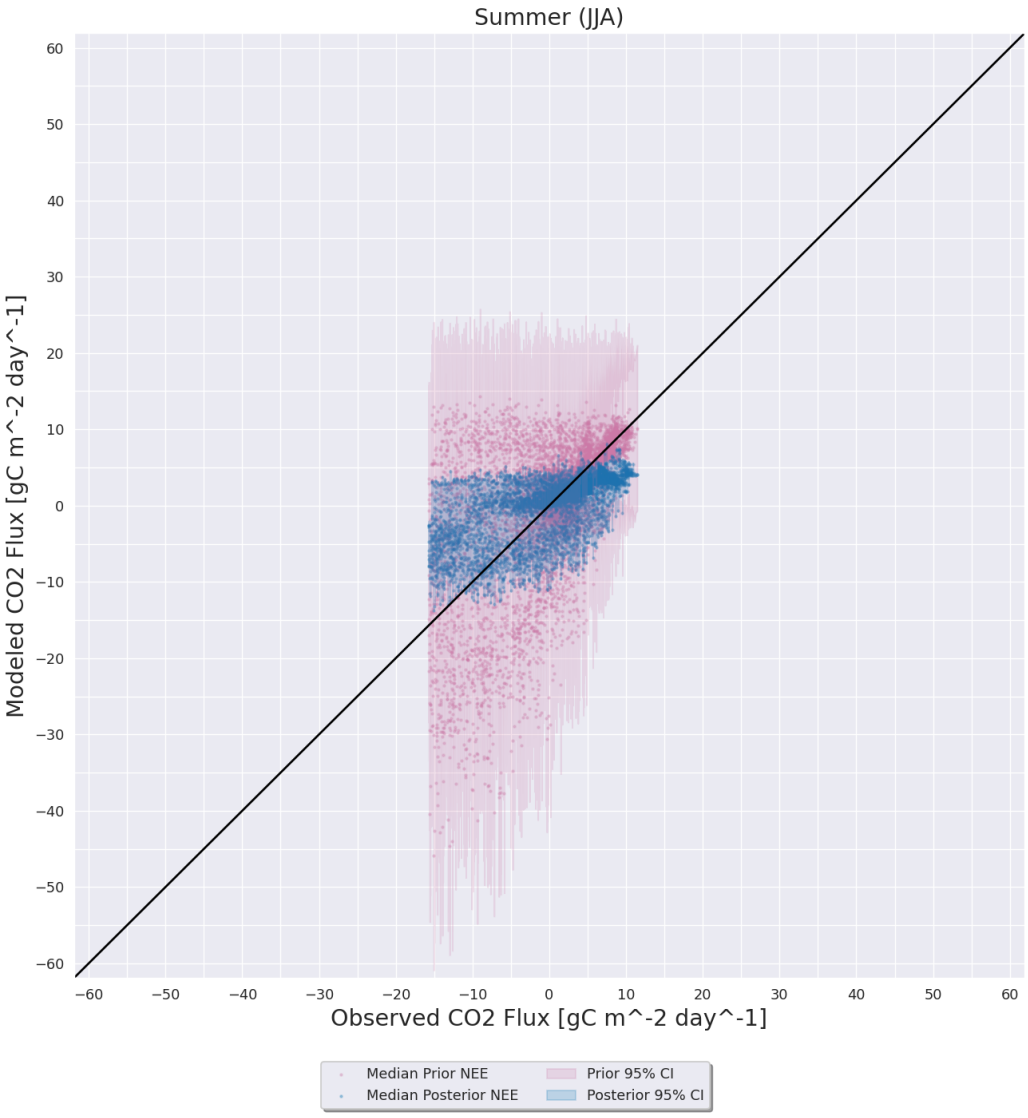

Figure D.70: Same as D.69 except for the Ne3 AmeriFlux site.

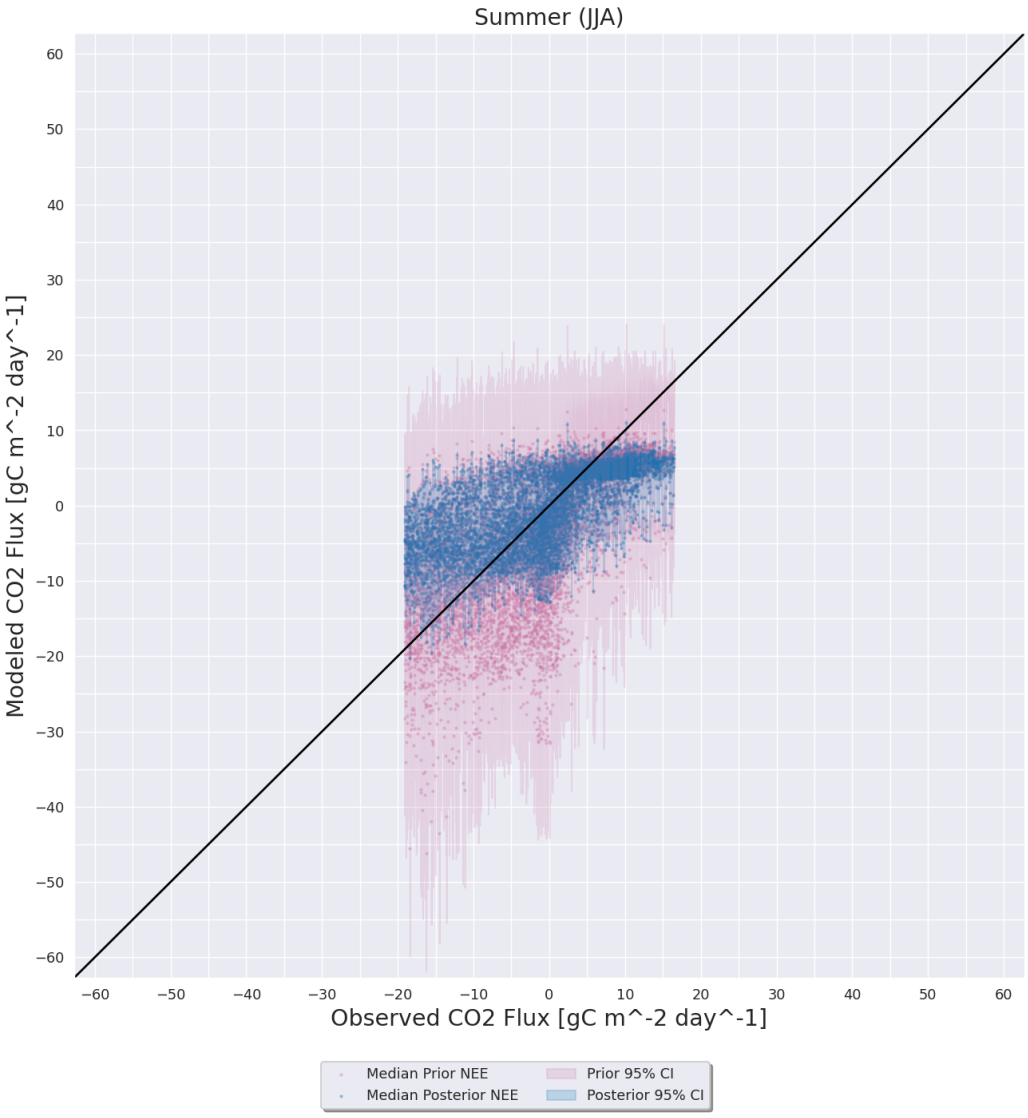

Figure D.71: Same as D.69 except for the KM1 AmeriFlux site.

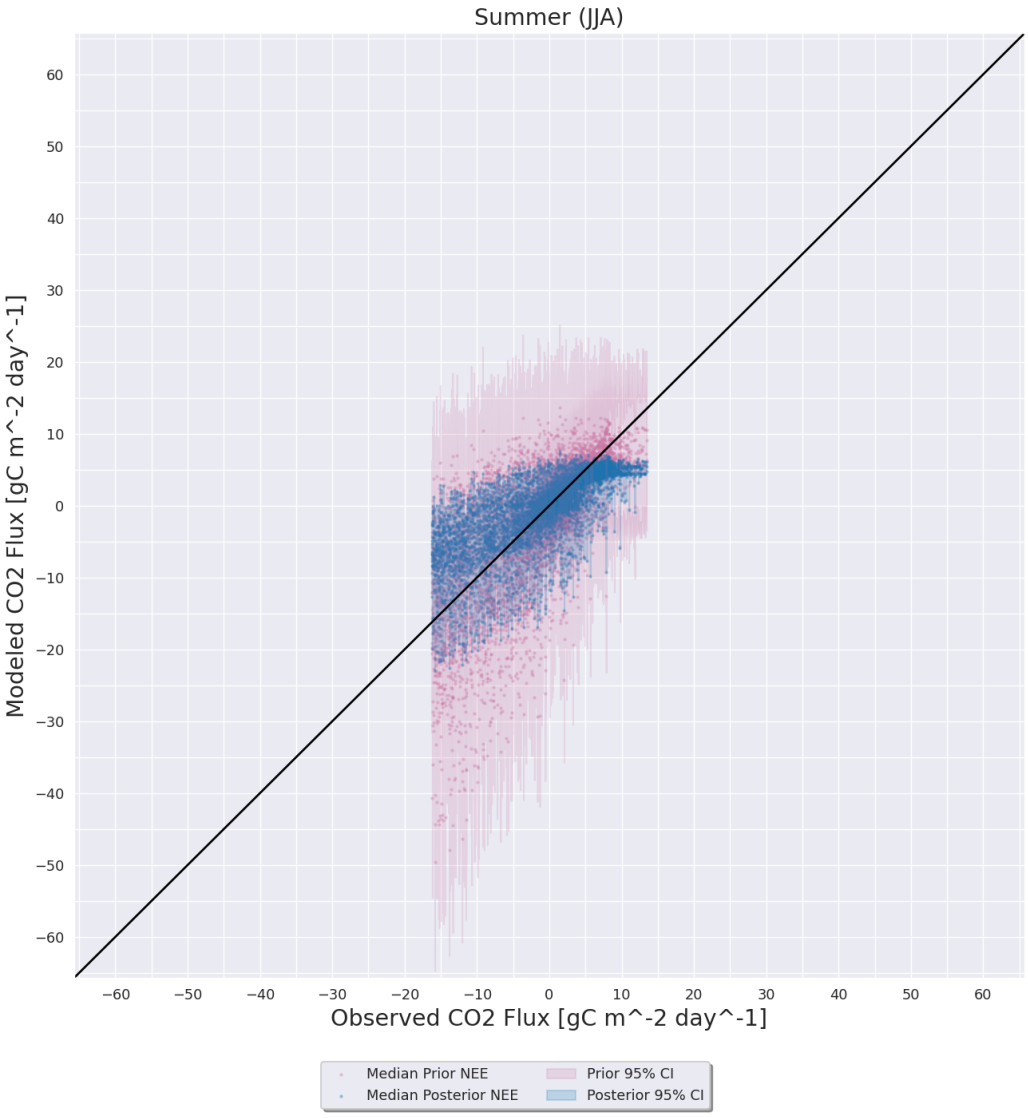

Figure D.72: Same as D.69 except for the Ro1 AmeriFlux site.

D.5.4 Autumn (SON)

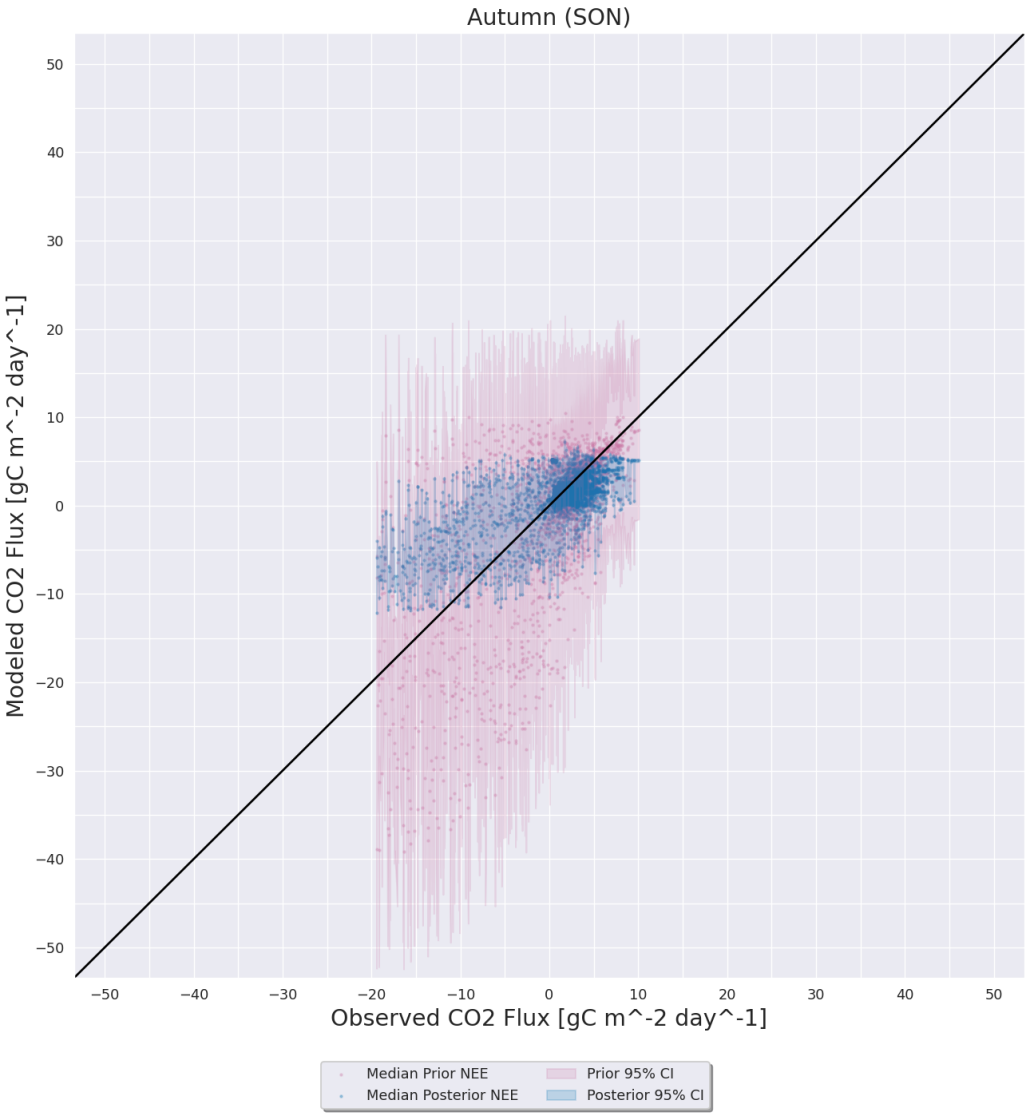

Figure D.73: Same as D.61 except for during the autumn (SON) months.

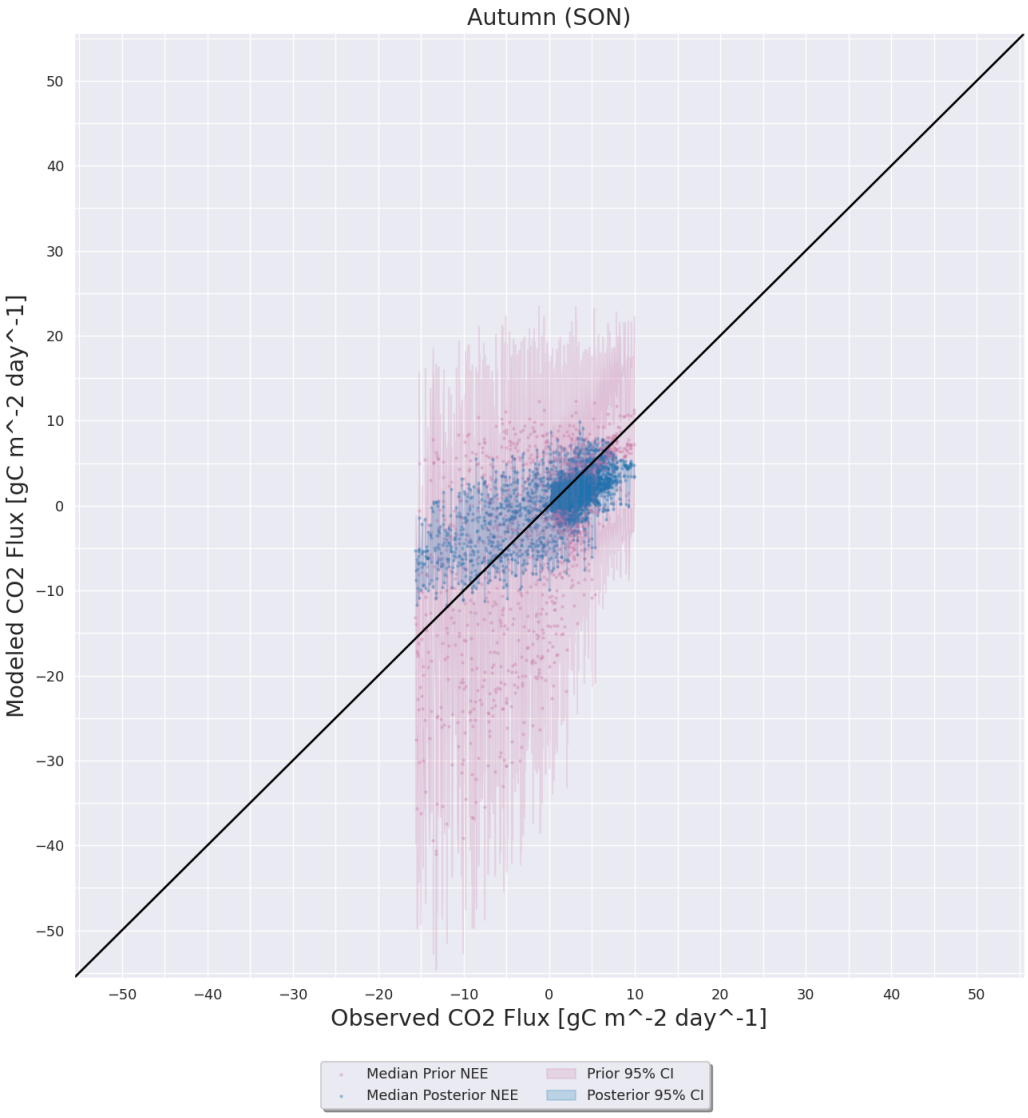

Figure D.74: Same as D.73 except for the Ne3 AmeriFlux site.

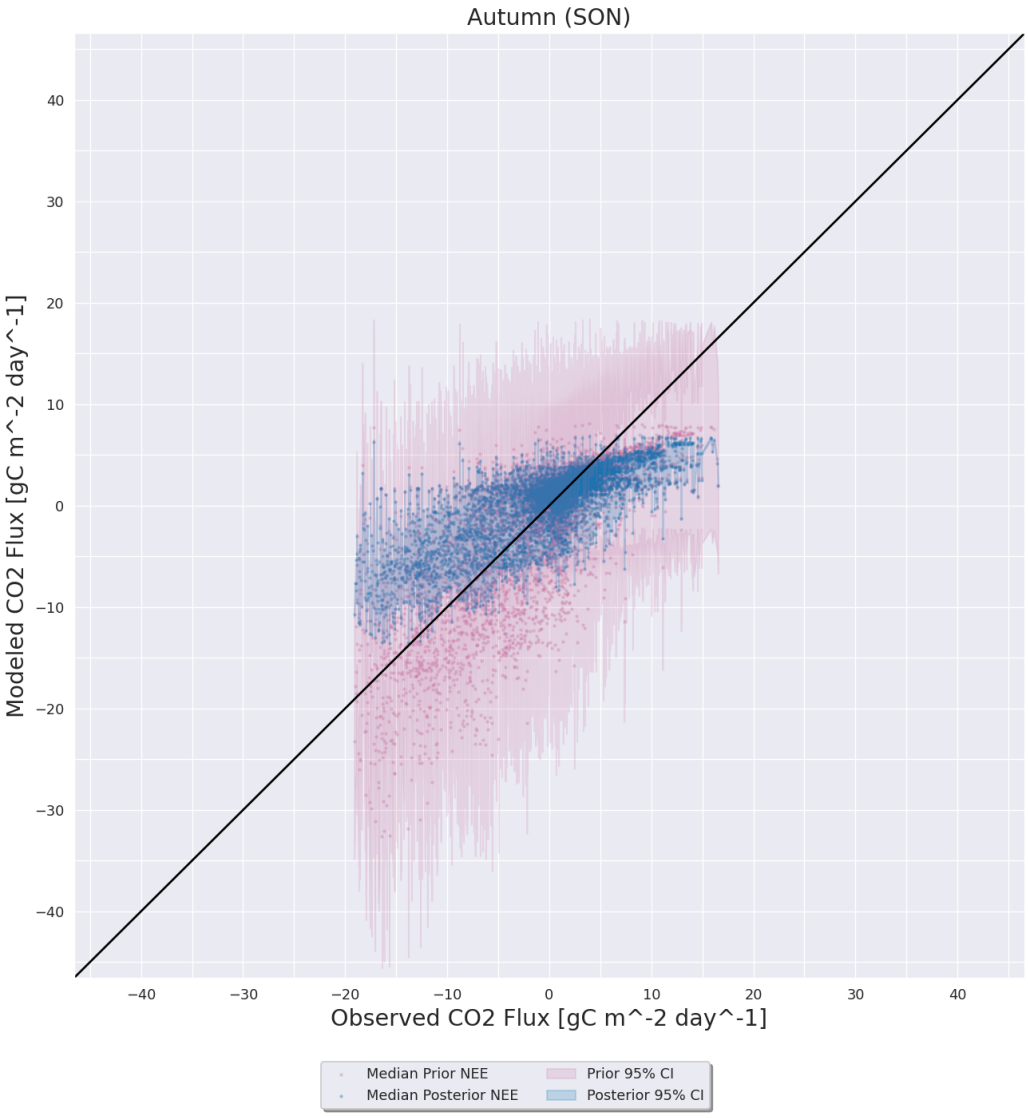

Figure D.75: Same as D.73 except for the KM1 AmeriFlux site.

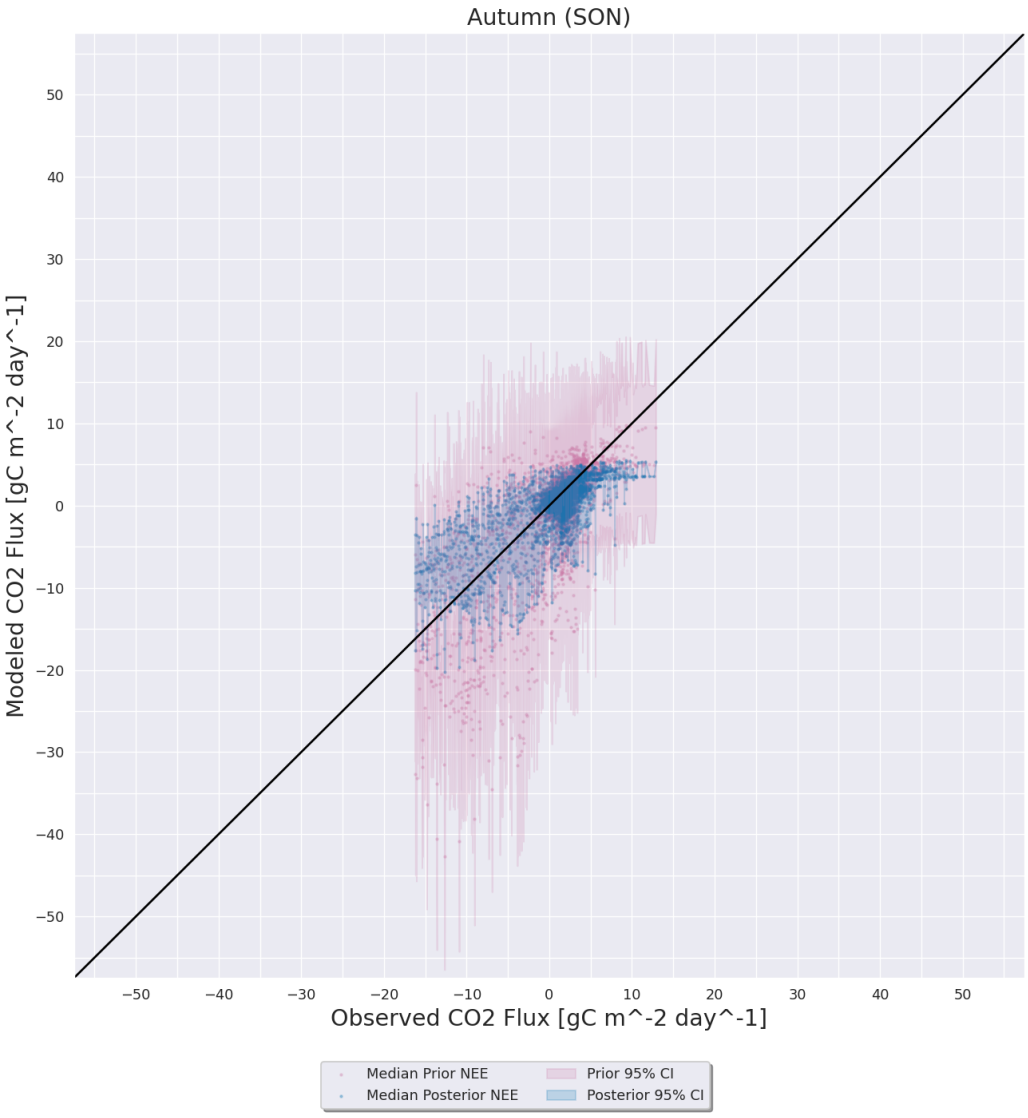

Figure D.76: Same as D.73 except for the Ro1 AmeriFlux site.

D.6 PAR_0 Drop Experiment

D.6.1 Winter (DJF)

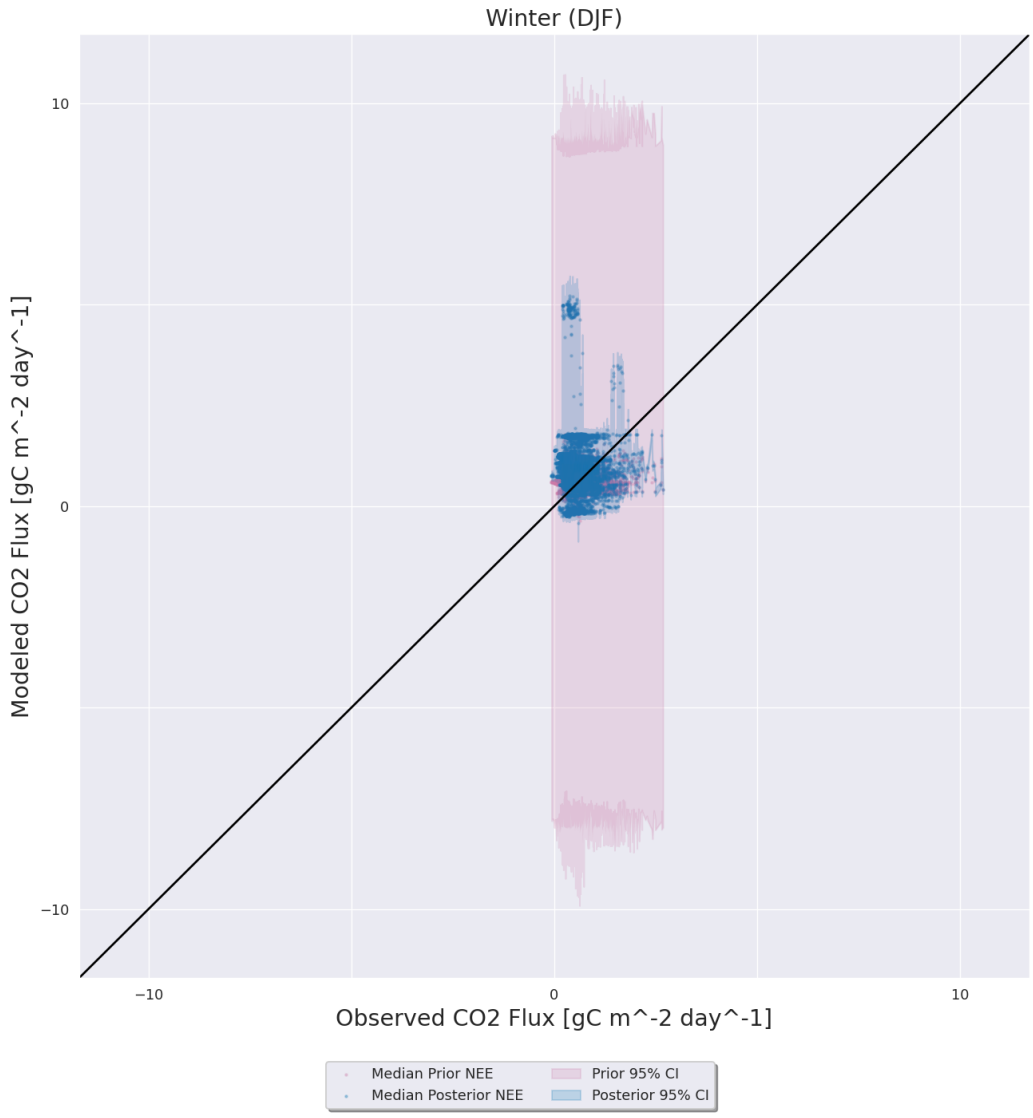

Figure D.77: Same as D.1 except for the PAR_0 parameter drop experiment.

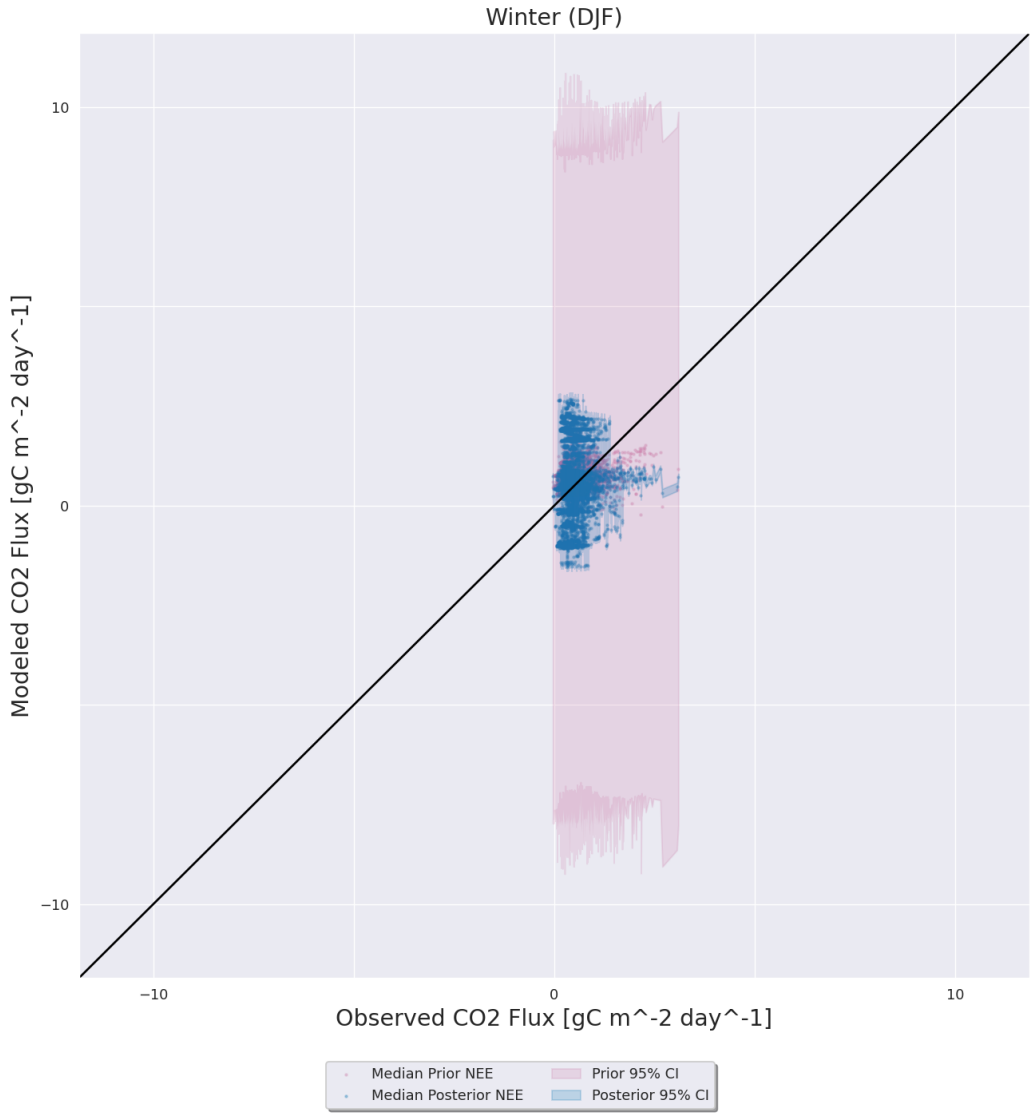

Figure D.78: Same as D.77 except for the Ne3 AmeriFlux site.

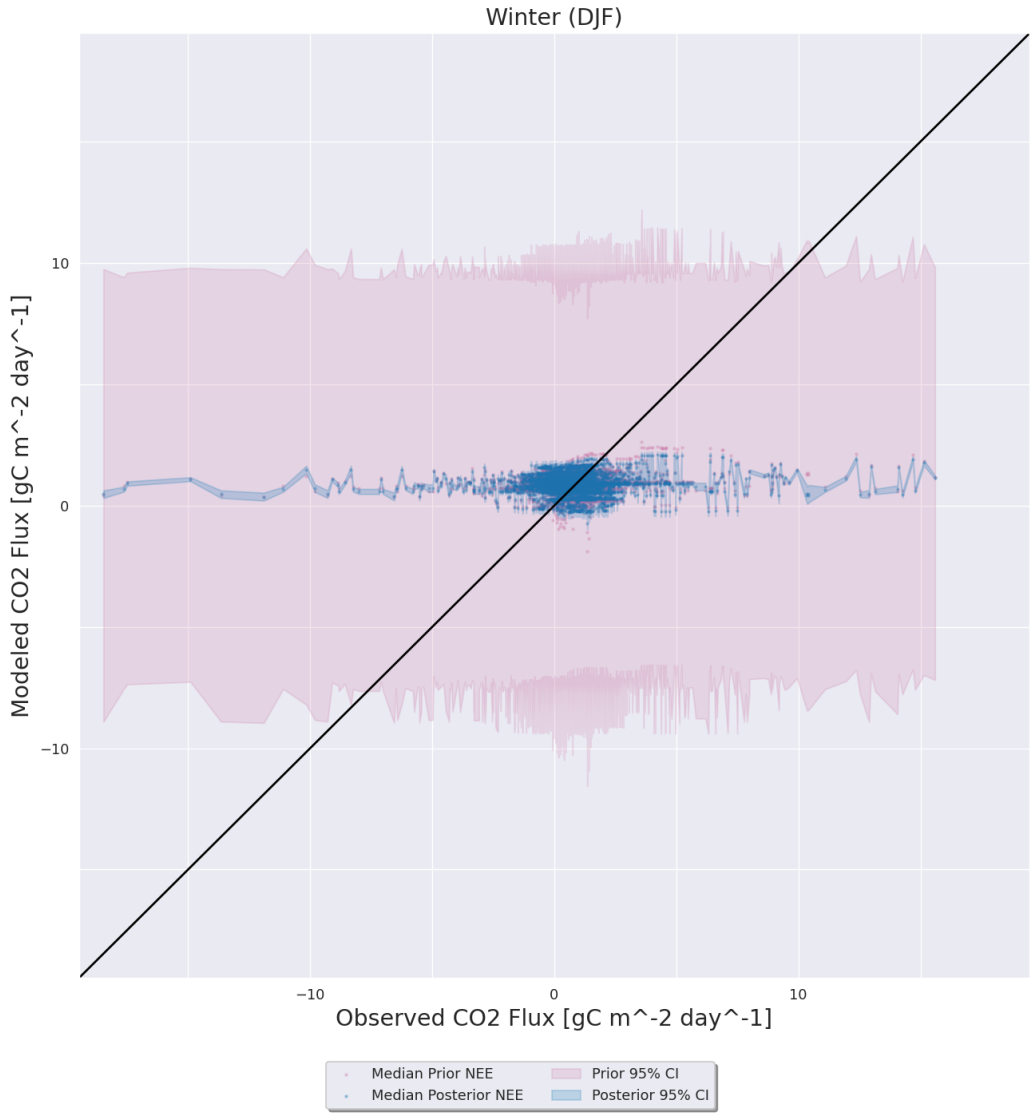

Figure D.79: Same as D.77 except for the KM1 AmeriFlux site.

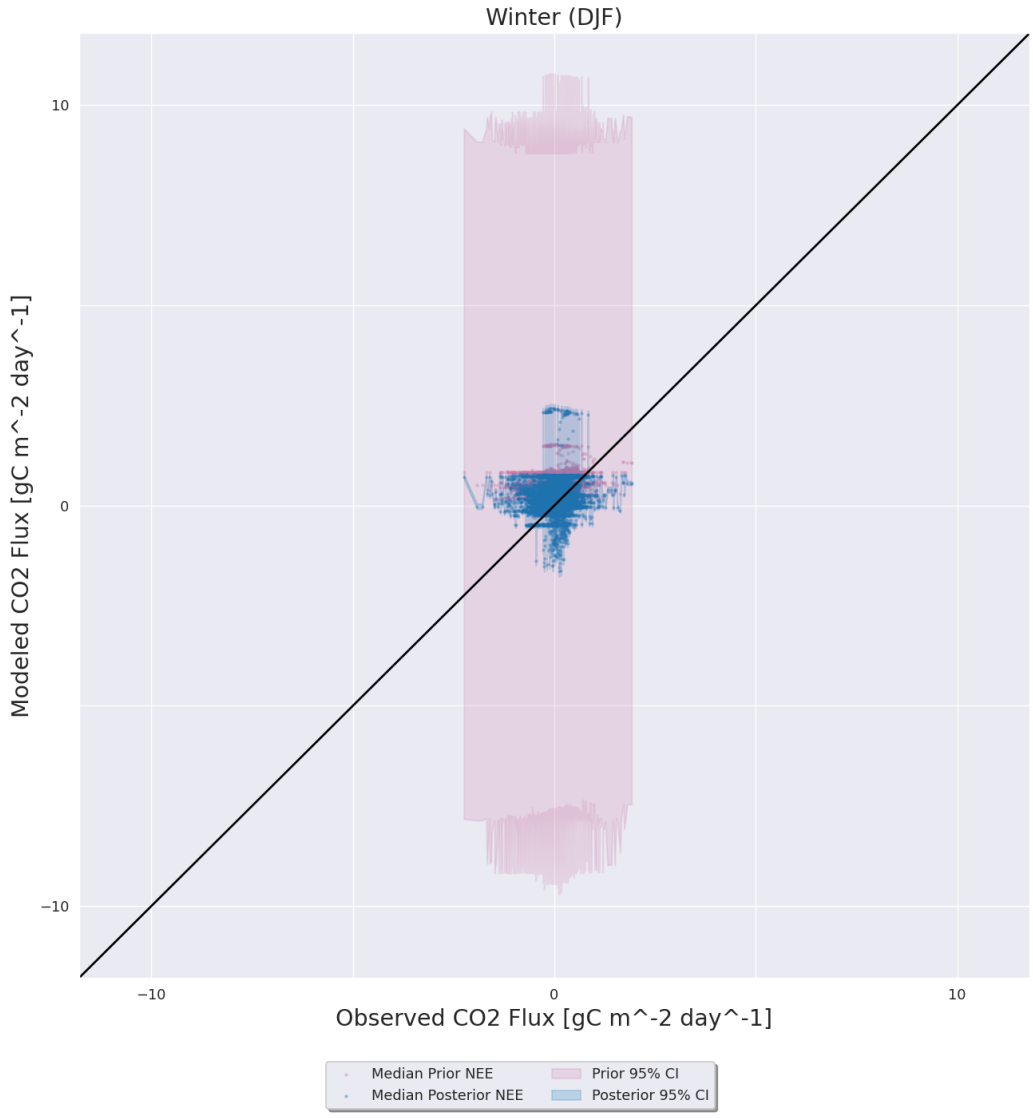

Figure D.80: Same as D.77 except for the Ro1 AmeriFlux site.

D.6.2 Spring (MAM)

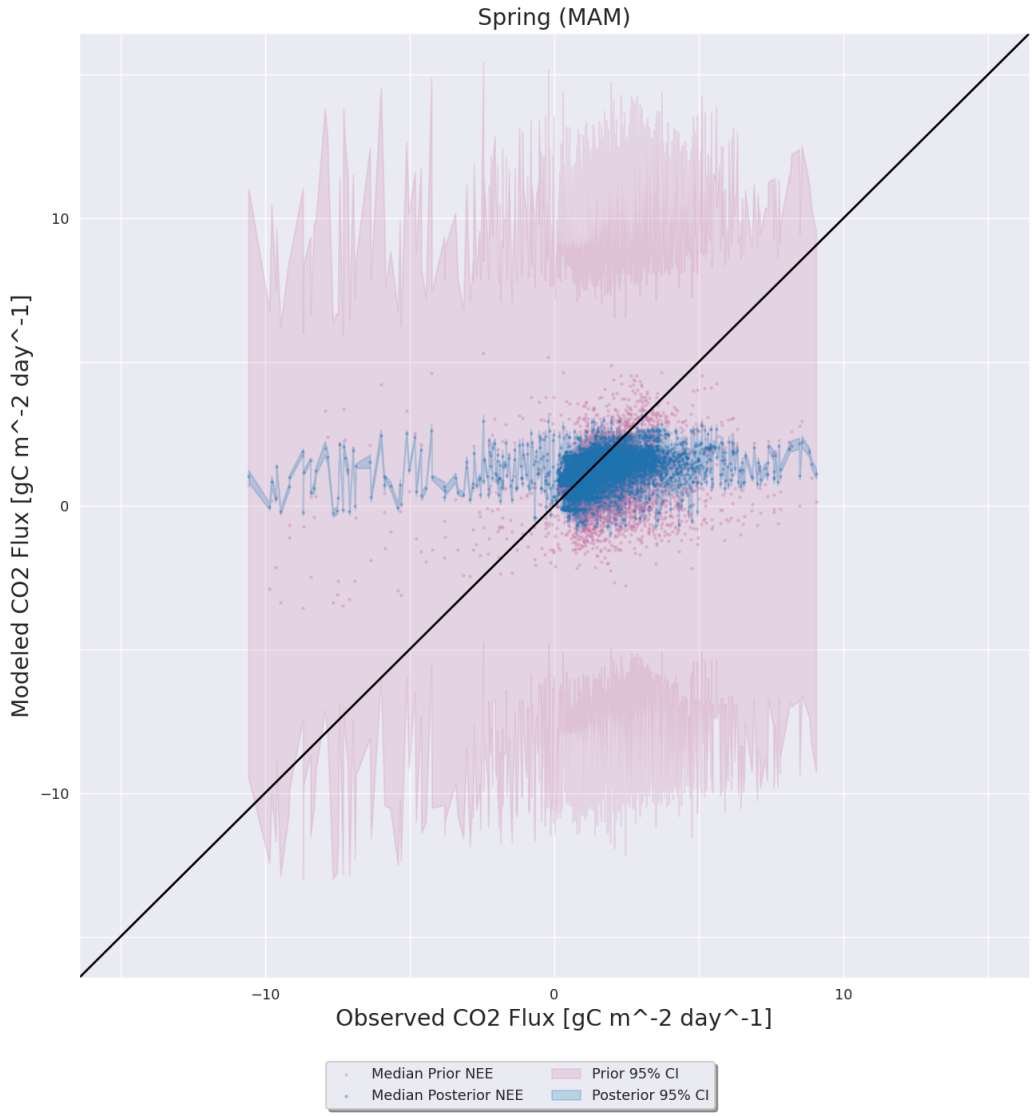

Figure D.81: Same as D.77 except for during the spring (MAM) months.

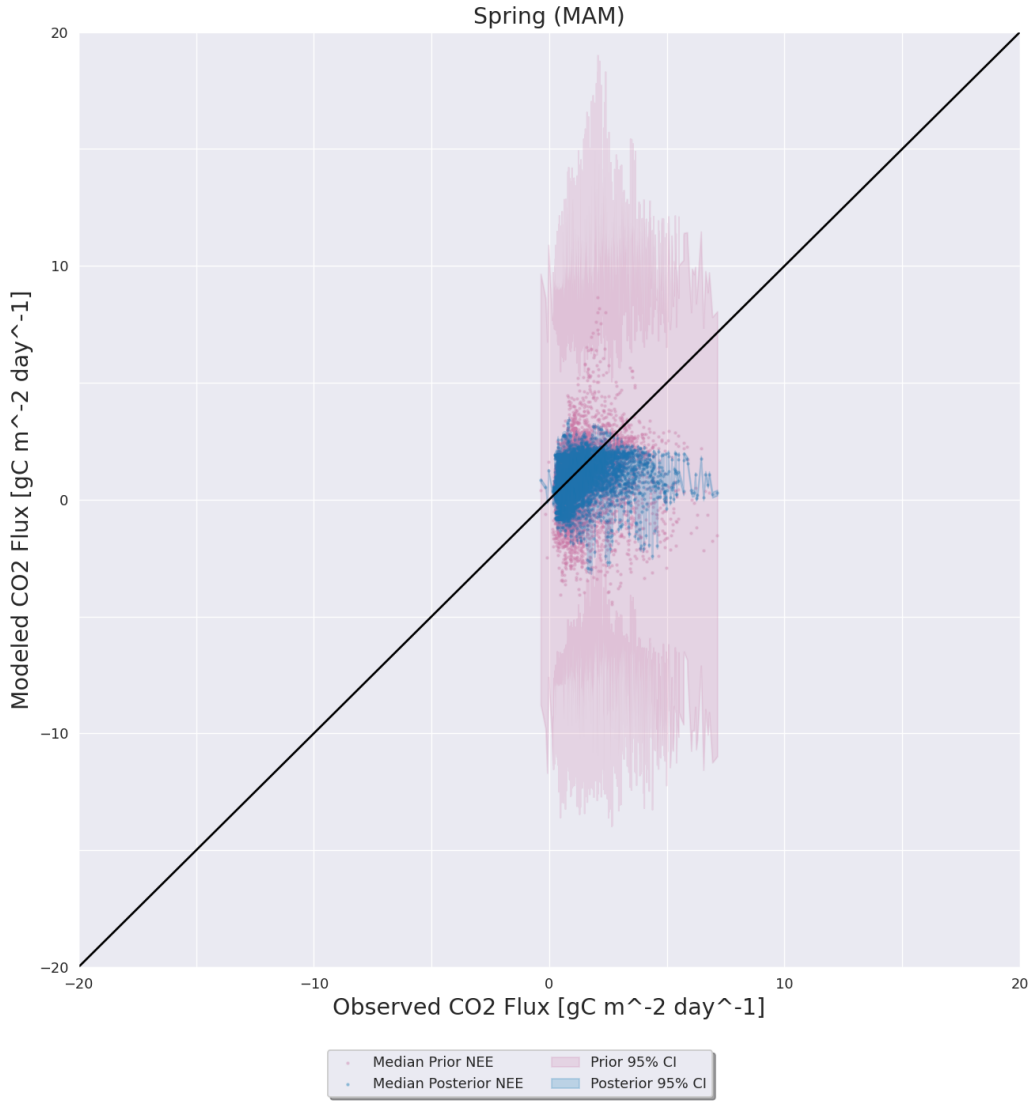

Figure D.82: Same as D.81 except for the Ne3 AmeriFlux site.

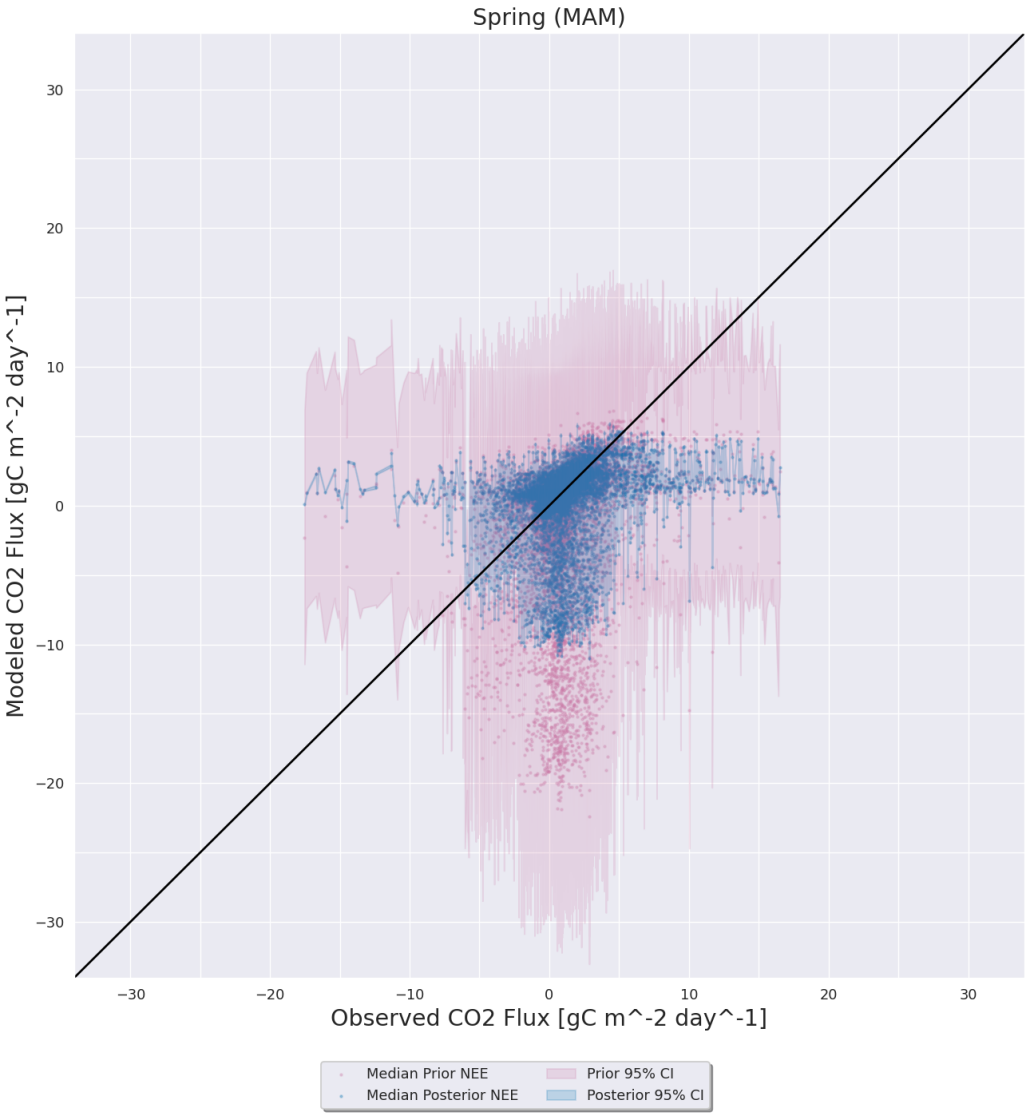

Figure D.83: Same as D.81 except for the KM1 AmeriFlux site.

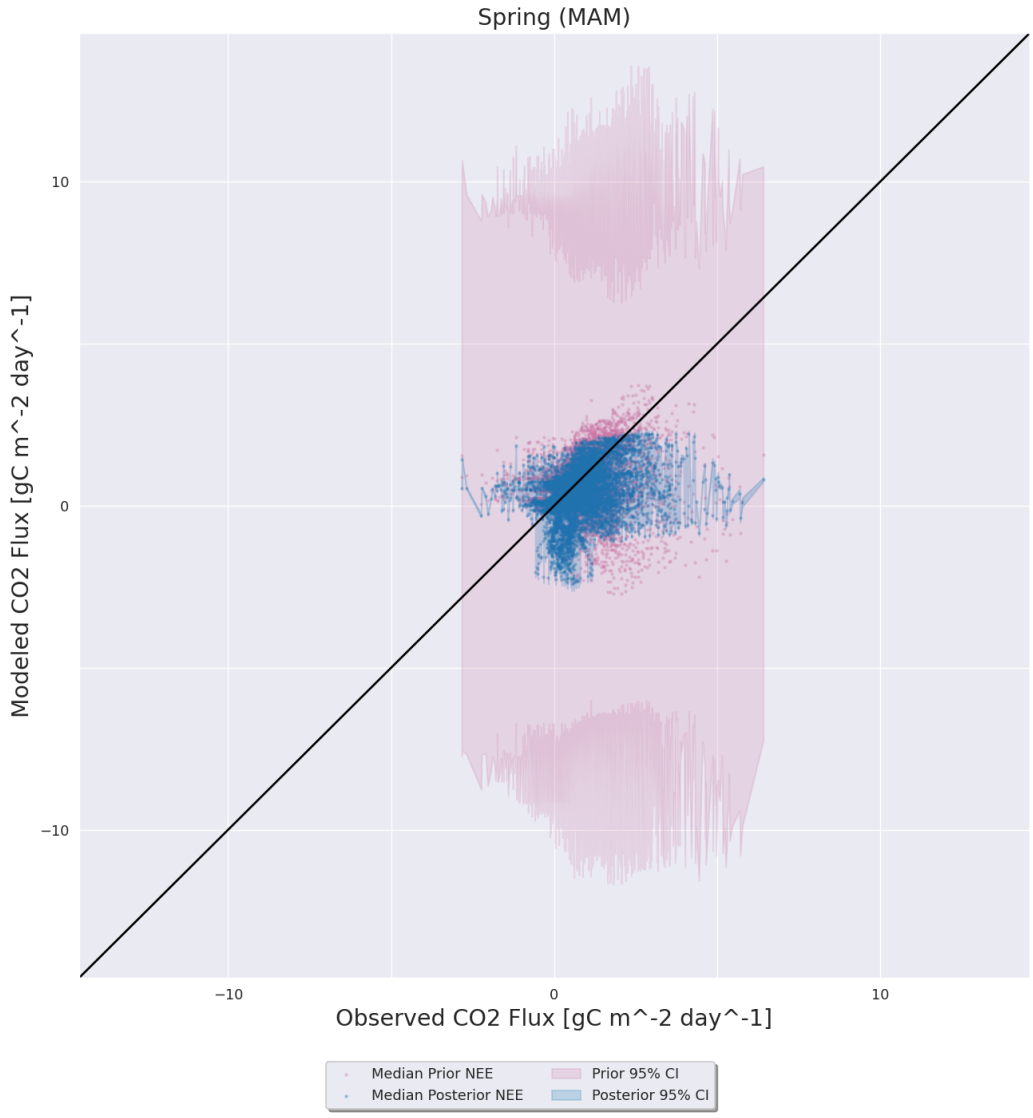

Figure D.84: Same as D.81 except for the Ro1 AmeriFlux site.

D.6.3 Summer (JJA)

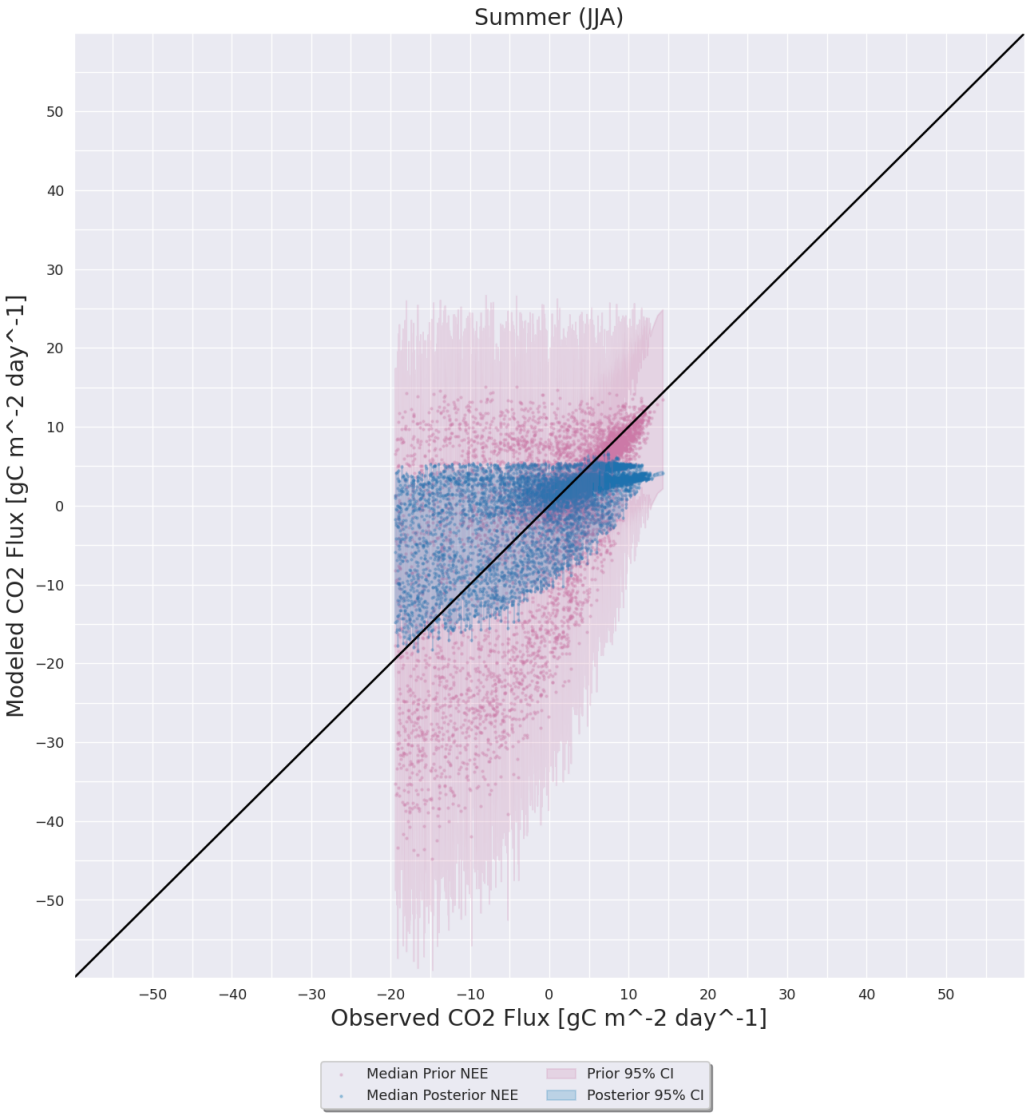

Figure D.85: Same as D.77 except for during the summer (JJA) months.

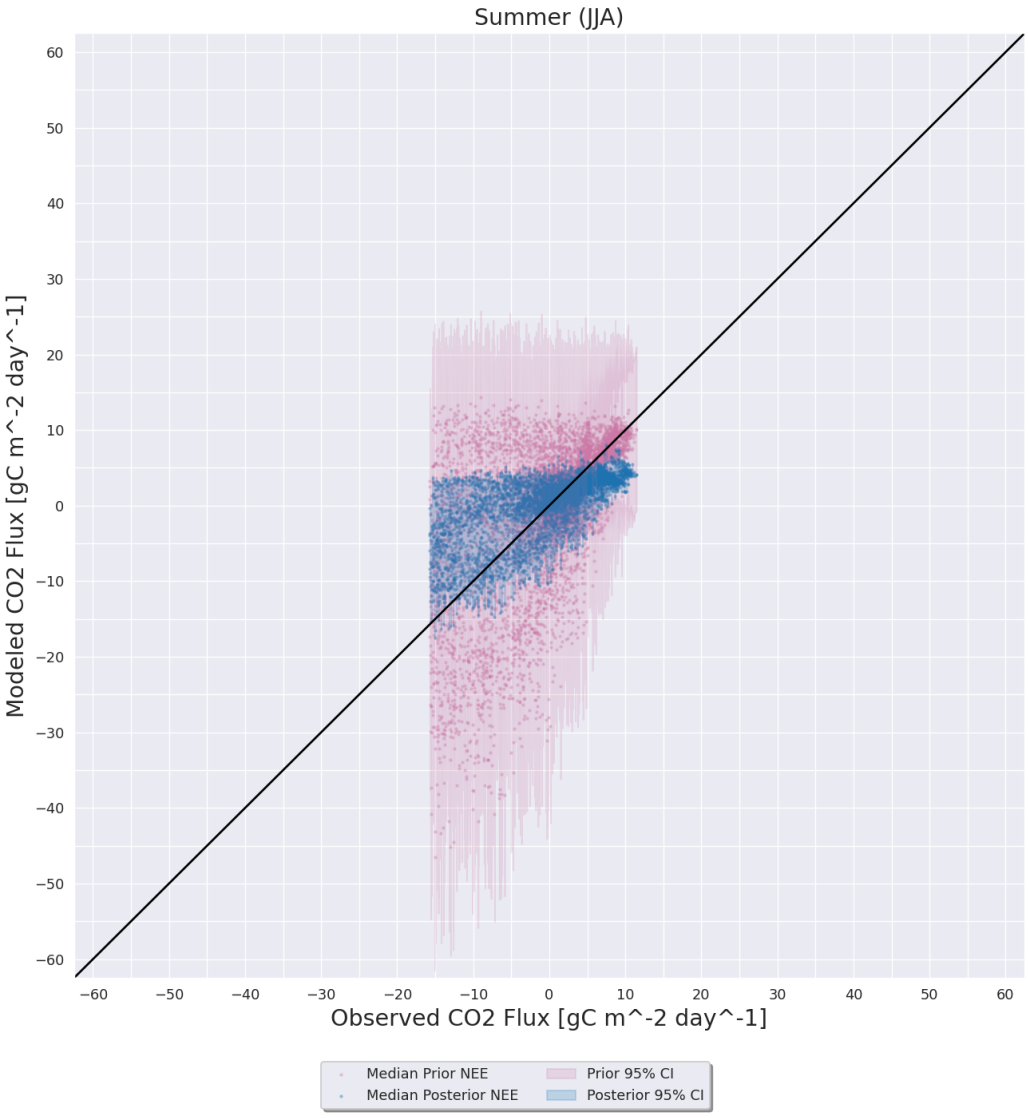

Figure D.86: Same as D.85 except for the Ne3 AmeriFlux site.

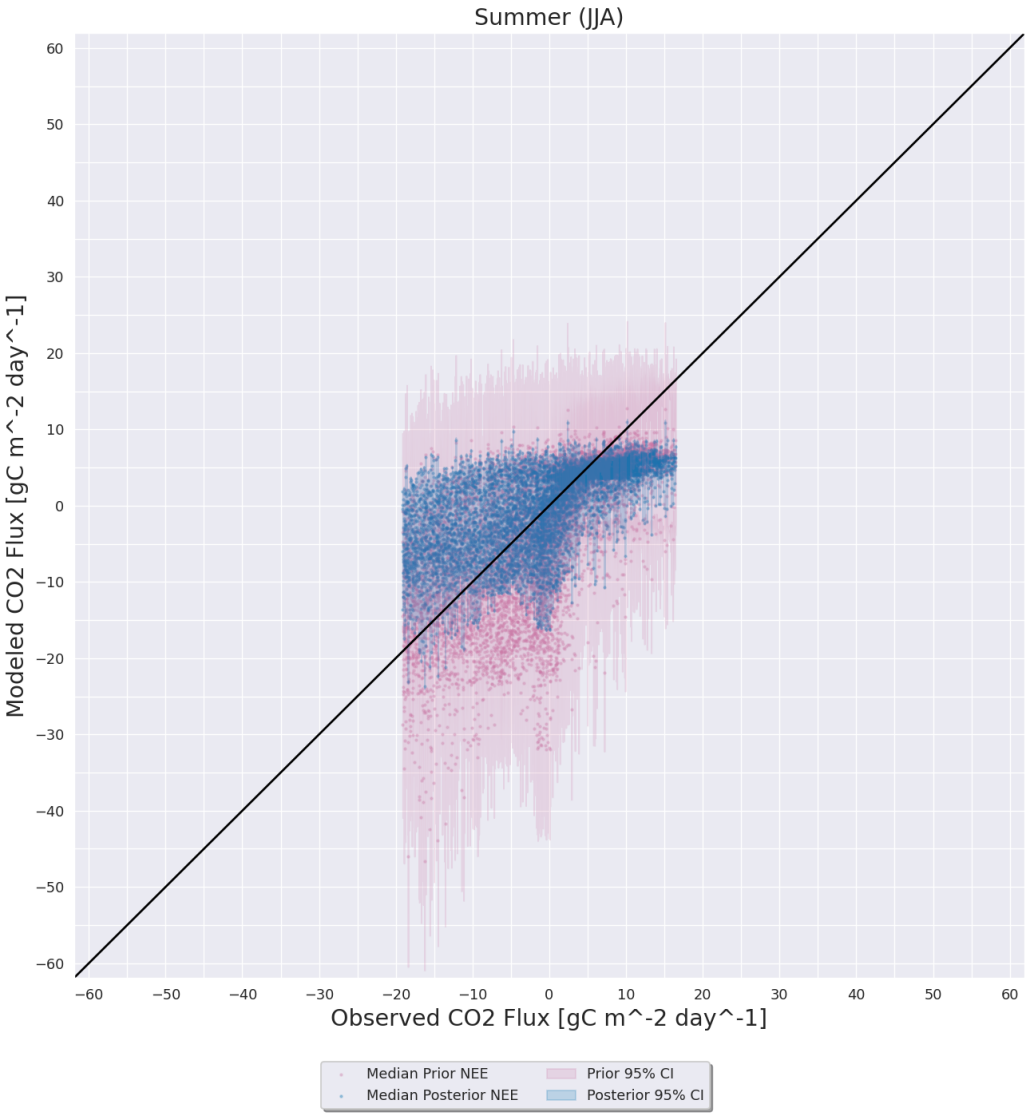

Figure D.87: Same as D.85 except for the KM1 AmeriFlux site.

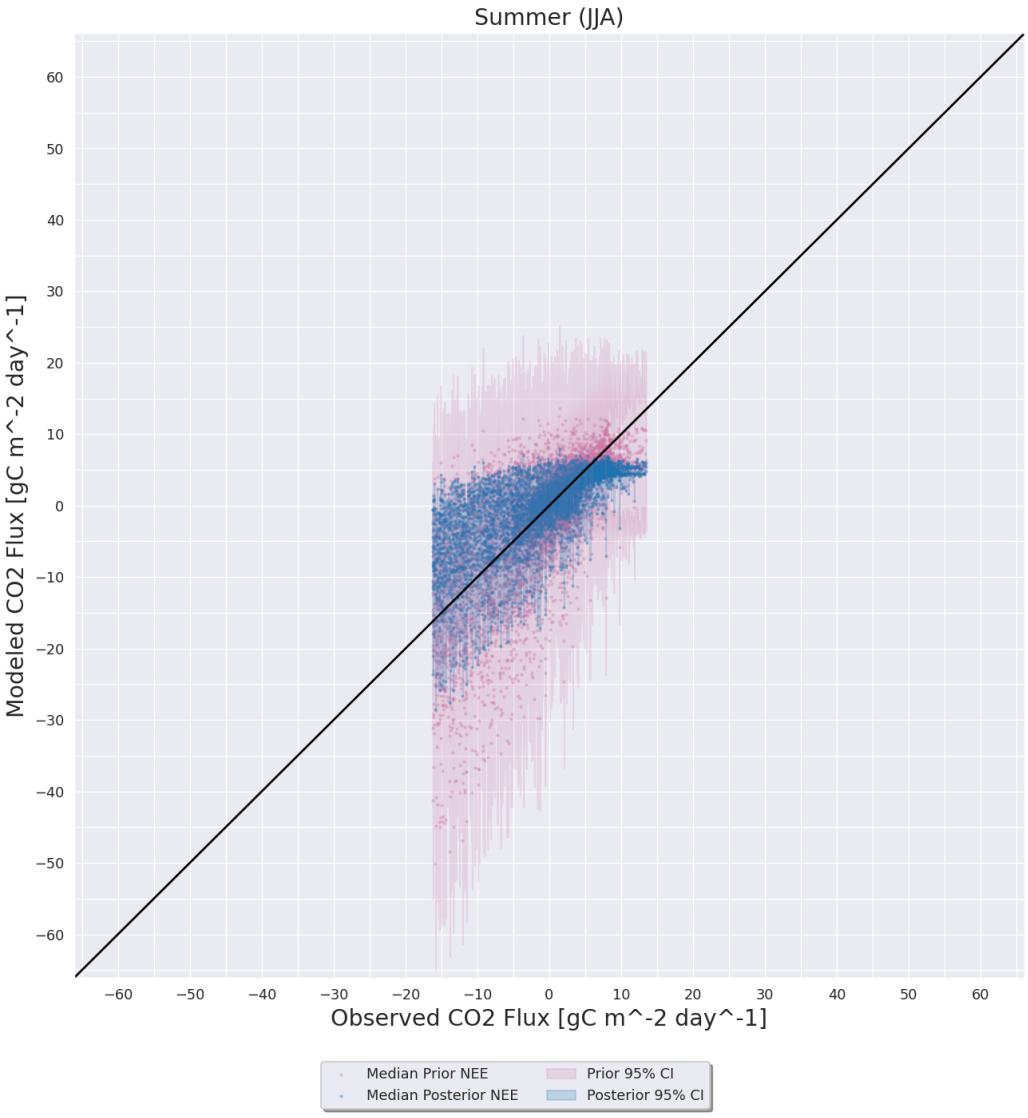

Figure D.88: Same as D.85 except for the Ro1 AmeriFlux site.

D.6.4 Autumn (SON)

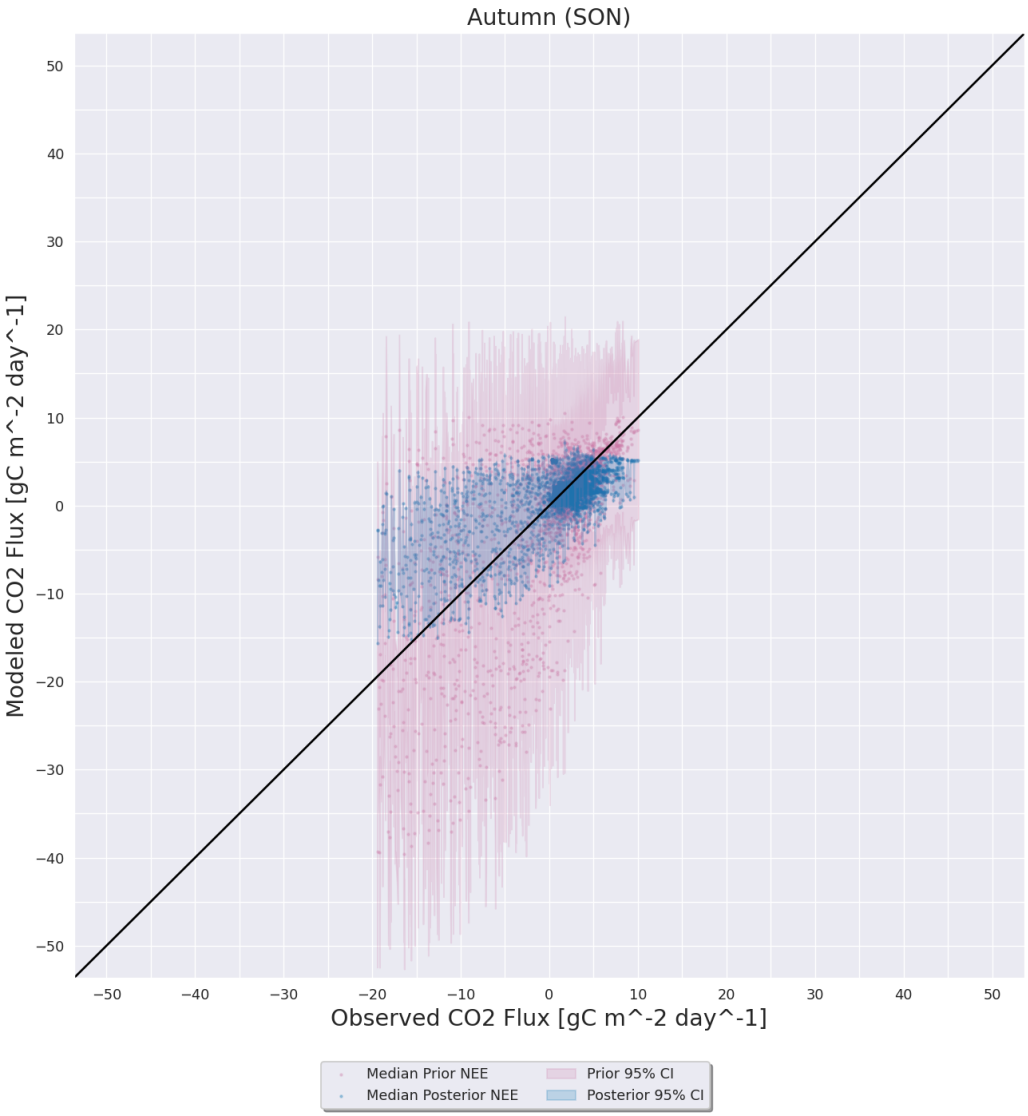

Figure D.89: Same as D.77 except for during the autumn (SON) months.

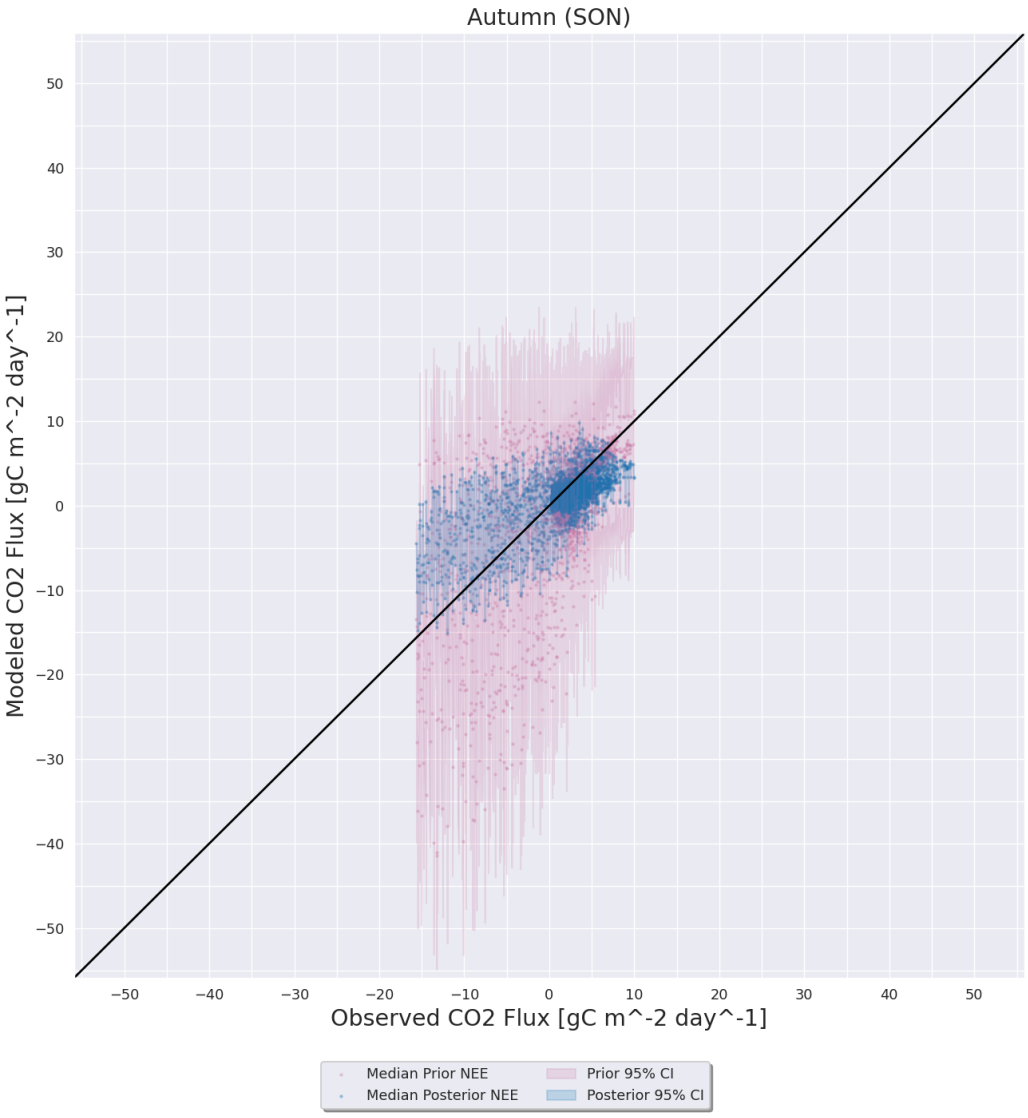

Figure D.90: Same as D.89 except for the Ne3 AmeriFlux site.

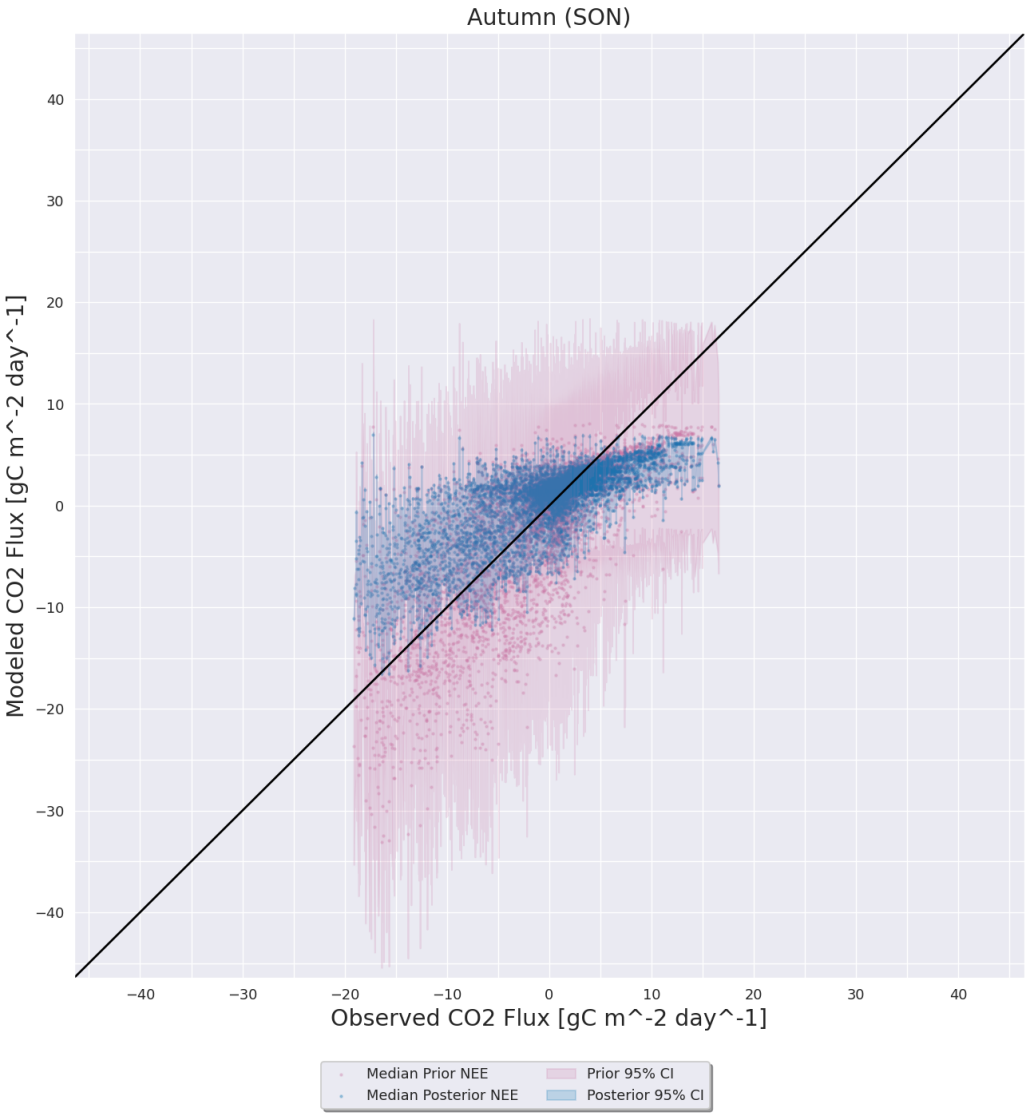

Figure D.91: Same as D.89 except for the KM1 AmeriFlux site.

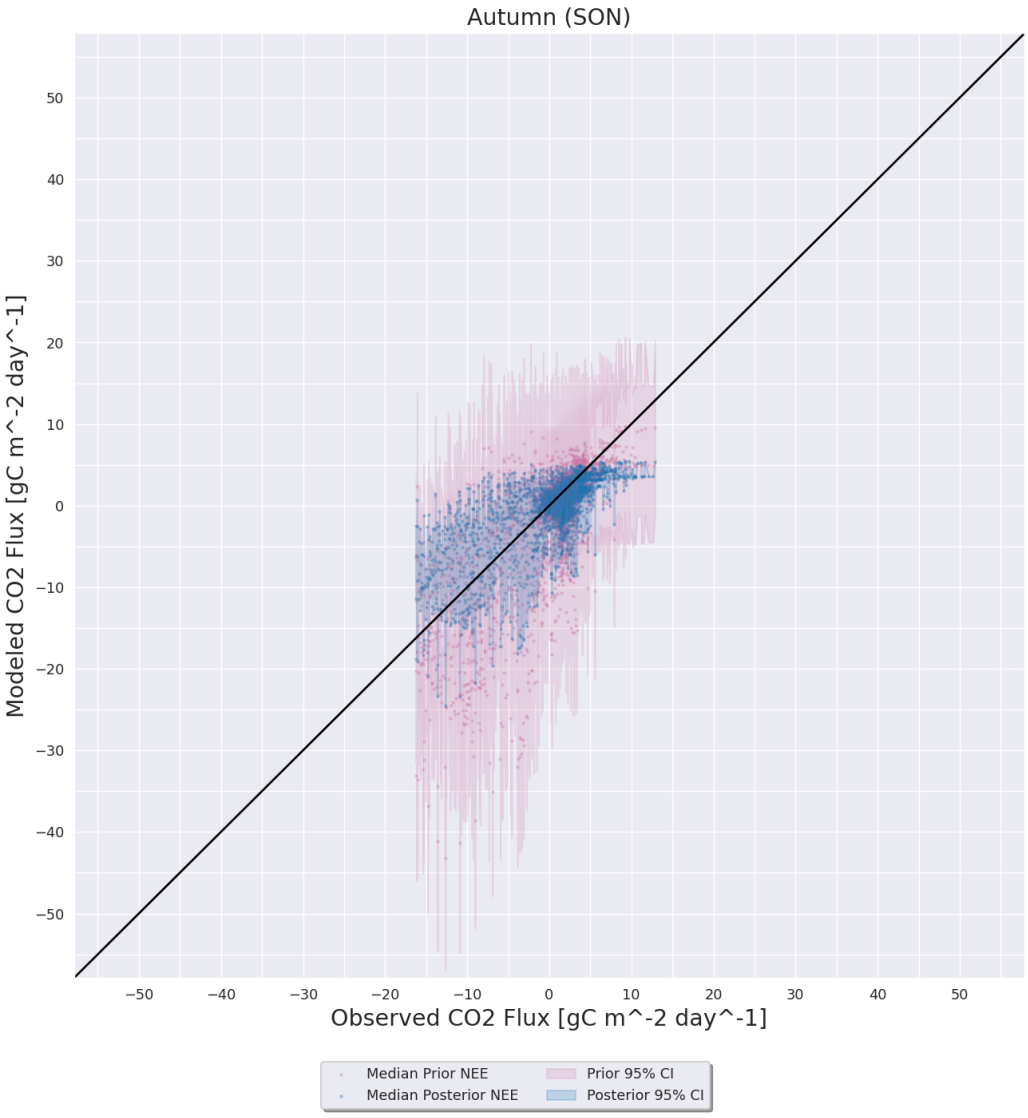

Figure D.92: Same as D.89 except for the Ro1 AmeriFlux site.